UNIVERSIDAD COMPLUTENSE DE MADRID
FACULTAD DE CIENCIAS FÍSICAS

TESIS DOCTORAL
Measurement of the large scale anisotropy in cosmic ray electrons, positrons and protons with the AMS-02 detector on the ISS

MEMORIA PARA OPTAR AL GRADO DE DOCTOR

PRESENTADA POR

Miguel Ángel Velasco Frutos

Director

Jorge Casaus Armentano

Madrid, 2019

© Miguel Ángel Velasco Frutos, 2018

Measurement of the large scale anisotropy in cosmic ray electrons, positrons and protons with the AMS-02 detector on the ISS

Medida de la anisotropía a gran escala en electrones, positrones y protones cósmicos con el detector AMS-02 en la ISS

Miguel Ángel Velasco Frutos

Doctoral Dissertation in Physics

Supervisor: Dr. Jorge Casaus Armentano

UNIVERSIDAD
COMPLUTENSE
MADRID

Facultad de Ciencias Físicas
Curso académico 2017-2018

Trabaja y esfuérzate
con humildad y con respecto.
Lucha contra la oscuridad,
sé la luz que dicen que hemos perdido.

— Campaña publicitaria de *Nike*, 2010-2011

Ars longa, vita brevis

— Hipócrates

ABSTRACT

The field of astroparticle physics started with the discovery of cosmic rays in 1912 by Victor Hess. Cosmic rays, which initially led to important advances in the field of Particle Physics, provide precious information about the violent phenomena in the Universe producing such high-energy particles and the mechanisms of their propagation in the interstellar medium.

In the last years, Cosmic Ray Physics has profited from the rise in space research, and space-based experiments are currently providing direct measurements with unprecedent precision. In this context, recent measurements of the spectra of several cosmic ray species cannot be fully explained within the current paradigm of cosmic ray origin and propagation, and constitute an open window into new phenomena.

In particular, AMS-02 has provided the most precise measurement of the positron fraction, and the positron and electron fluxes. These results allowed an accurate description of the rise in the positron fraction and led to a plethora of models proposed to explain the so-called *positron excess* non consistent with the standard secondary origin of antimatter in cosmic rays. For most cases, the observation requires the inclusion of primary sources, which are typically classified into two scenarios: dark matter or astrophysical origin.

On the other hand, the precise measurement of the proton flux performed by AMS-02 shows a progressive spectral hardening at rigidities above few hundreds of GV non consistent with the traditional single power law predicted by the standard paradigm of cosmic rays. The origin of the spectral hardening may be due to the injection of fresh high rigidity protons by local accelerators or non-standard cosmic ray transport in the Galaxy.

In both cases, the measurement of the anisotropy provides a complementary characterization of the features observed in their fluxes and may help to understand their origin.

Experimentally, the measurement of anisotropies is specially challenging due to the high sensitivity required to determine the small signals that the new phenomena may induce in the arrival directions of cosmic rays. Deviations from isotropy, described at first order by a dipole, are traditionally investigated by comparison with a reference map that provides the directional response of the detector to an isotropic flux.

In this context, this thesis presents a novel method in the construction of reference maps and a set of tools to determine the anisotropy of cosmic rays with space-based detectors, which are valid for any cosmic ray species. The method, which is based in the analysis in individual acceptance bins, does not require an explicit determination of the detector's acceptance. On the other hand, detector's effects, namely, variation of the efficiencies along the spacecraft orbit, are calculated in the

specific coordinate system of analysis. Finally, a binned-likelihood fit is used to compare the sample and the reference map and provides the dipole components.

The techniques developed in this thesis have been applied to the sample of cosmic ray electrons, positrons and protons collected by AMS-02 during its first five years of data taking, from May 2011 to May 2016. This thesis describes the strategy to achieve pure samples of electrons, positrons and protons by means of a cut based selection on the variables measured by the different AMS-02 subdetectors. In addition, a dedicated study of the geographical variations of the detection efficiencies and their implications in the analysis of anisotropies in galactic coordinates is exhaustively presented.

Results of the measurement of the dipole anisotropy in galactic coordinates of cosmic ray electrons, positrons and protons are consistent with isotropy and upper limits on the dipole amplitude are obtained. In particular, a 95% C.I. upper limit of $\delta < 0.01$ was obtained for protons with $R > 300$ GV, and $\delta < 0.02$ and $\delta < 0.006$ for positrons and electrons, respectively, in the energy range $16 < E < 350$ GeV.

In conclusion, this thesis presents a new method for anisotropy searches with space-based detectors, and reports the measurement of the dipole anisotropy in the 5-years samples of electrons, positrons and protons detected by AMS-02.

The outline of this thesis, covering the aforementioned topics, is:

- *Chapter 1* presents an introduction to Cosmic Ray Physics and the current paradigm of cosmic ray origin and propagation. In this context, recent results challenging the standard picture provide a motivation for anisotropy searches with AMS-02. In addition, the state of the art of the anisotropy measurements is reviewed.
- *Chapter 2* describes the AMS-02 experiment and its different subdetectors, with special emphasis in the reconstruction and measurement of the particle's variables.
- *Chapter 3* provides the theoretical framework in the measurement of cosmic ray anisotropies. A review of the coordinate systems where the analysis is carried out is presented. In addition, the chapter presents the new method and the set of statistical tools developed.
- *Chapter 4* validates the method and tools with an AMS-like Toy Monte Carlo detector.
- *Chapter 5* presents the strategy followed in the selection of the proton sample used in the analysis, and a detailed description of the effect that the geographical variation of the proton efficiencies has in the measurement of the proton anisotropies. Finally, the results on the dipole components and dipole amplitude in galactic coordinates are presented.
- *Chapter 6* describes the cut-based analysis used to provide pure samples of electrons and positrons. In addition, an exhaustive study of the geographical variation of the electron efficiencies and its implications in the measurement of lepton anisotropies is presented. The reported results include the anisotropy on the e^+/e^- ratio and individual measurements on e^- and e^+.

- *Chapter 7* summarizes the methodology and results obtained in this thesis and provides prospects of future work.
- *Appendix* provides additional details on some topics mentioned in the thesis as well as the tables containing the numerical results of this work.

RESUMEN

El campo de la física de astropartículas comenzó con el descubrimiento de los rayos cósmicos realizado por Víctor Hess en 1912. Los rayos cósmicos, que inicialmente permitieron importantes avances en el campo de la Física de Partículs, proporcionan información fundamental acerca de los fenómenos violentos en el Universo que los originan, y de los mecanismos de propagación en el medio interestelar.

En los últimos años, el auge de la investigación espacial ha permitido la construcción de experimentos de rayos cósmicos en el espacio, que actualmente están proporcionando medidas directas con una precisión sin precedentes. En este contexto, medidas recientes en los flujos de diversas especies desafían los actuales modelos de origen y propagación de los rayos cósmicos en la Galaxia.

En particular, AMS-02 ha proporcionado medidas precisas en la fracción de positrones y en los flujos individuales de electrones y positrones, que permiten una descripción detallada del llamado *exceso de positrones* no consistente con un origen exclusivamente secundario de la antimateria en los rayos cósmicos. La mayoría de los modelos propuestos para explicar este exceso requieren la inclusión de fuentes primarias de positrones, típicamente clasificadas en dos escenarios: materia oscura y fuentes astrofísicas.

Por otro lado, la medida precisa del flujo de protones realizada por AMS-02 muestra una desviación progresiva del flujo de la ley de potencias predicha por los modelos tradicionales. Esta desviación puede atribuirse a la inyección de protones de alta energía en fuentes próximas, o a mecanismos no convencionales de transporte en la Galaxia.

En ambos casos, la medida de anisotropías ofrece una caracterización complementaria de las observaciones realizadas en los espectros y podría ayudar a entender el origen de estos fenónemos.

Experimentalmente, la medida de anisotropías requiere una alta sensibilidad para determinar las pequeñas señales que los nuevos fenómenos podrían inducir en las direcciones de llegada de los rayos cósmicos. Las desviaciones respecto a la hipótesis de isotropía, descritas a primer orden por un dipolo, se investigan mediante comparación con un mapa de referencia que representa la respuesta direccional del detector a un flujo isótropo.

En este contexto, esta tesis presenta un nuevo método de construcción de los mapas de referencia y un conjunto de herramientas estadísticas para determinar la anisotropía de rayos cósmicos con experimentos en el espacio, válidos para cualquier especie. El método, basado en el análisis en bines individuales de aceptancia, no requiere la determinación explícita de la aceptancia del detector. Por otro lado, los efectos del detector debido a las variaciones de las eficiencias a lo largo de la órbita de la aeronave se determinan directamente en el sistema de coordenadas del análisis. Finalmente, un ajuste binned-likelihood proporciona las componentes dipolares de la anisotropía.

Las técnicas desarrolladas se han aplicado a la muestra de electrones, positrones y protones detectados por AMS-02 durante los primeros cinco años de toma de datos, desde mayo de 2011 a mayo de 2016. Esta tesis describe la estrategia seguida en la obtención de muestras puras de electrones, positrones por medio de cortes de selección aplicados sobre las variables medidas por los diferentes subdetectores.

Los resultados de la medida de la anisotropía dipolar en coordenadas galácticas de electrones, positrones y protones son consistentes con isotropía, lo que permite obtener límites superiores para la amplitud del dipolo. En particular, para protones con $R > 300$ GV se obtiene el límite $\delta < 0.01$ al 95% C.I, mientras que para electrones y positrones en el rango $16 < E < 350$ GeV los límites obtenidos son $\delta < 0.006$ y $\delta < 0.02$, respectivamente.

Para concluir, esta tesis describe un nuevo método para la búsqueda de anisotropías con detectores en el espacio, y presenta los resultados de la medida de anisotropía en las muestras de electrones, positrones y protones recogidas por AMS-02 durante los primeros cinco años de toma de datos.

El guión de la tesis, que desarrolla estos temas, es:

- El *capítulo 1* presenta una introducción a la Física de Rayos Cósmicos y al paradigma actual que describe su origen y propagagión. En este contexto, las medidas recientes que desafían el modelo tradicional motivan la medida de anisotropías con AMS-02. Además, se revisa el estado del arte en las medidas de anisotropías en rayos cósmicos.
- El *capítulo 2* describe el experimento AMS-02 y sus diferentes subdetectores, con especial énfasis en la reconstrucción y medida de las propiedades de la partícula.
- El *capítulo 3* proporciona el marco teórico en la medida de anisotropías, junto con una descripción de los sistemas de coordenadas de análisis. Además, el capítulo presenta el nuevo método y las herramientas estadísticas desarrolladas.
- El *capítulo 4* presenta una validación de los métodos de análisis con un Toy Monte Carlo que simula un detector ideal tipo AMS-02.
- El *capítulo 5* presenta la estrategia de selección de la muestra de protones, y una descripción detallada de la variación geográfica de las eficiencias de protones y su efecto en la medida de anisotropías en coordenadas galácticas. Finalmente, se proporcionan los resultados de las componentes dipolares y la amplitud dipolar de la anisotropía.
- El *capítulo 6* describe los cortes de selección utilizados para obtener muestras puras de electrones y positrones, y un estudio exhaustivo de la dependencia geográfica de las eficiencias de electrones y su impacto en la medida de anisotropías de leptones. Los resultados incluyen la medida de la anisotropía en e^+/e^- así como medidas individuales en e^- y e^+.
- El *capítulo 7* resume la metodología y resultados obtenidos en esta tesis y describe las perspectivas de futuro de este análisis.

- El *apéndice* contiene material adicional sobre algunos detalles mencionados a lo largo de esta tesis y recoge las tablas con los resultados numéricos de este trabajo.

LIST OF SELECTED PUBLICATIONS

The work reported in this thesis has been presented by its author in several AMS Collaboration meetings. In addition, the efforts carried out in this thesis as well as the obtained results gave rise to a number of contributions to international conferences. This list is not a complete record of the author's publications but rather an abbreviated summary of the works profiting the achievements of this thesis.

- M.A. Velasco and J. Casaus on behalf of the AMS Collaboration. Measurement of anisotropies in cosmic ray arrival directions with the AMS Detector on the Space Station, in *Proceedings of the The European Physical Society Conference on High Energy Physics*, July, 2017. https://doi.org/10.22323/1.314.0621 *Best poster award of EPS-HEP 2017*

- M.A. Velasco, J.Casaus and C. Mañá. Reference maps for anisotropy searches with AMS-02, in *Proceedings of the 35th International Cosmic Ray Conference (ICRC2017)*, July, 2017. https://pos.sissa.it/301/196/

- I. Gebauer on behalf of the AMS Collaboration. Measurement of anisotropies in cosmic ray arrival directions with the Alpha Magnetic Spectrometer on the ISS, in *Proceedings of the 35th International Cosmic Ray Conference (ICRC2017)*, July, 2017. https://pos.sissa.it/301/186/

- G. La Vacca on behalf of the AMS Collaboration. Search for Cosmic Ray Anisotropy with the Alpha Magnetic Spectrometer on the International Space Station, in *Proceedings of the XXV European Cosmic Ray Symposium*, September, 2016. https://arxiv.org/abs/1612.08957

- M. A. Velasco *et al.*. Estudio de la anisotropía dipolar en e^- y e^+ con AMS-02, in *Libro de Resúmenes de la XXXV Reunión Bienal de la RSEF y del 25o Encuentro Ibérico de Enseñanza de la Física* (RSEF), July, 2015.

CONTENTS

LIST OF FIGURES

LIST OF TABLES

1 COSMIC RAY PHYSICS

1.1 INTRODUCTION

Cosmic rays are relativistic elementary particles and nuclei constantly hitting the Earth's atmosphere from outer space. The first hints about its existence started at the beginning of the 20th century, when the independent measurements of the spontaneous discharge rate of the electroscope by C.T.R. Wilson in England [1], and J. Elster and H. Geitel in Germany [2] evidenced the existence of radiation outside the apparatus. Although an extraterrestrial origin of this radiation was proposed, this hypothesis was discarded in favor of an Earth's radioactive source. In order to discern the origin, measurements on the altitude variation of the ionization rate were carried out by T. Wulf (1909) [3] and D. Pacini (1912) [4]. Despite of their investigations on the altitude dependence of the radiation, the issue of its origin was still unclear. The puzzle was finally settled by V. Hess, who is attributed to be the discoverer of cosmic rays. Between 1911 and 1912, Hess carried out a set of balloon flights, where his precise measurements [5] on the ionization rate clearly showed a considerable increase with the height from an altitude of 1 km, which supported the external origin of radiation. The discovery was confirmed in 1926 by R. Millikan and G. Cameron, who called the radiation *cosmic rays* [6].

Since then, many experiments conducted with the aim of understanding the nature of cosmic rays led to important advances in the fields of Nuclear and Particle Physics. In particular, from the 1930s to the 1950s, cosmic rays were used to provide a source of high-energy particles that allowed the discovery of subatomic particles, such as positrons, muons and pions. On the other hand, apart from the contributions of Cosmic Ray Physics to other disciplines, the main investigation has been focused in the study of the origin, acceleration mechanisms and propagation in the galactic and intergalactic medium. In the last decades, Cosmic Ray Astrophysics, in synergy with Particle Physics and Cosmology, is providing precious information about fundamental questions regarding the nature and the ultimate constituents of matter in the Universe.

1.1.1 *Flux and composition*

Cosmic rays are charged particles, mainly fully ionized atomic nuclei (98%), and electrons (2%), as observed at the top of the atmosphere. In particular, the nuclei component is constituted by protons (87%), helium nuclei (12%) and heavier nuclei (1%). A small fraction of antimatter, namely, positrons and antiprotons, is also observed.

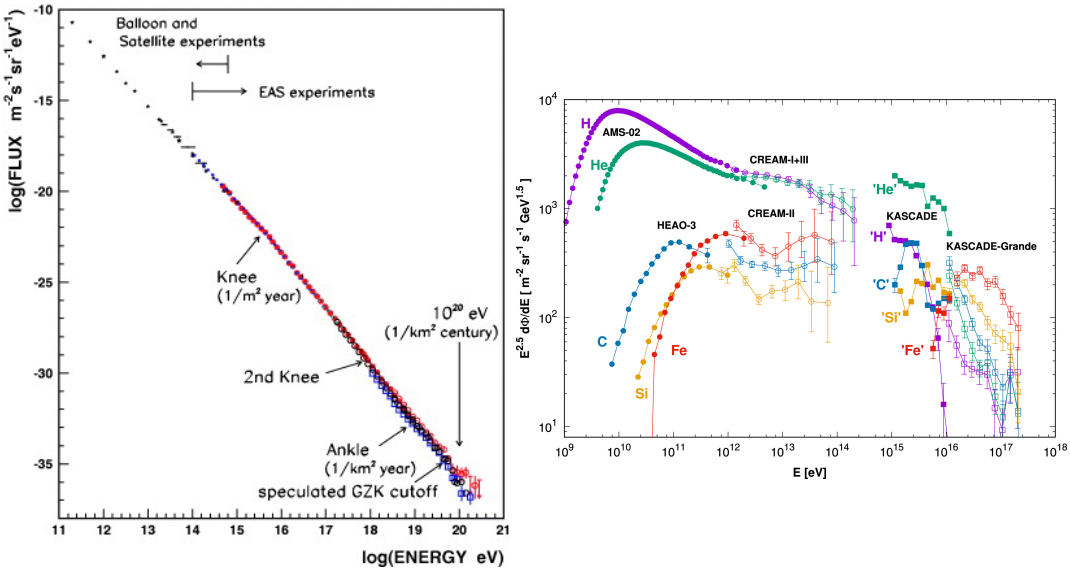

FIGURE 1.1: *(Left)* All-particle energy cosmic ray spectrum, showing the distinct features and changes of the spectral index, from [7]. *(Right)* Spectra of different elements by AMS-02, HEAO-3, CREAM and the air-shower arrays KASCADE and KASCADE-Grande, from [8]

Cosmic rays reaching the Earth from the outer space may remain unaltered from the sources, which are known as *primary cosmic rays*; or may be the product of inelastic collisions in the Interstellar Medium (ISM) in the so-called *spallation* or *fragmentation* processes, or decays of unstable species during its propagation, called *secondary cosmic rays*.

1.1.1.1 *Flux of cosmic rays*

The all-particle energy spectrum of cosmic rays observed at Earth spans 32 orders of magnitude in an energy range of 14 orders of magnitude, starting from below 1 GeV up to beyond 100 EeV (figure 1.1).

The very first part of the spectrum, from few eV to $\sim$ 1 GeV, cosmic rays are produced locally, as a result of *solar flare eruptions* or *coronal mass ejections*, where charge particles are released from the Sun's corona and constitute the so-called *solar wind*.

The vast majority of cosmic rays come from outside the solar system. At energies below $\sim$ 10 GeV/nucleon, the cosmic ray flux shows a suppression due to the effect of the solar wind. This phenomenon, called *solar modulation* is caused by energy losses produced when the incoming stream of cosmic rays enters the heliosphere and interacts with the solar wind. Therefore, solar modulation depends on the solar activity, which in turn translates into a time dependence of the cosmic ray fluxes at the low energy part of the spectrum.

At energies above few GeV, where the effects of the solar modulation are negligible, the all-particle differential energy spectrum of cosmic rays follows a steeply falling power law

$$\frac{dN(E)}{dE} \propto E^{-\gamma}, \tag{1.1}$$

with a spectral index close to $\gamma \sim 3$. The spectrum has several distinctive features:

- Above few GeV up to the so-called *knee* at $\sim 3 - 4 \times 10^6$ GeV/nucleon, the spectrum follows a simple power law of spectral index $\gamma \sim 2.7$.
- For energies above the *knee* and up to the so-called *second knee*, at $\sim 10^8$ GeV/nucleon, the spectrum steepens to $\gamma \sim 3.1$.
- Between the *second knee* and the so-called *ankle*, at $\sim 5 \times 10^9$ GeV/nucleon, the spectrum further steepens to $\gamma \sim 3.3$.
- At the ankle, the spectrum becomes harder, again to $\gamma \sim 2.7$.
- At energies above $\sim 4 - 5 \times 10^{10}$ GeV/nucleon, a strong suppression in the cosmic ray spectrum is observed, with spectral index $\gamma \sim 4.2$.

Cosmic rays below 10^9 GeV/nucleon are assumed to have a galactic origin. In this respect, many theories attribute the knee to be the limit on the maximum energy attainable by most cosmic ray accelerators in the Galaxy, namely, supernova remnants (SNRs). Other theories consider the effects of propagation and confinement in the Galactic Magnetic Field (GMF) to be the origin of the knee. According to this, the knee would be due to the leakage of particles out of the Galaxy during their propagation.

The mass composition in the 10^6-10^8 GeV range has been studied by several ground-based experiments and the majority of them concludes that the composition changes from lightweight particles, such as protons and helium, to heavier nuclei [9]. Therefore, the knee is attributed to be the *proton knee* and beyond that point the cosmic ray composition varies to heavier elements, dominated by iron at the second knee, or *iron knee* [10]. Above this second knee, the cosmic ray composition becomes gradually lighter again up to the ankle [11].

At the ankle, between 10^9-10^{10} GeV, the transition from galactic to extragalactic cosmic rays is supposed to occur. Cosmic rays at those energies cannot be confined within the Galaxy since the corresponding Larmor radius[1] becomes larger than the dimensions of the galactic disk.

Finally, at $\sim 5 \times 10^{10}$ GeV/nucleon a strong suppression in the flux is observed. This suppression, called *GZK cut-off* [12, 13], is attributed to the inelastic collisions of ultrahigh energy cosmic rays with the photons of the cosmic microwave background (CMB).

1.1.1.2 *Chemical abundances of galactic cosmic rays*

The chemical abundances of cosmic rays provide valuable information about the production and propagation processes from their sources to the Earth. In particular,

1 In a magnetic field the trajectory of a charged particle is curved. The radius of the curvature, Larmor radius or gyroradius is given by the relation between the energy, E, the charge of the particle, Ze, and the magnetic field, B, $r_{\mathrm{L}} \approx 1.08\mathrm{pc} \times \left(\frac{E}{10^6\ \mathrm{GeV}}\right)\left(\frac{\mu\mathrm{G}}{ZeB}\right)$.

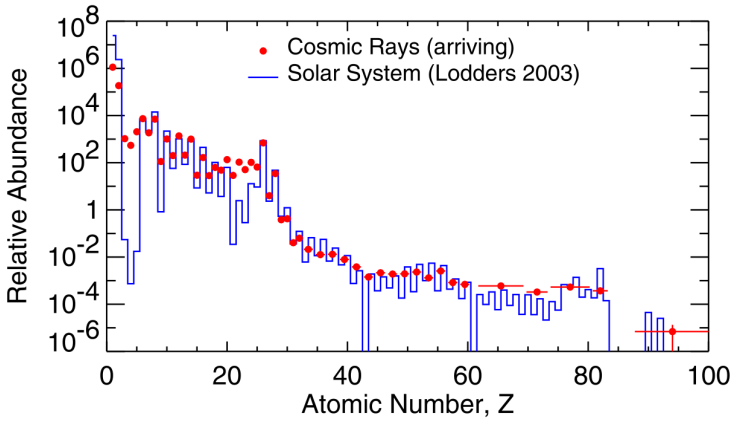

FIGURE 1.2: Elemental abundances of galactic cosmic rays for $E \leq 1$ GeV/nucleon, relative to carbon, compared to the solar system chemical composition, from [14].

the comparison of the relative abundance of elements in galactic cosmic rays and solar system reveals many similarities and some interesting discrepancies (figure 1.2). To some extent, similarities suggest an identical origin for both, namely, nucleosynthesis processes in the stellar interior. However, the discrepancies may be connected to different features during the cosmic ray production or propagation:

- The observed under-abundance of hydrogen and helium in the cosmic rays with respect to the solar system composition is poorly understood. Some explanations suggest that hydrogen and helium are relatively hard to ionize due to the high ionization energies for these elements, therefore, only a small amount can be accelerated efficiently. Other hypothesis propose a genuine difference in the composition at the source.
- The *odd-even effect*: even-even nuclei (even Z and N) are more stable and bound than odd-even and odd-odd nuclei, hence are more copiously produced in the stellar nucleosynthesis. This effect, known to be present in the solar system abundances is also observed in cosmic rays.
- The peaks of abundance observed at C, N, and O, and at the iron group are similar in both cosmic rays and Solar system abundances, which supports the identical origin due to the thermonuclear reactions in the stars.
- Some elements that are under-abundant in the solar system have much larger abundances in the cosmic rays. The over-abundance of these elements in the cosmic rays is due to spallation processes. In particular Li, Be, and B are products of the fragmentation of the much more abundant C, N, O. In a similar manner, the abundance of Sc, Ti, V, and Mn in the cosmic rays is due to spallation of the more abundant Fe and Ni nuclei.

1.2 ORIGIN AND PROPAGATION OF COSMIC RAYS

One of the open questions in Cosmic Ray Physics arises from the sources that are capable to accelerate particles up to such high energies. A good candidate as a cosmic ray accelerator should provide enough power to boost the particles and an intense

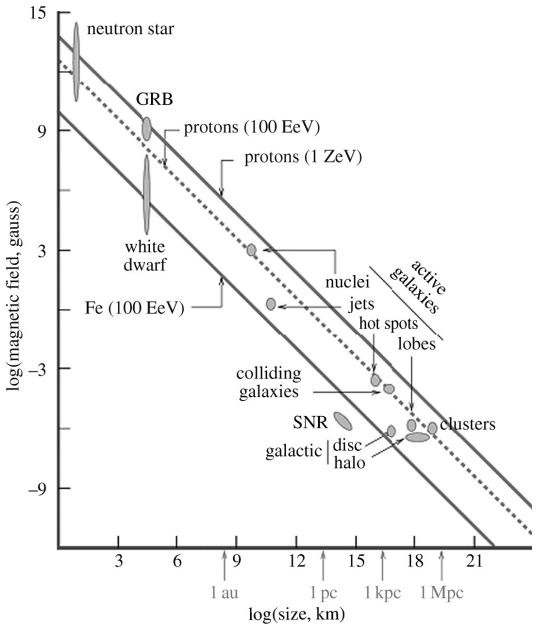

FIGURE 1.3: *Hillas Plot*, showing the relation between the intensity of the magnetic field and the size of different sources, from [16]. Lines corresponding to the maximum attainable for protons at $E = 100$ EeV and $E = 1$ ZeV, and Fe at $E = 100$ EeV are shown.

magnetic field in an extent region to confine them enough time. According to the *Hillas criterion* [15], once the Larmor radius of the cosmic ray particle is similar to the size of the accelerator the particle is likely to escape due to the impossibility to be magnetically confined. The so-called *Hillas plot* (figure 1.3) illustrates the relation between the magnetic field and the size of different sources for different attainable energies. Assuming that the accelerator, with a magnetic field B and size R, converts part of its kinetic energy to boost the particles in a shock wave, the maximum energy attainable is

$$E_{\max} \simeq Ze \left(\frac{B}{\mu\mathrm{G}}\right) \left(\frac{R}{\mathrm{kpc}}\right) 10^{18}\ \mathrm{eV}, \tag{1.2}$$

where Ze is the particle charge and β is the shock velocity.

According to these arguments, it is widely accepted that galactic cosmic rays are accelerated in supernova remnants (SNRs), where a conversion factor between the kinetic energy into relativistic particles of a few percent will be enough to keep the average cosmic ray energy density in the Galaxy [17]. At the end of its life, a very massive star cannot sustain the gravitational force through nuclear fusion processes and collapses. In this explosion, the outer shells are ejected at enormous speeds into the interstellar medium, therefore, expelling big amounts of material into the space. Typically, the explosion releases a big amount of kinetic energy, $\sim 10^{51}$ erg, which is transferred to the ejected material and finally provided to the charged particles in the ionized media. An efficiency of about 1-10 % in this conversion ensures the $\sim 10^{41}$ erg/s needed to keep the typical cosmic ray density in the Galaxy, $\rho_{\mathrm{CR}} \sim 1$ eV/cm^3.

The most plausible mechanism to explain the efficient conversion from the kinetic motion of the expanding material to kinetic energy of the charged particles, called *diffusive shock acceleration* (DSA), is based on the studies developed by Fermi [18]. In this mechanism, the particle gains huge amounts of kinetic energy by means of stochastic scattering on the magnetic turbulences of the shock wave. The magnetic inhomogeneities of the upstream and downstream plasma act as magnetic mirrors where the particle reflects back and forth. As a result, the particle traverses the boundary between the shocked plasma downstream and the unshocked region upstream, gaining an energy $\Delta E \propto E$ each time. After multiple interactions where the particles cross the shock boundary, the energy spectrum follows a power law $\frac{dN}{dE} \propto E^{-\alpha}$, with α in the range between 2.0 and 2.5 [19].

Once accelerated, the propagation of galactic cosmic rays is essentially a diffusive process in the random turbulent inhomogeneities of the galactic magnetic field, where the cosmic ray particles scatter [20, 21]. The common approach, based on the *quasi-linear approximation*, separates the contribution of the random fluctuations and the regular average field, assuming that the intensity of the magnetic inhomogeneities is much smaller than the regular magnetic field. The diffusive process is governed by the energy dependent *spatial diffusion coefficient*, $D(E) \propto E^{-\delta}$, which, ultimately, depends on the model of the turbulent magnetic fluctuations. Two models commonly cited in the literature are due to Kolmogorov, and Kraichnan, and lead to a diffusion coefficient $D(E) \propto E^{1/3}$ in the first case, and $D(E) \propto E^{1/2}$ in the second. As a consequence, taking into account the spectrum of cosmic rays accelerated in the shock waves, the diffusive process will eventually lead to a power law spectrum $\frac{dN}{dE} \propto E^{-\alpha-\delta}$.

Assuming that the propagation is purely diffusive, the ratio secondary-to-primary fluxes allows to deduce phenomenologically the energy dependence of the diffusion coefficient. In particular, the best data is the boron-to-carbon flux ratio (B/C), where the boron is purely a secondary cosmic ray species produced mostly by the fragmentation of carbon, nitrogen, and oxygen, and carbon is a primary cosmic ray produced directly in the sources. In that case the energy dependence of the B/C ratio should be proportional to $D(E) \propto E^{-\delta}$, thus allowing to constrain the diffusion coefficient. Recently, the precision measurement of the B/C flux ratio by AMS-02 provides a valuable piece of information to constrain the propagation models of cosmic rays [22]. In particular, at high energies the B/C is well described by a single power law with an spectral index in agreement with the Kolmogorov turbulence model (figure 1.5-*left*).

The propagation of galactic cosmic rays is also affected by other sub-dominant processes: *reacceleration* and *convection*. Diffusive reacceleration is due to the scattering of the charged particles in the turbulences of the GMF naturally connected to the diffusion process and its contribution is negligible at energies above few tens of GeV/nucleon. Convective transport due to the existence of galactic winds may result in an energy loss in the particle distribution, which affects again up to few tens of GeV/nucleon.

On the other hand, charged cosmic ray nuclei are subject to radioactive decay and inelastic collisions (*fragmentation*) with the interstellar H and He, where secondary

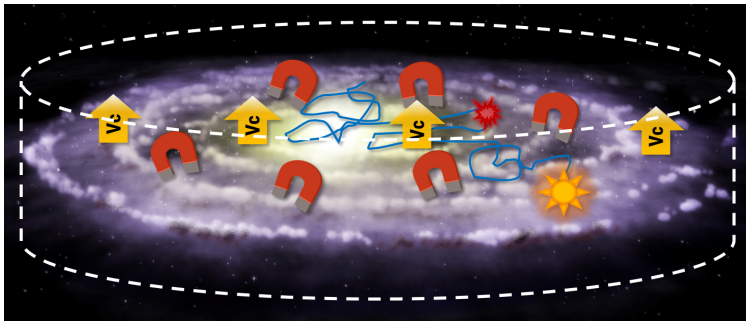

FIGURE 1.4: Scheme of cosmic ray propagation in the Galaxy. After being accelerated at the sources, the propagation of galactic cosmic rays is essentially a diffusive process. Other process, such as reacceleration, convection and fragmentation/decay take place. Finally, cosmic ray particles suffer from energy losses in their propagation.

cosmic rays are produced as a result. Secondary cosmic rays created in these interactions not only allow to constrain the diffusion coefficient (as the aforementioned B/C), but also other propagation parameters such as the *grammage*, and the *residence time* in the Galaxy. The grammage represents the mean amount of interstellar matter traversed by cosmic rays before escaping from the confinement volume, and the residence time stands for the average time of this confinement before escaping out of the Galaxy. The measurement of flux ratios of secondaries such as Li, Be and B, and primaries as C, N, O provides a constraint on the grammage parameter. On the other hand, the residence time can be estimated by means of secondary-to-primary ratios of unstable isotopes such as ^{10}Be. ^{10}Be has a half-life of 1.39×10^6 years and is produced in the fragmentation of C, N and O. Two ratios are commonly used in the literature, ^{10}Be/^{9}Be and ^{10}Be/^{10}B, which are expected to rise with the energy due to the relativistic time dilation (figure 1.5-*right*). The relative abundances in each case provide an estimation of the fraction of ^{10}Be which has decayed and, consequently, an estimation of the time elapsed [23].

Finally, cosmic rays suffer from continuous energy losses in their propagation. Typically, cosmic ray nuclei lose energy by means of ionization in the interstellar neutral matter and Coulomb interaction in the ionized plasma. Electrons and positrons, however, lose their energy quicker mainly due to synchrotron emission and inverse Compton interaction with the interstellar medium photons.

The current understanding of the mechanisms involved in the cosmic ray propagation is encoded in numerical simulations such as GALPROP [24], DRAGON [25] and USINE [26], which provide the theoretical predictions of the different observables. In this sense, experimental results not only provide measurements that allow to improve and refine the theoretical model, but also discrepancies may show distinct unknown features about the production and propagation of charged cosmic rays.

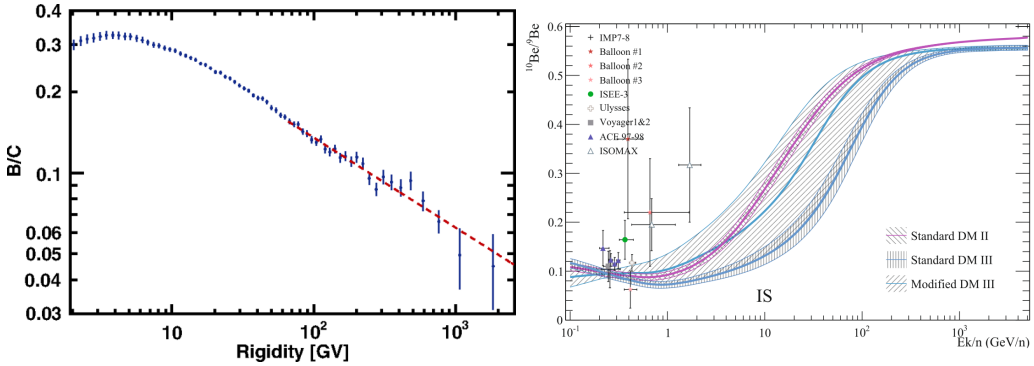

FIGURE 1.5: *(Left)* AMS-02 Boron to carbon flux ratio as a function of the rigidity from 1.9 GV to 2.6 TV. Above 65 GV, the B/C is well described by a power law, with an spectral index $\Delta \sim -\frac{1}{3}$, in agreement with a Kolmogorov model of the magnetic turbulences [22]. *(Right)* Measurements of ^{10}Be/^{9}B and models of the predicted ratio at Earth as a function of the kinetic energy per nucleon for different propagation scenarios [23].

1.3 COSMIC RAYS IN LOW EARTH ORBIT

In their travel from the sources to the Earth, cosmic rays are also affected by two local phenomena that produce distortions on the local interstellar spectrum (LIS). Once they arrive to the boundaries of the solar system, they are affected by the plasma of low energy protons and electrons emanating from the heliosphere. This interaction is modulated by the solar activity in the so-called solar modulation. On the other hand, as the cosmic rays approach the Earth the influence of the Earth's magnetic field plays a major role, acting as a shielding to the low energy particles from the Sun.

1.3.1 *Solar modulation*

Charged cosmic rays entering the solar system are affected by the interaction with the magnetic field carried by the expanding turbulent solar wind, known as Heliosphere Magnetic Field[2] (HMF) [27]. This magnetized plasma, consisting of low energy protons, electrons and ionized atoms constantly ejected from the solar corona to the interplanetary medium, decelerates and partially excludes the lower energy particles from the solar system. This effect, known as *solar modulation*, varies with time and, therefore, induces a time variation in the low energy part of the cosmic ray flux arriving to the Earth [28].

Since the Sun is composed of plasma, it does not rotate as a rigid body but its rotation depends on the latitude. In particular, the Sun equator rotates faster than the poles, which produces distortions in the Sun magnetic field and the field lines twist over time. These distortions of the field lines produce the appearance of *sunspots* in the outer shells of the Sun, usually accompanied, in periods of intense magnetic activity, by other phenomena such as prominences and magnetic reconnections which further produce more violent events like *solar flares* and *coronal mass ejections*.

2 In the literature is also referred as Interplanetary Magnetic Field (IMF).

The number of sunspots is a good indication of the solar activity, whose configuration changes approximately in an 11 years basis [29]. This variation constitutes the so-called *solar cycle*, where the Sun's activity alternates between two *minimum* passing through a *maximum*. During a minimum, the number of sunspots and the solar activity decreases and vice versa. In addition, during a minimum the Sun magnetic field is approximately a magnetic dipole whose axis is almost aligned with the rotational one. Depending on the orientation of the dipole with respect to the rotational axis the cycle is referred to $A > 0$, if parallel, or $A < 0$, if anti-parallel. During the maximum, dipole approximation is not valid, thus there is not well-defined polarity. Therefore, during a solar cycle there is a reversal in the polarity of the Sun magnetic field, from a $A > 0$ configuration to a $A < 0$ one or vice versa. The flux of low energy cosmic rays is correlated with the solar cycle, showing a depletion during the solar maximum, where the activity of the Sun is higher (figure 1.6). This is exploited by *neutron monitors*, which record the counts of low energy cosmic rays to track the solar activity and the space weather.

Due to the high conductivity of the ionized material, the magnetic field is frozen in the solar wind and dragged outwards from the Sun. Therefore, the field is bounded to the rotating Sun and the lines get wrapped into an Archimedian spiral pattern, also know as *Parker spiral*, which corresponds to the large-scale field structure and has two components: radial and azimuthal. At large distance from the Sun, the radial component vanishes and the azimuthal component, which can be approximated as circular, dominates.

Particles entering the HMF are subject to different processes, namely, convection, adiabatic energy losses, diffusion, and curvature and gradient drifts associated to the time variation of the field. As a result of these effects, the flux of cosmic rays measured at Earth is not representative of the LIS at energies below few GeV due to the distortions introduced by the solar modulation. These processes are accounted in a transport equation, first formulated by Parker in 1950s [30], which can be solved numerically, or analytically if some assumptions are made. In this regard, in the so-called *force field approximation* the solar modulation can be expressed in terms of a single parameter ϕ, which accounts for the energy losses of cosmic rays propagating in the heliosphere [31]. According to this, a particle with energy E_{IS} in the interstellar medium would reach the Earth with an energy $E = E_{\text{IS}} - |Z|e\phi$, where Ze is the charge. As a result, the flux modulated by the solar wind, Φ_{mod}, is related to that in the interstellar medium, Φ_{LIS}

$$\Phi_{\text{mod}}(E) = \frac{E^2 - m^2c^4}{(E + |Z|e\phi)^2 - m^2c^4} \times \Phi_{\text{LIS}}(E + |Z|e\phi), \tag{1.3}$$

where only particles with energy higher than $|Z|e\phi$ will reach the Earth. The first term in (1.3) accounts for the modulation and suppression of the flux, whereas the second term quantifies the particle energy loss. The suppression of the flux depends on the position within the heliosphere, and it is higher as one approaches the Sun. Some values of the ϕ parameters used are between $\phi = 400$ MeV at a solar minimum and $\phi = 1400$ MeV for a solar maximum.

The force-field approximation does not include the effect of drift in the solution, therefore, leading to the same modulation for positive and negative charged par-

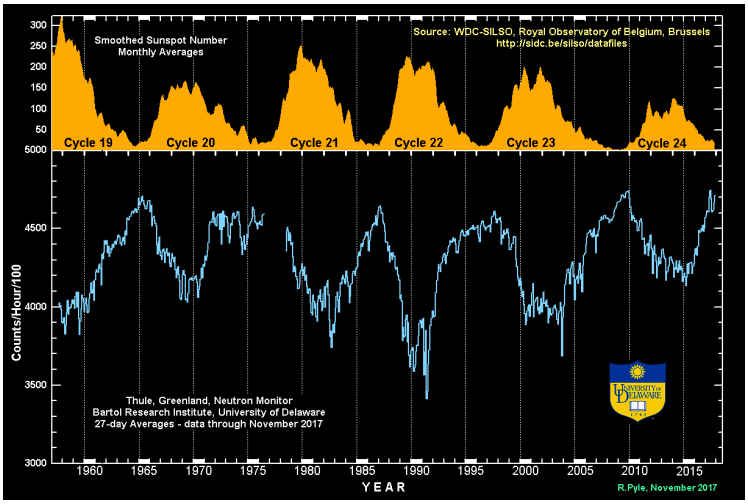

FIGURE 1.6: Correlation between the number of sunspots *(top panel)* and neutron monitor counts *(bottom panel)*, from the Thule Neutron Monitor (Greenland) of the Bartol Research Institute (University of Delaware, USA) [34]. Between a solar cycle, defined by the period between two alternative solar minimums, the number of sunspots and, therefore, the solar activity increases. The number of neutron monitor counts has the opposite behavior.

ticles. However, the different polarity configurations lead to a charge-sign dependence of the modulation, as positive and negative particles drift in opposite directions [32, 33].

1.3.2 *Earth magnetic Field*

Once cosmic rays have crossed the heliosphere, the Earth's magnetic field, or geomagnetic field, constitutes the last obstacle before the detection at Earth is possible. The geomagnetic field extends from the Earth's interior into the space, acting as a shielding from the stream of low energy particles ejected from the solar corona (figure 1.8). In this manner, once charged particles arriving to the Earth from outer space enter the geomagnetic field, they will follow curved trajectories around the field lines. As a result, some of them will loose their energy and slow down enough to get trapped in the geomagnetic field.

The Earth's magnetic field is attributed mainly to the dynamo effect due to the motion of electrical currents in the metallic conductive fluid of the Earth's outer core under rotation. Other contributions come from outer sources such as ionosphere electric currents.

In a first approximation, near the surface the Earth's magnetic field can be described by a magnetic dipole with a moment of $\mathcal{M}_{\mathrm{E}} = 7.71 \times 10^{22}$ A m^2 tilted 9.5° with respect to the Earth's rotation axis[3] and shifted by 342 km relative to the Earth's center. Based on this dipole approximation, in the 1920s Störmer developed a mathematical theory to explain some effects related to the geomagnetic field, in particular, the motion of charged particles inside it [35]. According to the Lorentz

3 Values of the geomagnetic dipole as of 2018.

force, a charged particle entering the geomagnetic field will be deflected following different trajectories depending on the intensity of the magnetic field and the magnetic rigidity of the particle, R, defined as

$$R = \frac{pc}{Ze} \qquad \text{(in Volts)}, \tag{1.4}$$

where p is the momentum of the relativistic particle, c is the speed of light in vacuum, Ze is the charge of the particle in electron units. Particles with different masses and charges will have same dynamics in the magnetic field if their rigidity is identical.

In this rigidity picture, a charged particle is allowed to penetrate the Earth's magnetic field if its rigidity is above a certain threshold called *geomagnetic rigidity cutoff*, R_c, which, according to Störmer's theory, is

$$R_c = \frac{\mathcal{M}_{\mathrm{E}} \cos^4 \lambda}{\mathcal{R}\left(1 + \sqrt{1 \mp \cos^3 \lambda \cos\varphi \sin\zeta}\right)}, \tag{1.5}$$

where $\mathcal{M}_{\mathrm{E}}$ is the Earth's magnetic dipole moment, $\mathcal{R}$ is the distance from the dipole center, λ is the geomagnetic latitude along the dipole. The value of the rigidity cutoff also depends on the arrival direction of the particle, being φ the azimuthal angle measured clockwise from the geomagnetic east direction, and ζ the angle from the local magnetic zenith direction. The sign $\mp$ stands for the particle's charge sign (-1 for positive and +1 for negative).

For vertically incident particles ($\zeta = 0$) the rigidity cutoff does not depend on the azimuthal angle of the particle's direction and simply depends on the geomagnetic latitude:

$$R_c^{\mathrm{vert}}(\lambda) = \frac{14.8}{(\mathcal{R}/\mathcal{R}_{\mathrm{E}})^2} \cos^4 \lambda \quad \text{(GV)}, \tag{1.6}$$

where $\mathcal{R}_{\mathrm{E}}$ is the Earth's radius. As a consequence, the rigidity cutoff is maximum at the geomagnetic equator, with an approximate value of $\sim$ 15 GV for vertical incident particles, and vanishes at the magnetic poles (figure 1.7). This *latitude effect* was first measured by J. Clay during two voyages between Java and Genova in 1927 and 1928, which allowed to conclude that cosmic rays were mostly charged particles [36, 37].

In addition, a remarkable consequence of the rigidity cutoff is the so-called *East-West effect*, which is due to the factor $\mp \cos\varphi$ in (1.5). As a result, for positive (negative) charged particles it is easier to penetrate the geomagnetic field from the West (East) direction. This effect was measured in 1933 independently by L. Álvarez and A. Compton [38], T. Johnson [39], and B. Rossi [40], thus evidencing that cosmic rays were composed mainly by positively charged particles.

Some under-cutoff particles are rejected by the geomagnetic field and blown out into the space while others are slowed down and get trapped by the field lines acting as magnetic mirrors bouncing back and forth or circling and drifting around the Earth. In this manner, zones of trapped charged particles, known as *Van Allen radiation belts* [41], are created around the Earth's magnetic field. There are two main belts, extending from an altitude of 500 to 60000 km, with an *inner belt*, which

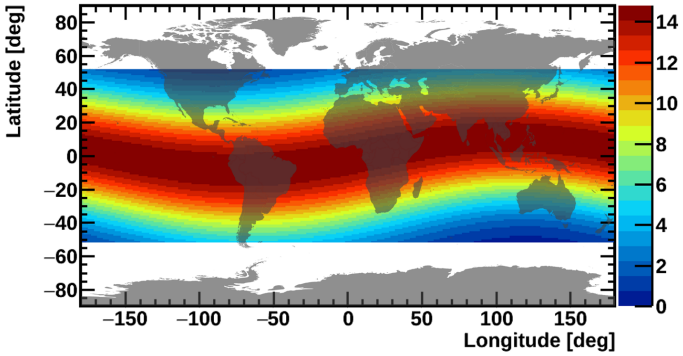

FIGURE 1.7: Values of the vertical rigidity Störmer cutoff computed from (1.6) as a function of the geographical position in a band of latitudes covered by the International Space Station.

consists in a combination of protons and electrons, and an *outer belt*, typically composed by energetic electrons. The high density of low energetic particles in this regions represents a hazard for the electronics of spacecrafts and satellites if their orbit is inside the radiation belts, and must include an adequate shielding to protect their electronic devices.

An additional feature of the tilt and shift of the Earth's magnetic field with respect to the rotation axis is the existence of a region located at about 200-300 km far from Brazil, in the South Atlantic, called the *South Atlantic Anomaly* (SAA), where the inner Van Allen belt gets closer to the surface, therefore increasing the flux of low energy trapped particles at this region.

The Störmer theory was revisited by M.S. Vallarta and G. Lemaître [42, 43], which recalculated the allowed and forbidden trajectories of charged particles in the dipole magnetic field and introduced the idea of the *penumbra* region. They showed that, in general, two values of the rigidity cutoff exist: the *lower rigidity cutoff*, such that rigidities below that value are always forbidden; and the *upper rigidity cutoff*, which ensures that rigidities above that value are always allowed. The penumbra corresponds to the intermediate values between the lower and upper rigidities cutoff, where allowed and forbidden trajectories coexist.

The dipole approximation is able to provide quantitative results about many effects associated with the behavior of charged particles in the Earth's magnetic field. However, the field is not a pure dipole and its intensity varies with time. For this reason, a more precise description is based on solution of the Laplace's equation for the Earth's magnetic field potential in terms of a spherical harmonic expansion. The coefficients of this expansion are provided by the International Geomagnetic Reference Field (IGRF) [44] in a 5 years basis, which describes the internal magnetic field of the Earth and its annual rate of change (secular variations) from 1900 up to the present day. The latest update, corresponding to the IGRF-12, was released on 2015 and provides the description of the main field model up to 2015, and a linear predictive secular variation model for 2015-2020.

The IGRF model of the Earth magnetic field allows to obtain more accurate values of the rigidity cutoff by means of the *backtracing technique* of individual particles inside the field. In this manner, the motion of a particle generated with a given rigidity at a certain direction is integrated numerically. If the particle reaches a certain distance far from the Earth, the particle is assumed to escape to outer space and, therefore, its rigidity is above the cutoff for that position and arrival direction. However, if the particle is trapped by the geomagnetic field it is considered to be under cutoff and the trajectory is forbidden. The backtracing method not only takes into account the model for the geomagnetic field, but also the presence of the Earth; in this manner, if the backtraced trajectory intersects the Earth surface the trajectory is also forbidden. This method allows to construct a cone of allowed and forbidden trajectories at the different positions inside the geomagnetic field and for different rigidities, in particular, determines the directional rigidity cutoff at a given point in the Earth.

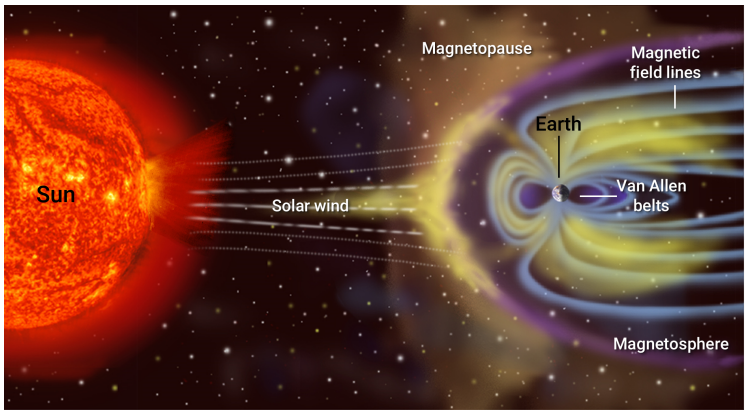

FIGURE 1.8: Scheme of the geomagnetic field and its interaction with the solar wind. Variations in the solar wind affect the magnetosphere at long distances from the Earth producing distortions in short time scales. *(Credits: NASA, Wikimedia Commons).*

Additionally, the influence of the solar wind produces distortions in the magnetosphere. Solar effects, such as storms, press and twist the shape of the magnetosphere at long distances far from the Earth. This kind of effects usually occur in short time scales compared to the secular variation of the Earth magnetic field, and the distortions that they induce in the magnetosphere are described by models of the external geomagnetic field such as Tsyganenko TS96 or TS05 [45, 46].

1.4 ANTIMATTER IN COSMIC RAYS. THE QUEST FOR DARK MATTER

Several observations from Cosmology and Astroparticle Physics show a Universe where matter dominates over antimatter. The origin of this *baryon asymmetry* is still unknown [47]. Regarding galactic cosmic rays, the vast majority of them is composed by particles of matter, whereas only a small fraction ($\sim 0.01\%$) is made of antimatter [48].

In the standard paradigm of cosmic rays, light particles of antimatter ($e^+, \bar{p}, \bar{D}$) are believed to have a pure secondary origin as a result of interactions of primaries

in the interstellar medium, and their flux at Earth can be predicted by means of the propagation models and the production cross sections of the interactions with the H and He nuclei of the interstellar medium [49]. On the other hand, the production of heavier antinuclei such as $\overline{\text{He}}$ as a result of nuclear fragmentation should be negligible, and its observation could be a hint of the existence of primordial antimatter domains.

Due to its tiny flux at Earth, the search for antimatter in cosmic rays constitutes a probe to test our understanding concerning the mechanisms of production and propagation in the Galaxy. In particular, light antimatter channels involving e^+ and $\bar{p}$ allow to further investigate additional contributions from non conventional sources such as nonthermal production or annihilation from Dark Matter particles.

1.4.1 *Positrons*

One of the most promising channels for the indirect search for Dark Matter is the so-called *positron fraction*, which stands for the ratio of the positron flux, Φ_{e^+}, to the total electron plus positron fluxes, $\Phi_{e^-} + \Phi_{e^+}$

$$\text{P.F.} = \frac{\Phi_{e^+}}{\Phi_{e^-} + \Phi_{e^+}}. \tag{1.7}$$

The flux of positrons can be predicted from the interaction of primary protons with the interstellar hydrogen atoms of the medium during the propagation. As a result, charged pions and kaons are produced which further decay producing electron and positron pairs [50]. A consequence of this secondary origin is that the positron spectral index should be greater than that of electrons in absolute value, $|\gamma_{e^+}| > |\gamma_{e^-}|$, which implies that the positron fraction is expected to decrease with the energy.

Due to its physical implications, the measurement of the positron fraction started in the late 1960s, where several results suggested a rise with the energy above few tens of GeV [51–55]. However, it was not clear if the origin of this rise was due to an additional contribution of positrons or a depletion of primary electrons. In the last decades, distinct experiments such as balloon-borne magnetic spectrometers (TS93 [56], CAPRICE94 [57], HEAT [58]) and space-borne detectors based on calorimeter techniques[4] (Fermi-LAT [59]) or spectrometers (PAMELA [60], AMS-01 [61]) not only confirmed the increase with the energy of the positron fraction but also attributed this rise to a significant increase of the positron flux non compatible with the standard paradigm of secondary production of antimatter.

In the last years, AMS-02 has provided the most precise measurement of the positron fraction, extending the energy range up to 500 GeV [63, 62], as shown in figure 1.9. The accurate results, not only in the positron fraction but also in the individual electron and positron fluxes [64] profiting the spectrometer separation, allow an accurate characterization of the lepton component of cosmic rays (figure 1.10-*left*). In particular, at low energies the positron fraction decreases with energy as expected from the pure secondary origin of cosmic ray positrons. At ∼8 GeV, it

4 Fermi-LAT profited from the geomagnetic field to separate both species

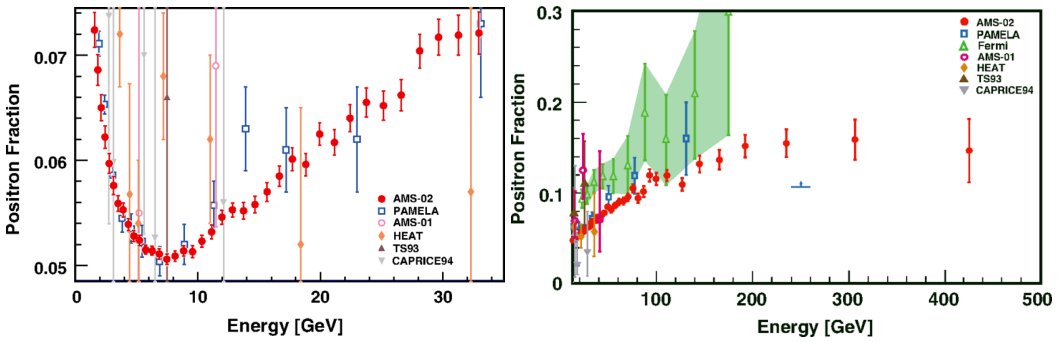

FIGURE 1.9: Precise measurement of the positron fraction by AMS-02 [62]. The AMS-02 positron fraction decreases with energy up to 8 GeV, and then increases steadily up to $\sim$ 200 GeV without structures.

starts rising steadily with energy up to $\sim$ 200 GeV, where the positron fraction is no longer increasing with energy. This rise is due to a hardening in the positron flux from $\sim$20 GeV, and not the reduction of electrons.

In addition, the $(e^+ + e^-)$ flux is a complementary measurement widely carried out by balloon-borne experiments (CAPRICE94 [57], HEAT [65], ATIC [66], PPB-BETS [67]), calorimeter (Fermi-LAT [68], CALET [69], DAMPE [70]) and spectrometer (AMS-02 [71]) detectors in space, and ground-based Cherenkov detectors (H.E.S.S. [72]). Recently, DAMPE reported a break in the $(e^+ + e^-)$ spectrum at a $E \approx 0.9$ TeV corresponding to a spectral hardening from $\gamma_1 \approx 3.1$ to $\gamma_2 \approx 3.9$, which confirmed the evidences found by H.E.S.S. [70]. A compilation of the $(e^+ + e^-)$ flux measurements is presented in figure 1.10-*right*.

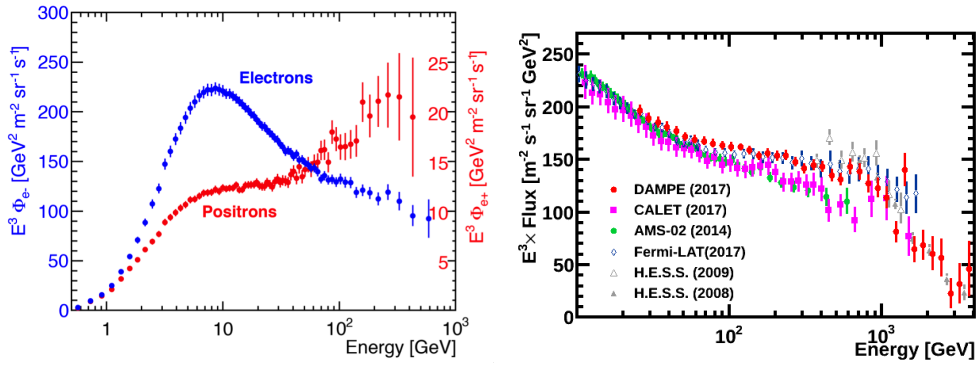

FIGURE 1.10: *(Left)* Individual positron and electron fluxes measured by AMS-02 [64]. The hardening of the positron flux allows to conclude that the rise in the positron fraction from few tens of GeV is due to an excess of positrons, not to the loss of electrons. *(Right)* Compilation of the $(e^+ + e^-)$ flux measurements by DAMPE [70], CALET [69], AMS-02 [71], Fermi-LAT [68] and H.E.S.S. [72].

The origin of these features in the lepton channels of cosmic rays remains unclear and a plethora of models has been proposed to explain the deviations from the standard paradigm. Some models include modifications to the standard cosmic ray propagation [73–75], although their predictions need to explain not only the observation in the positron fraction but also the results in many other channels such

as primary-to-secondary flux ratios (B/C) or $\bar{p}/p$. For most cases, the observation requires the inclusion of primary sources, which are typically classified into two scenarios: *dark matter* or *astrophysical origin*.

1.4.1.1 *Dark Matter scenario*

Many observations including galactic rotation curves [76–78], cosmic microwave background [79, 80], gravitational lensing [81, 82], etc., suggest the existence of a new fundamental kind of matter in the Universe which does not interact by means of the electromagnetic force. Extensions to the Standard Model (SM) of Particle Physics have been proposed to include Dark Matter particle candidates as well as to explain other open questions such as the origin of the baryon asymmetry, the existence of three families of leptons and quarks, or the hierarchy problem.

Within the Particle Physics frame, models including Dark Matter are composed of new non-baryonic particles that may annihilate or decay into SM particles [83]. This fact is exploited by indirect searches for Dark Matter, where possible signatures in gamma-rays, cosmic-rays and neutrinos are investigated. Some observations lead to constraints on the properties of the DM particles. For instance, particles electrically charged or interacting by means of the strong force are strongly disfavored. In addition, DM particles must cluster gravitationally to form galaxies, which favors the *cold* DM hypothesis, i.e., non-relativistic particles at the time of the structure formation.

In this Cold Dark Matter scenario (CDM) [84], one of the most promising candidates is a generic class of weak interacting massive particles (WIMPs). According to the Cosmology, WIMPs are considered to be remaining thermal relics from the early Universe, where the interactions and collisions with the SM particles during the radiation-dominated epoch kept them in thermal equilibrium at the high temperatures at that time. As the Universe expanded and cooled, these interactions became more inefficient and finally the WIMP abundance froze out. On the other hand, to reproduce the cosmological observations of the DM density in the Universe, the thermally averaged cross-section of these particles must be

$$\langle \sigma v \rangle \approx 3 \times 10^{26}\ \mathrm{cm}^3\mathrm{s}^{-1}, \tag{1.8}$$

which corresponds to a mass in the weak scale $\mathcal{O}(100\ \mathrm{GV})$ (*WIMP miracle*).

Gravitational and weak lensing effects allow to deduce only an approximate distribution of the DM in the Universe. DM hierarchically clusters in the so-called halos, formed through gravitational instability, and playing a major role in the formation of galaxies. Their size ranges from small substructures to galactic sized halos. In particular, the rotational curves evidenced that DM halos extend well beyond the furthest visible stars in the galaxy, dominating the total mass.

DM may annihilate or decay to SM particles, thus allowing an indirect search [85]. In the charged cosmic rays context, antimatter channels are suitable for these kind of indirect detections, since additional contributions of antimatter particles with respect to the expectations from standard propagation may be a footprint of DM interactions in the halo. In particular, the excess of positrons not compatible with a pure secondary origin in the standard paradigm of cosmic rays might be due to

DM annihilations [86–96]. Within the many models of DM proposed to explain this excess, leptophilic channels of mass $\mathcal{O}(1\ \mathrm{TeV})$ are favored.

1.4.1.2 *Astrophysical scenario*

Pulsars, fast-rotating magnetized neutron stars [97], constitute the leading candidate as fresh positron astrophysical factories. As a result of the collapse of a massive star, the high compression of the central region due to the gravitational force leads to the combination of protons and electrons into neutrons, thus forming a neutron star if the core is between 1 and 3 solar masses. Neutron stars, with a typical radius of few tens of kilometers are the most dense object known. Due to the dramatic reduction of the radius in the collapse, the conservation of the angular momentum is translated into a very high rotation speed.

In addition, the pulsar is surrounded by a magnetosphere extending up to a distance known as *light cylinder*[5], with the magnetic poles tilted with respect to the rotation axis. This pulsar magnetosphere is produced by the rotational energy of the pulsar, which in turn induces a large electric field that strips electrons from the surface and makes them drift along the magnetic field lines. On the other hand, the pulsar emits beams of electromagnetic radiation at very regular intervals ranging typically from miliseconds to seconds as a result of the synchrotron and curvature radiation of the stripped electrons. The high energy photons emitted are capable to produce electromagnetic cascades of electron and positron pairs in the strong pulsar magnetic field. Consequently, from a single primary particle leaving the pulsar surface a huge amount of electron and positron pairs is created, typically between 10^4-10^5.

These pairs produced in the magnetosphere emanate from the pulsar as a relativistic magnetized wind, which is later slowed down at the *termination shock* due to the interaction with the sub-relativistic expanding ejected material from the progenitor's collapse. Electron and positron pairs lose energy adiabatically, due to the expansion, and radiatively, because of the magnetic fields. At the termination shock, particles are accelerated and may escape out of the magnetosphere. Thus, processes in the pulsar magnetosphere are capable to inject electrons and positrons into the interstellar medium if a fraction of the rotation energy (namely, 1%-30%) is converted into electromagnetic cascades. This injection is usually assumed to follow a power law with an exponential cutoff at E_c, $\frac{dN}{dE} \propto E^{-\alpha} e^{-E/E_c}$, which typically depends on the spin-down rate related to the age of the pulsar [98, 99].

Customarily in the literature, contributions from pulsars such as Geminga (PSR J0633+1746), Monogem (PSR B0656+14), and Vela (PSR J0835-4510), or a collection of Gamma-Ray pulsars from the Australian Telescope National Facility (ATNF) catalogue are used to describe the positron fraction and the positron flux [100–108].

5 The extension of this light cylinder, R_L is given by the rotation speed of the pulsar, Ω, $R_L = \frac{c}{\Omega}$

1.4.2 *Challenges of the standard paradigm of Cosmic Rays*

The experimental results on the antimatter channels defy the current understanding of cosmic ray production and propagation. However, no conclusive answers about the new phenomena have been settled due to the uncertainties of the propagation models. In this context, the precision era in Cosmic Ray Astrophysics started with space-based experiments such as PAMELA, and later continued with AMS-02 and the recent experiments DAMPE and CALET, will allow to further improve and clarify our knowledge about the mechanisms and processes involved in the origin and propagation of cosmic rays.

In this sense, the precision measurements on primary and secondary fluxes performed by AMS-02 constitute an important piece of information to constrain propagation models of cosmic rays. In particular, AMS-02 has published a precise measurement of the proton flux between 1 GV and 1.8 TV [109], and helium flux between 1.9 GV and 3.2 TV [110]. The results show that both fluxes deviate from a single power law and the spectral index progressively hardens at rigidities larger than 100 GV (figure 1.11-*left*). The magnitude of the helium spectral index is different from that of the proton, but the rigidity dependence is similar for both. In fact, proton to helium flux ratio is well described by a single power law above 45 GV.

In addition, recent results from AMS-02 regarding light primary (C, O) and secondary (Li, Be, B) nuclei fluxes [111, 112]. Although their fluxes exhibit a progressively hardening of their spectral index above ~ 200 GV, the rigidity dependences of primary and secondary fluxes are distinctly different: secondaries harden more than primaries, as shown in figure 1.11-*right*.

The observed deviations of the fluxes from a single power law are challenging to understand in the framework of the conventional models of Galactic cosmic ray production and propagation. The progressively hardening of the spectral index in the primary and secondary fluxes and, in particular, in the proton flux, may be connected to new phenomena within the Galaxy. Possible explanations of these features include the existence of local sources of fresh high rigidity cosmic rays [113–115] or non-linear cosmic ray transport in the Galaxy [116–118].

1.5 LARGE SCALE ANISOTROPY

The measurement of the directionality of charged cosmic rays provides valuable information to help understand the open questions found about its origin and propagation. In this sense, the study of the anisotropy in their arrival directions is a complementary tool to the energy spectrum and chemical composition in the characterization of the observed features in cosmic rays.

Due to their interaction and scattering with the turbulences and non-regular inhomogeneities of the GMF, the trajectories of cosmic rays in the interstellar medium (ISM) are randomly bent and the distribution of its arrival directions is expected to be highly isotropic. Assuming that the GMF has a local intensity of $B_{\mathrm{GMF}} \sim 3\ \mu$G [119], the Larmor radius of particles with charge $Z = 1$ and energies below 10^{16}-10^{17} eV is much smaller than the typical distances to the sources (100-300 pc), which

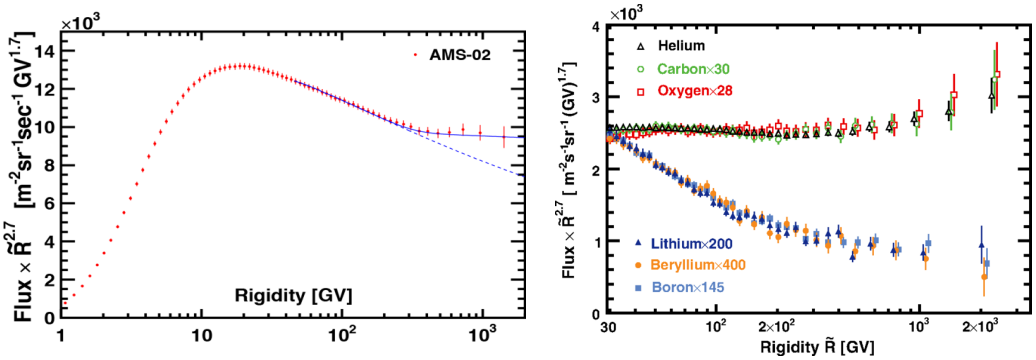

FIGURE 1.11: *(Left)* Precision measurement of the proton flux by AMS-02 [109] from 1 GV to 1.8 TV. At rigidities above few hundreds of GeV the flux is no longer described by a single power law due to a progressively hardening of the spectral index. *(right)* Precision measurement of the fluxes of light primary (He, C, O) and secondary (Li, Be, B) nuclei by AMS-02 [111, 112]. The rigidity dependences of primary cosmic rays and of secondary cosmic rays are distinctly different.

implies that the cosmic ray propagation up to those energies resembles a random walk well described by a diffusion mechanism.

Despite of the randomization in the cosmic ray trajectories due to the irregularities in the GMF, residual anisotropies of small amplitude (ranging from 10^{-2}-10^{-5}) may, however, exist. The measurement of such small signals is specially challenging and the analysis is customarily carried out in two categories depending on the angular size of the anisotropy:

- *Large Scale Anisotropy,* where patterns over the full sky, corresponding to angular scales greater than $60°$, are investigated. At first order, the anisotropy is described by a dipole of amplitude δ, corresponding to an angular scale of $180°$, i.e., asymmetries in the flux in one direction with respect to the opposite. In this case, assuming a pure dipole in the direction given by $\boldsymbol{n}$, the measured flux Φ in the direction of observation $\boldsymbol{u}$ is

$$\Phi(\boldsymbol{u}) = \Phi_0 + \Delta\Phi(\boldsymbol{u} \cdot \boldsymbol{n}), \tag{1.9}$$

  with Φ_0 the isotropic component of the flux and $\Delta\Phi$ the small directional fluctuation. Thus, the amplitude of the dipole anisotropy accounts the asymmetry between the maximum and minimum of the flux

$$\delta = \frac{\Phi_{\text{max}} - \Phi_{\text{min}}}{\Phi_{\text{max}} + \Phi_{\text{min}}} = \frac{\Delta\Phi}{\Phi_0}. \tag{1.10}$$

- *Intermediate and Small Scale Anisotropy*, where structures of angular size smaller than $60°$ and $10°$, respectively, are studied. The search for anisotropies at small scale is usually carried out at high enough cosmic ray energies ($E > 10^{19}$ eV), when the galactic magnetic fields do not affect their propagation trajectories significantly and local structures such as hot-spots or point sources can be investigated.

The study of anisotropies and its dependence on the energy may reveal valuable information on different topics about the origin and propagation of cosmic rays:

- *Diffusion mechanism.* Diffusion in the galactic medium produces density gradients, which ultimately give rise to a dipole anisotropy of amplitude

$$\delta = \frac{3D(R)}{v}\frac{\nabla N}{N}, \tag{1.11}$$

  where $D(R)$ is the diffusion coefficient as a function on the particle rigidity, v the particle velocity, and N the particle density. The dependence of the diffusion coefficient with the rigidity, $D(R)$, is different for each propagation model, so the study of the anisotropy may allow to discriminate among them.
- *Nearby sources.* The presence of nearby sources of cosmic rays may induce a large and/or small scale anisotropy in the arrival directions of cosmic rays with an amplitude which would depend on their spatial distribution and the cosmic ray injection.
- *Local environment.* The measurement of large scale anisotropy could reveal different configurations of the heliospheric magnetic fields. In addition, different models of the turbulent magnetic field in the galaxy may imprint anisotropies of distinct angular sizes, varying from large scale to small scale.
- *Origin of the knee.* If the knee is due to the existence of a maximum energy reachable by the galactic accelerators of cosmic rays, then a decrease in the amplitude of the anisotropy would be expected due to an increase in the contribution of the isotropic extragalactic component. On the contrary, if the knee is due to the leakage of cosmic rays out of the Galaxy, the amplitude of the anisotropy should increase with the energy.

1.5.1 *Ground-based experiments*

Traditionally, the search for anisotropies in cosmic rays has been carried out by surface array detectors, and Cherenkov or fluorescence telescopes measuring extensive air showers (EAS). In this kind of experiments, the atmosphere acts as a part of the detector, producing a cascade of particles when a primary cosmic ray hits an atom at the top of the atmosphere. Ground-based experiments, which are bounded to a fix position in the surface, profit from the Earth's rotation to scan a constant declination band in the sky in equatorial coordinates (see 3.2.3). As a result, only a fraction of the skymap is covered by these experiments.

1.5.1.1 *Method of analysis*

The measurement of the anisotropy demands the construction of a reference map, usually called *exposure*, which represents the detector response to an isotropic flux. In the most cases, the determination of the exposure through detector simulations at the required precision is challenging since the meteorological modulations affecting the development of the cascade are difficult to model. For this reason, collected data is used to build the reference map by means of, typically, two procedures:

- *Time-scrambling or shuffling technique,* where the reference consists of fake events generated by randomly coupling the measured distribution of local arrival directions and time of detection [120, 121].

- *Direct integration*, where the rate of events observed in the detector as function of the local sidereal time[6] is integrated against the relative acceptance during an integration period Δt [122].

For mid-latitude detectors, where the two aforementioned techniques do not provide satisfactory results, a new method based on an iterative maximum-likelihood procedure has been established [123]. However, all these techniques are equivalent to promediate the distribution of events in right ascension within the same declination band, which makes those experiments non sensitive to anisotropies in declination.

The standard analysis in the determination of large scale anisotropies in ground-based experiments is the so-called Rayleigh method [124] (also referred in the literature as harmonic analysis), where an expansion in Fourier series of the counting rate as a function of the right ascension is performed. As a result, the amplitude and phase of different harmonics are computed. According to this method, the distribution of a set of N collected events, with right ascensions $\alpha_1, \alpha_2, \ldots, \alpha_N$ is expanded as

$$f(\alpha) = \frac{a_0}{2} + \sum_{k=1}^{\infty} (a_k \cos(k\alpha) + b_k \sin(k\alpha)) = \frac{a_0}{2} + \sum_{k=1}^{\infty} A_k \sin(k\alpha + \varphi_k), \qquad (1.12)$$

where

$$A_k = \sqrt{a_k^2 + b_k^2} \qquad ; \qquad \varphi_k = \tan \frac{a_k}{b_k}, \qquad (1.13)$$

are the amplitude and phase of the kth harmonic, respectively. Thus, the one-dimensional analysis method on one angular coordinate (azimuth) provides only a bi-dimensional determination of the dipole in terms of its amplitude and phase. The coefficients of the expansion are obtained as usual in the Fourier analysis. In particular, the first-harmonic Fourier components are given by:

$$a_1 = \frac{2}{\mathcal{N}} \sum_{i=1}^{N} w_i \cos \alpha_i \qquad ; \qquad b_1 = \frac{2}{\mathcal{N}} \sum_{i=1}^{N} w_i \sin \alpha_i, \qquad (1.14)$$

where the weights w_i are often introduced to account for small non-uniformities in the exposure in the right ascension direction, and satisfy that $\mathcal{N} = \sum_{i=1}^{N} w_i$.

If the amplitude of the first-harmonic is found to be non-zero, the probability $\mathcal{P}$ that the observation arises from statistical fluctuations of an isotropic distribution is estimated as

$$\mathcal{P}(A_1) = \exp\left(-\frac{\mathcal{N} A_1^2}{4}\right) \qquad (1.15)$$

After normalizing the A_1 amplitude by the mean declination of the collected events, the Rayleigh formalism provides only the projection of the dipole onto the equatorial plane, $\delta_\perp$.

6 Due to the Earth's rotation, there is a correlation between the right ascension and the local time. In this sense, the time is measured from the Earth position with respect to the Sun or the Galactic center, which defines the *solar time* or *sidereal time*, respectively.

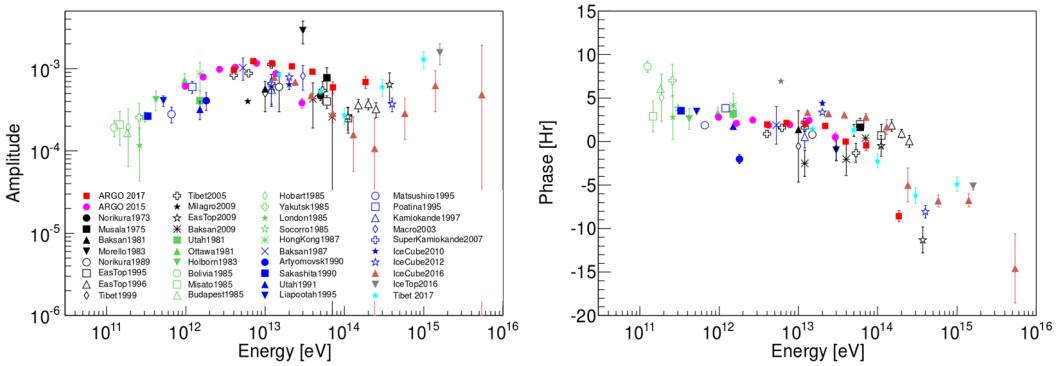

FIGURE 1.12: Compilation of the amplitude and phase of the first harmonic of the anisotropy measured by several ground-based experiments as a function of the cosmic ray energy, from [125].

1.5.1.2 *Experimental results*

A number of ground-based experiments has measured the amplitude, A_1, and phase, φ, of the anisotropy for energies 10^{11}-10^{15} eV, and their results are shown in figure 1.12 from [125]. In addition, a detailed description of the measurements can be found in [126] and [127].

Some specific topics in the anisotropy results obtained by ground-based detection deserve some comments:

- *Compton-Getting effect*

  The relative motion of an observer with velocity v/c with respect to the isotropic rest frame of cosmic rays is expected to induce a large scale anisotropy represented by a dipole with its maximum in the direction of the motion and a minimum in the opposite direction [128]. Assuming that the flux follows a power law spectrum with spectral index γ, the amplitude of the expected dipole anisotropy is given by

  $$\delta = \frac{\Delta\Phi}{\Phi_0} = (\gamma + 2)\frac{v}{c}\cos\theta \tag{1.16}$$

  where θ is the angle between the arrival direction of the cosmic rays and the direction of motion.

  The dipole anisotropy of two relative motions has been investigated:

  - The effect of the relative motion of the Earth around the Sun, with velocity $v \approx 30$ km/s, would induce a dipole anisotropy of about $\delta \simeq 5 \times 10^{-4}$ or less, which has been confirmed by several experiments (EAS-TOP [129], Tibet [130], Milagro [131], IceCube [132]) and constitutes a calibration test for detectors looking for large-scale anisotropies.
  - A similar effect due to the motion of the solar system around the galactic center at a velocity of $v \approx 220$ km/s should produce an anisotropy of amplitude $\delta \simeq 3.5 \times 10^{-3}$ if the cosmic ray plasma were at rest with respect to the Galaxy. However, although the sensitivity of ground-based detectors is enough to measure such signal if it were to exist, it has not

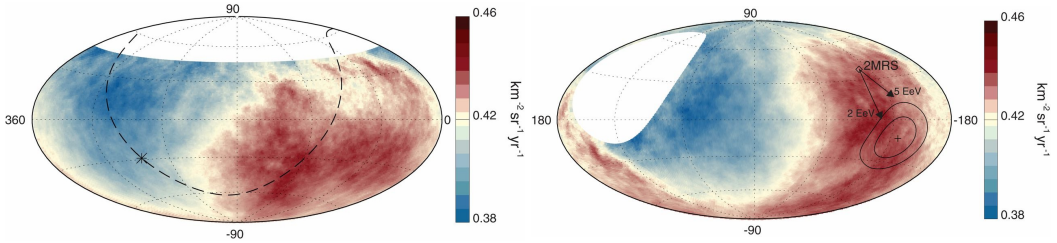

FIGURE 1.13: Skymap of the cosmic ray flux for $E \geq 8$ EeV in equatorial *(left)* and *(right)* coordinates as a result of the dipole anisotropy measured by Pierre Auger [141].

been observed. This null result suggests that the galactic cosmic rays corotate with the Galaxy [133].

- *Diffusion of cosmic rays*

  The diffusion of cosmic rays out of the Galactic halo may induce a large scale anisotropy. Since the matter density in the Galactic disk is higher than in the halo, the diffusion coefficient in the halo is much larger than the corresponding to the Galactic disk. Consequently, cosmic rays created in the Galactic disk would tend to diffuse out into the halo, therefore producing an anisotropy in the direction perpendicular to the disk. Predictions depend on the propagation model and, in particular, on the rigidity dependence of the diffusion coefficient $D(R)$ and give values between 10^{-2}-10^{-5} [131].

- *Local environment*

  At the sub-TeV energy range, Nagashima, Fujimoto, and Jacklyn (NFJ) reported the observation of an excess in the direction of the heliotail by combining data from muon telescopes in the northern and southern hemispheres [134, 135]. The excess in the direction of the heliotail was called *tail-in*, opposite to the proper motion of the solar system, whereas the deficit was referred in the literature as *loss cone*. The annual variation of the tail-in anisotropy showed a modulation with a maximum at December, when the Earth is closest to the heliotail and a minimum where the anisotropy almost disappears at June.

- *Origin of the high-energy cosmic rays*

  The origin of the knee and the second knee is explained by two hypothesis, namely, the leakage of cosmic rays from the Galaxy, or the maximum energy attainable by galactic cosmic ray accelerators. In the first case, a dipole anisotropy pointing towards the galactic center is expected [136], which seems to be favored by measurements in the 10^6-10^7 GeV range [137–140], although the results are still non conclusive.

  Recently, the Pierre Auger Observatory has published a result of the three-dimensional dipole anisotropy for energies above 4 EeV [141]. In the highest energy range, corresponding to $E \geq 8$ EeV, the detection of significant dipole amplitude of 6.5% pointing in Galactic coordinates to $(l, b) = (233°, -13°)$ (figure 1.13), far from the galactic center, indicates an extragalactic origin of the ultra high energy cosmic rays.

1.5.2 *Space-based experiments*

The measurement of anisotropies with space-based experiments profits from the direct identification of the primary cosmic ray before interacting with the atmosphere, which allows to determine the directionality of the individual cosmic ray species. In addition, due to their orbit around the Earth, space-based experiments have a nearly full coverage of the skymap where the anisotropy measurement is performed, therefore, are capable of a three-dimensional characterization of the dipole anisotropy.

Currently, the results of space-based experiments (PAMELA, Fermi-LAT, AMS-02) cover the lepton channel, mainly, motivated by the observed positron excess. In this context, the measurement of the anisotropy could be a tool to discriminate between the astrophysical and dark matter scenarios proposed as sources of fresh primary positrons [142–145]. The discriminating capabilities of the anisotropy measurement are related to the fact that astrophysical sources, namely, pulsars, act as point sources whereas dark matter are homogeneously distributed in the halo. Consequently, the expected dipole anisotropy in the astrophysical scenario [146–149] is larger than the corresponding to dark matter.

Positrons are excellent probes of the new phenomena, therefore, the measurement of the anisotropy in positrons is the preferred channel. In this sense, results on the e^+/e^-, e^+/p, $(e^+ + e^-)$ anisotropies have been provided by AMS-02 [63, 62, 150], PAMELA [151] and Fermi-LAT [152]. However, no absolute determination on the positron anisotropy has been provided yet.

On the other hand, the measurement of the anisotropy may help understand the change in the proton spectral index at high rigidities. In the context of the possible explanations to the hardening of the proton flux, the measurement of a sizable anisotropy could distinguish between the injection of fresh high rigidity protons by local sources or the non-standard propagation or acceleration mechanisms.

In the context of the precision era in Cosmic Ray Astrophysics, where features that challenge the standard paradigm of cosmic ray origin and propagation have been observed, the measurement of the anisotropy provides a complementary characterization to the energy spectra. The capabilities of AMS-02 to determine the fluxes of individual primary and secondary cosmic ray species can be profited to characterize their directionality. In this sense, a general strategy to achieve an absolute computation of the three-dimensional dipole anisotropy of the distinct cosmic ray species within the required precision (10^{-2}-10^{-4}) is needed.

This thesis presents the tools and techniques developed in the determination of absolute large-scale anisotropies with AMS-02, and its application to galactic cosmic ray electrons, positrons, and protons.

2

AMS-02 EXPERIMENT

2.1 Introduction

The Alpha Magnetic Spectrometer (AMS) is a multi-purpose particle physics detector designed for precision studies of cosmic rays up to TeV energies as an external module onboard the International Space Station (ISS). The large statistics collected in this unique environment, free from the atmospheric effects, is already providing results with unprecedent precision in the field of Cosmic Ray Physics and constitutes an open window to address fundamental physics questions such as the nature of the Dark Matter and the matter-antimatter asymmetry in the Universe.

The AMS-02 experiment is conducted by the AMS collaboration, which involves 46 institutes from 16 countries across Europe, America and Asia. The scientific goals of the experiment include the search for primordial antimatter, the quest for Dark Matter, and precision measurements on fluxes of cosmic ray species up to $Z = 26$ to help understand their origin and propagation in the Galaxy.

AMS principal investigator is the MIT physicist Nobel laureate Samuel Ting, who first proposed the project in 1995. The proposal, which was accepted by the U.S. Department of Energy (DOE), included the installation of a magnetic spectrometer in space, and the agreement of NASA for the space transportation, installation and supervision of the fulfillment of the strict safety regulations in space.

The experimental program was conducted in two phases: a precursor flight on a Space Shuttle, to assess the feasibility and performance of a prototype in space (AMS-01); and a long-term mission onboard the ISS (AMS-02). In both cases, the AMS collaboration was responsible of the design, construction and operation of the detectors. The collaboration is also in charge of the data analysis and the scientific exploitation of the results.

2.1.1 *AMS-01. The precursor flight*

From 2nd to 12th of June 1998, the AMS prototype, AMS-01, flew on the Space Shuttle Discovery on the STS-91 mission (figure 2.1-*left*). The primary goals of the mission included the verification of the spectrometer operation and performance in space, and the feasibility to use the technology developed for high-energy physics detectors in sizable experiments in orbit.

The AMS-01 was the first large magnetic spectrometer ever operated in space, and consisted of four major components as shown in figure 2.1-*right* [153]:

- A *permanent magnet* and a *silicon tracker detector* to measure the sign of the particle charge and its momentum.

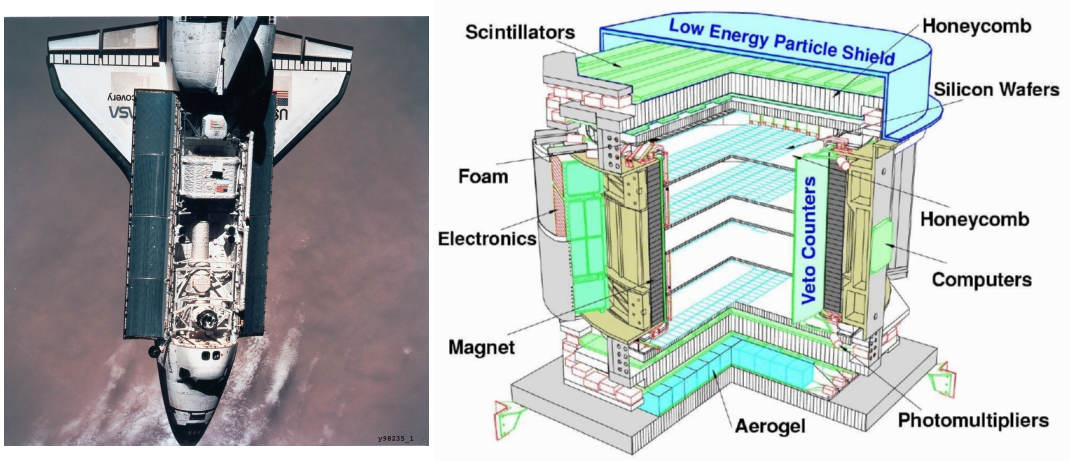

FIGURE 2.1: *(Left)* AMS-01 on board of the NASA Space Shuttle Discovery during the precursor flight in June 1998. *(Right)* Schematic view of the AMS-01 subdetectors and components [153].

- A *time of flight* hodoscope, which measures the velocity of the particle and provides the trigger of the experiment.
- A *threshold Cherenkov counter*, to separate low velocity from high velocity particles.
- An *anticoincidence counter*, to veto particles that traverse the detector outside the fiducial volume of the magnet.

During the ten days of flight and successful operation, AMS-01 recorded nearly 80×10^6 cosmic ray events. Apart from the detector verification, the collected statistics allowed the measurement of cosmic ray fluxes of electrons and positrons, protons and antiprotons, deuterons, helium, and light nuclei [154–160, 61].

2.1.2 *AMS-02. The long term mission*

The encouraging results of the AMS-01 mission supported the construction of the TeV particle physics detector AMS-02 onboard the ISS. The different subdetectors composing AMS-02 were built by the different institutes involved in the AMS Collaboration and were assembled at CERN. However, after the tragic loss of the Space Shuttle Columbia and its crew on 1 February 2003, the Space Shuttle program was suspended by NASA and a number of flights, including the one which would take AMS-02 to the ISS, was canceled. On 15 October 2009, President George W. Bush authorised NASA to add another Space Shuttle flight to transport AMS-02 to the ISS, which took place on 16 May 2011 onboard the Space Shuttle Endeavour. The STS-134 mission, which successfully installed AMS-02 three days later, was the last mission of the Endeavour Shuttle and the penultimate mission of the Space Shuttle program. AMS-02 was installed at the upper Payload Attach Point on the S3 Truss of the ISS (figure 2.2) and, shortly after the deployment, AMS-02 started data taking. Since then, AMS-02 has been continuously collecting science data at a rate of $\sim$ 16 billion events per year.

The AMS-02 detector is a large acceptance (0.5 m^{2}sr) magnetic spectrometer designed to carry out precision measurements of charged cosmic rays in a long-term mission which extends during the ISS lifetime until 2024 [161, 162]. Aboard the ISS, AMS-02 follows a low Earth orbit of altitude ~ 400 km and inclination of $51.6°$. On the ISS, the AMS-02 detector is tilted $12°$ with respect to the ISS vertical.

FIGURE 2.2: AMS-02 detector mounted on the upper Payload Attach Point on S3 Truss of the International Space Station.

Apart from the requirements imposed to operate in space, AMS-02 weight and power budgets are constrained to fulfill the conditions of the shuttle transportation and ISS boarding. In particular, AMS-02 has a weight of 7.5 tons and a size of $3\times4\times5$ m^3. The ISS provides the power supply to AMS-02, with an allocated power of 2 kW and a data down-link rate to ground of ~ 10 Mbit/s in average.

AMS-02 is specifically designed for the study of antimatter. In this sense, one of main goals of the experiments is the search for primordial antimatter, produced in the Big Bang. For instance, the measurement of anti-helium nuclei in cosmic rays could be an evidence of the existence of antimatter domains in the Universe, due to the low probability of anti-helium production in cosmic ray interactions within the ISM.

On the other hand, the precise determination of the spectra of cosmic ray antimatter particles, such as positrons and antiprotons, and possible deviations from the expectations derived from the standard model of cosmic ray origin and propagation may be a hint of annihilation or decay of Dark Matter particles.

Finally, AMS-02 is performing high statistics measurements of the flux of cosmic ray species up to $Z = 26$, allowing to test the precision of the current models about the origin and propagation of galactic cosmic rays, and providing accurate results to further constrain the predictions and improve our knowledge about cosmic ray physics.

The pursuit of new physics phenomena relies in the detector's particle identification capabilities. Redundancy in the measurement of the particle properties is mandatory, not only because it is essential in any space-based experiment, but also because it allows to improve the precision in the particle identification. In this sense, AMS-02 is composed of 6 subdetectors, as shown in figure 2.3:

- A *Permanent Magnet* and a *Silicon Tracker Detector* (STD). The trajectory of the particle inside the permanent magnet is reconstructed by a set of nine planes of silicon detectors, thus providing the measurement of the particle momentum and charge with its sign, and allowing for tracking capabilities.
- A *Transition Radiation Detector* (TRD), to distinguish between light and heavy particles of the same charge and momentum and, in particular, between positrons and protons.
- A *Time of Flight* (TOF) hodoscope, which consists of four layers of scintillator counters providing a measurement of the particle velocity and acting as a trigger of the experiment.
- A *Ring Imaging Cherenkov Detector* (RICH), which provides a measurement of the particle velocity and allows for isotope identification.
- An *Electromagnetic Calorimeter* (ECAL), to determine precisely the energy of electromagnetic particles up to few TeV, allowing the separation between leptons and hadrons.
- An array of *Anti-Coincidence Counters* (ACC), to provide a veto for particles traversing the detector laterally.

In addition, the electronics provide the readout of the particle signals, allowing a data reduction without science information loss.

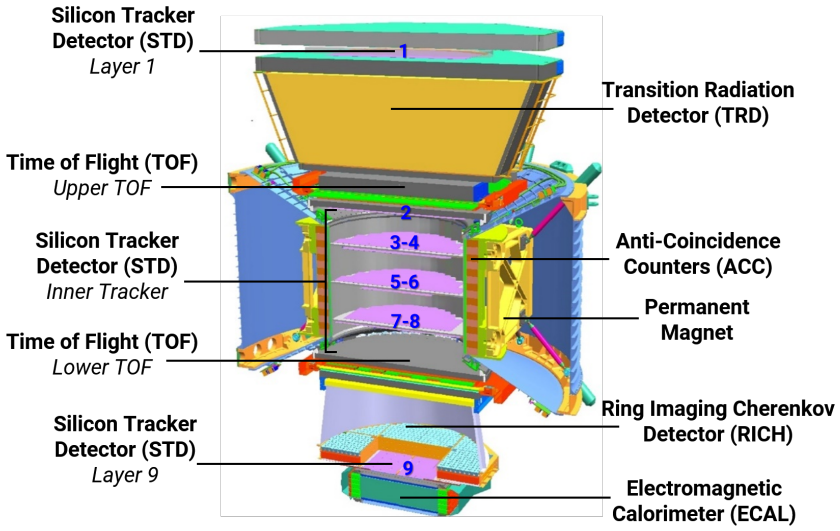

FIGURE 2.3: AMS-02 detector schematic layout.

2.2 THE PERMANENT MAGNET AND THE SILICON TRACKER DETECTOR

One of the main goals of AMS-02 is the identification of antimatter particles, which ultimately relies on the measurement of the charge sign. This is achieved by the reconstruction of the curved trajectory of a charged particle inside a magnet. A silicon tracker inside a permanent magnet constitutes the core of the detector and provides the magnetic spectrometer capabilities of AMS-02.

2.2.1 *The Permanent Magnet*

The central part of AMS-02 is occupied by a cylindrical permanent magnet, with an inner diameter of 111.5 cm, an outer diameter of 129.9 cm, and a height of 80.0 cm (figure 2.4-*left*).

The permanent magnet is made of an alloy of high-grade Nd-Fe-B. Neodymium magnets are currently among the strongest permanent magnets due to their crystalline properties, and are widely used in daily life devices.

The AMS-02 permanent magnet is composed of 64 sectors, each one consisting of 100 blocks with dimensions $5.08 \times 5.08 \times 2.54\,\mathrm{cm}^3$, glued together with epoxy resin which also protects them from corrosion [163–165].

As a result, the AMS-02 permanent magnet produces a magnetic field of intensity 0.15 T, highly uniform along the direction perpendicular to the magnet bore defined as X axis (figure 2.4-*right*). In this manner, the permanent magnet also provides a reference frame within the detector, with the Y axis in the bending direction and the Z axis corresponding to the vertical direction, perpendicular to the XY plane. As a consequence, the trajectory of charged particles is deflected by the magnetic field in the YZ *bending plane*.

The permanent magnet has a negligible dipole moment in order to avoid couplings with the Earth magnetic field resulting in undesirable forces on the space shuttle or the ISS. In addition, in fulfillment of the strict NASA safety regulations, a negligible magnetic flux leakage is required[1] not to interfere with the life support system of the astronauts.

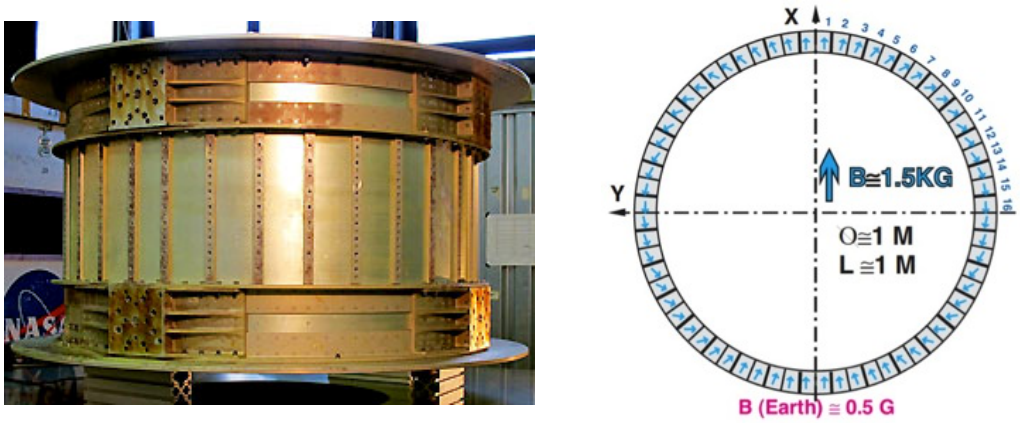

FIGURE 2.4: *(Left)* AMS-02 permanent magnet. *(Right)* Magnetic field produced by the permanent magnet. The direction of the field defines a reference frame within the detector.

2.2.2 *The Silicon Tracker Detector (STD)*

The trajectory of the particle inside the detector is measured by 9 high precision silicon layers arranged in 6 planes along the Z axis covering the full span of AMS-02

1 The flux leakage at a 2-meter distance from the center of the magnet is required to be smaller than 3G.

at different heights. A total of $2,284$ double-sided microstrip silicon sensors of size $\sim 72 \times 41 \times 0.3$ mm^2 overlaying a total active area of 6.75 m^2 are assembled in 192 readout units called *ladders*, with a total of $\sim 200,000$ readout channels. Each ladder constitutes a mechanical and electrical unit composed by a linear arrangement of 9 to 15 sensors glued to a light support structure [166–168]. Ladders are fixed on supporting planes made of low density aluminum honeycomb sandwiched between two carbon fiber skins, matching the cylindrical shape of the magnet.

The bi-dimensional measurement of the particle's position at the different heights of the layers is achieved by means of p^+ (junction) and n^+ (ohmic) strips running in orthogonal directions and implanted on opposite sides of the silicon sensors. The p-side strips, running in the longitudinal direction of the ladder, provide the measurement in the bending coordinate (Y) whereas the n-side strips, disposed orthogonally to the ladder length, measure the position along the non-bending coordinate (X). Both p and n sides are separately connected in different daisy chains to the front-end electronics. This makes a total of $2,568$ implanted strips for 640 readout strips on the p-side and 384 implanted strips for 192 readout strips on the n-side.

A singly-charged particle traversing a silicon sensor creates approximately $24,000$ electron-hole pairs along its trajectory, which drift to opposite sides due to the electric field in the depletion zone within a time interval of ~ 10 ns. The center of gravity of these cluster signals allows to calculate the position with an accuracy better than 10 μm in the bending direction (Y), and 30 μm in the non-bending one (X) [169].

Three honeycomb planes, with silicon layers on both sides from layer 3 to layer 8, are placed inside the magnet bore. An additional support plane with a single layer (layer 2) of silicon detectors is located at the top end of the magnet. Layers 2-8 constitute the so-called *Inner Tracker*. Finally, two additional single layer planes are installed on top of the TRD detector (layer 1) and in-between the RICH and ECAL (layer 9) to get a maximum lever arm of about 3 m.

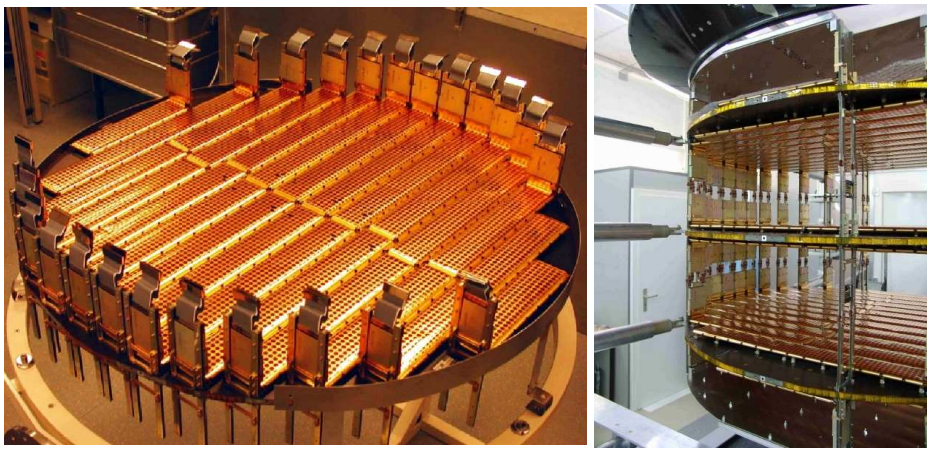

FIGURE 2.5: *(Left)* AMS-02 Tracker silicon ladders in a single plane. *(Right)* Three inner tracker planes, composed of double-sided layers with silicon detectors.

2.2.2.1 *Tracker Alignment System (TAS)*

The determination of the relative position between the tracker elements is critical to achieve an accurate measurement of the particle trajectory. In particular, due to the extreme conditions in the ISS space environment, with external temperatures varying several tens of degrees, mechanical deformations and misalignments may occur. In this sense, the mechanical stability of the Inner Tracker is monitored using the Tracker Alignment System (TAS), which is mounted outside the Inner Tracker volume. The TAS provides optical generated signals corresponding to straight trajectories in the Inner Tracker. The generated infrared laser beams are capable to penetrate simultaneously the seven layers of the Inner tracker, thus allowing a determination of module displacements with a position accuracy better than $5\ \mu$m.

2.2.2.2 *The Tracker Thermal Control System (TTCS)*

The high number of tracker readout channels produce 200 W, which are removed by the Tracker Thermal Control System (TTCS). The TTCS is a redundant mechanically pumped loop system filled with two-phase (liquid and gas) CO_2. The heat from the Tracker front-end electronics is transferred to the cooling system by means of thermal bars. As a result, the liquid CO_2 absorbs the heat and makes a liquid/gas phase transition. Outside the tracker volume, the vapor is conducted to condensers on radiators panels directed to the deep space. In this manner, the TTCS contributes to keep an homogeneous temperature in the Inner Tracker.

2.2.3 *Reconstruction of the particle track and rigidity measurement*

The passage of a charged particle through the detector is estimated by the calculation of the center of gravity of the cluster signals induced in each tracker layer. To reconstruct the trajectory from the individual cluster signals in X and Y directions, a track finding algorithm is needed. Due to the large number of readout channels, the typical number of clusters per event is 100 while a track is supposed to have at most 18 [167], which hinders the track finding.

In AMS-02, the track finding algorithm consists in 4 steps: seed searching, hit combination optimization within the track road, external layers hit searching, and track fitting [170]. The first two steps are performed in the Inner Tracker, where the algorithm initially searches for Y clusters due to the ambiguity on the X coordinate[2]. Among the candidates on the Y side, a similar search for 3D hits is performed by accepting combinations of X and Y clusters with reasonable χ^2. A good track candidate should contain hits in all 4 Inner planes. The ambiguities on the X coordinate are removed by matching the position and direction of the track with the TRD track, or the TOF track if the former is not available. Finally, the extrapolation of the inner track to the external layers, layer 1 and 9, and the search for X and Y hits is performed. If the track extrapolation to that outer layers, within a rigidity-dependent

2 Contrary to the Y coordinate, which is precisely known, the X coordinate is ambiguous because the X readout channels of adjacent sensors are connected with each other.

window, finds associated X and Y clusters, the track is extended to include these hits.

As a result of the track finding algorithm, four types of tracks (*tracker patterns*) can be defined

- Inner track: no hits on the external layers
- L1+Inner track: hit on layer 1 and no hit on layer 9
- Inner+L9: hit on layer 9 and no hit on layer 1
- L1+Inner+L9: hits on layer 1 and layer 9

The measurement of the particle rigidity is obtained by a path integral fit of the track trajectory in the AMS-02 magnetic field. Three different algorithms for the rigidity reconstruction are used, two of them are based on different implementations of the path integral fit (along lines connecting the measured points or along the expected trajectory by means of a Runge-Kutta tracking) with treatment of the multiple scattering; and a third one based on an implementation of a Monte Carlo fit including multiple scattering and energy losses.

The rigidity resolution can be estimated from Monte Carlo once the point resolution and the effects of residual misalignments are correctly simulated. Since the determination of the rigidity depends on the bending of the particle trajectory inside the magnet, as the rigidity increases the bending decreases and the rigidity resolution, $\frac{\Delta R}{R}$, steadily worsens. In particular, the rigidity resolution (as well as the single hit resolution) reaches the 100% at a point called *Maximum Detectable Rigidity* (MDR), which depends on the intensity of the magnetic field and the lever arm of the track reconstruction. The aforementioned four types of tracks provide distinct lever arm configurations which, in turn, translates into a measurement of the rigidity with different resolutions. Among the four, the L1+Inner+L9, so-called *fullspan*, configuration has the highest lever arm, thus profiting the full capabilities of AMS-02 in the determination of the rigidity with the best resolution available. In particular, fullspan protons have an MDR of 2 TV [168] (figure 2.6).

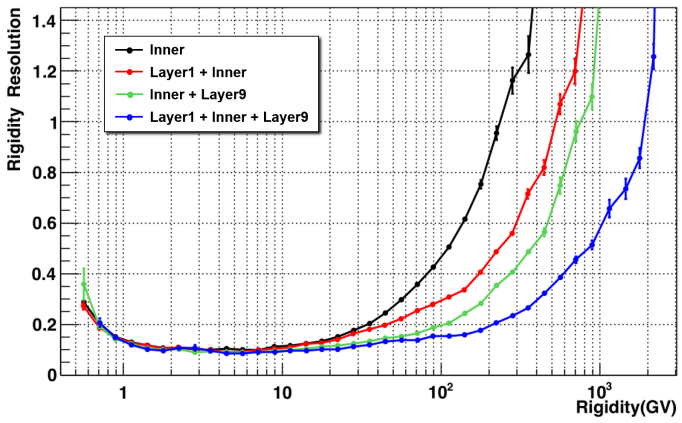

FIGURE 2.6: AMS-02 Tracker rigidity resolution for protons estimated from the Monte Carlo simulation as a function of the generated rigidity for the distinct tracker patterns [167].

2.2.4 *Charge measurement*

The amplitude of the cluster signals has several contributions: a constant offset (pedestal), a noise component, and the signal corresponding to the energy deposited by the particle. A threshold applied to signal-to-noise ratio allows to define a valid signal from which the energy can be inferred. This ionization energy is proportional to the square of the particle charge according to the Bethe formula, $\frac{dE}{dx} \propto Z^2$, which allows to provide a precise measurement of the particle charge in the dynamical range up to iron ($Z = 26$) [171, 172].

In addition, with the combination of the measurement of the trajectory inside the magnet and the TOF determination of the particle incidence (downward or upward-going particles), the tracker provides the sign of the charge, thus allowing the separation between matter and antimatter.

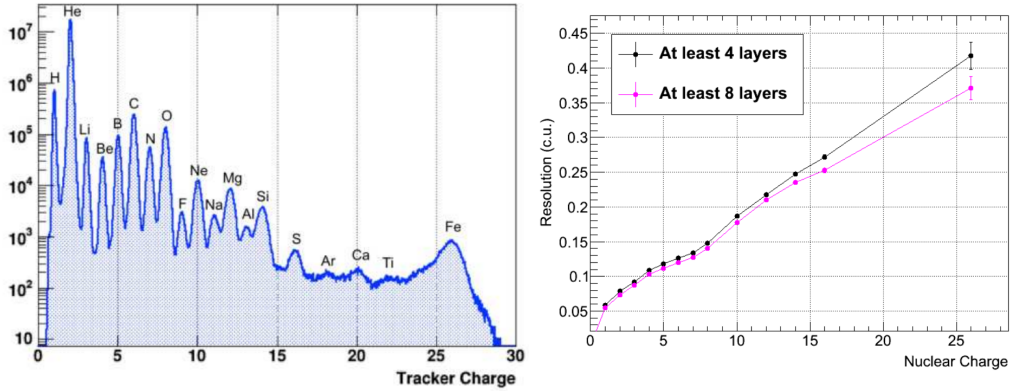

FIGURE 2.7: *(Left)* Tracker charge up to silicon determined from the combination of p and n-side measurements [173]. *(Right)* Tracker charge resolution, in charge units, for nuclei up to silicon [171].

2.3 THE TRANSITION RADIATION DETECTOR (TRD)

The Transition Radiation Detector (TRD) is placed on top of AMS-02, in-between the layer 1 of the Tracker and the upper TOF, and it is suitable to distinguish the light electrons and positrons from the heavy protons.

The basic operating principle of the TRD consists in an efficient detection of the *transition radiation* emitted by a charged particle traversing an inhomogeneous material, such as the interface of two media with different dielectric properties, as a result of an electric field rearrangement. In particular, transition radiation becomes observable for relativistic charged particles, where soft X-rays of energy of $\mathcal{O}(10\ \text{keV})$ are emitted. In that case, the total energy loss is proportional to the Lorentz factor of the particle, $\gamma = \frac{E}{m}$, which makes transition radiation suitable as a mechanism to identify particles of different masses. On the other hand, the emitted radiation is extremely forward peaked, with an angle of $\sim 1/\gamma$, and the number of radiated photons produced per particle crossing one interface is generally low, of the order of the fine-structure constant, $N \sim \alpha = \frac{1}{137}$. However, the probability

of emission can be enhanced by using a multilayered dielectric radiator spaced in vacuum, with the interfaces separated a minimum distance which is proportional to the radiation wavelength [174–176].

The AMS-02 TRD has an inverted octagonal pyramid shape and is composed of 328 modules arranged in 20 layers [177]. Each module consists of 20 mm of fleece radiator and 16 straw tube proportional counters of 6 mm diameter. The support structure is made of aluminum and carbon fiber honeycomb sandwich (figure 2.8). The fleece radiator is composed of 10 μm thick polypropylene/polyethylene fibers with a density of 0.06 g/cm^3 which yields a large number of interfaces thus increasing the emitted transition radiation. On the other hand, the straw tubes are filled with a Xe:CO_2 gas mixture in a proportion 90:10, and operate in the full avalanche regime at 1600 V providing a high efficient X-ray conversion. When the charged particle crosses the sub-detector, the emitted X-rays ionize the gas and produce an ionization avalanche near the wire, thus inducing an electric signal. In the tubes, xenon is used to detect the ionization signal of the charged particle, whereas carbon dioxide acts as a quenching gas for charge multiplication.

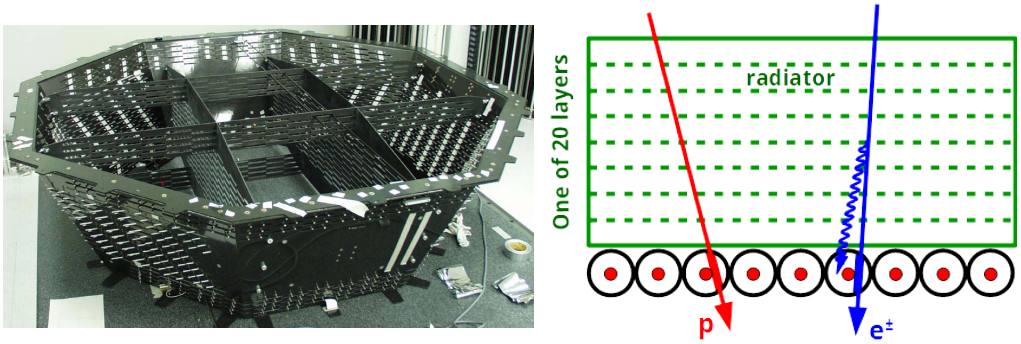

FIGURE 2.8: *(Left)* AMS-02 TRD octagon support structure. *(Right)* One TRD module showing the interaction of a lepton and a proton in the fleece radiator. X-rays produced by the charged particle produce an ionization avalanche near the wire in the straw tubes. Electrons and positrons have an additional contribution to the ionization due to the transition radiation.

Two tanks of 49 kg xenon and 5 kg carbon dioxide at the time of the launch store the mixture that fill the gas circuit, which ensure an effective livetime of more than 30 years in space. The total volume of the TRD gas system amounts to 230 L, with a measured leak rate of 6 μg/s, mainly due to the diffusion of the carbon dioxide.

In addition, the particular arrangement of the TRD layers allows 3D tracking capabilities. The proportional tubes in the 4 upper and lower layers run parallel to the non-bending direction (X), along the magnetic field direction, whereas the central 12 layers are parallel to the bending direction (Y).

2.3.1 *Electron and positron identification*

The AMS-02 TRD detector is capable to distinguish electrons and positrons from protons by means of an statistical estimator based on a likelihood ratio of probabil-

ities for the different cosmic ray species. These probabilities are calculated taking into account the energy deposition dE_i along the path length dx_i in a tube, which is determined from the extrapolation of the tracker trajectory [178].

The probabilities of the electron and proton hypothesis allow to construct a likelihood ratio which defines the TRD estimator, $\mathcal{L}_{\text{TRD}}$ used in the lepton identification

$$\mathcal{L}_{\text{TRD}} = -\log \frac{L_{\text{e}}}{L_{\text{e}} + L_{\text{p}}} \quad ; \quad L_{\text{e,p}} = \sqrt[n]{\prod_i^n p^i_{\text{e,p}} \left(\frac{dE_i}{dx_i} \right)} \tag{2.1}$$

where $p^i_{\text{e,p}}$ are the probability density functions for electrons (e) and protons (p), and $\frac{dE_i}{dx_i}$ is the cluster deposited energy for every cluster i of the event scaled by the path length along the tube. The probability density functions for clean samples of electrons and protons are shown in figure 2.9-*left*, where the peak and the characteristic Landau-shaped tail from the ionization losses are evidenced. Contrary to protons, the emission of transition radiation in electrons gives rise to a higher energy deposition.

The TRD proton rejection based on the TRD estimator is shown in figure 2.9-*right*. In particular, a rejection of more than 10^3 up to 200 GeV is achieved.

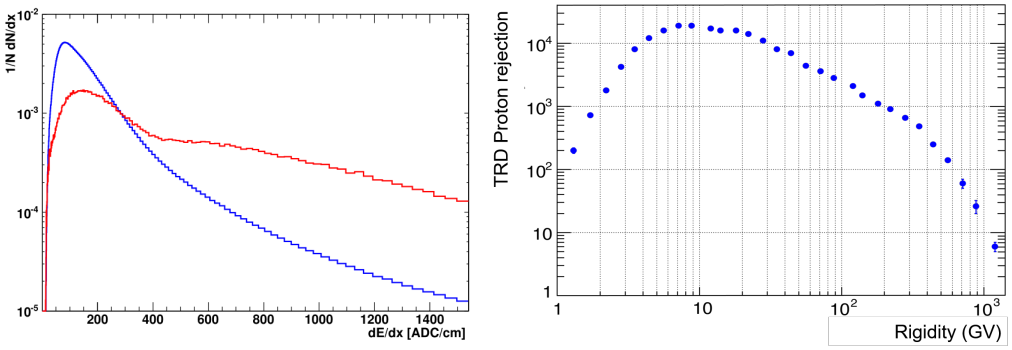

FIGURE 2.9: *(Left)* Probability density function for the energy depositions in the TRD of electrons (red) and protons (blue). Due to the emission of the transition radiation, the energy deposition for electrons is higher than that of protons [178]. *(Right)* TRD proton rejection by means of the TRD estimator as a function of the rigidity [178].

In order to get a robust TRD estimator, a minimum number of hits above a certain threshold are required. In addition, a refit of the TRD track is performed to identify misreconstructed events. On the other hand, the calculation of the path length depends critically on the alignment and gain calibration of the TRD. Thus, to ensure an efficient lepton separation, the TRD is constantly monitored online, taking care of gas refills, gas gains and alignment [179].

2.4 THE TIME OF FLIGHT (TOF)

The AMS-02 Time of Flight (TOF) consists of four layers of fast plastic scintillator counters, arranged in two planes covering the full AMS-02 acceptance, separated a distance of about 120 cm, and located at the top of the magnet bore (*upper TOF*,

UTOF) and below it (*lower TOF*, LTOF) as shown in figure 2.10-*left* [180, 181]. The TOF provides the main trigger system of the experiment and allows precision measurements of the particle charge and velocity ($\beta = v/c$).

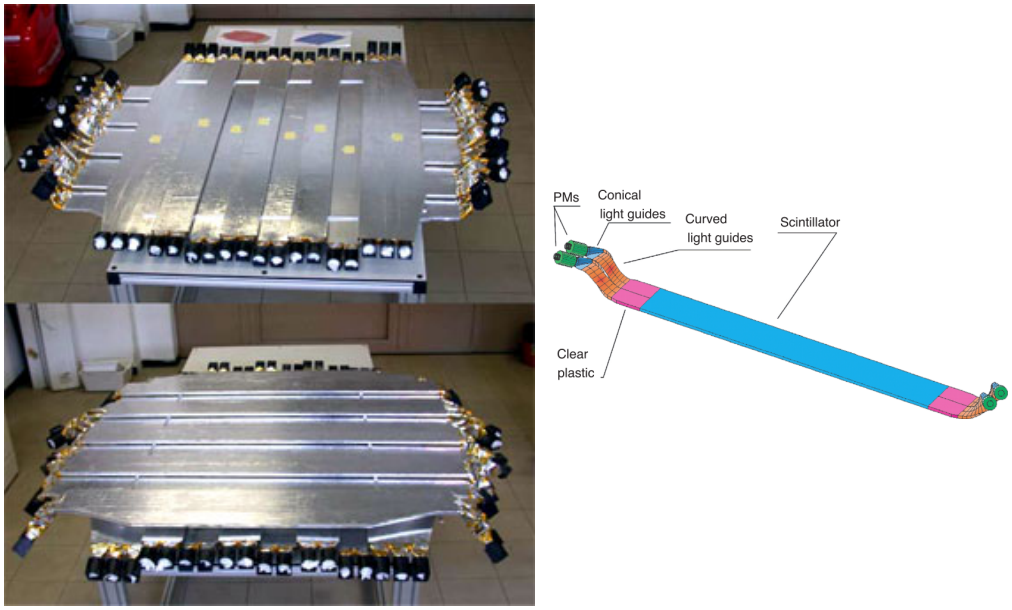

FIGURE 2.10: *(Left)* TOF planes of AMS-02, upper and lower TOF, respectively, separated by a distance of 1.2 m. *(Right)* Scheme of a TOF paddle.

From the top to the bottom, the four TOF layers consists of 8, 8, 10 and 8 scintillator paddles of 1 cm thick, 12 cm width, and variable lengths (from 117 and 134 cm), as shown in figure 2.10-*right*. The external paddles have a trapezoidal geometry to maximize the acceptance. The paddles are oriented alternatively in the X and Y directions to provide a granularity of 12×12 cm^2 in the reconstruction of the interaction point, with an overlap of 0.5 cm to avoid geometrical inefficiencies.

The light emitted when a charged particle traverses a TOF paddle is collected at both ends of the counter. Each side of the paddles is optically connected to 2 or 3 fine-mesh Hamamatsu photomultipliers tubes (PMTs), for redundancy, wich are able to keep good timing characteristics while working in high magnetic fields. The optical coupling between the scintillators and the PMTs is made of plexiglass light guides, tilted or twisted in order to minimize the effect of the magnetic field on the PMT signal. In total, the 144 PMTs connected to the 34 scintillator paddles are applied a high voltage, between $1,700$ V and $2,250$ V, and have a nominal gain of 10^6.

The anode signals from the 2 or 3 PMTs of the paddle are summed up to be used at a trigger level and to provide a measurement of the particle charge and velocity.

2.4.1 *Velocity measurement*

The velocity of a particle, $\beta = \frac{v}{c} = \frac{\Delta s}{c\Delta t}$, crossing the detector can be determined by measuring the time of flight Δt between the upper and lower TOF and the trajec-

tory length Δs provided either by the Tracker or the TOF. The velocity resolution $\Delta\beta$ is ∼4% for protons, corresponding to a time resolution of ∼160 ps, and improves to ∼1.2% for $Z \geq 6$ for a time resolution of ∼48 ps (figure 2.11).

In addition, the precise measurement of the time of flight allows to separate downward and upward-going particles at the 10^{-9} level, which is crucial to identify matter and antimatter by means of the curvature of the particle trajectory in the magnetic field.

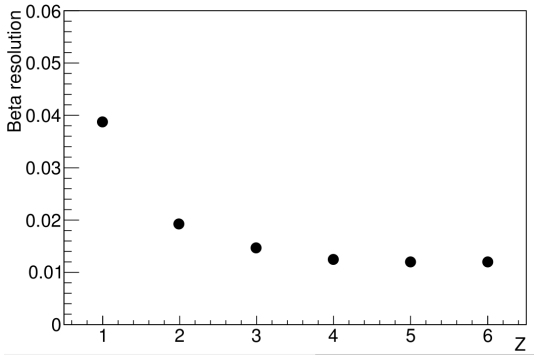

FIGURE 2.11: TOF velocity (β) resolution as a function of the particle charge Z [181].

2.4.2 *Charge measurement*

The measurement of the charge by the TOF counters is based in the energy deposited by the passage of a charged particle, $\frac{dE}{dx} \propto Z^2$. The signals from the PMTs anode and dynode are used to determine the particle charge with high resolution. In particular, low charges ($1 \leq Z \leq 3$) are measured using anodes; middle charges ($4 \leq Z \leq 8$), when anodes start to saturate, are measured using both anodes and dynodes; and high charges ($Z \geq 8$) are measured using dynodes due to its large dynamical range of measurement.

In this manner, the TOF is able to measure the charge of nuclei up to $Z = 30$ (figure 2.12-*left*), thus allowing to distinguish the different cosmic ray species. The charge resolution of a single TOF counter is shown in figure 2.12-*right*. In particular, for Carbon (Z=6) the charge resolution is ~ 0.16 charge units (c.u.), and for Iron ($Z = 26$) it is found to be ~ 0.4 c.u.

2.4.3 *Threshold for trigger logic*

The anode signals are compared to three different thresholds, which are used in the level 1 of the AMS-02 trigger logic:

- *Low Threshold* (LT) for time measurements, corresponding to ∼20% of the minimum ionizating proton (MIP) signal.
- *High Threshold* (HT) for the charged particle trigger, $Z \geq 1$, set at ∼60% of the MIP signal.

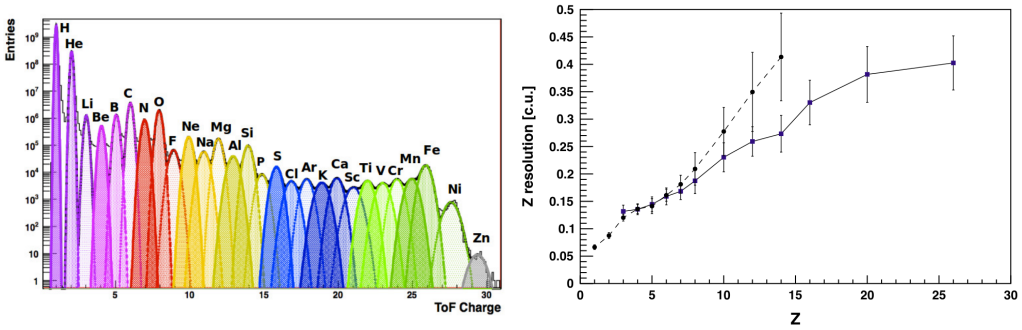

FIGURE 2.12: *(Left)* TOF charge measurement up to $Z = 30$ [181]. *(Right)* Charge resolution measured in charge units (c.u.) for anode (dashed line) and dynode (solid line) as a function of the particle charge [180].

- *Super-High Threshold* (SHT) for the $Z \geq 2$ particle (ions) trigger, at ∼400% of the MIP signal.

2.5 THE RING IMAGING CHERENKOV (RICH)

The AMS-02 Ring Imaging Cherenkov (RICH), placed in-between the lower TOF and the ECAL, is designed to separate charged isotopes in cosmic rays by measuring their velocity β and absolute charge up to $Z < 26$ [182, 183].

The basic operating principle of the RICH consists in the detection of the Cherenkov radiation emitted when an incoming charged particle traverses a dielectric medium characterized by a refractive index $n > 1$ with a velocity β higher than the velocity of light in that medium[3], $\beta > \frac{1}{n}$, as a result of an asymmetric polarization of the medium [184]. The radiation is emitted in spherical wavefronts confined in a cone of angle θ_c given by $\cos\theta_c = \frac{1}{n\beta}$. The amount of photons dN produced in a distance dx per wavelength $d\omega$ is given by the Frank-Tamm formula $\frac{d^2N}{dxd\omega} \propto Z^2 \sin^2\theta_c$, allowing the determination of the particle charge once the angle of the radiation cone is known [185]. As a consequence, Cherenkov radiation is emitted in a continuous spectrum, with high frequencies (in the blue region) being the most intense. Since the refractive index of the medium depends on the frequency, this spectrum usually exhibits a cutoff above ultraviolet frequencies.

In essence, the AMS-02 RICH consists of a layer of radiator material, a conical reflector and a detection plane (figure 2.13-*left*). The radiator plane, of a 60 cm radius, is made of 92 tiles of 2.5 cm thick silica aerogel with a refractive index $n = 1.05$ and a central square built of 16 tiles of 0.5 cm thick of NaF with a refractive index $n = 1.334$. This combination allows to measure particles with $\beta > 0.95$ (aerogel) and $\beta > 0.75$ (NaF).

In the detection plane, placed at a distance of 47 cm below the radiator plane, a matrix of 680 4×4 multi-anode Hamamatsu PMTs are disposed in eight grids, four with rectangular shape and four with triangular shape, forming an octagonal structure of 67 cm radius. This structure has a central part not instrumented (*ECAL hole*),

3 Known as Cherenkov threshold, $\frac{1}{n}$.

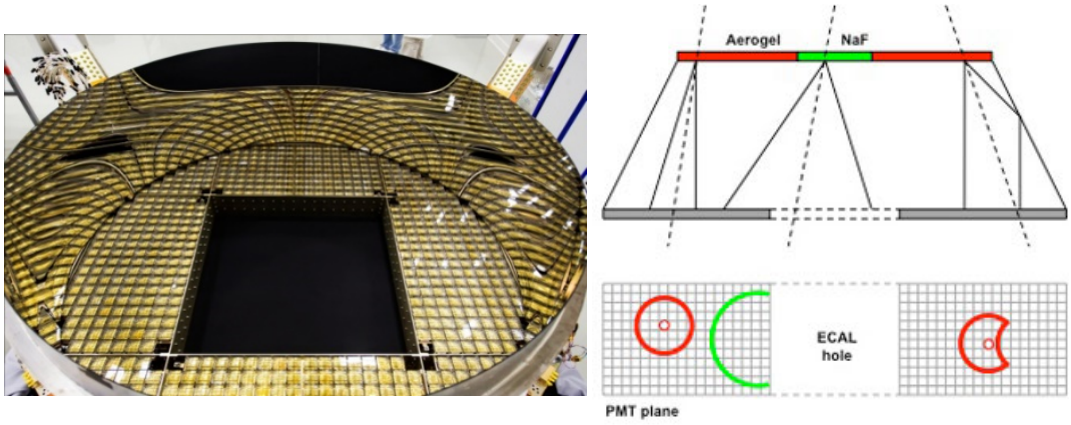

FIGURE 2.13: *(Left)* RICH detector, showing the PMT detection plane, the conical mirror and the ECAL hole. *(Right)* Cherenkov cones emitted by a charged particle crossing the radiator plane at the aerogel or NaF regions. Cherenkov cone emitted by a particle traversing the NaF region has a higher aperture angle, thus producing a circle despite of the ECAL hole.

with an area of 64×64 cm^2 corresponding to the geometrical shape of the ECAL placed below the RICH and designed to allow the particles to reach the ECAL unaffected (figure 2.13-*right*). The PMTs, equipped with independent light guides, operate in a moderate voltage ($\sim$ 800 V) regime, providing a fast and uniform response with a gain of 10^6 and allowing an effective spatial granularity of 8.5×8.5 mm^2.

When a charged particle crosses the radiator plane at a velocity higher than the Cherenkov threshold for the material, a cone of Cherenkov radiation is emitted. The photons radiated are collected by the PMT matrix and the Cherenkov cone can be reconstructed. The combination of aerogel and NaF optimizes the reconstruction efficiency since the radiation cone emitted by the NaF has a higher aperture angle, thus allowing to detect particles that fall in the ECAL hole.

In addition, to increase the detection efficiency and recover photons emitted in directions falling outside the detection plane, a truncated conical mirror covering the lateral structure is used. The mirror has a height of 47 cm and consists of three 120° segments of highly reflective material (100 nm aluminum and 30 nm SiO_2), with a reflectivity of $\sim$ 85% at $\lambda = 420$ nm, placed over a multi-layer support structure of carbon fiber reinforced composite substrate.

2.5.1 *Measurement of the particle velocity and charge*

The particle velocity is determined from the angle of the Cherenkov cone, which is reconstructed in AMS-02 by means of two different algorithms: a geometrical method based on a single-hit reconstruction, and a maximum likelihood method. An accurate knowledge of the aerogel refractive index is demanded to have a precise measurement of the particle velocity. In particular, the in-flight high statistics allowed to determine its refractive index with a precision of $\frac{\Delta n}{n} < 2 \times 10^{-5}$ and its stability with time. This leads to a velocity resolution $\frac{\Delta \beta}{\beta} \sim 0.8 \times 10^{-3}$ for He and $\sim 0.5 \times 10^{-3}$ for $Z > 5$ ions (figure 2.14-*left*).

On the other hand, since the particle reconstructed mass depends on its velocity,

$$m = RZ\frac{\sqrt{1-\beta^2}}{\beta} \tag{2.2}$$

the high precision in the determination of the particle velocity allows to separate charged isotopes in cosmic rays by using combined information from other subdetectors.

Finally, the measurement of the particle charge relies in the determination of the number of photoelectrons collected along the Cherenkov ring and the PMTs photon yield [186]. The latter constitutes the major contribution to the charge resolution, which is found to be ~ 0.3 c.u. for He and ~ 0.5 for Si ions (figure 2.14-*right*).

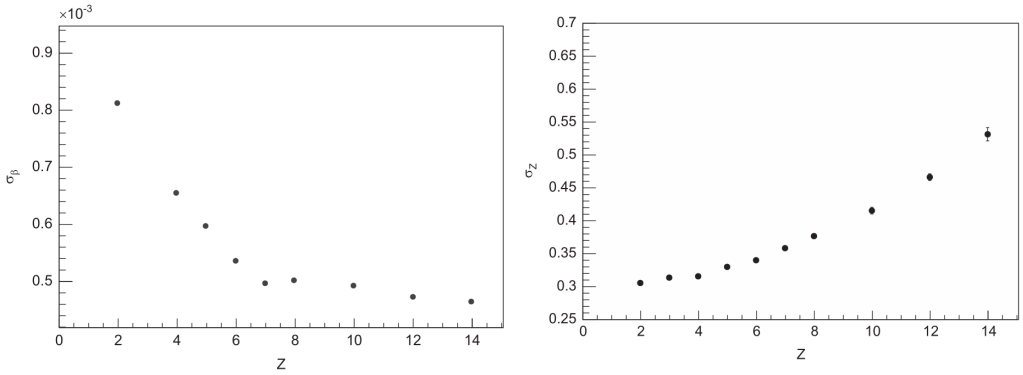

FIGURE 2.14: RICH velocity resolution *(left)* and charge resolution *(right)* as a function of the particle charge [182].

2.6 THE ELECTROMAGNETIC CALORIMETER (ECAL)

The AMS-02 Electromagnetic Calorimeter (ECAL), placed at the bottom of the detector, is a sampling calorimeter made of lead-scintillating fibers with the goal of providing an accurate measurement of the energy deposited by electromagnetic particles [187–191].

The ECAL has an active area of 648×648 mm^2, a thickness of 166 mm, and a weight of 496 kg, for a total weight of 638 kg including mechanical structure and readout cables (figure 2.15-*left*). It consists of 9 modules called *superlayers* with a thickness of 18.5 mm, each of one composed of 11 grooved lead foils of 1 mm thick interleaved with 10 scintillating fiber layers of 1 mm diameter glued together with optical epoxy (figure 2.15-*right*). Fibers run parallel in a superlayer, being alternatively aligned along the bending coordinate Y (4 superlayers) and along the non-bending direction X (5 superlayers), thus allowing a 3D imaging of the particle shower.

Each of the 9 superlayers is read out by 36 multianode Hamamatsu PMTs, with the anodes arranged at both opposite ends of the superlayer to read out the fibers with no dead areas. Each anode covers an 9×9 mm^2 area defined as *cell*, which corresponds to 35 fibers and divides the ECAL into 18 layers. In total, 324 PMTs

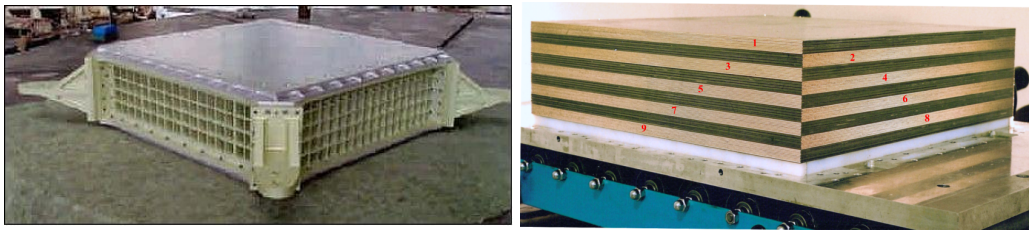

FIGURE 2.15: *(Left)* ECAL honeycomb structure. PMTs are installed on the squared holes. *(Right)* Distribution of the nine superlayers, with the fibers arranged in alternating directions.

cover 1296 cells and allow a precise sampling of the longitudinal shower profile by means of independent measurements on each 18 layers, and a lateral sampling due to 72 measurements in the transversal direction. Each cell corresponds to a $\sim 0.94X_0$ radiation length[4] in the longitudinal direction and ~ 0.5 Molière radius[5] in the transversal one, thus the AMS-02 ECAL has a $17X_0$ with only a 0.7 nuclear interaction lengths, which allows to discriminate hadrons from leptons.

2.6.1 *Measurement of the energy*

The design of the AMS-02 ECAL allows to achieve an almost complete containment of the electromagnetic showers of electrons, positrons and photons up to $\mathcal{O}(1 \text{ TeV})$[6]. In addition, about $1/3$ of the protons escape the ECAL without interacting (MIPs), while the remaining ones develop hadronic showers, which are only partially contained and have a longitudinal profile different from the characteristic Gamma function of electromagnetic showers.

The energy of electrons, positrons and photons is determined from the deposited energy in the calorimeter after applying two corrections:

- A first correction due to the anode efficiency, which is lower at the border of the cell than in the center, and the small dead space at the edge of each cell. These effects are more important for particles with vertical incidence between two adjacent cells. This correction is calculated by means of the lateral development of the shower, in particular, using the ratio of the energy deposited in 1 Molière radius with respect to the energy deposited in 3 Molière radius.
- A second correction takes into account a rear leakage after the $17X_0$ of the AMS-02 ECAL. The leakage is proportional to the number of particles escaping the ECAL which, in turn, is nearly proportional to the energy deposited in the last part of the shower. This correction profits from the longitudinal development of the shower and is calculated in terms of the fraction of energy deposited in the last superlayer and the total energy deposited in the calorimeter.

4 The mean distance over which a particle losses all but $1/e$ of its energy by bremsstrahlung, and $7/9$ of the mean free path for pair production by a high energy photon.
5 Radius that contains the 90% of the shower and characterizes its lateral spread.
6 The $17X_0$ of the AMS-02 ECAL contain ∼75% of the energy of 1 TeV electrons.

The ECAL energy resolution, as a result of a Test Beam measurement, is well parametrized by

$$\frac{\sigma(E)}{E} = \sqrt{\frac{(0.104)^2}{E} + (0.014)^2} \tag{2.3}$$

as shown in figure 2.16-*left*.

In addition, the ECAL has tracking capabilities and allows to obtain the direction of the incoming particle from the shower by fitting the shower axis position in each layer. The angular resolution is found to be better than 1° for particles above few tens of GeV (figure 2.16-*right*).

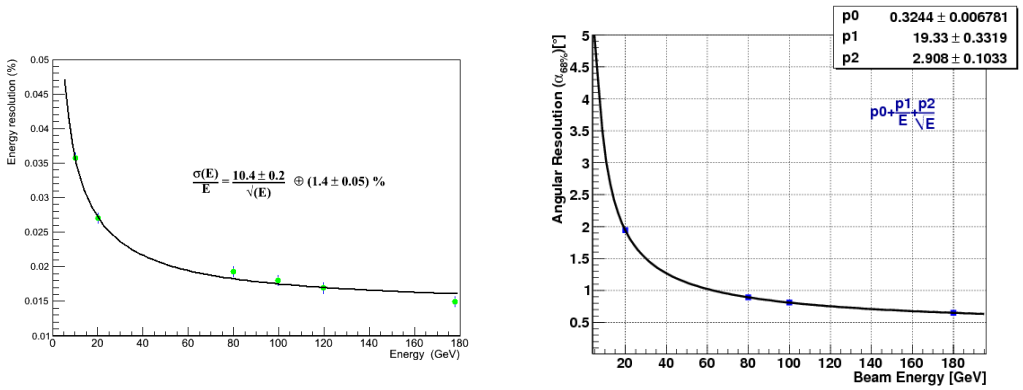

FIGURE 2.16: *(Left)* ECAL energy resolution as a function of the energy from the test beam calibration at CERN Super Proton Synchrotron (SPS) [191]. *(Right)* ECAL angular resolution, defined as the angular interval containing the 68% of the reconstructed angles, as a function of the energy from the test beam. In the case of leptons, the angle corresponds to that between the tracker track and the shower axis direction [191].

2.6.2 *Electron and positron identification*

The capabilities of separation between protons and leptons are based on the differences in the showers developed in the ECAL in each case.

From the 3D imaging capabilities of the ECAL, a multivariate method, based on a Boosted Decision Tree (BDT) technique, is used to discriminate leptons from protons. The method exploits non-linear correlations between variables that separates two different populations, tagged as signal and background. Over this set of variables, the BDT provides an estimator which quantifies the identification power and allows to distinguish electrons and positrons from protons at the desired level. In the case of the ECAL BDT estimator, a set of 32 variables related to the shower lateral and longitudinal shape, and the energy deposited is used.

Additionally, the ratio between the deposited energy measured by the ECAL and the momentum determined by the Tracker, E/p, provides a discrimination between leptons and protons. Since the electromagnetic shower of electrons and positrons is almost fully contained, the matching energy-momentum would be close to 1. However, a fraction of the protons will not interact in the ECAL and those interacting

will develop hadronic showers partially contained in the calorimeter, thus having a ratio E/p close to 0.

The proton rejection of the ECAL estimator combined with a cut in the matching between the energy and the momentum measured by the tracker is shown in figure 2.17. In particular, the ECAL proton rejection is found to be greater than 10^4 up to ~ 300 GeV, and above 10^3 up to 1 TeV.

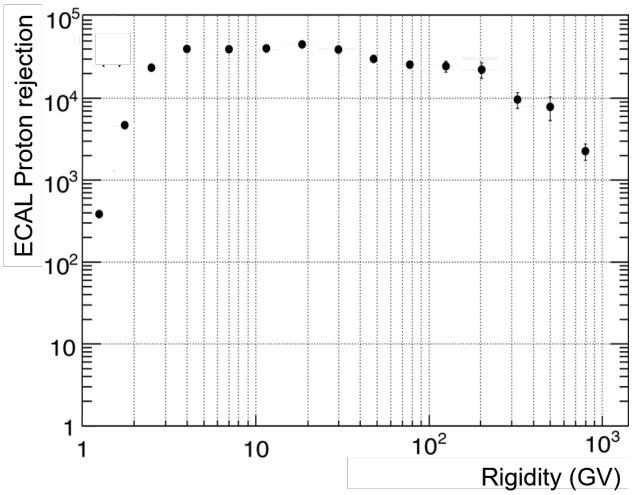

FIGURE 2.17: Proton rejection as a function of the rigidity measured by the tracker of the ECAL estimator combined with a cut on the energy-momentum match [189].

2.7 THE ANTI COINCIDENCE COUNTER (ACC)

The AMS-02 Anti Coincidence Counter (ACC) surrounds the Inner Tracker and allows a clean reconstruction of the events by rejecting particles entering the detector laterally, outside the AMS-02 geometrical acceptance; or interactions taking place inside the detector that may spoil the measurement [192].

The ACC is made of 16 scintillator paddles of $826 \times 826 \times 8$ mm, arranged in a cylindrical structure of diameter 1.1 m around the Inner Tracker (figure 2.18). The ultraviolet scintillation ($\lambda \sim 400$ nm) produced as a result of the ionization losses of the charged particles is absorbed by wavelength shifting fibers of 1 mm diameter embedded into the paddles, and guided to 16 fine-mesh Hamamatsu PMTs. These PMTs, arranged 8 at the top and 8 at the bottom, are similar to those of the TOF and are oriented with their axes parallel to the stray field in order to assure optimal operating conditions in strong magnetic fields.

To profit from the full capabilities of AMS-02 and the redundant measurement of the particle properties, cosmic rays traversing the detector from top to bottom ensure an optimal reconstruction of their variables by means of the passage through several subdetectors. Particles entering the detector from the side or produced as a result of secondary interactions with the detector material do not provide valuable information and are efficiently removed by the ACC. This ACC rejection is specially important in periods of high flux, such as when the ISS passes over the

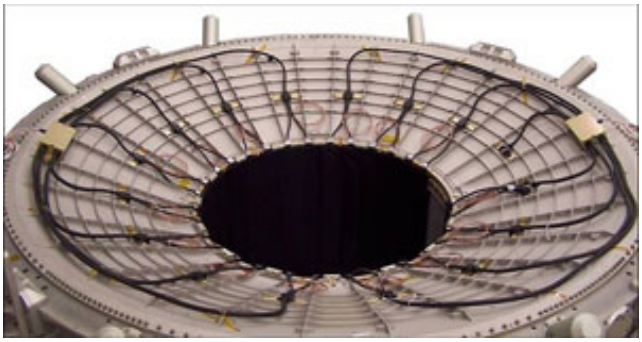

FIGURE 2.18: The AMS-02 Anti Coincidence Counter surrounding the Inner Tracker.

South Atlantic Anomaly or in regions close to the geomagnetic poles, where a high amount of cosmic ray particles per second hit the detector from all directions. In this manner, the ACC contributes to reduce the trigger rate in that case, acting as an efficient veto for the trigger decision (figure 2.19).

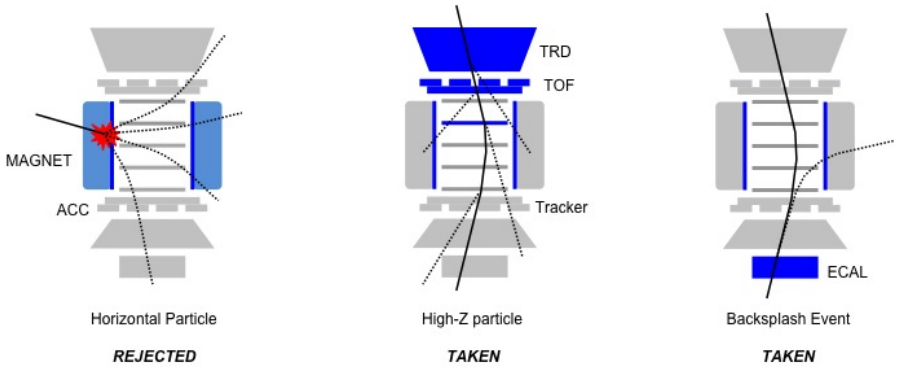

FIGURE 2.19: AMS-02 ACC operation. Particles entering the detector laterally are rejected. On the other hand, particles producing secondaries as a result of the interaction in the detector material or backsplash events produced in the ECAL are accepted [193].

2.8 THE TRIGGER LOGIC

The AMS-02 trigger system is able to provide fast start signals for the readout system once a cosmic ray particle crosses the detector and take decisions about the recording of events with valuable information or the rejection of undesirable events.

The AMS-02 trigger processes combined information from the TOF, ACC and ECAL, in an interval of about 200 μs, which represents a significant contribution to the dead-time of the experiment [194]. Two different stages in the AMS-02 trigger logic are sequentially adopted in order to minimize this dead-time: *Fast Trigger* and *Level 1 Trigger*.

2.8.1 *The Fast Trigger*

The Fast Trigger (AMS-02) relies on the signals received from the TOF and ECAL subdetectors and provides an extremely fast response which is based on the properties of the particle as measured by the two aforementioned subdetectors [195]:

- The TOF digital signals are combined to produce one of the following FT categories:
  - Charged Particle (CP): constructed from the digital signals of the TOF paddles, and it is set if at least one is above the HT.
  - Charged Particle in Tracker Acceptance (CT): constructed from the signals of the TOF paddles inside the Tracker acceptance.
  - Big Z Particle (BZ-TOF): similar to the CP category but, in this case, at least one digital signal of the TOF paddle is above the SHT, which usually corresponds to nuclei crossing the detector.
- ECAL provides two categories which are based on the X and Y signals within the superlayers and a minimum number of neighboring cells with energy deposit above a certain threshold.

The combination of the TOF and ECAL categories produces one of the following FT signals:

- FTC: if any of the CP or CT conditions are set.
- FTZ: with an extended decision time window for particles with low velocity and high charge, typically, slow ions.
- FTE: which include the categories from the ECAL and is dedicated to particles producing electromagnetic showers.

After the DAQ system is triggered by the FT signals, the next step in the logic corresponds to the Level 1 trigger, whose evaluation takes $1\ \mu$s.

2.8.2 *The Level 1 Trigger*

The Level 1 trigger checks the following conditions:

- Charged Particles ($Z = 1$): a gate of 240 ns is opened to latch the CP and CT charged particle signals. Events with signal coincidences in 3 or 4 out of 4 TOF planes are accepted.
- High Charged Particles ($Z \geq 2$): requires large energy deposition in the TOF.
- ACC veto: the anticoincidence signals provide a veto for particles with lateral incidence or for events with secondary interactions with the detector material.
- Events with electromagnetic showers: requires a energy deposition in the ECAL.

Out of these trigger signals, 5 *physics triggers* are built:

- Single charge ($Z = 1$): requires 4 out of 4 TOF planes passing the HT and no ACC hits.
- Ions ($Z \geq 2$): requires 4 out of 4 TOF planes passing the SHT and a number of ACC hits less than 5.

- Slow ions: requires 4 out of 4 TOF planes passing the SHT in an extended time gate.
- Electrons: requires 4 out of 4 TOF planes passing the HT, and 2 out of 2 ECAL projections with an energy deposit above a certain threshold. Once the ECAL trigger is set, the ACC are disabled.
- Photons: requires 2 out of 2 ECAL projections with an energy deposit above a threshold, and a shower angle in the geometric acceptance.

In addition, two *unbiased triggers* are defined to satisfy looser conditions and are used to calculate the trigger efficiency from data:

- Unbiased charge: requires 3 out of 4 TOF planes passing the HT. Events are prescaled by a factor 100.
- Unbiased ECAL: requires an energy deposit above a threshold. Events are prescaled by a factor 1000.

Depending on the location within the ISS orbit, AMS-02 has a trigger rate varying from 200 Hz, near the Earth magnetic equator, to 1400 Hz, near the SAA or at high magnetic latitudes, as shown in figure 2.20-*left*.

2.8.3 *Livetime*

The different steps in the processing of the signals introduce a dead time interval in which the experiment cannot detect new particles. In addition to the 1 μs dead time for the Level 1 trigger, other processes, such as the digitization of the signals and its compression introduce up to $\sim$ 200 μs. The livetime represents the efficiency of the data acquisition and is precisely evaluated by means of a 20 ns scaler which samples continuously the status of the data acquisition. As a consequence of the variable trigger rate, the average livetime also depends on the location within the ISS orbit, as displayed in figure 2.20-*right*. Geographical regions with a high trigger rate have a high number of particles hitting the detector and, therefore, reducing the livetime.

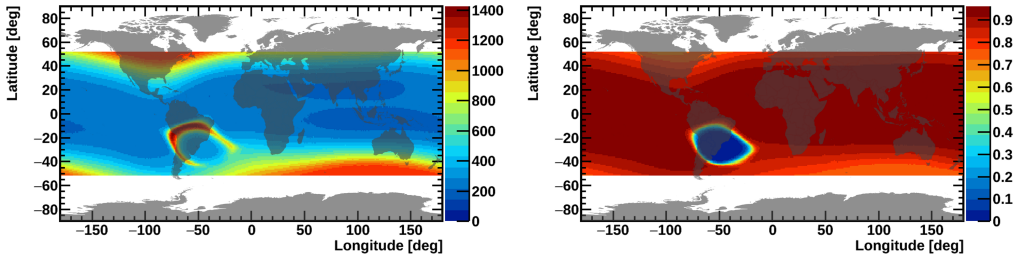

FIGURE 2.20: Dependence of the AMS-02 average trigger rate *(left)* and livetime *(right)* as a function of the ISS geographical position. In particular, in regions with low rigidity cut-off, near the geographical poles, the average trigger rate increases due to the high rate of particles hitting the detector. As a consequence, the livetime in those regions decreases.

2.9 THE AMS-02 ELECTRONICS AND DATA ACQUISITION SYSTEM

Each subdetector in AMS-02 is equipped with a dedicated Front-End electronics with a maximum readout time of 90 μs, which collect the signals from the corresponding electronic channels. In total, the AMS-02 has about 300,000 electronic channels out of which about 200,000 are dedicated to the Tracker readout, with event rates of $\sim 2 - 4$ kHz and 16 bits of information each one, thus giving rise to a raw data rate of about 7 Gbit/s. The electronics of AMS-02 are able to reduce the event size to the allocated 10 Mbit/s downlink data rate [196–198].

The main challenge for the AMS-02 electronics is due to the extreme conditions of a space experiment. In particular, the electronics have to be specifically designed to ensure a reliable operation in an environment subject to variations of temperature of few tens of degrees, high radiation and mechanical vibrations during launch. In addition, the electronic devices must satisfy the strict NASA requirements for space operations and operate nominally during the AMS-02 long mission in the ISS.

The AMS-02 performance relies on about 650 electronic boards, which can be grouped in different categories according to their function:

- *Common electronics* handle general tasks, such as the Power Distribution System (PDS), which distributes the power supply from the ISS photovoltaic arrays to all the AMS-02 electronics; or the Main Data computer of AMS-02 (JMDC), which monitors the entire detector performance, and sends commands and receives replies from the rest of electronic boards of AMS-02.
- *Subsystems electronics* are devoted to specific tasks, such as the Tracker Thermal Control Electronics (TTCE), which controls the heaters and pumps of the TTCS.
- *Data acquisition (DAQ) electronics* involved directly in the process of signal readout from the subdetectors, such as the Data Reduction boards (xRD, where x is a generic letter assigned for each subdetector: E for ECAL, R for RICH, T for Tracker, S for TOF and ACC, an U for TRD) that compressed the signals from the subdetectors.

A unified approach for all subdetectors has been adopted in the DAQ process, as shown in figure 2.21. In this approach, analog signals from each subdetector enter the corresponding Application Specific Integrated Circuit (ASIC) and are digitized via an Analog-to-Digital Converter (ADC). After a compression in the Data Reduction boards, the signals are collected, collated and buffered in Low Level DAQ computers (JINF-x). In parallel, data from TOF, ACC and ECAL are collected into a dedicated board JLV1 to provide the Level 1 Trigger. The next node in the chain are the High Level DAQ computer (JINJ), which collects all the event signals as well as the trigger information and finally passes data to the JMDC. The JMDC receives the information of the complete event and performs a first analysis to decide whether the information contain interesting physics.

All nodes in the DAQ process are interconnected through a serial wired link protocol (AMSWire), designed with very low latency, lower power consumption, and a typical transfer rate of 60 Mbits/s. To minimize the dead-time, an event buffering is performed at the different nodes of the DAQ chain. In particular, the JMDC con-

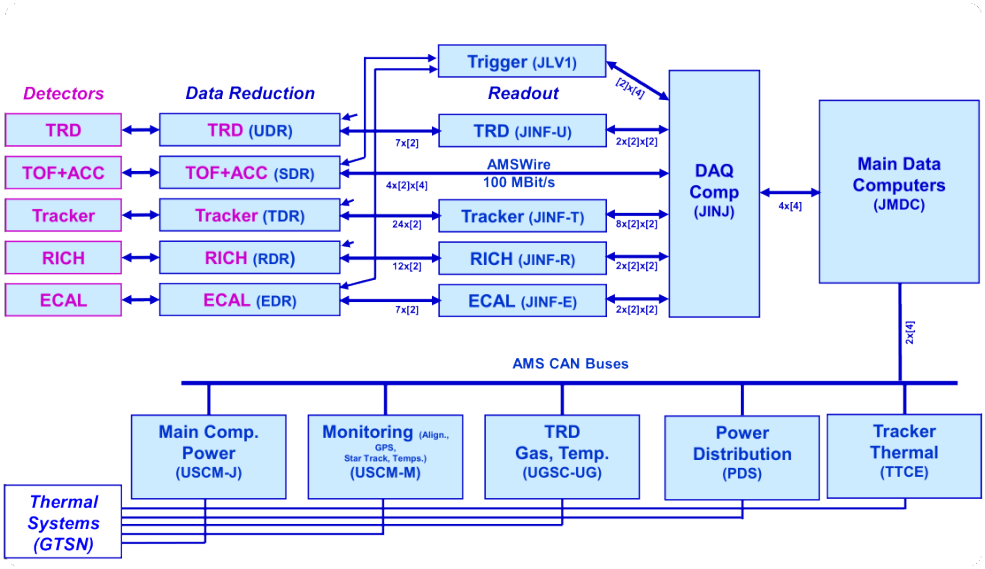

FIGURE 2.21: Scheme of the AMS-02 DAQ process. Starting from the detectors readout and the Data Reduction Boards, the signals are transmitted to the JINF-x Low Level DAQ computers and collected by the JINJ High Level DAQ computer. The Main Data computer of AMS-02, JMDC, collects the information of the complete event and transmits the data to ground. In addition, the subsystem electronics dedicated to specific tasks and depending on the JMDC are shown [199].

tains a large buffer (JBUX), which allows to store the data recorded in about one day to avoid science loss when the transmission between the ISS and the ground is interrupted.

Redundancy is fundamental in space missions. For this reason, the AMS-02 DAQ system has been designed with high redundancy: each board, cable and connector is, at least, duplicated. In particular, the JMDC is four times redundant whereas the Data Reduction boards and the Low Level DAQ computers are twice.

The DAQ is organized in 23 minute runs, with a total of 4 runs per ISS orbit. A full calibration of the subdetectors is performed every 2 runs at the Earth equator.

Apart from the Power Interface, which supplies electric power to the payload, AMS-02 has two additional interfaces with the ISS, in charge of the data transmission to ground:

- *Low Rate Data Link* (LRDL), dedicated to housekeeping data and commanding in the S-band (2-4 GHz), with an allocated bandwidth of around 20 Kbits/s of data.
- *High Rate Data Link* (HRDL), to transmit the event data and a copy of the monitoring data in the Ku-band (12-18 GHz), with an allocated bandwith of 10 Mbits/s (event data) and 30 Kbit/s (monitoring) downlink.

This transmission from the ISS to ground is achieved by means of the NASA Tracking and Data Relay Satellites (TDRS), which relay it to the satellite reception dishes at NASA's White Sands Test Facility in New Mexico. From there, the data is directed to NASA's Payload Operations Integration Center (POIC) at the Marshall

Space Flight Center (MSFC, Alabama), where the AMS Ground Support Computers are placed. Finally, the data is copied to to the AMS Payload Operations Control Center (POCC) at CERN Prevessin site and to the Taiwan control center, where the status of the payload and the data-taking is monitored in real time in shifts of 8 hours.

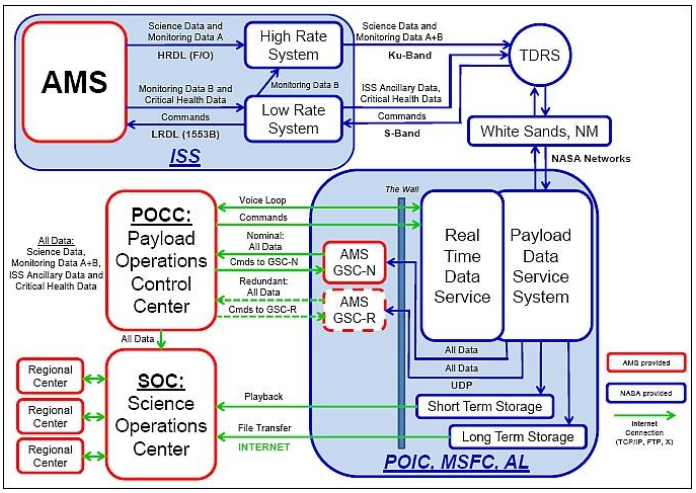

FIGURE 2.22: AMS-02 data flow. Data transmission to ground, by means of the HRDL and LRDL interfaces, is done by the NASA Tracking and Data Relay Satellites (TDRS). Data is received at ground at NASA White Sands Test Facility and directed to the Payload Operations Integration Center (POIC) at the Marshal Space Flight Center (MSFC). Finally, data is copied to the Payload Operations Control Center (POCC) and Science Operations Center (SOC) both at CERN Prevessin site, where operations take place [200].

3

MEASUREMENT OF LARGE SCALE ANISOTROPIES

3.1 INTRODUCTION

The measurement of anisotropies in cosmic rays requires a definition of the framework to quantify directional fluctuations. This implies the introduction of reference maps representing the isotropic case, from which deviations in the sample map are investigated. Two types of anisotropies are commonly cited in the literature: relative anisotropies, where the arrival directions of a cosmic ray sample are used as reference, and absolute anisotropies, where the reference characterizes the directional response of the detector to an isotropic flux. Both sample and reference maps are built in a given coordinate system, which provides a frame to represent any direction in the sphere and is chosen depending on the motivation of the measurement.

For large scale anisotropies it is mandatory to determine directions in which the signal is decomposed. Frequently, a basis of periodic functions is used to expand the flux, and the coefficients of the expansion quantify the magnitude of the anisotropy. Statistical methods to retrieve those coefficients from data and reference are required and, in particular, they should account for possible background contamination in the sample. Finally, from the measured anisotropy it is possible to make inferences on the true anisotropy; in particular, upper limits on the value of this magnitude are frequently established.

3.2 COORDINATE SYSTEMS FOR ANISOTROPY SEARCHES

The analysis of data in the sphere relies on the definition of a *coordinate system* (or *reference frame*), which provide a unique determination of a point or direction in the unitary sphere. In the three-dimensional space, the *Cartesian coordinate system* defines three fundamental orthogonal directions of, called *axes*, (X, Y, and Z), which constitute a right-hand trihedron. Thus, a direction in the three-dimensional space is univocally determined by its projections onto the fundamental axes, (x, y, z). On the other hand, in the *spherical coordinate system*, a direction in the unitary sphere can be specified by two angular distances with respect to two fundamental planes of the cartesian one (figure 3.1):

- *Azimuthal angle*. (φ), corresponding to the angular distance between the orthogonal projection of the direction onto the XY plane and the X-axis, positive if measured counter-clockwise.
- *Polar/Zenith angle*, (θ), corresponding to the angular distance between the direction and the Z-axis (known as *zenith*).

These two angular distances are customarily referred as *longitude* and *colatitude*, respectively. Commonly, the *latitude* (λ) is used instead of the colatitude, and it is defined as $\lambda = 90^\circ - \theta$. Lines corresponding to points on the sphere with the same latitude are known as *meridians*, whereas those corresponding to the same longitude are referred as *parallels*. The latitude and longitude define four cardinal directions: *North* and *South*, towards Z positive and negative, respectively; and *East* and *West*, towards Y positive and negative, respectively.

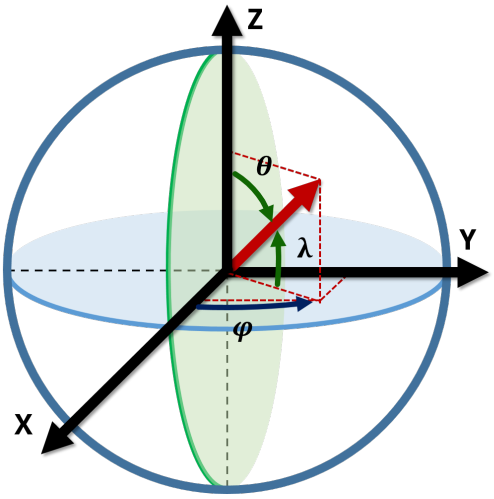

FIGURE 3.1: Cartesian and cylindrical coordinate systems. A unitary direction can be defined by the (x, y, z) projections onto the fundamental axes X, Y, Z; or by the angular distances (φ, θ) to the fundamental directions.

Depending on the election of the fundamental axes, X, Y and Z, from which the azimuthal and polar angles are measured, a number of coordinate systems are established. In many coordinate systems used in astronomy, the choice of the fundamental axes are determined from directions defined by celestial objets in the Universe used as reference. Since these objects are actually moving, the definition of a coordinate system is usually accompanied by a time identifier, called *epoch*, from which the angular distances to the celestial objects of reference at the epoch time are measured. A dedicated discussion about the different coordinate systems as well as the mathematical coordinate transformations among them can be found in references [201–206].

In particular, the search for anisotropies in the arrival directions of cosmic ray particles can be carried out in multiple coordinate systems depending on the motivation of the measurement. In this regard, we would like to use the reference system where the effect or signal we are measuring is intrinsic, because its amplitude is enhanced in there and may be totally or partially diluted in other coordinate systems.

The search for astronomical sources or astrophysical phenomena is usually carried out in *inertial* reference frames[1], which are defined on the celestial sphere and

1 Strictly speaking, in this context the word *inertial* means that the reference frame is fixed with respect to stationary stars, at least at human time scales.

decoupled from the movement of the Earth. These coordinate systems, suitable for the study of physics topics, astrophysical sources or processes, are known in the literature as *celestial coordinate systems*. Other coordinate systems are, however, more sensitive to instrumental effects and, therefore, suitable for calibration and assessment of the understanding of the detector. In this sense, the evaluation of the detector effects is mandatory as a previous step before the measurement of any physical property. For these reasons, two kind of coordinate systems are established and used in the analysis: *physical systems*, associated to the search for a physical signal; and *calibration systems*, where the comprehension of the detector is evaluated.

In addition, any coordinate system can be used to describe either the position of the spacecraft or the arrival direction of the particle. Consequently, we shall distinguish between *positional systems*, in the first case; and *directional systems*, in the second. Positional coordinate systems, usually bounded to the Earth, are specially suitable for the understanding of the detector, since many effects associated to the data acquisition are related to the position of the spacecraft within the orbit. Hereinafter, unless otherwise stated, the coordinate systems presented in the following sections are used to describe the arrival direction of the cosmic ray particle.

3.2.1 *Greenwich True of Date (GTOD)*

Greenwich True of Date (GTOD), or geographic, is a right-handed reference frame fixed to the Earth and co-rotating with it. This coordinate system is defined by its main direction, corresponding to the X-axis, pointing towards the Prime Meridian (Greenwich) whereas the Z-axis matches the Earth's True of Date rotational axis. Finally, the XY plane is determined by the Earth's True of Date Equator. The epoch *True of Date* takes into account the effects due to precession and nutation[2] associated to the time of interest.

Any direction in the GTOD coordinate system is represented by its *geographical latitude* (λ) and *longitude* (φ). The geographical latitude[3] corresponds to the angular distance, defined as positive towards the North Pole, between the direction and its projection onto the equatorial plane. The geographical longitude measures the angular distance from the Prime Meridian (Greenwich), being positive if determined counter-clockwise.

Since GTOD is a co-rotating Earth-centered reference system, the effect of the variations of detector efficiencies and data acquisition along the spacecraft orbit are expected to be enhanced in this coordinate system, whereas a possible astrophysical signal may be diluted due to the Earth's rotation. For this reason, GTOD is adequate to assess the understanding the effects that the detector introduces in the measurement of anisotropies.

2 Since the mass distribution of the Earth is not a perfect symmetric sphere, the gravitational interaction with the Sun and the Moon causes the Earth rotation axis to precess and nutate. Contrary to the *Mean of Date* or *Mean of Epoch*, which only includes precession.

3 Also known as *geocentric latitude* by astronomers and geographers.

Hereinafter we shall refer to the *ISS Geographical Position* coordinate system when the position of the spacecraft is projected into this reference frame, and shall reserve the term *GTOD* only for representing the arrival direction of the particle.

3.2.2 *Geomagnetic coordinate system*

The geomagnetic coordinate system is defined from the geographic one by tilting the Z-axis 9.5°, so that it matches the geomagnetic dipole axis. Thus, meridians and parallels are distorted accordingly from those of GTOD, with the Earth equator and the geogmagnetic equator intersecting at $\sim \pm 90°$ geomagnetic latitude.

In a similar manner, since the geomagnetic coordinate system is, essentially, a rotation from GTOD, is also suitable for the calibration of the detector's response. Furthermore, we shall called *ISS Geomagnetic Position* when explicitly referring to the position of the ISS in this coordinate system.

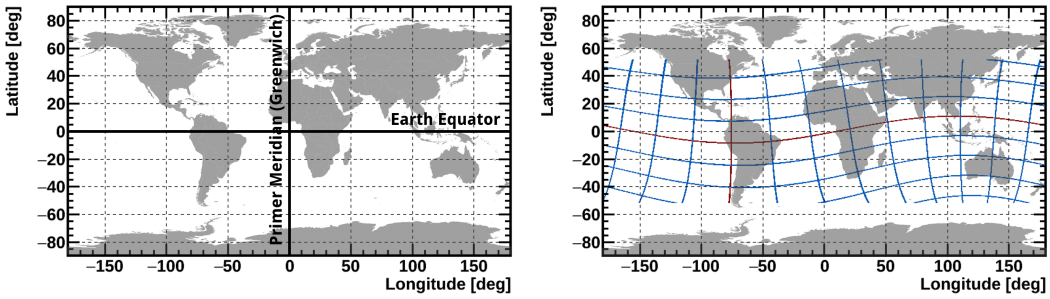

FIGURE 3.2: *(Left)* GTOD or geographic coordinate system in the equirectangular projection. The fundamental elements are shown. *(Right)* Relation between geomagnetic and geographic coordinates. Meridians and parallels in geomagnetic coordinates correspond to the blue lines. In particular, the geomagnetic equator and the $\varphi = 0°$ meridian are shown in red.

3.2.3 *Equatorial coordinate system*

The equatorial coordinate system is an inertial right-handed reference frame with its origin at the center of the Earth (figure 3.3-*left*). The fundamental plane XY, called *equatorial plane*, is defined by the Earth equator, whose projection onto the celestial sphere constitutes the *celestial equator*. The Z-axis corresponds to the Earth's rotational axis, thus defining the North and South celestial poles, towards positive and negative z, respectively. Contrary to GTOD, where the X-axis was established in terms of a fixed point on the Earth, in the equatorial coordinate system the X-axis is defined by a fixed astronomical point called *vernal equinox*[4].

4 The orbit of the Earth around the Sun is contained in the so-called *ecliptic plane*, which is tilted an angle called *obliquity of the ecliptic* (23.44° as of 2018) with respect to the equatorial plane. Thus, the ecliptic and equatorial plane intersect in two points called *orbital nodes*, which correspond to the equinoxes. In particular, the *vernal equinox*, also known as *first point of Aries*, is the *ascending node*, where the Earth moves towards the north with respect to the equatorial plane.

Several time epochs are used in the literature, being the standard in astronomy the one corresponding to the 12:00 UT on 2000 January 1st, denoted as J2000.

As it is customary in astronomy and astrophysics, the celestial latitude and longitude in the equatorial coordinate system are referred as *declination* (δ) and *right ascension* (α), respectively. The right ascension coordinate is usually measured in hours ($^{\mathrm{h}}$), minutes ($^{\mathrm{m}}$) and seconds ($^{\mathrm{s}}$), with 24^{h} corresponding to $360°$. This fact arises from the relation between GTOD and equatorial coordinate systems, as shown in figure 3.3-*right*. In the equatorial reference frame, where the X-axis points towards a fixed astronomical point, the GTOD system rotates with a period of 24 hours[5]. For this reason, equatorial coordinates are convenient for ground-based experiments, whose field of view describes a band of constant declination as the Earth rotates.

Equatorial coordinate system is, thus, a suitable reference frame for astronomical and astrophysical studies.

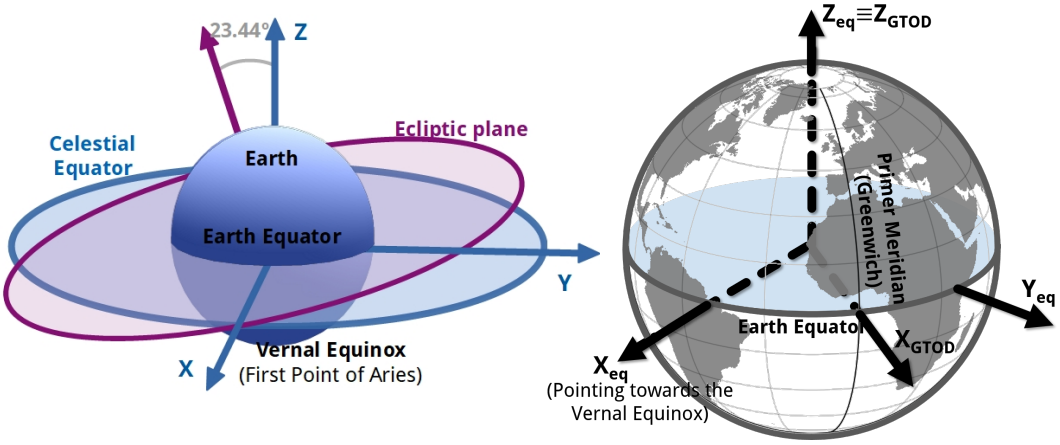

FIGURE 3.3: *(Left)* Definition of the equatorial coordinate system, with the X direction pointing towards the vernal equinox, and the celestial equator correspoding to the earth equatorial plane. The ecliptic plane, defined by the Earth's orbit around the Sun, is tilted $23.44°$ with respect to the equatorial plane. *(Right)* Relation between GTOD and equatorial coordinates.

3.2.4 *Galactic coordinate system*

The galactic coordinate system (figure 3.4), is an inertial reference frame with its origin on the Sun's center of mass and the fundamental XY plane corresponding to the Milky Way galactic plane, which is tilted an angle of $\sim 62.6°$ with respect to the celestial plane. The Z-axis, perpendicular to the galactic plane, defines the North (pointing towards Coma Berenices constellation) and South (towards Sculptor constellation) galactic poles. The X-axis points towards the galactic center (Sagittarius

5 24 hours with respect to the Sun, and 23 hours, 56 minutes, and 4 seconds with respect to the stars. This is used to define the *solar time*, in the first case; and the *sidereal time*, in the second, which are widely used in the analysis of anisotropies by ground-based experiments.

A), and the Y-axis, opposing the Solar System motion around the Galaxy, completes the right-handed trihedron.

The coordinate transformation from the equatorial reference system is, in essence, a rotation; thus, the time epoch corresponding to the galactic coordinate system is the standard J2000.

A direction in the galactic coordinate system is represented by the galactic latitude and longitude, denoted in the literature as b and l, respectively.

As in the case of the equatorial reference frame, galactic coordinates are well motivated for the search of astrophysical sources; in particular, for the measurement of anisotropies of galactic cosmic rays in this thesis.

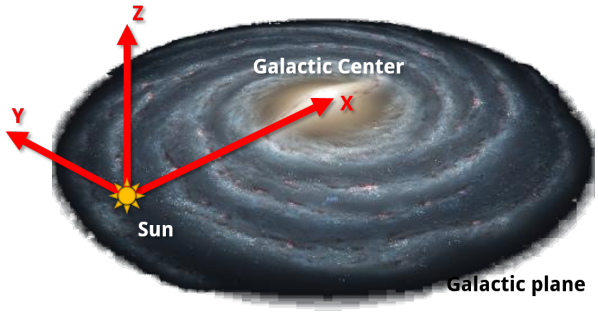

FIGURE 3.4: Definition of the fundamental directions in the galactic coordinate system. The X and Y directions are contained within the galactic plane, with the X direction pointing towards the galactic center, and the Y direction opposing the motion of the Solar System around the Galaxy.

3.2.5 *Geocentric Solar Ecliptic (GSE) coordinate system*

Geocentric Solar Ecliptic (GSE) is a non-inertial Earth-centered reference frame, which has its fundamental X-axis pointing towards the Sun (figure 3.5). The fundamental plane XY corresponds to the ecliptic plane, with the Y axis opposing the planetary motion around the Sun. Finally, the Z-axis completes the right-handed system. The position of an object is given by the GSE latitude and longitude.

Due to the primary direction pointing towards the Sun, GSE is a coordinate system suitable for the study of solar effects connected to the heliosphere. However, since days and nights are folded into opposite directions ($x > 0$ and $x < 0$, respectively) a day/night effect in the detector should be intrinsic to this coordinate system.

3.2.6 *Summary of coordinate systems*

A summary of the aforementioned coordinate systems and their classification into positional/directional categories as well as the motivation for calibration/physical searches is presented in table 3.1.

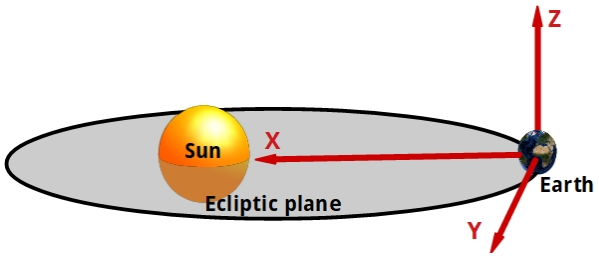

FIGURE 3.5: Definition of the GSE coordinate system. The X and Y directions are contained within the ecliptic plane, with the X direction pointing towards the Sun, and the Y direction opposing the Earth motion around the Sun.

TABLE 3.1: Summary of coordinate systems.

Coordinate system	Calibration	Physical	Positional	Directional
Geographic				
GTOD	✓	✗	✗	✓
ISS Geographical Position	✓	✗	✓	✗
Geomagnetic				
ISS Geoagnetic Position	✓	✗	✓	✗
Equatorial	✗	✓	✗	✓
Galactic	✗	✓	✗	✓
GSE	✓	✓	✗	✓

3.3 MULTIPOLE EXPANSION OF COSMIC RAY FLUXES

The analysis of large scale anisotropies consists in obtaining the directionality of the absolute flux or the flux ratio of cosmic ray species. The directional dependence of the flux can be described in terms of two components

$$\Phi(\theta, \varphi, t) = \Phi_0 + \Delta\Phi(\theta, \varphi) = \Phi_0 \left(1 + \Delta(\theta, \varphi)\right) \tag{3.1}$$

where $\Delta\Phi(\theta, \varphi)$ characterizes the potential directional fluctuations of the flux over the isotropic component, Φ_0, with $\Delta = \frac{\Delta\Phi}{\Phi_0} \ll 1$ the anisotropy we are interested to quantify.

As it is customary, the analysis and modelization of data distributed in spherical surfaces is carried out in terms of spherical harmonics. Spherical harmonics are a complete set of orthonormal complex functions defined on the sphere, $(\theta, \varphi) \in \Omega \equiv [0, \pi] \times [0, 2\pi)$, and constitute a basis of the Hilbert space of square integrable functions [207, 208]. In the analysis of anisotropies it is more convenient to use the real form of spherical harmonics, which are defined in terms of the complex analogues and have identical properties [209]. Therefore, any well-behaved real

function $f(\theta, \varphi)$ defined on a unit spherical surface can be expanded as a linear combination of real spherical harmonics:

$$f(\theta,\varphi) = \sum_{\ell=0} \sum_{m=-\ell}^{m=+\ell} c_{\ell m} Y_{\ell m}(\theta,\varphi) \tag{3.2}$$

being $Y_{\ell m}(\theta, \varphi)$ the real spherical harmonic of degree ℓ and order m, with $\ell = 0, 1, 2, \ldots$ and $m = 0, \pm 1, \pm 2, \ldots, \pm \ell$; and $c_{\ell m}$ the coefficients of the expansion.

In particular, the absolute flux or flux ratio can be expanded in terms of spherical harmonics, yielding to

$$\Phi(\theta,\varphi) = c_{00}Y_{00} + \sum_{\ell=1} \sum_{m=-\ell}^{m=+\ell} c_{\ell m} Y_{\ell m}(\theta,\varphi) = c_{00}Y_{00} \left(1 + \sum_{\ell=1} \sum_{m=-\ell}^{m=+\ell} \frac{c_{\ell m}}{c_{00}Y_{00}} Y_{\ell m}(\theta,\varphi) \right) \tag{3.3}$$

where $\Phi_0 \equiv c_{00}Y_{00}$ is the isotropic flux and successive terms in the series describe the directional fluctuations. Hereinafter we will use

$$\Phi(\theta,\varphi) = \Phi_0 \left(1 + \sum_{\ell=1} \sum_{m=-\ell}^{m=+\ell} a_{\ell m} Y_{\ell m}(\theta,\varphi) \right) \tag{3.4}$$

where $a_{\ell m} = \dfrac{c_{\ell m}}{\Phi_0}$ are the multipole components we are interested in.

In the case of $\ell = 1$, the three real spherical harmonics (fig. 3.6) are

$$Y_{1-1} = \sqrt{\frac{3}{4\pi}} \sin\theta \sin\varphi = \sqrt{\frac{3}{4\pi}} \frac{y}{r} \tag{3.5}$$

$$Y_{1+0} = \sqrt{\frac{3}{4\pi}} \cos\theta \qquad = \sqrt{\frac{3}{4\pi}} \frac{z}{r} \tag{3.6}$$

$$Y_{1+1} = \sqrt{\frac{3}{4\pi}} \sin\theta \cos\varphi = \sqrt{\frac{3}{4\pi}} \frac{x}{r} \tag{3.7}$$

which define three orthogonal directions in $\mathbb{R}^3$ corresponding to axis y, z and x, respectively, and form a right-handed system. Hereinafter, these three directions will be denoted as *East-West*, *North-South* and *Forward-Backward*, respectively.

As a consequence, the spherical harmonics expansion of the flux up to $\ell = 1$ is

$$\Phi(\theta,\varphi) \sim \Phi_0 \left(1 + a_{1-1}\sqrt{\frac{3}{4\pi}} \sin\theta \sin\varphi + a_{1+0}\sqrt{\frac{3}{4\pi}} \cos\theta + a_{1+1}\sqrt{\frac{3}{4\pi}} \sin\theta \cos\varphi \right) \tag{3.8}$$

which motivates to define the *dipole components* in terms of the three dipole coefficients a_{1m}, each one corresponding to the projection of the dipole anisotropy onto one orthogonal axis

$$\rho_{\text{EW}} = \sqrt{\frac{3}{4\pi}} a_{1-1} \quad ; \quad \rho_{\text{NS}} = \sqrt{\frac{3}{4\pi}} a_{1+0} \quad ; \quad \rho_{\text{FB}} = \sqrt{\frac{3}{4\pi}} a_{1+1} \tag{3.9}$$

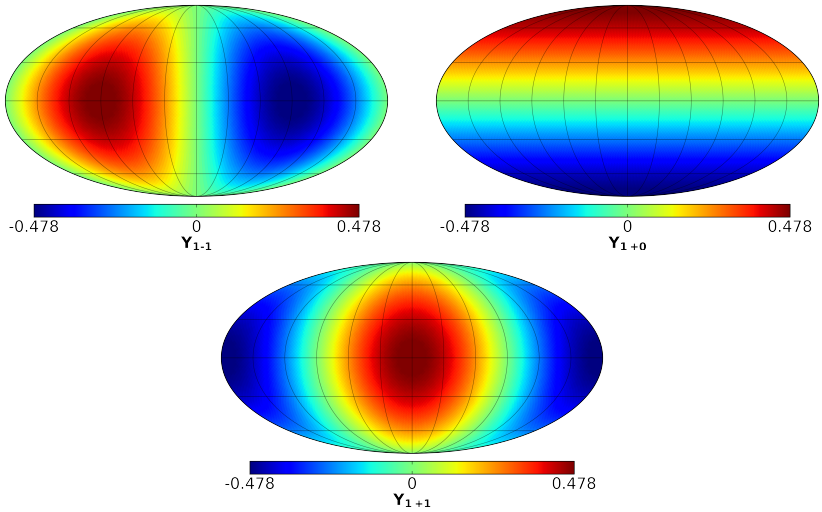

FIGURE 3.6: Real spherical harmonics for $\ell = 1$: East-West (*top-left*), North-South (*top-right*) and Forward-Backward (*bottom*) directions.

Finally, the *dipole amplitude* (1.10) can be defined in terms of the dipole components

$$\begin{aligned}\delta = \frac{\Phi_{\max} - \Phi_{\min}}{\Phi_{\max} + \Phi_{\min}} = \left(\frac{\Delta\Phi}{\Phi_0}\right)_{\ell=1} = \sqrt{\rho_{EW}^2 + \rho_{NS}^2 + \rho_{FB}^2} \\ = \sqrt{\frac{3}{4\pi}\left(a_{1-1}^2 + a_{1+0}^2 + a_{1+1}^2\right)}\end{aligned} \tag{3.10}$$

Apart from the determination of the dipole components of the cosmic ray anisotropy in the arrival directions, in this thesis we will make use of the quadrupole components to extend the verification of the method of analysis. In this sense, we define *ad-hoc* the *quadrupole components* from the a_{2m} coefficients as

$$\rho_{2m} = \sqrt{\frac{3}{4\pi}} a_{2m}. \tag{3.11}$$

Experimentally, the anisotropy of the flux is investigated with a finite sample of events, N, whose arrival directions in a certain coordinate system provide an estimation of the true multipole components. In that case, $a_{\ell m}$ constitute an unbiased estimator distributed according to a Gaussian distribution centered in the true dipole component with a variance given by [210]

$$\sigma^2(a_{\ell m}) = \frac{4\pi}{N} \quad ; \quad \sigma^2(\rho_i) = \frac{3}{N}, \tag{3.12}$$

if the multipole components are small, $a_{\ell m} \to 0$.

3.4 REFERENCE MAPS FOR ANISOTROPY SEARCHES

The directionality of the sample is investigated by comparing the observed distribution of arrival directions with a reference map. Any deviation will be regarded

as a signal. Depending on the election of the reference map, there are two types of anisotropies discussed in the literature:

- *Absolute anisotropies*, where the map describing the directional response of the detector to an isotropic flux is used as reference. The computation of this true isotropic map requires a precise understanding of the detector's behavior. Absolute anisotropies provide a measurement of the intrinsic directionality of cosmic ray species.
- *Relative anisotropies*, where a data sample is used as reference. This sample can be chosen in two different manners:
  - Use another cosmic ray species as reference and study the deviations of one with respect to the other (as in e^+/e^-)
  - Use the same cosmic ray species but at different energies to study a possible change in the directionality with the energy (the anisotropy of high rigidity protons with respect to low rigidity protons [211])

  The main advantage of relative anisotropies is that correlated systematic errors of the sample and reference cancel. However, a signal may be totally or partially diluted if present in both samples.

3.4.1 *Absolute anisotropies*

3.4.1.1 *Differential flux of cosmic rays*

The analysis of anisotropies involves the study of the directional distribution of cosmic ray fluxes in the sky. Therefore, a clear definition of cosmic ray flux should be presented. For our purposes, the differential flux of cosmic rays (in units of $\mathrm{s^{-1}m^{-2}sr^{-1}GeV^{-1}}$) detected in a given direction $\hat{r}_g \equiv \hat{r}_g(\theta_g, \varphi_g)$ with energies in the range $[E, E + dE]$ is defined as

$$\Phi(\hat{r}_g, E) = \frac{dN}{\mathcal{A}_{\text{eff}}(\hat{r}_d, E)\ \mathcal{E}(t)\ \alpha(t)\ dE\ dt\ d\Omega_g}. \tag{3.13}$$

In (3.13), dN is the number of particles measured in the time interval dt, in a solid angle $d\Omega_g$ around the direction of observation $\hat{r}_g$. The subindex g stands for the generic coordinate system used in the analysis. The quantity $\alpha(t)$ is the *livetime* of the detector at time t, and represents the effective fraction of time during which the apparatus is ready to detect a particle. The term $\mathcal{A}_{\text{eff}}(\hat{r}_d, E)$ is the effective acceptance of the detector (in units of $\mathrm{m^2}$ sr), and characterizes the directional response of the detector. It includes both the geometrical acceptance factor, $\mathcal{A}_{\text{geom}}$, and the reconstruction and selection efficiencies, $\mathcal{E}$,

$$\mathcal{A}_{\text{eff}}(\hat{r}_d, E) = \mathcal{A}_{\text{geom}}(\hat{r}_d, E) \cdot \mathcal{E}(\hat{r}_d, E) \tag{3.14}$$

which depend on the energy, E, and the incoming direction of the particle in the detector reference frame, $\hat{r}_d(\theta_d, \varphi_d)$. The coordinate system in the analysis of anisotropies and the local frame of the detector are connected by means of a unitary transformation depending on time $\hat{r}_g = \hat{r}_g(\hat{r}_d, t)$ and the inverse $\hat{r}_d = \hat{r}_d(\hat{r}_g, t)$. Thus, the effective acceptance can be written as

$$\mathcal{A}_{\text{eff}}(\hat{r}_d, E) \equiv \mathcal{A}_{\text{eff}}(\hat{r}_d(\hat{r}_g, t), E) \tag{3.15}$$

Finally, in (3.13) we have assumed that any possible time dependence of the geometrical acceptance can be factorized and absorbed in the term $\mathcal{E}(t)$. Consequently, $\mathcal{E}(t)$ stands for potential time corrections to the geometric acceptance arising from the fact that the detection efficiencies may change during the entire life of the experiment due to possible variations in the operating conditions of the detector.

3.4.1.2 *Exposure function*

Using (3.13), it is possible to calculate the number of cosmic rays per unit of energy and solid angle that would be detected during an interval of time Δt. Assuming a time-independent flux, we find

$$\frac{dN(\hat{r}_g)}{dEd\Omega_g} = \Phi(\hat{r}_g, E) \int_{\Delta t} dt \int_{\Omega_d} d\Omega_d \, \mathcal{A}_{\text{eff}}\left(\hat{r}_d(\hat{r}_g, t), E\right) \, \mathcal{E}(t) \, \alpha(t) \tag{3.16}$$

that can we written in a more compact form

$$\frac{dN(\hat{r}_g)}{dEd\Omega_g} = \Phi(\hat{r}_g, E) \cdot \mathcal{F}(\hat{r}_g, E) \tag{3.17}$$

where

$$\mathcal{F}(\hat{r}_g, E) := \int_{\Delta t} dt \int_{\Omega_d} d\Omega_d \, \mathcal{A}_{\text{eff}}\left(\hat{r}_d(\hat{r}_g, t), E\right) \mathcal{E}(t)\alpha(t) \tag{3.18}$$

is the *exposure function* (with units m^2 s) [212, 213]. As a result, the exposure function is the projection of the detector's effective acceptance, second by second, to the coordinate system in which the analysis of anisotropies is performed. This convolution of the acceptance and the coordinate transformation is weighted by the livetime and efficiency correction at each second.

From an experimental point of view, it is usual to consider a partition of each variable in the following way

$$\begin{aligned} \Delta t &= \textstyle\sum_i \Delta t^i \\ \Delta E &= \textstyle\sum_j \Delta E^j \\ \Omega_d &= \cup_r \Omega_d^r \Rightarrow \hat{r}_d^r(\theta_d^r, \varphi_d^r) \in \Omega_d^r \\ \Omega_g &= \cup_s \Omega_g^s \Rightarrow \hat{r}_g^s(\theta_g^s, \varphi_g^s) \in \Omega_g^s \end{aligned} \tag{3.19}$$

where the period of analysis, Δt, is divided into time intervals Δt^i (usually seconds); the energy range, $\Delta E \equiv [E_{\text{min}}, E_{\text{max}}]$, is discretized into energy bins of width ΔE^j; and directions (θ, φ) in both local and analysis frames are divided into small pixels of area $\Delta\Omega$.

In this manner, the number of events in an energy bin ΔE^j and pixel direction s is

$$\begin{aligned} n_{j,s} \equiv \left(\frac{\Delta N}{\Delta E \Delta\Omega_g}\right)_{j,s} &= \Phi_{j,s} \sum_i \sum_r \mathcal{A}_{\text{eff}}^{j,r(s,i)} \, \mathcal{E}^i \, \alpha^i \\ &= \Phi_{j,s} \cdot \mathcal{F}_{j,s} \end{aligned} \tag{3.20}$$

In (3.17) and (3.20), we see that the number of events per bin (j, s) depends on the flux and on the exposure function. An excess in the number of events with respect to other direction of observation could be due to the intrinsic response of the detector (acceptance, efficiencies...) or could arise from a real anisotropy in the flux of cosmic rays (or both of them). According to this, one of the main goals in the search for anisotropies is to disentangle the flux of cosmic rays from the effects related to the performance of the detector itself. In addition to this, the exposure function provides the distribution of events that we would expect from an isotropic flux, allowing the construction of skymaps with no anisotropy that show the sky seen by the detector and represent the null hypothesis in the search for anisotropies. These skymaps are called *reference maps*, so the analysis can be performed by comparison with the corresponding maps for real events.

In space-based experiments there are two potential time dependences of the term $\mathcal{E}(t)$:

- *Short-term variations* associated to possible changes of efficiencies along the spacecraft orbit related to distinct environmental conditions. The measured rates of cosmic rays are very different depending on the position due to the variation of the geomagnetic field values along the orbit, which in turn translates into geographical variations of subdetector efficiencies.
- *Long-term variations* of efficiencies due to intrinsic changes in the performances of the subdetectors with time.

In AMS-02, this can be expressed as:

$$\mathcal{E}(t) \equiv \mathcal{E}_s(\hat{r}_{\text{ISS}}(\hat{r}_g, t), E) \cdot \mathcal{E}_l(t) \tag{3.21}$$

where $\hat{r}_{\text{ISS}}$ is the instantaneous position of ISS in geographical coordinates, which is correlated to the reference frame of the analysis by means of a coordinate transformation (see section 4.3.3).

In the case of the short-term variation, since the effects of the magnetic field depend on the energy of the particle, the efficiencies along the ISS orbit may also depend on the energy. Using the previous notation, in 3.21 we can write $\mathcal{E}(t^i) \equiv \mathcal{E}^{i(s),j}$, so that the exposure function is

$$\mathcal{F}^{j,s} = \sum_i \sum_r \mathcal{A}_{\text{eff}}^{j,r(s,i)} \; \mathcal{E}^{i(s),j} \; \alpha^i \tag{3.22}$$

Usually, the calculation of the exposure function relies on the understanding of the detector behavior through a Monte Carlo simulation. As discussed in section 1.5.1, in some ground-based experiments this quantity is difficult to compute since they are affected by changes in meteorological conditions, so alternative methods, such as shuffling tecnhique , are proposed. In the case of detectors with field of view smaller than the angular size of the anisotropies under study, such as AMS-02, these techniques cannot be used, so a new method has been developed.

3.4.1.3 *Determination of exposure function. Exposure maps*

From (3.20), it can be seen that it is possible to divide the acceptance in small bins or pixels in local coordinates, such that for each pixel $\hat{r}_d^r(\theta_d^r, \varphi_d^r) \in \Omega_d^r$ we have

$$\begin{aligned} n_{j,s}^r \equiv \left(\frac{\Delta N}{\Delta E \Delta \Omega_g}\right)_{j,s}^r &= \Phi_{j,s} \sum_i \mathcal{A}_{\text{eff}}^{j,r(s,i)} \, \mathcal{E}^{i(s),j} \, \alpha^i \\ &= \Phi_{j,s} \cdot \mathcal{F}_{j,s}^r \end{aligned} \tag{3.23}$$

where, in this case, each acceptance pixel r and energy bin j has its corresponding exposure function, which is obtained from the projection, second by second, of the local coordinates of the pixel $\hat{r}_d^r(\theta_d^r, \varphi_d^r)$ to the coordinate system of analysis, weighted by the livetime and the efficiency correction.

As a result, the exposure function for the acceptance pixel r and energy bin j is

$$\mathcal{F}_{j,s}^r = \mathcal{A}_j^{0,r} \, \mathcal{T}_{j,s}^r \, \mathcal{E}_{j,s} \tag{3.24}$$

The first term of (3.24) refers to the value of the acceptance for pixel r, which has no variation within the pixel if it is small enough. The second term of (3.24), which constitutes the distribution in the sky of the livetime integrated over the time period of analysis, is the *exposure time map* for a given energy range and acceptance pixel. The third term in (3.24) is the *efficiency correction map*, i.e., the integrated projection of the geographical dependence of efficiencies to the coordinate system of analysis. These terms will be discussed in detail in the next paragraphs.

► ACCEPTANCE AND EXPOSURE TIME MAPS Based on the aforementioned considerations, exposure time maps represent the amount of time that a certain direction in the skymap, $(\theta_g^s, \varphi_g^s)$, is observed by a given pixel $(\theta_d^r, \varphi_d^r)$ in which the acceptance is divided. The procedure can be summarized in the following steps:

1. For each second of the analysis, t^i, a coordinate transformation from local coordinates of each acceptance pixel r to generic coordinate system is done: $(\theta_d^r, \varphi_d^r) \rightarrow (\theta_g^{s(r)}, \varphi_g^{s(r)})$.
2. The direction $(\theta_g^{s(r)}, \varphi_g^{s(r)})$ in the skymaps associated to the acceptance bin r and corresponding to energies above the maximum rigidity cutoff is filled with the value of the livetime in that second.
3. Repeat 1 and 2 for each acceptance pixel, r, and second of the analysis, i.

In our case, HEALPix scheme [214] is used to divide the acceptance in pixels of equal area, with a parameter $N_{\text{side}} = 32$, which corresponds to 12288 pixels of ~ 3 deg^2. In the case of AMS-02, the arrival directions in the standard selection of electrons, positrons and protons form a cone of 25° half-opening angle, which corresponds to 544 of these 12288 pixels. Skymaps of events and exposure in the coordinate system of analysis are built using the same pixelization scheme with identical HEALPix parameters.

In addition, to select primary cosmic rays, well above the geomagnetic cutoff, the measured rigidity is required to be greater than 1.2 times the maximum rigidity cutoff within the acceptance. Exposure time maps are filled accordingly (figure 3.7)

and, since this rigidity cutoff depends on the instantaneous ISS position within the orbit, not all the energies are equally exposed. Consequently, the exposure time maps may be different for different energies.

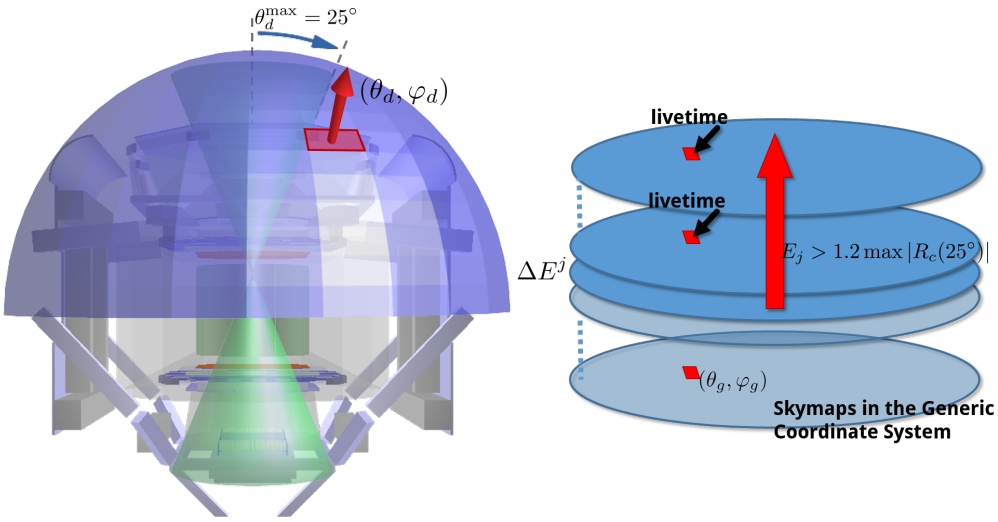

FIGURE 3.7: Directions in local coordinates are divided in small pixels of constant acceptance. For each second, the direction of the skymap (θ_g, φ_g) corresponding to an acceptance pixel (θ_r, φ_r) is filled for energies $E_j > 1.2 \max |R_{cut}(25°)|$ with the value of the livetime for that second. This procedure is repeated for all pixels of acceptance and all seconds of the time period of analysis.

As a result, each acceptance pixel r has a corresponding set of exposure time maps (one per energy bin ΔE^j), which correspond to the integrated projection of the livetime into the coordinate system of analysis for that local direction $(\theta_d^r, \varphi_d^r)$. A binned-likelihood fit combining the information of exposure time and event maps for each acceptance pixel and energy bin provides the multipole coefficients $a_{\ell m}$ (section 3.5). Since the acceptance is constant within the pixel, thus acting simply as a normalization factor in the binned-likelihood, the method does not require the explicit determination of the acceptance.

► EFFICIENCY CORRECTION MAPS The reference system of analysis and the geographical position of the spacecraft are connected by means of coordinate transformations (see section 4.3.3 for the effective coordinate transformation applying to AMS-02). Depending on the nature of these transformations, a geographical dependence of the efficiencies may project onto the coordinate system of analysis and induce a spurious signal if their effect is not accounted for. For this reason, a precise understanding of positional dependence of efficiencies and its projection into physical systems is needed. We shall remark that, since we are looking for directionality in cosmic rays, the relevant quantity is not the average value of the efficiency but its dependence on the coordinates of analysis.

The skymap efficiency distribution, $\varepsilon(\theta, \varphi)$ can be obtained as

$$\varepsilon(\theta, \varphi) = \frac{N_{\text{ok}}(\theta, \varphi)}{N_{\text{ok}}(\theta, \varphi) + N_{\text{ko}}(\theta, \varphi)} = \frac{1}{1 + \eta(\theta, \varphi)} \tag{3.25}$$

where $N_{\rm ok}(\theta,\varphi)$ and $N_{\rm ko}(\theta,\varphi)$ are, respectively, the skymap distribution of events accepted and rejected by the cuts used to evaluate the efficiency, and $\eta(\theta,\varphi) = \frac{N_{\rm ko}(\theta,\varphi)}{N_{\rm ok}(\theta,\varphi)}$.

The skymap efficiency distribution can be parametrized in terms of the same set of functions used to expand the flux in the analysis of anisotropies. In our case, we parameterize our efficiencies in terms of the real spherical harmonic basis in the coordinate system of analysis

$$\varepsilon(\theta,\varphi) = \varepsilon_0 \left(1 + \sum_{\ell=1} \sum_{m=-\ell}^{m=+\ell} \varepsilon_{\ell m} Y_{\ell m}(\theta,\varphi)\right) \tag{3.26}$$

The parametrization of the efficiency is achieved in two steps:

1. Obtain the spherical harmonics expansion of $\eta(\theta,\varphi)$ up to a certain multipole, $\ell_{\rm max}$
$$\eta(\theta,\varphi) \sim \eta_0 \left(1 + \sum_{\ell=1}^{\ell=\ell_{\rm max}} \eta_{\ell m} Y_{\ell m}(\theta,\varphi)\right) \tag{3.27}$$
where $\eta_0 \sim \frac{N_{\rm ko}}{N_{\rm ok}}$ is related to the average efficiency in the energy range $\Delta E \equiv [E_{\rm min}, E_{\rm max}]$ and $\eta_{\ell m}$ are the coefficients of the multipolar expansion of $\eta(\theta,\varphi)$, which can be computed from the relative analysis of anisotropies (described in 3.4.2 and 6.7.2) of the $N_{\rm ko}$ sample with respect to the $N_{\rm ok}$ sample in that energy range.
2. Insert the multipolar expansion of $\eta(\theta,\varphi)$ in (3.25) to obtain the parametrization of the efficiency.

The parametrization calculated with this procedure is used to correct exposure time maps in the same reference frame of analysis. Due to the orthonormality of spherical harmonics, the correction introduced will bias the value of $a_{\ell m}$ by an amount $\Delta_{\ell m}$

$$a_{\ell m}^{corr} \sim a_{\ell m} + \left(\frac{\eta_0}{1+\eta_0}\eta_{\ell m}\right) = a_{\ell m} + \Delta_{\ell m} \tag{3.28}$$

where only the component ℓm of the efficiency will modify the multipole component ℓm of the analysis.

Apart from the smooth description provided by the parametrization, the main advantage of the technique relies on the calculation of the efficiency dependence directly on the coordinate system of the analysis. In this manner, the projected effect of the geographical variation of efficiencies along the period of analysis is parametrized. Consequently, there is no need to account for possible time dependences of these variations.

Finally, the combination of the efficiency correction maps and exposure time maps constitute the exposure maps, which are the reference in the measurement of absolute anisotropies.

3.4.2 *Relative anisotropies*

In the analysis of relative anisotropies the flux ratio of cosmic rays is expanded in the real spherical harmonic basis. Relative anisotropies can be performed by comparison of the analysis sample with a reference sample

$$\frac{\Phi(\theta,\varphi)}{\Phi_{\rm ref}(\theta,\varphi)} = \left(\frac{\Phi}{\Phi_{\rm ref}}\right)_0 \left(1 + \sum_{\ell>0}\sum_{m=-\ell}^{m=+\ell} a_{\ell m} Y_{\ell m}(\theta,\varphi)\right) \tag{3.29}$$

where the multipole expansion characterizes the directional fluctuations over the isotropic flux ratio, $\left(\frac{\Phi}{\Phi_{\rm ref}}\right)_0$, and the reference, $\Phi_{\rm ref}$, can be the flux of another cosmic ray species, or the same species but at different energy. In both cases, according to (3.24), the ratio of events in the bin (r,j,s) is

$$\left(\frac{n}{n_{\rm ref}}\right)^r_{j,s} \propto \left(\frac{\Phi}{\Phi_{\rm ref}}\right)_{j,s} \left(\frac{\mathcal{T}}{\mathcal{T}_{\rm ref}}\right)^r_{j,s} \left(\frac{\mathcal{E}}{\mathcal{E}_{\rm ref}}\right)_{j,s} \tag{3.30}$$

which allows to write

$$\begin{aligned}(n)^r_{j,s} &\propto \left(\frac{\Phi}{\Phi_{\rm ref}}\right)_{j,s} \left(\frac{\mathcal{T}}{\mathcal{T}_{\rm ref}}\right)^r_{j,s} \left(\frac{\mathcal{E}}{\mathcal{E}_{\rm ref}}\right)_{j,s} (n_{\rm ref})^r_{j,s} \\ &\propto \left(\frac{\Phi}{\Phi_{\rm ref}}\right)_{j,s} \mathcal{R}^r_{j,s}\end{aligned} \tag{3.31}$$

where the term

$$\mathcal{R}^r_{j,s} := \left(\frac{\mathcal{T}}{\mathcal{T}_{\rm ref}}\right)^r_{j,s} \left(\frac{\mathcal{E}}{\mathcal{E}_{\rm ref}}\right)_{j,s} (n_{\rm ref})^r_{j,s} \tag{3.32}$$

constitutes the set of reference maps for the measurement of relative anisotropies. The comparison of the distribution of numerator events with the skymaps of denominator including the ratio of exposure time maps and efficiency corrections, provides the anisotropy in the flux ratio.

In most cases, the numerator and denominator samples share the same exposure time maps so that the reference maps for relative anisotropies are

$$\mathcal{R}^r_{j,s} = \left(\frac{\mathcal{E}}{\mathcal{E}_{\rm ref}}\right)_{j,s} (n_{\rm ref})^r_{j,s} \tag{3.33}$$

On the other hand, if the geographical dependence of efficiencies is the same for both numerator and denominator samples, the reference map is simply the distribution of events of the denominator sample.

$$\mathcal{R}^r_{j,s} = (n_{\rm ref})^r_{j,s} \tag{3.34}$$

Finally, if both numerator and denominator samples have the same geometrical acceptance, usually because they are selected in a similar manner, the analysis can be carried out combining the skymaps for all acceptance pixels and the reference map is the distribution of events for each energy bin

$$\mathcal{R}_{j,s} = \sum_r \mathcal{R}^r_{j,s} \tag{3.35}$$

3.5 DETERMINATION OF THE LARGE SCALE ANISOTROPY

A set of statistical tools to retrieve the multipole components of the flux expansion has been developed for both absolute and relative anisotropies. In both cases, a binned-likelihood fit, which takes into account the differences in exposure for the different energies, provides the multipole components of the anisotropy.

3.5.1 *Absolute anisotropies*

In the skymap corresponding to an acceptance pixel r and energy bin j, the total number of events, N_j^r, is given by the sum over the skymap pixels s

$$N_j^r = \sum_s^{N_{\rm pix}} n_{j,s}^r, \tag{3.36}$$

being $N_{\rm pix}$ the number of pixels of the skymap.

The distribution of events in this skymap can be assumed to be described by a multinomial probability distribution

$$f_j^r \equiv f_j^r\left(n_1,\ldots,n_{N_{\rm pix}}|N_j^r,\mu_1,\ldots,\mu_{N_{\rm pix}}\right) = \frac{N_j^r!}{\prod_{s=1}^{N_{\rm pix}} n_{j,s}^r!}\prod_{s=1}^{N_{\rm pix}}\left(\mu_{j,s}^r\right)^{n_{j,s}^r}, \tag{3.37}$$

where, as stated in (3.23) and (3.24), the expected number of events is given by the flux and the exposure function

$$\mu_{j,s}^r = \frac{1}{\mathcal{N}_j^r}\Phi_{j,s}\mathcal{F}_{j,s}^r = \frac{1}{\mathcal{N}_j^r}\Phi_{j,s}\mathcal{A}_j^{0,r}\,\mathcal{T}_{j,s}^r\,\mathcal{E}_{j,s}. \tag{3.38}$$

The term $\mathcal{N}_j^r$ is a normalization factor relative to the skymap j,r. In this manner, this term ensures that the discrete probability function in (3.37) is normalized, so that $\sum_s^{N_{\rm pix}}\mu_{j,s}^r = N_j^r$, and accounts automatically for the regions that are exposed in the case that the sky coverage is not complete.

The flux is then expanded in terms of spherical harmonics up to a maximum multipole

$$\Phi_{j,s} = \Phi_{0,j}\left(1+\sum_{\ell=1}^{\ell_{\rm max}}\sum_{m=-\ell}^{m=+\ell} a_{\ell m}Y_{\ell m}^s\right), \tag{3.39}$$

where the multipole components $a_{\ell m}$ are assumed to be energy independent, i.e., the anisotropy is constant within the energy range of analysis. As a result, the expected number of events is given by

$$\begin{aligned}\mu_{j,s}^r &= \frac{1}{\mathcal{N}_j^r}\Phi_{0,j}\left(1+\sum_{\ell=1}^{\ell_{\rm max}}\sum_{m=-\ell}^{m=+\ell} a_{\ell m}Y_{\ell m}^s\right)\mathcal{A}_j^{0,r}\,\mathcal{T}_{j,s}^r\,\mathcal{E}_{j,s}\\ &\propto \frac{1}{\mathcal{N}_j^r}\left(1+\sum_{\ell=1}^{\ell_{\rm max}}\sum_{m=-\ell}^{m=+\ell} a_{\ell m}Y_{\ell m}^s\right)\mathcal{T}_{j,s}^r\,\mathcal{E}_{j,s}\end{aligned} \tag{3.40}$$

since the product $\Phi_{0,j}\mathcal{A}_j^{0,r}$ is constant for a fixed acceptance pixel r and energy bin j.

The discrete probability function involving the total number of acceptance pixels and energy bins of the analysis is, thus $f = \prod_{j,r} f_j^r$, and motivates the use of a binned-likelihood statistical method in which the log-likelihood function is defined as

$$\log \mathcal{L} = \sum_{j,r} \log \mathcal{L}_j^r = \sum_{j,r} \sum_s n_{j,s}^r \log \mu_{j,s}^r \tag{3.41}$$

and, therefore

$$\log \mathcal{L} = \sum_{j,r,s} n_{j,s}^r \log \left[\frac{\left(1 + \sum_{\ell=1}^{\ell_{\max}} \sum_{m=-\ell}^{m=+\ell} a_{\ell m} Y_{\ell m}^s\right) \mathcal{T}_{j,s}^r \mathcal{E}_{j,s}}{\mathcal{N}_j^r} \right] \tag{3.42}$$

with

$$\mathcal{N}_j^r = \sum_s \mathcal{T}_{j,s}^r \mathcal{E}_{j,s}^r \left(1 + \sum_{\ell=1}^{\ell_{\max}} \sum_{m=-\ell}^{m=+\ell} a_{\ell m} Y_{\ell m}^s\right) \tag{3.43}$$

The maximization of the log-likelihood function provides the coefficients of the multipolar expansion $a_{\ell m}$.

3.5.2 *Relative anisotropies*

In the case of relative anisotropies, one has to deal with the potential problem of having low number of reference events in each generalized pixel and Li-Ma log-likelihood [215] is used instead. Following the same notation as in the case of absolute anisotropies,

$$\log \mathcal{L} = \sum_{j,r,s} \left[n_{j,s}^r \log \alpha_{j,s}^r - \left(n_{j,s}^r + (n_{\text{ref}})_{j,s}^r\right) \log(1 + \alpha_{j,s}^r) \right] \tag{3.44}$$

where $n_{j,s}^r$ and $(n_{\text{ref}})_{j,s}^r$ are the number of measured events in the generalized pixel $\equiv (r, j, s)$ of numerator and denominator samples, respectively, and

$$\alpha_{j,s}^r = \frac{1}{\mathcal{N}_j^r} \frac{N_j^r}{(N_{\text{ref}})_j^r} \left(1 + \sum_{\ell=1}^{\ell_{\max}} \sum_{m=-\ell}^{m=+\ell} a_{\ell m} Y_{\ell m}^s\right) \tag{3.45}$$

with

$$N_j^r = \sum_s n_{j,s}^r \qquad ; \qquad (N_{\text{ref}})_j^r = \sum_s (n_{\text{ref}})_{j,s}^r \tag{3.46}$$

and, in a similar manner, the normalization of the skymap $j, r, \mathcal{N}_j^r$, ensures that the total number of events is preserved and accounts for the possible limited coverage of the sky

$$\mathcal{N}_j^r = 1 + \frac{1}{(N_{\text{ref}})_j^r} \sum_{\ell=1}^{\ell_{\max}} \sum_{m=-\ell}^{m=+\ell} a_{\ell m} \sum_s (n_{\text{ref}})_{j,s}^r \, Y_{\ell m}^s \tag{3.47}$$

As in the case of absolute anisotropies, the maximization of the log-likelihood function provides the multipolar components of the relative anisotropy.

3.5.3 *Statistical treatment of background in anisotropy searches*

The measurement of anisotropies is performed in a cosmic ray sample within a given enery range. As a result of the event selection, the sample may contain background events, either from other cosmic ray species or with energies different to those in the range of analysis. The fraction of signal and background events is, thus, described in terms of the *purity of the sample*, p

$$p = \frac{N_{\text{sig}}}{N_{\text{tot}}} = \frac{N_{\text{sig}}}{N_{\text{sig}} + N_{\text{bkg}}} \tag{3.48}$$

The definition of purity can be extended to the most general case in which each event has a probability of being signal that depends on the values of a certain set of variables, $\vec{x}_i \equiv (x_1, \ldots, x_n)$. In this event-based definition of purity, each event has a probability $p_i(\vec{x}_i) \equiv p(x_1, \ldots, x_n)$ of being signal, such that the total number of signal events in the sample is

$$N_{\text{sig}} = \sum_{i=1}^{N} p_i(\vec{x}_i) \tag{3.49}$$

Models on the anisotropy of the background sample can be established; the most neutral and economic one, which will be used in the following, assumes that the background is isotropic.

The effect of having a sample with background contamination can be automatically included in the log-likelihood function in terms of the purity. In the case of absolute anisotropies, under the assumption that the exposure function for the generalized pixel i is the same for both signal and background samples, then

$$\begin{aligned} \mu^r_{j,s} = (\mu^r_{j,s})_{\text{sig}} + (\mu^r_{j,s})_{\text{bkg}} &\propto \frac{1}{\mathcal{N}^r_j}\left(p^r_{j,s}\Phi^{\text{sig}}_{j,s} + (1-p^r_{j,s})\Phi^{\text{bkg}}_{j,s}\right)\mathcal{T}^r_{j,s}\,\mathcal{E}_{j,s} \\ &= \frac{1}{\mathcal{N}^r_j}\left(1 + p^r_{j,s}\sum_{\ell=1}^{\ell_{\max}}\sum_{m=-\ell}^{m=+\ell} a_{\ell m}Y^s_{\ell m}\right)\mathcal{T}^r_{j,s}\,\mathcal{E}_{j,s} \end{aligned} \tag{3.50}$$

As a result, the log-likelihood function for absolute anisotropies is modified

$$\log\mathcal{L} = \sum_{j,r,s} n^r_{j,s}\log\left[\frac{\left(1 + p^r_{j,s}\sum_{\ell=1}^{\ell_{\max}}\sum_{m=-\ell}^{m=+\ell} a_{\ell m}Y^s_{\ell m}\right)\mathcal{T}^r_{j,s}\mathcal{E}_{j,s}}{\mathcal{N}^r_j}\right] \tag{3.51}$$

with

$$\mathcal{N}^r_j = \sum_s \mathcal{T}^r_{j,s}\mathcal{E}^r_{j,s}\left(1 + p^r_{j,s}\sum_{\ell=1}^{\ell_{\max}}\sum_{m=-\ell}^{m=+\ell} a_{\ell m}Y^s_{\ell m}\right) \tag{3.52}$$

In the case of relative anisotropies, the term $\alpha^r_{j,s}$ in (3.44) includes the purity $p^r_{j,s}$

$$\alpha^r_{j,s} = \frac{1}{\mathcal{N}^r_j}\frac{N^r_j}{(N_{\text{ref}})^r_j}\left(1 + p^r_{j,s}\sum_{\ell=1}^{\ell_{\max}}\sum_{m=-\ell}^{m=+\ell} a_{\ell m}Y^s_{\ell m}\right) \tag{3.53}$$

as well as the normalization

$$\mathcal{N}_j^r = 1 + \frac{1}{(N_{\text{ref}})_j^r} p_{j,s}^r \sum_{\ell=1}^{\ell_{\max}} \sum_{m=-\ell}^{m=+\ell} a_{\ell m} \sum_s (n_{\text{ref}})_{j,s}^r \, Y_{\ell m}^s \tag{3.54}$$

The effect of including the purity as a multiplicative factor of the multipolar coefficients is to reduce the sensitivity of the analysis due to the presence of background contamination. If $a_{\ell m}$ are the dipole components of the analysis including the purity of the sample and $\tilde{a}_{\ell m}$ are the results assuming the sample contains no background, then

$$a_{\ell m} \approx \frac{\tilde{a}_{\ell m}}{\langle p \rangle} \quad ; \quad \sigma(a_{\ell m}) \approx \frac{\sigma(\tilde{a}_{\ell m})}{\sqrt{\langle p^2 \rangle}} \tag{3.55}$$

where

$$\langle p \rangle = \frac{\sum_{i=1}^N p_i}{N} \quad ; \langle p^2 \rangle = \frac{\sum_{i=1}^N p_i^2}{N} \tag{3.56}$$

are the first and second moments of the purity distribution, respectively.

3.6 COMPUTATION OF UPPER LIMITS

The techniques presented in the previous sections allow to obtain the multipole components of the flux expansion in terms of spherical harmonics. From the measured values of $a_{\ell m}$ and, therefore, the measured dipole amplitude δ_{M}, we will be interested in making inferences on the true dipole anisotropy parameter, δ_{T}, which is the physical quantity predicted by models.

Considering that dipole components are Gaussian distributed random variables of variance inversely proportional to the number of events, (3.12), it is possible to compute the probability distribution function of $p(\delta_{\text{M}}|\delta_{\text{T}})$ for a certain value of δ_{T}. In particular, the distribution of $p(\delta_{\text{M}}|\delta_{\text{T}})$ for the case of no anisotropy, $\delta_{\text{T}} = 0$, is shown in figure 3.8. Due to statistical fluctuations of a finite sample, N, and since the measured dipole amplitude, δ_{M}, is a positive-defined quantity, this probability distribution function has a non-zero expected value ($\text{E}[\delta_{\text{M}} \times \sqrt{N}] \sim 2.76$).

In many circumstances, we may be interested in quoting one-sided intervals on δ_{T}, $[0, \delta_{\text{T}}^{\text{U.L.}}]$, and, therefore, establish an upper limit on the value of that parameter from the measured results. Frequentist and Bayesian prescriptions can be used to calculate upper limits on δ_{T}. A comparison between the two treatments in the computation of upper limits is discussed in appendix A. Due to the advantages of the Bayesian approach, this prescription will be used to compute upper limits on the dipole anisotropy in this thesis.

In particular, in the Bayesian procedure the upper limit corresponds to the value $\delta_{\text{T}}^{\text{U.L.}}$ that contains a fraction α of the posterior probability

$$\alpha = \int_0^{\delta_{\text{T}}^{\text{U.L.}}} p(\delta_{\text{T}}|\delta_{\text{M}}) \, d\delta_{\text{T}} \tag{3.57}$$

i.e., that the probability for δ_{T} being above $\delta_{\text{T}}^{\text{U.L.}}$ is $1 - \alpha$. The posterior probability is defined in terms of a Bayesian prior, δ_{T}, for the parameter δ_{T}

$$p(\delta_{\text{T}}|\delta_{\text{M}}) \propto \pi(\delta_{\text{T}}) p(\delta_{\text{M}}|\delta_{\text{T}}) \tag{3.58}$$

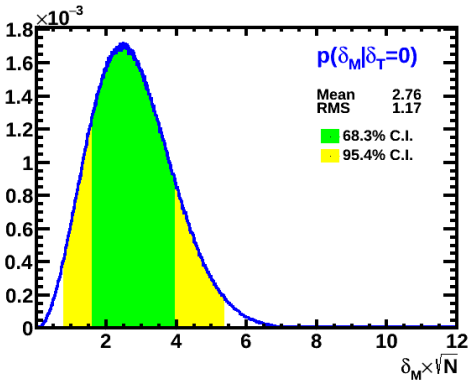

FIGURE 3.8: Probability distribution function $p(\delta_{\rm M}|\delta_{\rm T})$ for scaled $\delta_{\rm M} \times \sqrt{N}$ in the case of no anisotropy, $\delta_{\rm T} = 0$. Two-sided credible intervals (C.I.) corresponding to 68.3% (1σ) and 95.4% (2σ) probability content are displayed.

Procedures to obtain the reference prior for $\delta_{\rm T}$ are well-established [216], and yield to [217]

$$\pi(\delta_{\rm T}) \sim \text{const} \tag{3.59}$$

This allows to obtain the Bayesian posterior probability, from which it is possible to make inferences (see [217] for the analytical expressions) and compute the upper limit on $\delta_{\rm T}$ for any value of measured dipole amplitude, $\delta_{\rm M}$.

Figure 3.9 illustrates the procedure to obtain upper limits in the Bayesian prescription. Figure 3.9-*left* corresponds to the distribution of the probability distribution function $p(\delta_{\rm M}|\delta_{\rm T})$ for different values of $\delta_{\rm T}$ uniformly distributed according to the constant prior (3.59), for both scaled $\delta_{\rm T} \times \sqrt{N}$ and $\delta_{\rm M} \times \sqrt{N}$. Projections onto the vertical axis for a measured value $\delta_{\rm M} \times \sqrt{N}$ provide the posterior probability, $p(\delta_{\rm T}|\delta_{\rm M})$, from which Bayesian inference can be applied.

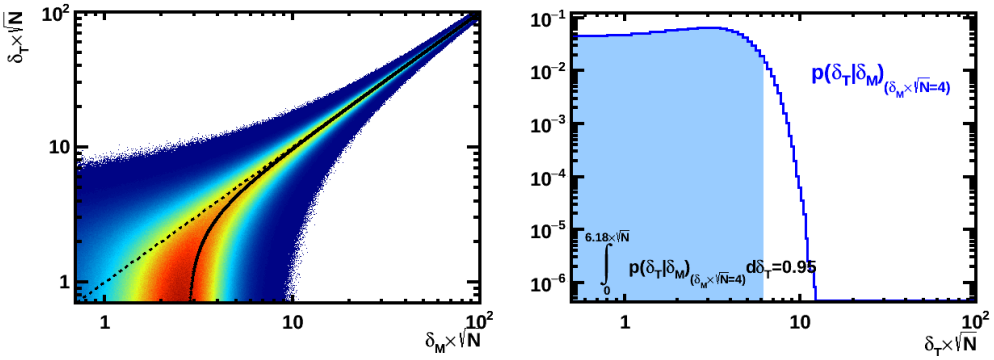

FIGURE 3.9: *(Left)* Distribution of $\delta_{\rm M}$ for different values of $\delta_{\rm T}$, both scaled by the sample size, $\sqrt{N}$. Solid black line shows the expected value of $\delta_{\rm M}$ according to the $p(\delta_{\rm M}|\delta_{\rm T})$ distribution for each value of $\delta_{\rm T}$. In particular, for $\delta_{\rm T} = 0$, the expected value $\mathrm{E}[\delta_{\rm M} \times \sqrt{N}] \sim 2.76$ is recovered. *(Right)* Posterior probability $p(\delta_{\rm T}|\delta_{\rm M})$ for $\delta_{\rm M} \times \sqrt{N} = 4$ and upper limit computation according to Bayesian prescription.

As an example, figure 3.9-*right* corresponds to the vertical projection for a measured value of $\delta_{\rm M} \times \sqrt{N} = 4$ and provides the posterior probability for Bayesian

inferences. Thus, according to (3.57), the upper limit that ensures a 95% probability content ($\alpha = 0.95$) of the posterior probability (95$ C.I. upper limit) on $\delta_{\rm T}$ is found to be $\delta_{\rm T}^{\rm U.L.} \times \sqrt{N} \sim 6.18$.

The previous calculation can be extended to any value of the measured dipole amplitude, $\delta_{\rm M}$. In this sense, figure A.2 shows the 95% C.L. upper limits on $\delta_{\rm T}$ that one may quote for a certain value of $\delta_{\rm M}$, both scaled by the sample size. In particular, the asymptotic value of the upper limit curve for $\delta_{\rm M} \to 0$, which is obtained in the case of measuring $a_{1-1} = a_{1-1} = a_{1+1} = 0$, constitutes the *statistical limit*, i.e., the smaller upper limit on $\delta_{\rm T}$ one may set for a sample size of N. In the Bayesian approach this value corresponds to $\delta_T^{95\%\rm U.L.} \times \sqrt{N} \sim 3.40$.

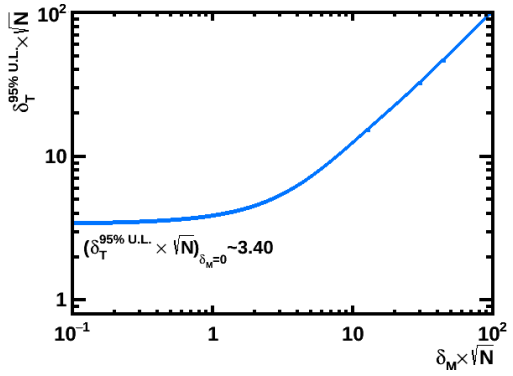

FIGURE 3.10: Bayesian 95% C.I. upper limits on $\delta_{\rm T}$ for any value of $\delta_{\rm M}$, both scaled by the sample size.

4

MEASUREMENT OF LARGE SCALE ANISOTROPIES WITH AMS-02

4.1 INTRODUCTION

Experimentally, the specific operating conditions of the detector have to be considered in the measurement of anisotropies. In this sense, space-based experiments are subject to variations in the detector status and, therefore, it is needed to define a set of conditions to ensure that the data is collected under stable and nominal configurations.

In addition, an AMS-like Toy Monte Carlo detector has been simulated to reproduce the period of analysis and is used to validate the method of analysis presented in the chapter 3. This simulation also helps to understand how the transformation between coordinate systems affects a simulated signal under the specific detector operating conditions, angular aperture and period of analysis.

4.2 AMS-02 DATA TAKING

The quality of the data taking is examined to guarantee that only events detected when AMS is under nominal operating conditions contribute to the selected sample. This includes not only the definition of good time periods (*runs*) from the point of view of instrumental settings but also the evaluation of the global status for each second of the data taking period. In the first case, time periods involving detector operations, such as calibrations or TRD gas refills, or external configurations like the ISS solar arrays or the robotic arm inside AMS-02 field of view are tagged as bad periods and, consequently, removed from the analysis. In the latter case, an efficient acquisition is assured by evaluating a set of conditions on individual seconds of data taking from a *Real Time Information* (RTI) database, which contains orbital parameters provided by NASA as well as AMS-02 DAQ and status variables (table 4.1). In particular, the requirement of a minimum value of the livetime in each second allows to reject seconds where the rate of cosmic rays is high and noisy events reduce the livetime, especially, avoiding the South Atlantic Anomaly. Furthermore, since ISS is subject to orbital maneuvers (such as docking of spacecrafts, extra-vehicular activities or debris avoidance maneuvers), a loose cut on the instantaneous angle between the vertical axis of AMS and the local zenith is applied to remove non-horizontal ISS attitudes.

In the case of the measurement of anisotropies, since a precise understanding of detector is mandatory, additional cuts are used to improve the quality of data taking seconds. In particular, a tighter cut on the ISS attitude is applied to remove non-horizontal configurations. On the other hand, since TRD is sensitive to envi-

ronmental conditions such as the increase of rates of low energy particles at high geomagnetic latitudes (figure 4.1), noisy seconds with high occupancy in this sub-detector are discarded.

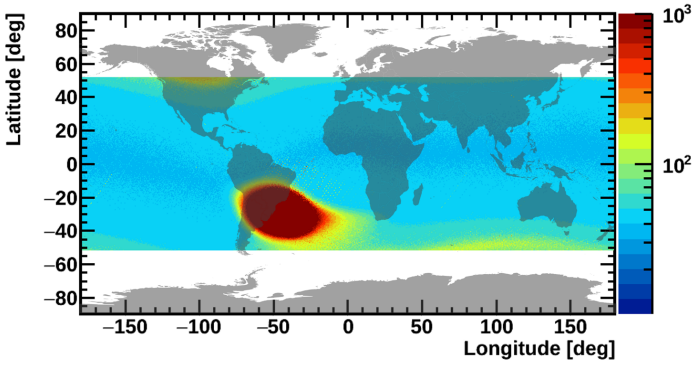

FIGURE 4.1: Average number of TRD hits as a function of the ISS geographical position. Regions close to the geomagnetic poles and the SAA have a higher number of TRD hits, due to a higher rate of cosmic ray particles.

TABLE 4.1: Criteria used to define good seconds of data taking.

Standard cuts on good seconds
• AMS-02 is in nominal status of data taking
• The detector livetime is above 0.5
• AMS-02 is not in the South Atlantic Anomaly
• Zenith angle of AMS-02 vertical axis less than 40°
Additional quality cuts
• Horizontal ISS attitudes: zenith angle of AMS-02 vertical axis [1] between $[10^\circ, 14^\circ]$
• Normal occupancy in TRD

The time stability of the AMS data acquisition (DAQ) is shown in figure 4.2. In the five years in orbit used in this analysis, AMS has been collecting data 93.5% of the time. Out of the total number of seconds where AMS is recording data, a fraction of about 85% are tagged as good quality seconds for the measurement of anisotropies[2], and amount to 1.27×10^8 s. Finally, the total exposure time considering the livetime of each second is 1.13×10^8 s, which corresponds to an average livetime of the 89%.

1 AMS-02 vertical axis has a tilt of 12° with respect to the zenith angle.
2 The introduction of the additional quality cuts in the definition of good seconds for the analysis of anisotropies is highly efficient and implies a loss of a 2.7% on top of the standard cuts.

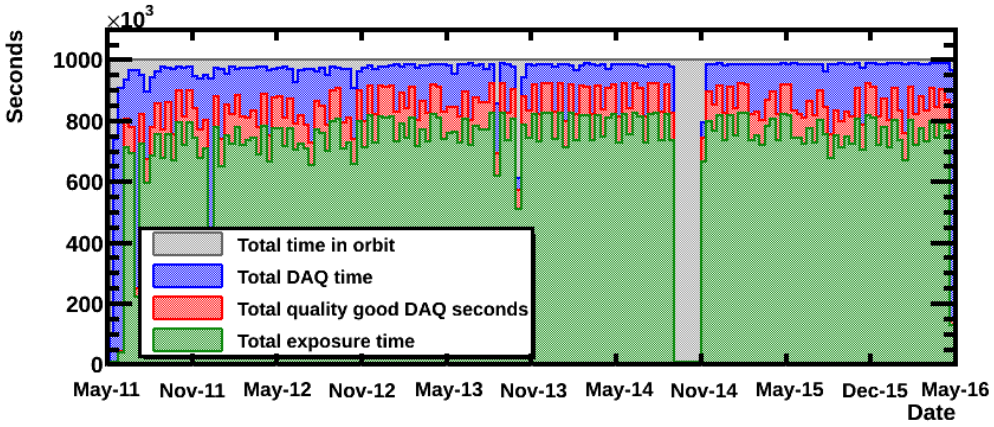

FIGURE 4.2: Time stability of the AMS-02 DAQ during the first 5 years in orbit analyzed in this thesis. The initial gap corresponds to the period of comissioning, from the AMS-02 activation to June 5, 2011. Finally, the gap from October till the end of November 2014 is due to a test of the tracker thermal control system.

4.3 TOY MONTE CARLO SIMULATION

A Toy Monte Carlo simulation for an ideal AMS-like detector has been carried out as a test bench of the tools developed for the analysis of anisotropies. The simulated AMS-like detector is a cylinder of 25° half-opening on board the ISS and tilted 12° with respect to the local zenith. The orbital parameters of the ISS (position, velocity and attitude) as well as the livetime are taken from the RTI database. The period of simulation, from 2011 May 19 to 2016 May 26, corresponds to the first 5 years of data taking, and the definition of the good seconds in the simulation is identical to that used in the final analysis and presented in section 4.2.

The Toy Monte Carlo simulation can be summarized as follows:

- For each second tagged as good during the period of analysis, an isotropic distribution of particles is generated on top of the detector. A particle is generated randomly with an incoming direction (θ, φ) in a point (x, y) of the upper plane of the cylinder. The simulated distribution of particles follows a power-law energy spectrum with spectral index $\gamma = 2.7$.
- A particle is tagged as detected, and thus, is accepted, if the generated incoming trajectory hits the bottom plane of the detector when propagated in straight line. Furthermore, the generated energy is required to exceed 1.2 times the maximum cutoff at the position of the ISS for an aperture of 25°. If any of these two conditions is not satisfied, the particle is rejected (figure 4.3-*left*).
- In addition, events are accepted with a probability given by the livetime of the second from the RTI database.
- The resulting acceptance includes two contributions: the one corresponding to the geometry of the detector, which imposes a maximum incident angle of $\theta_{\text{max}} = 25^\circ$; and a factor $\cos\theta$ between the generated direction and the normal to the upper detection plane. The relative acceptance is calculated nu-

merically and the result is shown in figure 4.3-*right*. As the trajectory becomes more inclined, the relative acceptance decreases.

- Apart from the livetime of detection, taken from the RTI database, the detector is ideal, i.e., fully efficient along the orbit.

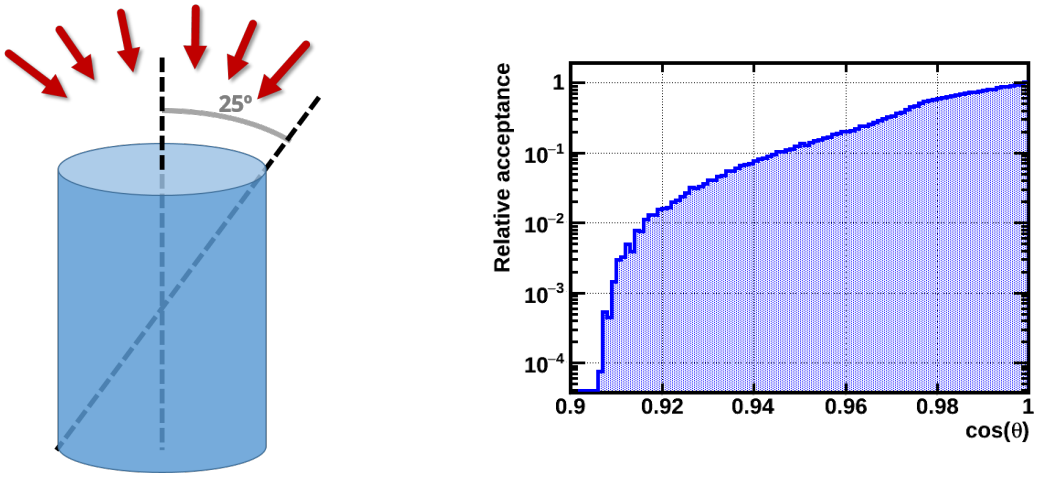

FIGURE 4.3: *(Left)* Scheme of an AMS-like ideal detector, defined as a cylinder of 25° half-opening onboard the ISS. The simulated period consists of the five years used in this thesis, from May 2011 to May 2016, where only good seconds and runs of the data taking are considered. *(Right)* Relative acceptance of the AMS-like ideal detector as a function of the cosine of the incident angle with respect to the vertical, calculated numerically from a generated distribution of isotropic events.

4.3.1 *Exposure time maps*

The Toy Monte Carlo simulation allows to build the exposure time maps[3] for an ideal AMS-like detector in space. The skymaps are created in the standard format that will be used hereinafter in this thesis, following a HEALPix scheme pixelization with 12288 pixels in a Mollweide projection. The skymaps also follow the astronomical convention, where the East (longitude $+90°$) is placed towards the left of the map and the West (longitude $-90°$) is towards the right.

A review of the skymaps obtained above the maximum rigidity cutoff in the different coordinate systems is presented in the following sections.

4.3.1.1 *Geographic coordinate systems*

In the ISS Geographical Position coordinate system, the exposure time map extends in the range of latitudes from $-51.6°$ to $+51.6°$ due to the ISS orbit (figure 4.4-*left*). The region corresponding to the South Atlantic Anomaly is removed from the analysis, as mentioned in section 4.2. On the other hand, regions close to the geographic poles are more exposed since the ISS spends more time in there. In addition, the low

3 Since the efficiencies of detection are equal to one in this ideal simulation, the exposure time maps and the exposure maps introduced in section 3.4.1 are equivalent.

exposure time line corresponding to the Earth equator is due to the full calibration of subdetectors performed every 2 runs.

The exposure time map in GTOD (figure 4.4-*right*), for arrival directions, shows these features convoluted with the detector's acceptance, which allows to have an almost full coverage of the skymap despite of the fact that the ISS position does not completely cover the sphere. In particular, the polar regions are reached only by inclined trajectories of low acceptance within the detector, thus corresponding to directions of low exposure. This fact, combined with the orbit and the detector's tilt of 12° with respect to the local zenith, is responsible of the North-South asymmetry: the North pole is more exposed than the South.

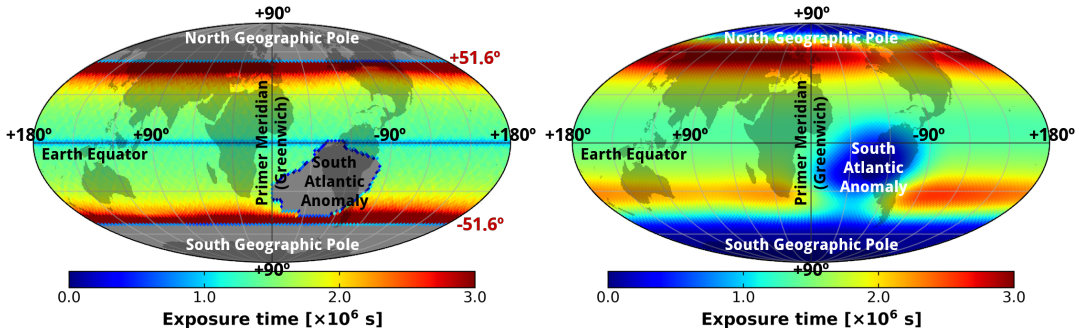

FIGURE 4.4: AMS-like exposure time maps in positional *(left)* and directional *(right)* geographical coordinates, ISS Geographical Position and GTOD, respectively. As illustration, a shadowed world map as well as other characteristic elements are displayed.

4.3.1.2 *Geomagnetic coordinate system*

The exposure time map in the ISS Geomagnetic Position (figure 4.5-*left*) is similar to that in the geographical one, but rotated in order to the be aligned with the geomagnetic dipole. In particular, this is evidenced by the edges of the ISS orbit, as seen in figure 4.5-*left*.

4.3.1.3 *Equatorial coordinate system*

The exposure time skymap obtained in the equatorial reference frame (figure 4.5-*right*) can be understood from the one in GTOD coordinates. In fact, as GTOD is an Earth-centered co-moving system, it rotates around the vernal equinox with a period of 24 h. Thus, the resulting exposure time skymap in equatorial coordinates can be regarded as the one obtained after averaging the skymap in GTOD along the azimuthal coordinate.

Similarly, because of the characteristics of the ISS orbit and the position of AMS-02 within the ISS, the North Celestial Pole is more exposed than the South one.

4.3.1.4 *Galactic coordinate system*

The exposure time map in galactic coordinates (figure 4.6-*left*) shows the same features as the one in the equatorial system but distorted. In particular, the North

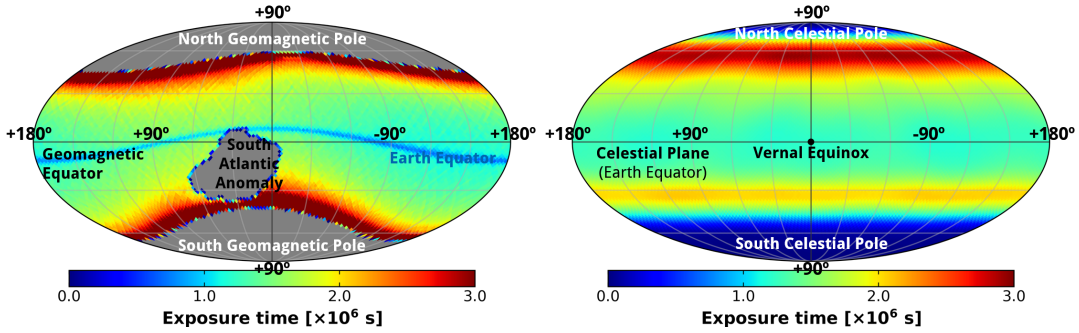

FIGURE 4.5: AMS-like exposure time maps in ISS Magnetic Position *(left)* and equatorial *(right)* coordinates.

and South Celestial Poles have been displaced approximately to $(+30°, +120°)$ and $(-30°, -60°)$, respectively. The Celestial equator (and, thus, the Earth equator) corresponds to the band shown in figure 4.6-*left*.

4.3.1.5 *GSE coordinate system*

The exposure time map in the GSE reference frame (figure 4.6-*right*) can be derived from the one in equatorial coordinates. The prime direction in GSE, pointing from the Earth towards the Sun, rotates with respect to the vernal equinox as the Earth moves around the Sun in the ecliptic plane. Thus, the exposure time map in the GSE frame can be regarded as the one obtained after averaging azimuthally the skymap in equatorial system. In addition, the rotation of $23.44°$ in the Z-axis from the equatorial to the ecliptic plane, combined with the Earth's orbit, introduces a small averaging effect in the latitudinal coordinate.

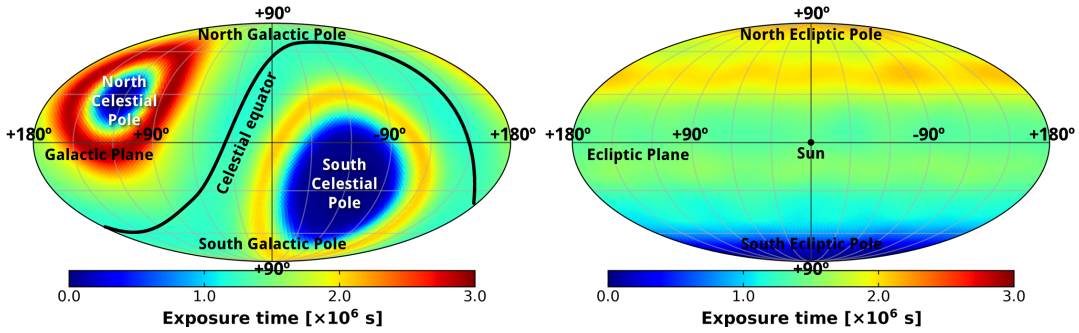

FIGURE 4.6: AMS-like exposure time maps in galactic *(left)* and GSE *(right)* coordinates.

4.3.2 *Test of the analysis methods for dipole determination*

The validation of the statistical methods developed to determine the dipole components is carried out by means of the Toy Monte Carlo simulation. In this validation, two kind of reference maps are created in any coordinate system according to section 3.4:

- Exposure time maps, for absolute analysis
- Isotropic distribution of events, following the exposure time map, for relative analysis

In addition, an anisotropic distribution of events is generated by injecting a signal in any coordinate system. The sample size and the multipole component ℓm where the signal is injected as well as its amplitude can be modified *ad lib*. The multipole components are retrieved by means of the maximization of the log-likelihood function in each case.

In particular, a pure dipole signal of amplitude varying from 0 to 1 is simulated in the three different dipole directions. The reconstructed dipole amplitude from the retrieved dipole components is calculated in each case. As an example, figure 4.7 shows the reconstructed dipole amplitude as a function of the simulated signal injected in the East-West direction in galactic coordinates, when the exposure time maps are used as a reference. A similar result is obtained when the isotropic distribution of events is considered. Thus, the statistical methods presented in section 3.5 allow the full recovery of the injected dipole.

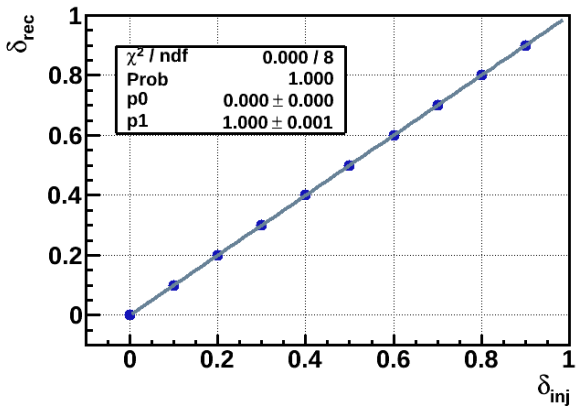

FIGURE 4.7: Reconstructed dipole amplitude for the different values of the injected dipole signal using the Toy Monte Carlo simulation. A full recovery of the injected signal is obtained.

Furthermore, to ensure that there is no bias in the recovery of the simulated signal, a sampling of 500 anisotropic distributions is performed. The number of events of each anisotropic sample, 10^7, is high enough to be sensitive to possible bias in the reconstruction of the dipole components. The simulated dipole has an amplitude of $\delta_{\text{inj}} = 0.5$ and is injected in the Forward-Backward component in galactic coordinates. For each sample i, the three dipole components $(\rho_{\text{EW}}, \rho_{\text{NS}}, \rho_{FB})_i^{\text{rec}}$ are obtained and the distribution of pulls, defined as $\left(\frac{\rho_i^{\text{rec}} - \rho_i^{\text{sim}}}{\sigma(\rho_i^{\text{rec}})}\right)$ is calculated for each component, where, in this case, $(\rho_{\text{EW}}, \rho_{\text{NS}}, \rho_{\text{FB}})^{\text{sim}} = (0, 0, 0.5)$. Figure 4.8 shows the distribution of pulls for each dipole component and their consistency with a normal distribution allows to conclude that there is no bias in the determination of the dipole components for both absolute and relative anisotropies.

A similar verification is carried out when the sample of study is composed by a mixture of signal and background events according to a simulated purity. The log-

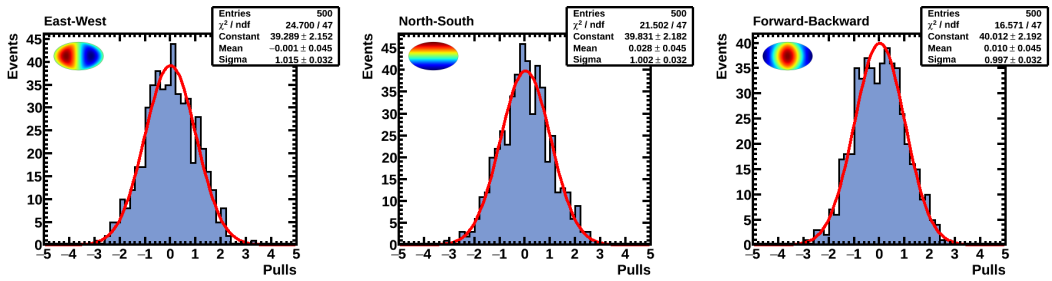

FIGURE 4.8: Distribution of pulls for the three dipole components obtained from a sampling of 500 Toy Monte Carlo simulations. The agreement with a normal distribution in each case is also displayed, and indicates that the statistical tools developed allow to determine the dipole components without bias.

likelihood function accounting for the purity of the sample is able to recover the injected dipole anisotropy without bias.

Finally, the determination of the dipole components proved to be stable against different sample statistics and map pixel size.

4.3.3 *Effective coordinate transformations*

The coordinate transformation between reference systems not only reflects on the skymaps, as it has been presented in section 4.3.1, but also affects the manner that a signal (and, in particular, its multipole components) projects from one coordinate system into another one.

The transformation of the multipole components of a signal when a change of coordinate system is performed can be quantified by means of the Toy Monte Carlo simulation. In this sense, a distribution of events where a signal is injected in a given multipole $(\ell m)_i$ in a coordinate system i is generated. The anisotropic distribution of events is, thus, transformed into the second coordinate system j, and the analysis of anisotropies is performed to retrieve the transformed components of the signal $(\ell m)_j$. Therefore, the matrix $(\ell m)_{ij}$ quantifies the transformation of a signal between two coordinate systems, from i to j. Thus, the matrix elements, m_{ij}, provide the transformation of a signal, $\rho^j_{\ell m} = m_{ij}\rho^i_{\ell m}$. In particular, for $\ell = 1$ the three components define the three fundamental axes of the coordinate system, thus, the matrix can be regarded as the *effective coordinate transformation* between two reference frames. We shall remark that, since the coordinate transformation are frequently time dependent, the transformation matrices are only applicable to the simulated period of analysis. In addition, they strongly depend on the specific characteristics of the detector (field of view, orbit, etc.) and should be calculated for each experiment taking into account its operating conditions.

A review of the transformation matrices between the coordinate systems is presented in the following sections.

4.3.3.1 *Transformations between positional coordinate systems*

The matrix in figure 4.9-*left* shows the transformation between signals injected in dipole and quadrupole components in ISS Geographical Position (horizontal axis) and transformed into ISS Geomagnetic Position (vertical axis). In each axis, apart from the multipole components where the signal is injected or transformed, a term corresponding to the isotropic component is considered, ρ_{iso}. This isotropic term quantifies the dilution of a signal because of the coordinate transformation assuming that $\rho_{\text{iso}} = \sqrt{1 - \sum_{\ell m} m_{\ell m}^2}$.

In particular, the matrix transformation evidences that geomagnetic and geographic coordinates are connected by means of a time independent rotation. The North-South axis, represented by the ρ_{NS} component is almost identical in both cases (due to the fact that the angle between the rotational axis and the geomagnetic dipole is $9.5°$). The East-West and Forward-Backward components show that both coordinates are connected by a rotation in that components.

In addition, quadrupole components in ISS Geographical Position transform into quadrupole components in Geomagnetic Position without loss of signal. In conclusion, from the point of view of signal transformation both reference frames are equivalent.

4.3.3.2 *Transformation between positional and directional coordinate systems*

On the other hand, the transformation between ISS Geographical Position and GTOD, both geographic, illusrates the difference between positional and directional coordinate systems. The matrix of the effective transformation (figure 4.9-*right*) is diagonal with no signal dilution for dipole signals and a partial dilution in some quadrupole components.

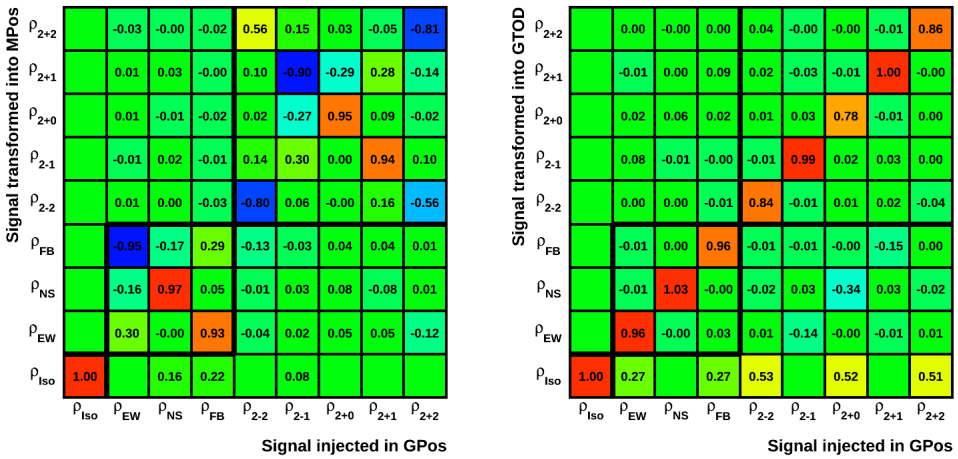

FIGURE 4.9: Effective matrix coordinate transformation between positional and directional coordinate systems, from ISS Geographical Position to ISS Magnetic Position *(left)* and from ISS Geographical Position to GTOD *(right)*.

4.3.3.3 *Transformation between inertial coordinate systems*

Inertial coordinate systems are suitable for astrophysical searches, thus, it is valuable to understand how a signal transforms between them. In this sense, the transformation matrix between equatorial and galactic coordinates, in figure 4.10, is a block diagonal matrix. In consequence, a pure dipole component in the equatorial system transforms into a pure dipole in galactic, and the same applies to the quadrupole. The components rotate, i.e., a pure signal transforms into several components in galactic, but no signal dilution takes place.

This result is a consequence of the fact that both coordinate systems are defined on the celestial sphere and connected by means of a time independent rotation once the epoch is fixed for both. Thus, inertial coordinate systems are equivalent from the point of view of signal transformation.

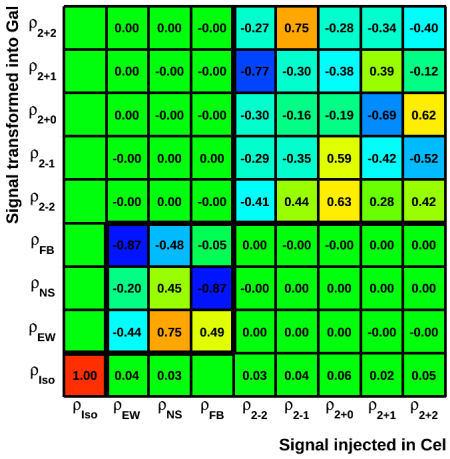

FIGURE 4.10: Effective matrix coordinate transformation between equatorial and galactic coordinate systems.

4.3.3.4 *Transformation between inertial and non-inertial coordinate systems*

Inertial and non-inertial coordinate transformation are connected by means of time dependent rotations, whose effect is an average of the distributions in the skymap along the rotating coordinate. Thus, in the transformation between inertial and non-inertial frames we expect a signal dilution in the components where this rotation takes place.

Figure 4.11-*left* shows the transformation between ISS Geographical Position and galactic coordinates. It is remarkable that only the azimuthally symmetric components (ρ_{NS} and ρ_{2+0}), associated to the North-South axis in ISS Geographical Position, transform into the galactic frame without signal loss. The remaining dipole and quadrupole components are fully suppressed due to the Earth's rotation. In addition, the three dipole components in galactic coordinates inherit the signal in the ρ_{NS} component of ISS Geographical Position. The same conclusion holds for the

quadrupole components, where a partial reduction in the transformation into the galactic system of the ρ_{2+0} component takes place.

The transformation between GSE and galactic coordinates (figure 4.11-*right*) shows similar features: only the azimuthally symmetric components are transformed without signal dilution. The rest of the dipole and quadrupole components, in particular, those contained in the ecliptic plane (ρ_{EW} and ρ_{FB}), are totally diluted.

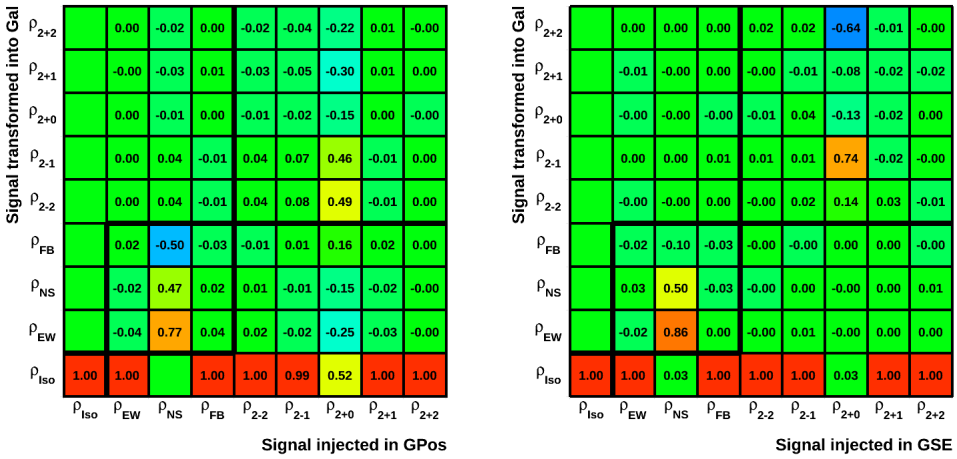

FIGURE 4.11: Effective matrix coordinate transformation from ISS Geographical Position *(left)* and GSE (*right*) to galactic coordinates.

4.3.3.5 *Summary of the effective coordinate transformations*

The study of the coordinate and signal transformations between reference frames is relevant to decide the optimal coordinate system for our purposes. In our case, the search for anisotropies can be carried out in any inertial coordinate system without loss of information. In particular, the ultimate goal of this thesis consists in characterizing/measuring the dipole anisotropy that possible sources or processes of galactic origin may imprint in the arrival directions of primary charged cosmic rays. Consequently, galactic coordinates are convenient for our purposes.

On the other hand, the coordinate systems suitable for the understanding of the detector (ISS Geographical and Geomagnetic Position, and GTOD) are almost equivalent. In this thesis we will use ISS Geographical Position to evaluate the dependence of the efficiencies within the orbit, as it provides a clear and intuitive picture of the possible variations. In addition, potential day/night modulations in the detection, which are intrinsic to the GSE reference frame, are associated to components fully contained in the ecliptic plane, thus, have no impact in the analysis of anisotropies in an inertial coordinate system.

We shall remark that the effective coordinate transformations not only apply to a true signal but also to spurious signals associated to detector effects. In particular, any detector effect along the North-South direction in geographical coordinates will

project to all dipole components in the galactic reference frame, especially, in the East-West direction.

Finally, detector effects associated to variations of the efficiencies along the position within the ISS orbit could be calculated in geographical position, where they are intrinsic, and projected into galactic coordinates by means of the transformation matrices. However, since the geographical variation of the detector efficiencies may depend on time, the exact determination of the detector effects in galactic coordinates is obtained when they are evaluated directly in the coordinate system of the final analysis.

5

MEASUREMENT OF THE DIPOLE ANISOTROPY IN COSMIC RAY PROTONS

5.1 INTRODUCTION

Protons constitute the most abundant component in cosmic rays, which makes the measurement of its anisotropy especially challenging from the point of view of the precision required in the determination of the reference maps. Due to the high statistics of the proton sample, a remarkably accurate knowledge of the instrumental effects is needed in order to avoid spurious signals in the analysis.

This chapter is devoted to the measurement of the absolute anisotropy in Galactic cosmic ray protons. The selection of a proton sample and the evaluation of the instrumental effects involved, with special emphasis on the effect of efficiencies in the measurement of anisotropies are presented. Finally, the results of the dipole absolute anisotropy are reported.

5.2 SELECTION OF PROTONS

5.2.1 *Data sample*

AMS-02 started collecting cosmic rays on 2011 May 19 at 9:35 CDT and since then, it continues operating steadily. So far, AMS-02 has recorded more than 10^{11} events of Galactic cosmic rays in more than 6 years. The eported results on anisotropies are based on the data collected from 2011 May 19 to 2016 May 26, corresponding to the first 5 years (60 months) of data taking.

5.2.2 *Preselection*

A first preselection is commonly carried out with the aim of removing background events not interesting for the analysis of charged one particles (protons, electrons and positrons), thus reducing the volume of AMS-02 data with a very high efficiency on the signal. The preselection consists in a minimal set of loose cuts that allows to define a tractable sample of relativistic downward-going unitary charged particles which can be used to study performances of subdetectors. Additional quality cuts on these preselected events define the selected sample involved in the measurement of anisotropies.

In the case of protons, the procedure follows the one described in [109]. Events are preselected by requiring a set of loose cuts on different subdetectors and variables (table 5.1). First, we demand downward-going relativistic particles with a

TABLE 5.1: List of cuts applied in the preselection of relativistic downward-going particles of unitary charge.

Subdetector	**Preselection cuts**
TOF	• Reconstructed track with 4 TOF planes • TOF charge compatible with $\|Z\| = 1$: $Q_{\text{UTOF}} > 0$ and $0.5 < Q_{\text{LTOF}} < 2$ • Relativistic downward-going particles: $\beta > 0.3$
Inner Tracker	• At least one Y hit in all of 4 inner planes • Reconstructed inner rigidity • Inner tracker charge compatible with $\|Z\| = 1$ $0.7 < Q_{\text{inner}} < 1.5$
L1, L9	• Hit XY in L1,L9 • Reconstructed rigidity with inner + L1,L9 • Charge compatible with $\|Z\| = 1$ $0.6 < Q_{\text{L1,L9}} < 1.9$ • $\chi^2 < 20$

velocity $\beta = \frac{v}{c} > 0.3$ reconstructed with the 4 TOF planes. In addition to a TOF track, a reconstructed track in the Inner Tracker is required by demanding at least one hit in the Y direction in all the 4 inner planes (layers 2-8) and a reconstructed inner rigidity. Charge compatibility with $|Z| = 1$ is imposed by cuts on the two independent measurements of the particle charge in TOF and Inner Tracker subdetectors. The existence of additional hits on external tracker layers, layers 1 and 9, allow to classify the sample in four tracker patterns associated to distinctive lever arm configurations: L1+Inner+L9, L1+Inner, Inner+L9 and Inner.

5.2.3 *Selection*

After the initial preselection, a selection of positive charged particles is achieved by means of a cut in the sign of the rigidity associated to the trajectory inside the Inner Tracker. Additional quality criteria on track reconstruction is imposed by demanding a good $\chi^2/d.f.$ in both bending and non-bending planes. Furthermore, a hit in the X and Y directions is required on the layer 2 of the Inner Tracker to stabilize the track finding.

Since protons are the dominant component of cosmic rays, the selected sample has negligible contributions of other species. Only a small background of pions produced in the upper part of the detector is present in the low energy region (below 2 GeV). Those low energetic pions are efficiently removed by means of a cut in the particle mass, which is determined by a combination of the TOF velocity and tracker rigidity. The efficiency of this cut is $\sim 100\%$ above 2 GeV.

TABLE 5.2: List of cuts applied in the selection of the proton sample.

Subdetector	**Selection cuts**
Fiducial volume	• Inner tracker track extrapolation inside Layer 1 and Layer 9
TOF	• Physical trigger
Inner Tracker	• Inner track $\chi^2(X,Y) < 10$ • Hit in X and Y directions in Layer 2 • Tracker pattern : L1+Inner+L9
	Mass cut
Inner Tracker	• $1/\beta > \sqrt{1+\left(\frac{1.5}{R+0.5}\right)^2} - 0.25$ • $\frac{1}{R} < 1.25$
	Above geomagnetic rigidity cutoff
	• R> 1.2 R^{+}_{cutoff}

Finally, in order to determine the proton rigidity with the best available resolution, events are required to have associated tracker pattern L1+Inner+L9 (*fullspan* protons). Those fullspan protons profit from the full capabilities of the tracking reconstruction and, therefore, have a highest MDR and the best rigidity resolution. This condition defines the fiducial volume of the analysis, as the extrapolation of the inner tracker trajectory is required to pass through the volume determined by layers 1 and 9.

In order to avoid secondary particles trapped in the geomagnetic field contaminating the sample, the measured rigidity of the particle is required to exceed the geomagnetic rigidity cutoff at the location where the event was detected. A conservative safety factor of 20% above the maximum rigidity cutoff within the AMS-02 field of view is applied to further ensure the selection of primary cosmic rays.

The complete set of selection cuts is summarized in table 5.2.

The analysis of the proton anisotropy is carried out in 8 cumulative ranges determined by a minimum rigidity $R_{\text{min}} = 18, 30, 45, 80, 150, 300, 500, 1000$ GV. At the same time, each rigidity range is divided into differential rigidity bins of width chosen according to the rigidity resolution. Table 5.3 collects the number of measured protons in the rigidity ranges of the analysis as well as the differential rigidity bins in each cumulative range.

TABLE 5.3: Number of measured protons and differential rigidity bins in the 8 cumulative rigidity ranges of the anisotropy study.

R_{min} [GV]	Rig. bins	Meas. protons ($\times 10^6$)
18	90	75.91
30	77	34.07
45	66	16.65
80	50	6.07
150	33	2.03
300	19	0.64
500	13	0.29
1000	7	0.12

5.3 PROTON EFFICIENCIES

Any cut applied to the sample has an associated efficiency, which is defined as the fraction of events passing the cut over the total number of events before that cut was applied

$$\varepsilon = \frac{N_{\rm ok}}{N_{\rm tot}} = \frac{N_{\rm ok}}{N_{\rm ok} + N_{\rm ko}}, \tag{5.1}$$

where the initial sample, $N_{\rm tot}$, is divided into two exclusive samples: those events passing the cuts, $N_{\rm ok}$, and the rejected sample, $N_{\rm ko}$. In particular, the relevant distribution in the analysis of anisotropies is not the value of the efficiency but its distribution in the skymap and, more precisely, its spherical harmonic parametrization. These two exclusive and no correlated samples allow the determination of the relative anisotropy according to (3.25) and (3.26) and, therefore, the parametrization of the efficiency $(\theta, \varphi)-$dependence in any coordinate system.

The efficiencies of the cuts applied in the proton selection have been evaluated using a data-driven approach, where each cut (and, consequently, the corresponding efficiency) is studied sequentially, i.e., the sample of events passing one cut constitutes the initial sample for the successive one. Formally, this procedure aims to avoid correlations between efficiencies, so that the total efficiency can be factorized directly in terms of the individual ones. On the other hand, the use of data in the evaluation of the efficiencies is justified since the effects that we are interested to quantify, associated to their geographical position, are not reproduced by the Monte Carlo simulation. In this manner, intrinsic quantities related to the performance of the subdetectors involved in the analysis are obtained and used to correct, in an unbiased manner, the reference maps for the absolute anisotropy searches.

Since the main subdetector involved in the proton selection is the tracker, the efficiencies that will play a role in the analysis are related to the reconstruction

efficiencies and quality cuts imposed on the track, as well as the hit association of a inner track in the outer layers (*picking efficiencies*).

5.3.1 *Trigger efficiency*

The trigger efficiency is evaluated from data through a sample of events passing all selection cuts and satisfying looser trigger conditions. In particular, the initial sample consists of two exclusive ones: events verifying any physics trigger, N_{phys}; and particles with a coincidence of signals from at least 3 TOF planes that do not satisfy any physics trigger. The latter, tagged as *unbiased*, N_{unbias}, is recorded with a prescaling factor of 1/100 applied on board to reduce the data size. Consequently, the trigger efficiency is calculated as the fraction of events selected passing the physics trigger over the total number of events

$$\varepsilon_{\text{trig}} = \frac{N_{\text{phys}}}{N_{\text{phys}} + 100 \cdot N_{\text{unbias}}}. \tag{5.2}$$

5.3.2 *Reconstruction and selection efficiencies*

5.3.2.1 *Tracking efficiency*

The efficiency of the cuts applied to the track of the particle are evaluated sequentially as shown in figure 5.1. First, the *tracking reconstruction efficiency* is examined by calculating the fraction of events having a corresponding track in the Inner Tracker contained in the fiducial volume of the analysis. Since the track is not available to define the fiducial volume, we take advantage of the standalone reconstruction of the TOF track. In fact, any particle satisfying the conditions of the physics trigger has associated signals in the TOF subdetector, which can be used to build an approximated path of the particle through the detector. Consequently, the TOF track inside the geometry determined by tracker layers 1 and 9 defines the fiducial volume for the evaluation of the tracking efficiency. On the other hand, since the track information is not available, the deposited energy in ECAL is used as a proxy for the proton rigidity. Thus, the efficiency corresponds to the fraction of the initial events with associated hit Y in all 4 inner planes and reconstructed rigidity.

Once the Inner Tracker track (and, consequently, the rigidity of the particle) is available, the extrapolation of the trajectory to layers 1 and 9 allows to determine the fiducial volume for the successive efficiencies. In particular, the *tracking selection efficiency* is calculated as the fraction of events with reconstructed Inner Tracker track (therefore, the sample passing the previous efficiency) that have unitary inner charge.

Finally, the *efficiency of the quality cuts* applied to the track are examined separately.

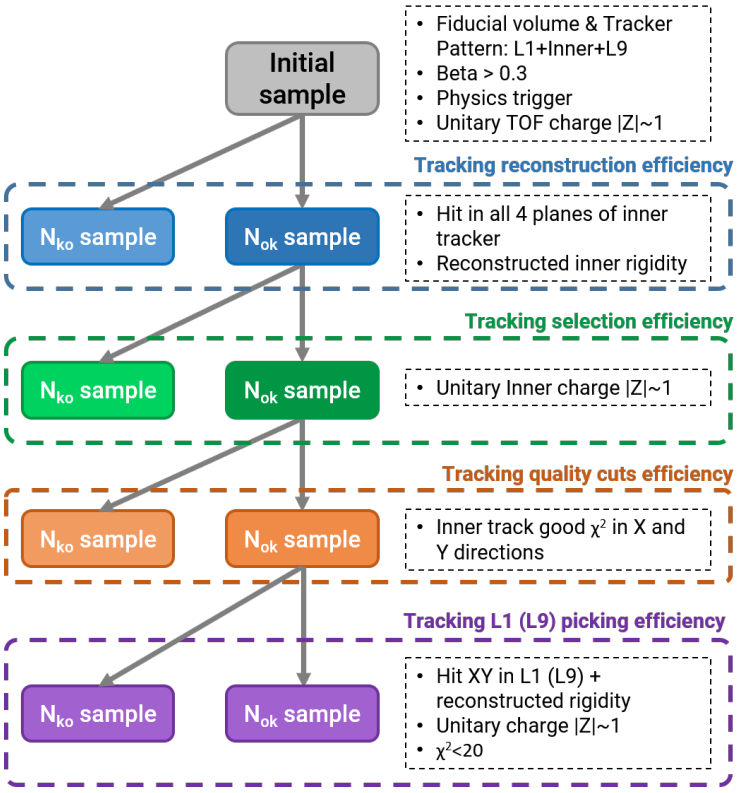

FIGURE 5.1: Scheme of the strategy followed in the calculation of the efficiencies associated to the tracker on the proton sample.

5.3.2.2 *Layer 1 and layer 9 picking efficiencies*

In order to measure the proton rigidity with the best available resolution, additional quality hits on the outer planes, layer 1 and layer 9 were required (figure 5.1). Layer 1 and layer 9 picking efficiencies are evaluated separately and account for the fraction of events with associated quality hits in layer 1 or layer 9, respectively, out of those with a quality track in the inner tracker.

Layer 1 and layer 9 picking efficiencies not only take into account possible geometrical inefficiencies but also include the performance of the algorithms searching for hit associations on the external layers.

5.4 FINITE RESOLUTION OF TRACKER

The selection described in section 5.2.3 provides a clean sample of protons with a negligible contribution from other cosmic ray species. However, due to the finite resolution of the tracker in the measurement of the particle's rigidity, the main source of contamination in the analysis of anisotropies on the proton sample arises from rigidity migrations. Finite resolution of tracker implies that an event with a given true rigidity has a non-zero probability of having a reconstructed rigidity falling in a different bin. Therefore, a proton sample selected in a certain recon-

structed rigidity range may have contributions from protons whose true rigidity is not in that range.

We shall remark that the treatment of the finite resolution of the tracker as well as its impact in the purity of the sample presented in this section is exclusive for the measurement of the proton anisotropy, whereas other techniques, such as unfolding, are applied in the measurement of fluxes.

The probability of the rigidity migrations has been estimated through a sample of Monte Carlo protons together with the measured flux by AMS-02 and the exposure time, and is summarized in the *migration matrix* shown in figure 5.2-*left*. Projections onto the horizontal axis of this matrix provide the probability density function, $p(R_{\text{True}}|R_{\text{Rec}})$, for a certain reconstructed rigidity (figure 5.2-*right*).

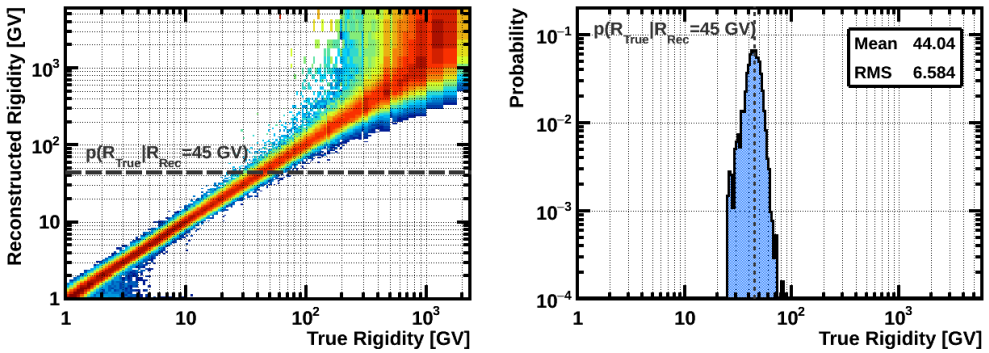

FIGURE 5.2: *(Left)* Full span migration matrix calculated from Monte-Carlo simulated protons, the exposure time and the AMS-02 proton flux. The matrix is normalized so that horizontal projections provide the probability distribution for a given reconstructed rigidity, R_{Rec}, of being in $[R_{\text{True}}, R_{\text{True}} + dR_{\text{True}}]$, $p(R_{\text{True}}|R_{\text{Rec}})$. As the rigidity increases, the distribution becomes wider due to the steady worsening of the rigidity resolution. *(Right)* Probability distribution function, $p(R_{\text{True}}|R_{\text{Rec}})$, obtained for a reconstructed rigidity $R_{\text{Rec}} = 45$ GV.

On the other hand, the analysis of anisotropies defines a signal region corresponding to a given range in true rigidity. However, the selection of protons is carried out in terms of their reconstructed rigidity, which means that, due to the finite resolution of the tracker, a fraction of events with true rigidity outside the signal region will fall in it. In contrast, rigidity migrations within the signal range do not affect the analysis, as those events are still contained in true rigidity[1]. For this reason, a definition of purity, based on the fraction of events whose true rigidity, whatever it is, falls within the signal region, is established

$$\mathcal{P}(R_{\text{Rec}}) = \frac{N(R_{\text{True}} > R^{\text{min}}_{\text{True}}|R_{\text{rec}})}{N(R_{\text{rec}})}, \tag{5.3}$$

1 This is true under our assumption that the anisotropy is constant within the energy range of analysis (section 3.5)

and can be computed for each event with reconstructed rigidity, R_{Rec}, in terms of the aforementioned probability distribution function

$$\mathcal{P}(R_{\text{Rec}}) = \int_{R_{\text{True}}^{\text{min}}}^{\infty} p(R_{\text{True}}|R_{\text{Rec}})\, dR_{\text{True}}. \tag{5.4}$$

In this manner, the definition of purity relevant to our analysis depends on the rigidity range of the measurement, which defines the signal region. Figure 5.3-*left* shows the purity of the sample for rigidities $R_{\text{true}} > 45$ GV as a function of the reconstructed rigidity. On the other hand, the distribution of signal and background events with $R_{\text{true}} > 45$ GV in figure 5.3-*right* is consequence of the purity distribution. Due to the finite resolution of the tracker, the purity is not a step function and rigidity migrations introduce background events whose true rigidity lies outside the signal region, and vice versa.

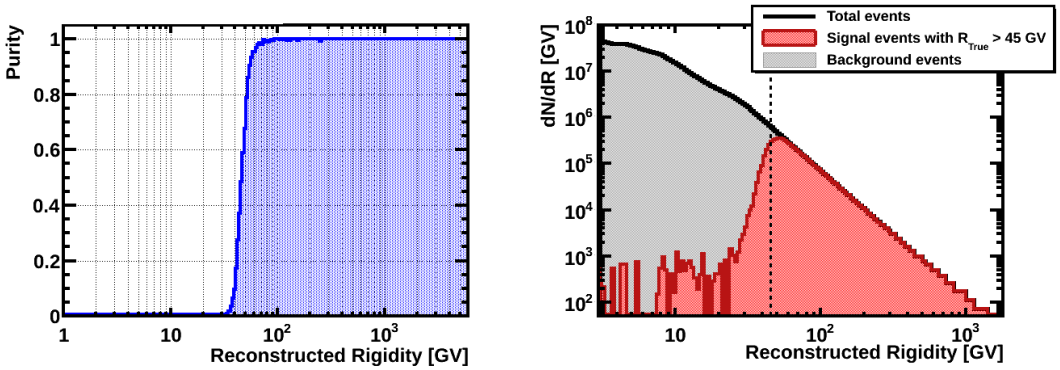

FIGURE 5.3: *(Left)* Purity of the full span proton sample for the range $R_{\text{True}} > 45$ GV, i.e., fraction of events whose true rigidity is in that range, as a function of the reconstructed rigidity. Due to the finite resolution of the tracker, non-negligible rigidity migrations in the low edge of the range take place and contribute to reduce the purity. Migrations of events inside the rigidity range does not have any impact in the purity. (*Right*) Distribution of signal and background events with $R_{\text{True}} > 45$ GV as a function of their reconstructed rigidity.

The purity of the proton sample is calculated for each rigidity range of the analysis according to (5.4) and the collection of all of them is shown in figure 5.4. Since the rigidity resolution worsens at high rigidities, the effect of rigidity migrations reducing the purity of the sample is more evident.

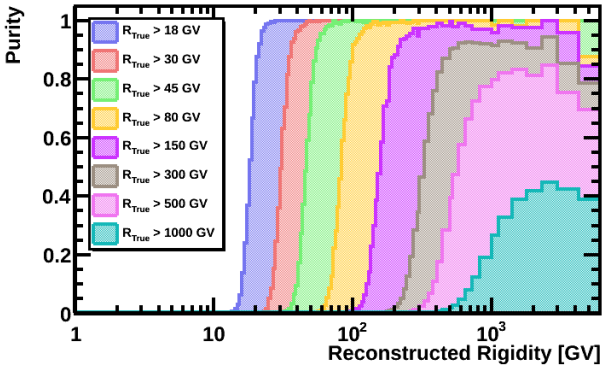

FIGURE 5.4: Purities of the full span proton sample for the different true rigidity ranges of the analysis. As the rigidity increases, migrations become more important and reduce the purity accordingly.

5.5 VALIDATION OF THE SAMPLE

The quality of the proton sample selected as well as the understanding of the efficiencies involved in the analysis is evaluated in terms of the time stability of the proton rate. Time variations of the raw rate, defined as the number of particles detected per unit of time, may be due to instrumental effects, i.e., efficiencies, and/or underlying physical phenomena, namely, solar modulation. At high enough rigidities, where the solar modulation does no longer affect, the rate should be time independent after variation of efficiencies are accounted. Thus, the time stability of the rates is investigated in two subranges: $18 - 30$ GV, where the solar modulation may affect; and $R > 30$ GV where its effect should be negligible.

The relative time variation of the raw rate in monthly intervals for protons in $18 < R < 30$ GV is presented in the figure 5.5. The time variation of the total efficiency[2] normalized to the average is also shown. The corrected rate, after including the variation of the total efficiency is displayed in figure 5.5-*bottom* and shows a decreasing trend up to December 2014 followed by an steady increase. This results is in agreement with measurements by PAMELA [218] and neutron monitors [219]. The observed time variation in the proton corrected rate is consistent with the solar activity during the period of data taking, in particular, with the polarity reversal of the heliospheric magnetic field (HMF), which took place between 2013 and 2014.

In addition, the relative time variation of the proton raw rate and the total efficiency is presented in figure 5.6-*top*. The corrected rate, in figure 5.6-*bottom* is not affected by the solar modulation and, therefore, is consistent with a constant value within a systematic uncertainty of 0.8%, which is smaller than the 2% of systematic uncertainty associated to the acceptance in the flux measurement [109].

2 The total efficiency is here defined as the product of the individual efficiencies participating in the analysis, which where described in section 5.2.3.

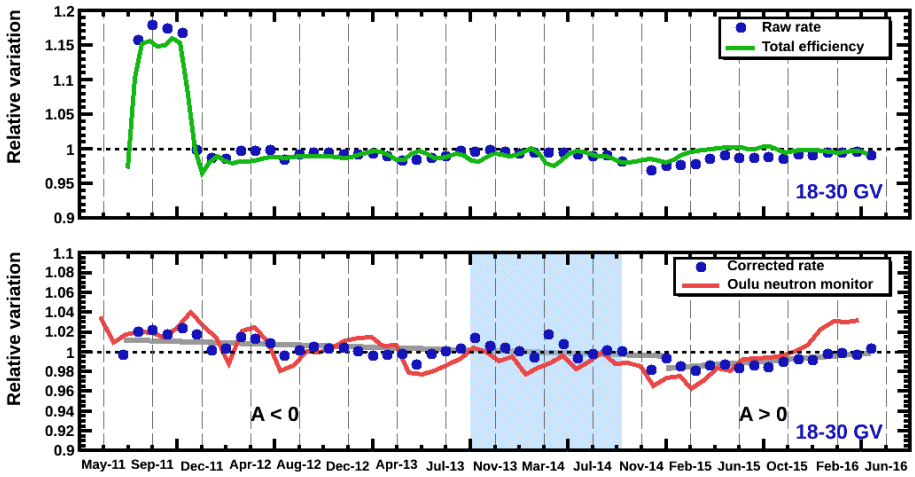

FIGURE 5.5: *(Top)* Time dependence of the normalized to the average proton raw rate blue dots) and total efficiency (green line) in monthly intervals for $18 < R < 30$ GV. The rise in the raw rate in Fall 2011 is due to a variation in the tracker reconstruction efficiency. *(Bottom)* Time dependence of the normalized corrected proton rate (blue dots) and Oulu neutron monitor count rate (solid line). A decreasing trend followed by and steady increase is consistent with the polarity reversal of the HMF (from the so called A < 0 polarity cycle 23 to the A > 0 polarity cycle 24). The blue shaded area corresponds to the period with no well-defined HMF polarity.

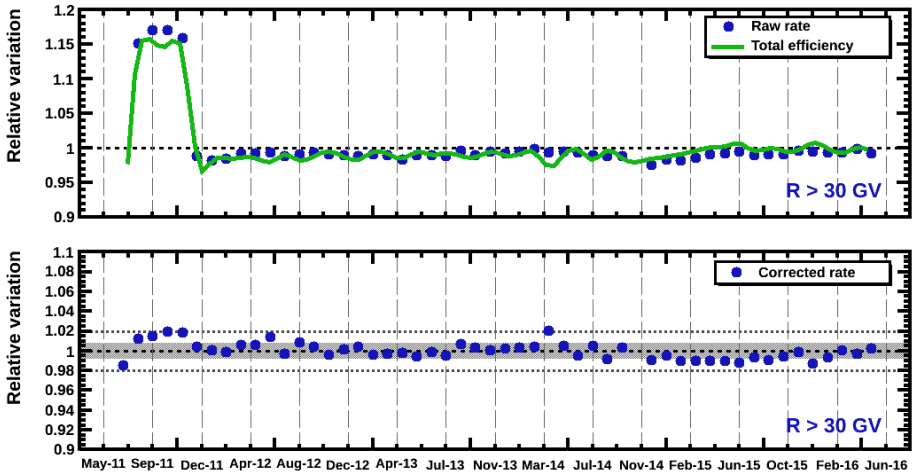

FIGURE 5.6: *(Top)* Time dependence of the normalized proton raw rate (blue dots) and total efficiency (green line) for rigidities $R > 30$ GV. *(Bottom)* Time variation of the normalized corrected proton rate (blue dots), where no trend due to solar modulation is observed. The time variation is consistent with a constant value within a systematic of 0.8%, smaller than the 2% uncertainty due to the determination of the acceptance.

5.6 PARAMETRIZATION OF THE PROTON EFFICIENCIES

The analysis of anisotropies may be affected by instrumental effects that may induce spurious signals in the coordinate system where the measurement is per-

formed. Although in our case the measurement is carried out in galactic coordinates, possible effects which are genuine in other coordinate systems may project and give rise to fake contributions in some multipole components.

The aim of this section is to develop a systematic study the origin of those contributions and quantify their effect in the analysis. In particular, two potential effects should be adressed:

1. *Geographical dependence of efficiencies*, whose latitudinal variation along the North-South axis is directly projected into all the dipole components in galactic coordinates according to the transformation matrix (figure 4.11-*left* in section 4.3.3.4), therefore, playing a major role in the measurement. The scheme used to quantify the correction that this dependence introduces in the analysis is based on a spherical harmonics parametrization of the efficiencies, as mentioned in section 3.4.1.2.
2. *Day-night cycles* may produce variations in the performances of some subdetectors which would introduce a bias in the measurement of certain reconstructed magnitudes, such as the energy or rigidity, without inducing a significant change in the efficiencies. This day-night variation in the measurement of the energy or rigidity naturally translates directly into an artificial dependence in the populations selected within a certain energy range, therefore, giving rise to a fake signal. This effect is genuinely studied in the ecliptic plane in the GSE reference frame and, although has no impact in the measurement of anisotropies in galactic coordinates, it may be interesting for other analyses. For this reason, the effect of day-night cycles is discussed in appendix B.

5.6.1 *One-dimensional study in geomagnetic colatitude*

The starting point to understand and characterize the positional dependence of the efficiencies is the analysis of them in terms of positional coordinates. The study of one-dimensional distributions, such as the dependence of the raw rate with the geomagnetic colatitude, provides valuable information about the behavior of the acquisition rate and efficiencies. In this regard, figure 5.7-*left* shows the raw rate normalized to the average as a function of the cosine of the geomagnetic colatitude from $\theta_{\rm M} = 0^\circ$ ($\cos\theta_{\rm M} = +1$), corresponding to the northern geomagnetic pole, to $\theta_{\rm M} = 180^\circ$ ($\cos\theta_{\rm M} = -1$), for the southern pole. The relative variation of the total efficiency is also shown. It is remarkable that the raw rate for rigidities $R > 18$ GV exhibits a drop of $\sim 6\%$ in the regions close to the poles with respect to the equator. This drop is consistent with an identical decrease of the efficency in the same regions, where the rates of low energy particles are higher due to a lower geomagnetic cutoff, therefore reducing the efficiency of some subdetectors.

As mentioned in 3.4.1.3, the positional variation of the efficiencies plays a major role in the measurement of the anisotropies. For this reason, in this one-dimensional approach, the variation of both raw rate and efficiency distributions in figure 5.7-*left* is parametrized in terms of the same function

$$f(\cos\theta_{\rm M}) = p_0 + p_1 \times \cos\theta_{\rm M} + p_2 \times (\cos\theta_{\rm M})^2, \tag{5.5}$$

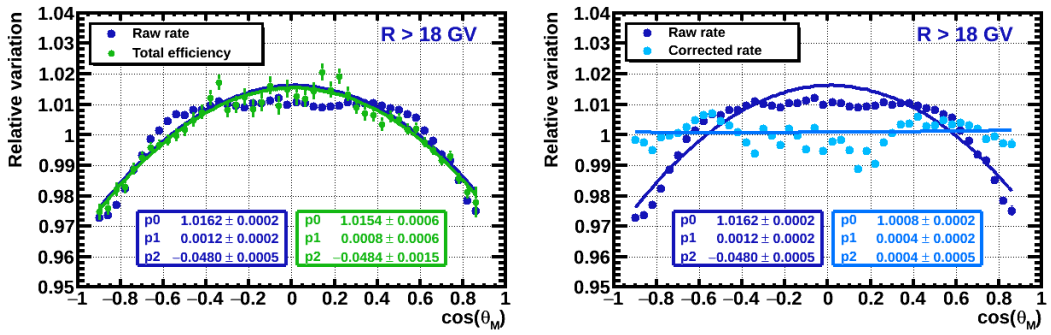

FIGURE 5.7: *(Left)* Dependence of the proton raw rate *(blue)* and total efficiency *(green)* with the geomagnetic colatitude for $R > 18$ GV, both normalized to their average. Both quantities are parametrized in terms of a quadratic polynomial in cosine of the geomagnetic colatitude *(solid lines)* and exhibit a consistent drop at high latitude regions. *(Right)* Variation of the raw rate (dark blue) and corrected rate (clear blue) with the geomagnetic colatitude. The parabolic fit of the corrected rate provides parameters consistent with a flat distribution.

where the parameter p_1 quantifies the North-South asymmetry and p_2 describes the symmetric drop of both magnitudes in the high magnetic latitudes. We shall remark that this one-dimensional function used to describe the rates fully agrees with the azimuthally symmetric terms of the spherical harmonic expansion up to $\ell = 2$, a_{1+0} and a_{2+0}, in ISS Magnetic Position coordinates, and the following identities hold when the distributions are normalized to the average

$$\begin{aligned} a_{1+0} &= \sqrt{\frac{4\pi}{3}} p_1, \\ a_{2+0} &= \frac{1}{3}\sqrt{\frac{16\pi}{5}} p_2 = \sqrt{\frac{16\pi}{5}}(1 - p_0), \end{aligned} \tag{5.6}$$

which justifies the election of this parametrization in cosine of geomagnetic colatitude.

On the other hand, the parameters from the fit to 5.5 of both raw rate and total efficiency provide quantitative information about their behavior, in particular, about the dipole and quadrupole component in positional coordinates. The agreement between the parabolic descriptions of both raw rate and efficiency is further confirmed by the consistency of the p_1 and p_2 parameters. As a consequence, the fit parameters of the corrected rate, shown in figure 5.7-*right*, are compatible with zero, which implies that the correction due to the efficiency will cancel the North-South components in positional coordinates when the spherical harmonic analysis is performed.

Furthermore, this simple one-dimensional scheme can be used to have a first look into the rigidity dependence of the variation of efficiencies. Figure 5.8-*left* shows the distribution of the layer 1 picking efficiency normalized to the average for $R > 18$ GV and $R > 80$ GV, both parameterized in terms (5.5). The ratio between the efficiency variation for those two rigidity ranges is presented in figure 5.8-*left* and evidences that the colatitudinal dependence of an efficiency may change with the rigidity. This conclusion is confirmed by the p_1 and p_2 parameters from the parabolic fit.

In particular, since p_2 accounts for the drop, it is sensitive to higher amplitudes and, therefore, higher variations with the rigidity.

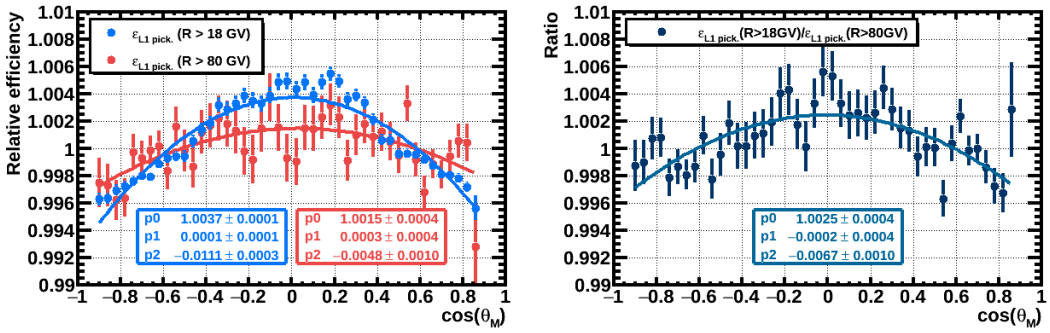

FIGURE 5.8: *(Left)* Geomagnetic colatitude dependence of proton layer 1 picking efficiency for rigidities $R > 18$ and $R > 80$ GV, both normalized to their average and parametrized by a quadratic polynomial.*(Right)* The shape of the colatitudinal dependence of the efficiency may vary with the rigidity. In particular, in this case, a more prononunced drop is observed in the range $R > 18$ GV, which is also evidenced by the ratio of the two distributions.

The one-dimensional study of the geographical dependence of efficiencies allows to have a first and clear picture of the problem, but it does not provide a complete information since the behavior along the azimuthal axis is missing. For this reason, a full description of the (θ, φ)-dependence is preferred.

5.6.2 *Spherical harmonic parametrization in ISS Geographical Position coordinates*

The one-dimensional study of the colatitudinal dependence of the proton rate and efficiencies can be extended to the most general case of skymap distributions, which are the ones relevant for the measurement of the anisotropy, in particular, the skymap of measured events and the exposure time skymap. Figure 5.9-*left* shows the distribution in the sky of protons with reconstructed rigidity $R > 18$ GV, $N(\theta, \varphi)$, in the ISS Geographical Position coordinate system. On the other hand, the distribution of the expected number of events according to only the exposure time, $\langle N(\theta, \varphi) \rangle$, for the same rigidity range is displayed in figure 5.9-*right*.

Although both skymaps are, apparently, similar at first glance, small discrepancies may exist and, for this reason, a statistical estimator is built to quantify the compatibility of the two distributions. In this case, a significance estimator is defined in each pixel i of the skymap as

$$S_i = \frac{N_i - \langle N \rangle_i}{\sqrt{\langle N \rangle_i}}, \tag{5.7}$$

in terms of the measured and expected number of events, N_i and $\langle N \rangle_i$, respectively. This allows the construction of significance skymaps that provide not only qualitative and visual information about the compatibility of data and reference, but also quantify in a model independent manner how well the reference map describes the

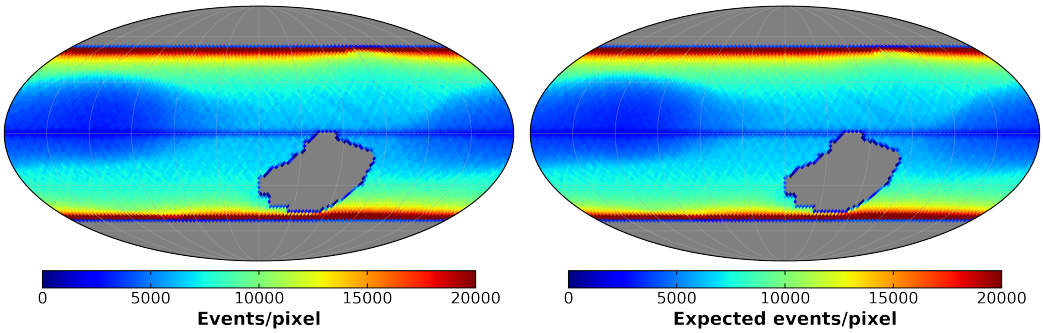

FIGURE 5.9: Skymap distribution of measured protons *(left)* and expected number of events from the exposure time *(right)* for rigidities $R > 18$ GV in ISS Geographical Position coordinates.

distribution of measured events. In this regard, figure 5.10 shows the significance map and significance distribution obtained from measured and expected events in figure 5.9. The significance map reveals clear structures corresponding to the regions close to the geomagnetic poles, which imply that the measured number of events is significantly smaller than the expectation from the exposure time. Consequently, the significance histogram shows a negative tail that makes the distribution wider and highly asymmetric. Furthermore, the comparison of measured and expected number of events provides a chi-square value[3] of $\chi^2/d.f. = 19698.7/9233$, which evidences that the reference does not describe the distribution of data. This result fully agrees with the one-dimensional study, where the observed decrease of the proton rate at high geomagnetic latitudes is well reproduced by the same behavior of efficiencies; if the reference map includes only exposure time and no efficiency correction is applied, data is not well reproduced and, therefore, a spurious signal will appear.

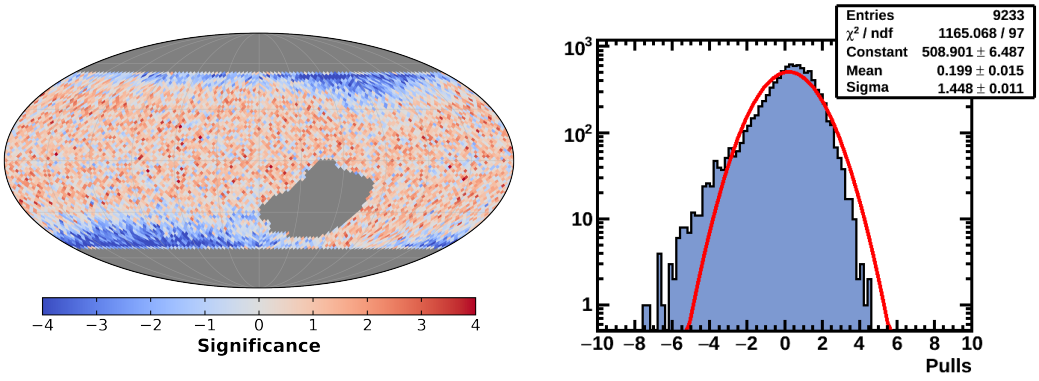

FIGURE 5.10: Significance skymap *(left)* and distribution *(right)* of the proton distribution with respect to the expectation from the exposure time for rigidities $R > 18$ GV in ISS Geographical Position coordinates.

3 The chi-square of the comparison of two skyamps is defined as $\chi^2 = \sum_i^{N_{\text{pix}}} S_i^2$, where S_i is the significance of each pixel skyamp as defined in (5.7).

Following the same approach used in the one-dimensional scheme, where both the rate and the efficiency were described in terms of the same function, the (θ, φ)-dependence of each efficiency is parametrized in terms of spherical harmonics.

As discussed in section 3.4.1.2, a relative anisotropy analysis of the samples of accepted and rejected events, N_{ok} and N_{ko} respectively, for each efficiency cut provides the multipole components $\eta_{\ell m}$ needed for the spherical harmonic parametrization of the efficiency in each cumulative rigidity range. Thus, since the correction, $\Delta^i_{\ell m}$, that an efficiency introduces is, according to (3.28)

$$\Delta^i_{\ell m} = \frac{\eta^i_0}{1+\eta^i_0}\eta^i_{\ell m} \text{ , where } \eta^i_0 = \frac{N^i_{\text{ko}}}{N^i_{\text{ok}}}, \tag{5.8}$$

the associated uncertainty is given by the statistics involved in the computation of the efficiency amplified by the factor associated to the inefficiency of the sample. Therefore, the total efficiency correction will be the sum of the individual efficiency corrections

$$\Delta_{\ell m} = \sum_i^{N_{\text{effs}}} \Delta^i_{\ell m}. \tag{5.9}$$

The error in the total efficiency correction is, consequently, affected by the errors of the individual ones. In particular, in order to optimize the error in the total efficiency correction, two questions are addressed

- At high rigidities, where the statistics is low, the dispersion in the values of the correction may be high. For this reason, a parametrization of the rigidity dependence of the correction that each efficiency introduces is used.
- Due to statistical fluctuations, it is possible to obtain corrections which are consistent with zero but, consequently, introduce an uncertainty in the analysis. Therefore, a procedure to determine whether a correction is significant in a given multipole component is needed.

5.6.2.1 *Rigidity dependence of the efficiency corrections*

As pointed out in the one-dimensional study, the $(\theta, \varphi)-$dependence of an efficiency correction may depend on the rigidity. In order to minimize the error of the efficiency correction at high rigidities, where the statistics is low, and with the aim of having a smooth description of the rigidity behavior of the correction in each component, a polynomial parametrization of the corrections as a function of the minimum rigidity of each range is used. From the one-dimensional scheme of figure 5.8, it can be seen that the quadratic terms, which model the symmetric drop at high latitudes, are more sensitive to rigidity variations and high amplitudes than the linear ones. For these reasons, the rigidity dependence of the corrections for each efficiency is described in terms of

$$g(R_{\text{min}}) = \begin{cases} m_0 + m_1 \times \log(R_{\text{min}}) & \text{for } \ell = 1 \\ m_0 + m_1 \times \log(R_{\text{min}}) + m_2 \times (\log(R_{\text{min}}))^2 & \text{for } \ell = 2 \end{cases} \tag{5.10}$$

Figure 5.11 shows the results of the corrections Δ_{NS} and Δ_{2+0}, related to the North-South axis in geographical coordinates, of the layer 1 picking efficiency, obtained from the relative analysis of samples N_{ok} and N_{ko} in each rigidity range. A linear and parabolic parametrization in terms of the logarithm of the minimum rigidity, according to (5.10), describes the rigidity dependence of the corrections. This is repetead for each component and each efficiency.

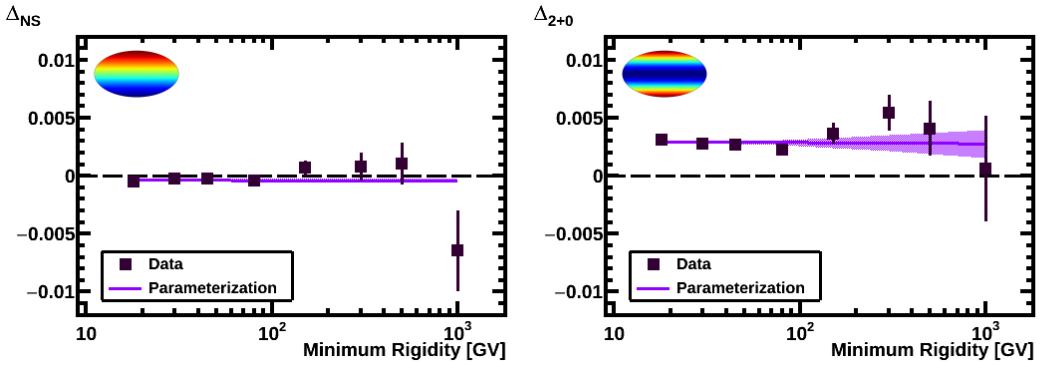

FIGURE 5.11: Results of the corrections Δ_{NS} *(left)* and Δ_{2+0} *(right)* for the proton L1 picking efficiency as a function of the minimum rigidity. The square dots show the results obtained directly from the relative analysis of the N_{ko} and N_{ok} samples in cumulative rigidity ranges, and the line corresponds to the parametrization of the rigidity dependence of the correction in terms of (5.10).

5.6.2.2 *Determination of significant efficiency corrections*

The relative analysis of the samples N_{ok} and N_{ko} for each efficiency and rigidity range may provide corrections compatible with statistical fluctuations in some multipole components. Since the error associated to the individual efficiency corrections propagates to the total one, in order to optimize the total error only significant contributions should be included. A procedure to reject non-significant corrections has been established and can be summarized in the following steps:

1. The distribution of pulls, obtained as the ratio $\Delta^i_{\ell m}/\sigma(\Delta^i_{\ell m})$ for each energy, component and efficiency, is drawn (figure 5.12). According to this, corrections compatible with statistical fluctuations will be grouped in a central core consistent with a normal distribution, whereas the tails correspond to the significant corrections.
2. This pull distribution allows to establish a cut value or threshold to reject non-significant corrections. To retrieve this threshold, a fit to a Gaussian is performed in the interval $[-x, +x]$. A scan in the mean and the sigma of the fit as a function of x provides the optimum cut value such that the Gaussian is centered around zero and width equal to one. (figure 5.13). In this manner, this threshold value ensures that the corrections with pull below it are consistent with statistical fluctuations, i.e., follow a normal distribution.
3. Those efficiencies that are tagged as significant at the lowest rigidity range, are also introduced at higher rigidities. The correction introduced is given by the polynomial description of the rigidity dependence (5.10).

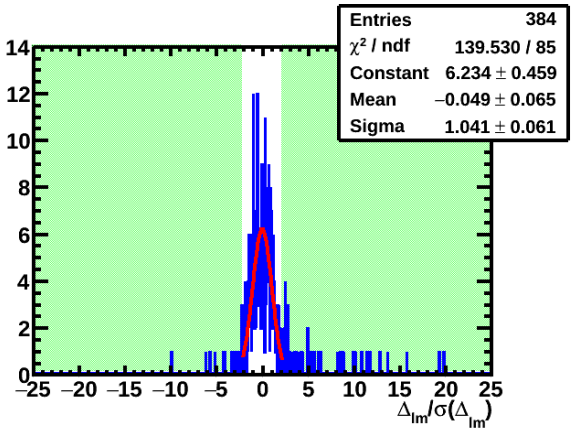

FIGURE 5.12: Distribution of efficiency correction pulls for each rigidity range (8), dipole and quadrupole components (8) and efficiencies (6) in ISS Geographical Position coordinates. The efficiency corrections whose pull is above a certain threshold in absolute value (in the green colored area) are tagged as significant. Efficiency corrections inside the threshold value are consistent with statistical fluctuations and, therefore, well described by a normal distribution.

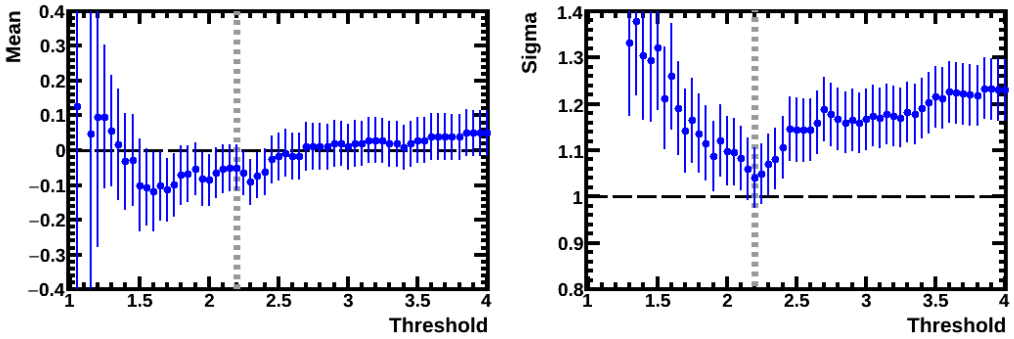

FIGURE 5.13: Scan in the mean *(left)* and sigma *(right)* parameters of the fit to a Gaussian function of the pulls distribution in figure 5.12 as a function of the threshold value. The optimum value of a threshold, which corresponds to mean ~ 0 and sigma ~ 1, ensures that the efficiency corrections with pull below that value are well described by a Gaussian distribution and, therefore, consistent with statistical fluctuations.

The summary plot in figure 5.14-*top* shows the dipole and quadrupole components for each efficiency, for rigidities $R > 18$ GV. Efficiency corrections consistent with statistical fluctuations are set to zero according to the aforementioned procedure. As can be seen, only few components are significant and, therefore, yield a contribution to the anisotropy analysis, mostly related to the azimuthally symmetric components. In the bottom panel the total efficiency correction, i.e. the sum of the individual corrections, is shown. In particular, efficiency corrections affect mainly the North-South direction, represented by the Δ_{NS} and Δ_{2+0} components, with an additional contribution in the Δ_{2-1} direction due to the asymmetry of the Northern and Southern geomagnetic poles in ISS Geographical Position coordinates. Furthermore, the main contribution to the total efficiency correction arises from the proton trigger efficiency. In the regions close to the magnetic poles, the

high rate of low energetic particles causes accidental hits in the ACC veto, which reduce the proton trigger efficiency.

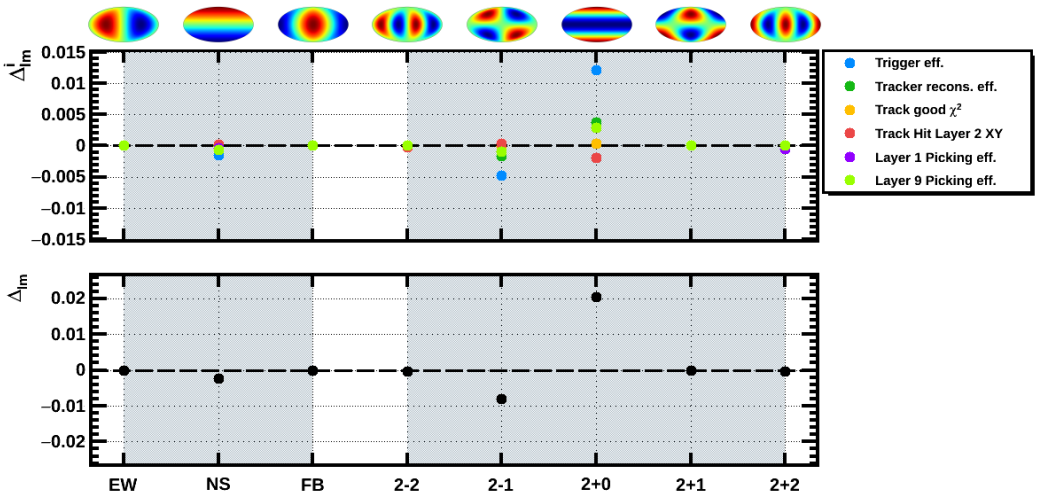

FIGURE 5.14: Individual *(top)* and total *(bottom)* proton efficiency correction for $R > 18$ GV in ISS Geographical Position coordinates, where the main directions affected are those corresponding to the North-South direction. Due to its dependence with the geomagnetic latitude, proton trigger efficiency is the most important contribution to the final correction.

The aforementioned procedure is used to calculate the spherical harmonic parametrization of each efficiency and, finally, the total efficiency is produced as the product of the individual ones, where only the significant components are included. As an example, figure 5.15 shows the parametrization of the proton layer 1 picking efficiency and the total efficiency up to $\ell = 2$ for rigidities $R > 18$ GV. In both cases, a geographical dependence is observed due to the decrease of the efficiency at high magnetic latitudes, which is consistent with the colatitudinal study presented figure 5.7. Furthermore, this dependence is found to be similar to the structures observed in the significance skymap in figure 5.10, which shows how that variations of a few percent in the total efficiency inside the ISS orbit may induce huge deviations from isotropy if they are not included in the reference map.

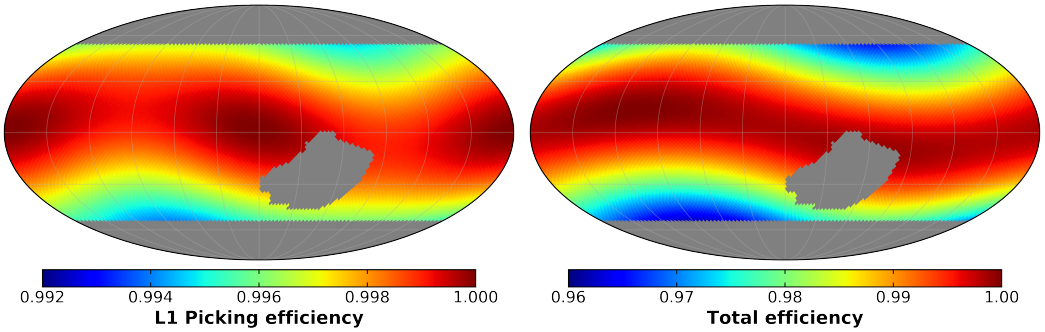

FIGURE 5.15: ISS Geographical Position skymap of the spherical harmonic parametrization of the proton layer 1 picking efficiency *(left)* and the proton total efficiency *(right)* up to $\ell = 2$, where only the significant components are included.

5.6.2.3 *Corrected exposure time maps*

Finally, the parametrization of the total efficiency is applied to correct the exposure time maps and produce the corrected exposure maps, which constitute the reference for absolute anisotropies. The improvement introduced by the efficiency correction in the reference can be quantified by means of the significance skymap and histogram in figure 5.16. The strong deviations in the skymap that were observed initially are now removed and, although some residual patterns corresponding to higher multipoles are visible, their impact in the description is minor. This is confirmed by the significance histogram, where now the negative tails are removed and the distribution is symmetric and well described by a normal one. In addition, now a chi-square value of $\chi^2/d.f. = 11031/9233$ quantifies the improvement in the description of the data distribution in the skymap in ISS Geographical Position coordinates. The noticeable improvement indicates that the strong suppression of the spurious structures arises from the introduction of corrections up to $\ell = 2$. Further multipoles would introduce minor improvements in the description, which would not affect the measurement of the dipole anisotropy.

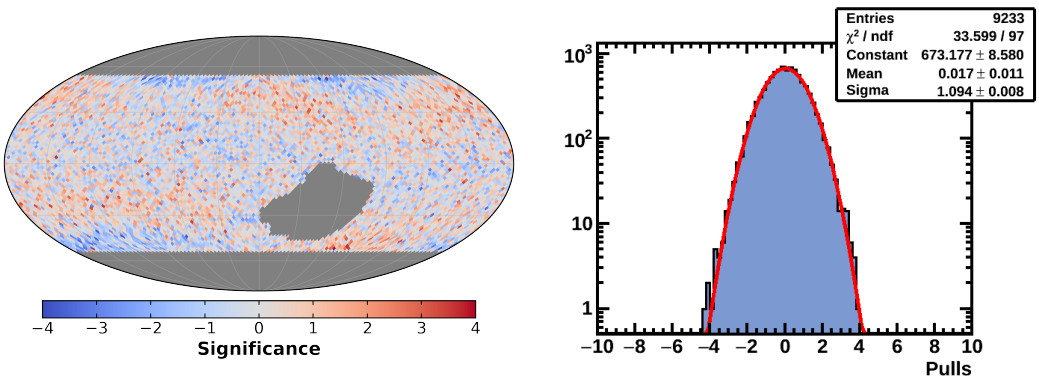

FIGURE 5.16: Significance skymap *(left)* and distribution *(right)* of the proton distribution with respect to the expectation from the corrected exposure for rigidities $R > 18$ GV in ISS Geographical Position coordinates.

5.6.3 *Spherical harmonic parametrization in Galactic coordinates*

Once the effect of efficiencies and efficiency corrections is understood in the intrinsic reference frame, where their contribution is enhanced, an identical procedure can be applied in the coordinate system of the analysis. Following the same approach, the skymap distributions of measured and expected number of protons in galactic coordinates for $R > 18$ GV are presented in figure 5.17.

From these two distributions, we compute the significance skymap and significance distribution in figure 5.18. From the significance skymap, two regions of negative significance are clearly recognized to be the projection of the high geomagnetic latitudes into galactic coordinate system. Contrary to ISS geographical position, where the effect of efficiencies is focused mainly in the North-South direction, in galactic coordinates the contribution is partially diluted over the skymap.

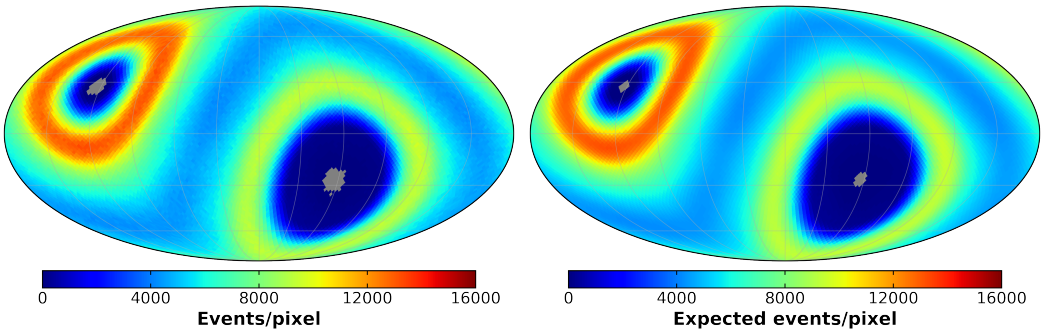

FIGURE 5.17: Skymap distribution of measured protons *(left)* and expected number of events from the exposure time *(right)* for rigidities $R > 18$ GV in galactic coordinates.

Consequently, we still observe structures associated to the negative deviations, but they are less significant than in the case of the geographical position of ISS. This conclusion is also reflected in the significance histogram, where the negative tail that was clearly visible iin ISS Geographical Position is not visible and the distribution is symmetric in this case. However, the fit to a Gaussian provides a value of $\sigma \sim 1.2$, which reveals that the deviations are not consistent with statistical fluctuations. In addition, a chi-square of $\chi^2/d.f. = 17528.9/12215$ further supports the conclusion that the reference does not reproduce the data skymap and efficiency corrections are needed.

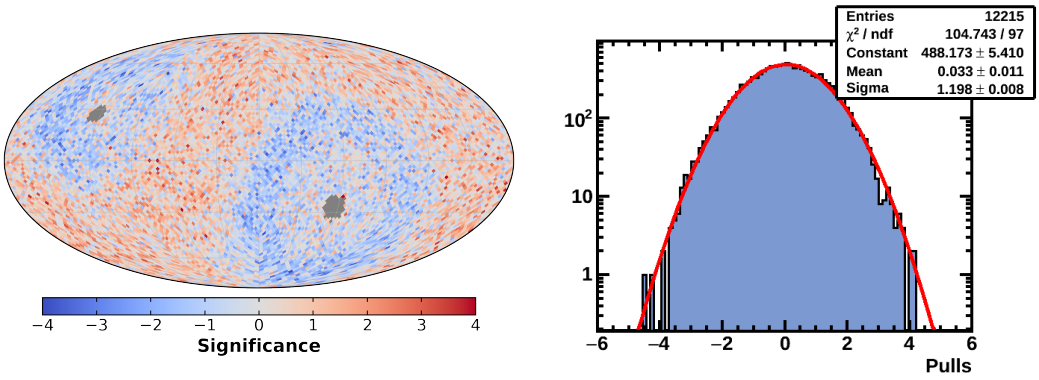

FIGURE 5.18: Significance skymap *(left)* and distribution *(right)* of the proton distribution with respect to the expectation from the exposure time for rigidities $R > 18$ GV in galactic coordinates.

The spherical harmonic parametrization of efficiencies in the galactic coordinate system starts with the relative analysis of the skymaps of samples N_{ok} and N_{ko} in the cumulative rigidity ranges for each efficiency. Linear and parabolic parametrizations of the rigidity dependence of the efficiency correction according to (5.10) is also used. The identification of significant corrections is carried out by means of the same method, based on the distribution of pulls (figure 5.19) and the estimation of the threshold value that reject contributions consistent with statistical fluctuations (figure 5.20).

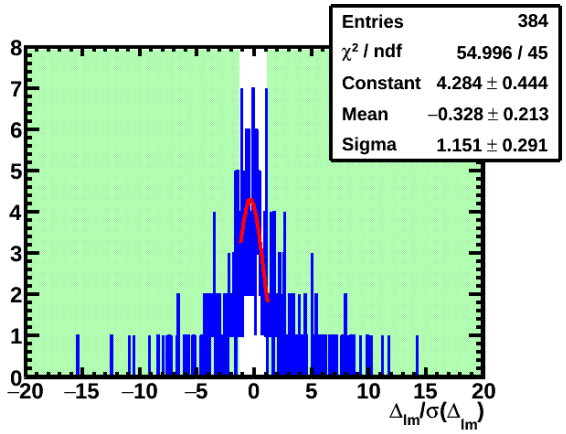

FIGURE 5.19: *(Left)* Distribution of efficiency correction pulls for each rigidity range (8), dipole and quadrupole components (8) and efficiencies (6) in galactic coordinates. Efficiency corrections whose pull is above a certain threshold in absolute value (in the green colored area) are tagged as significant. Efficiency corrections inside the threshold value are consistent with statistical fluctuations and, therefore, well described by a Gaussian distribution.

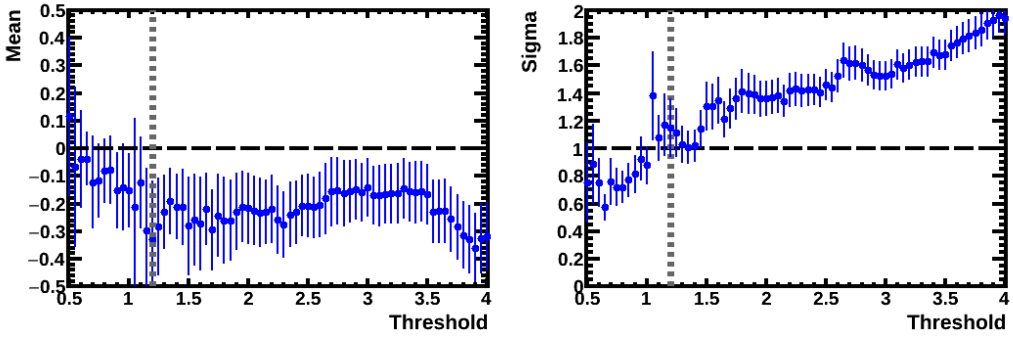

FIGURE 5.20: Scan in the mean *(left)* and sigma *(right)* parameters of the fit to a Gaussian function of the pulls distribution in figure 5.19 as a function of the threshold value. The optimum value of a threshold, which corresponds to mean ~ 0 and sigma ~ 1, ensures that the efficiency corrections with pull below that value are well described by a Gaussian distribution and, therefore, consistent with statistical fluctuations.

Contrary to ISS Geographical Position, where only few components have a contribution to the analysis, figures 5.12-*left* and *right* point out that most components in galactic coordinates are significant. This is, again, related to the fact that the North-South direction in ISS Geographical Position is projected into all directions in galactic coordinates. The summary plot in figure 5.21 for the individual and total efficiency correction for $R > 18$ GV also supports this conclusion.

Figure 5.22 shows the parametrization of the proton layer 1 picking efficiency and the total efficiency up to $\ell = 2$ for rigidities $R > 18$ GV in galactic coordinates. Again, the observed galactic (θ, φ)-dependence of the total efficiency has the same structure as the significance skymap (figure 5.17), therefore, explaining the deviations found between data and reference. In particular, this conclusion is clear from the significance skymap and significance distribution obtained after the efficiency

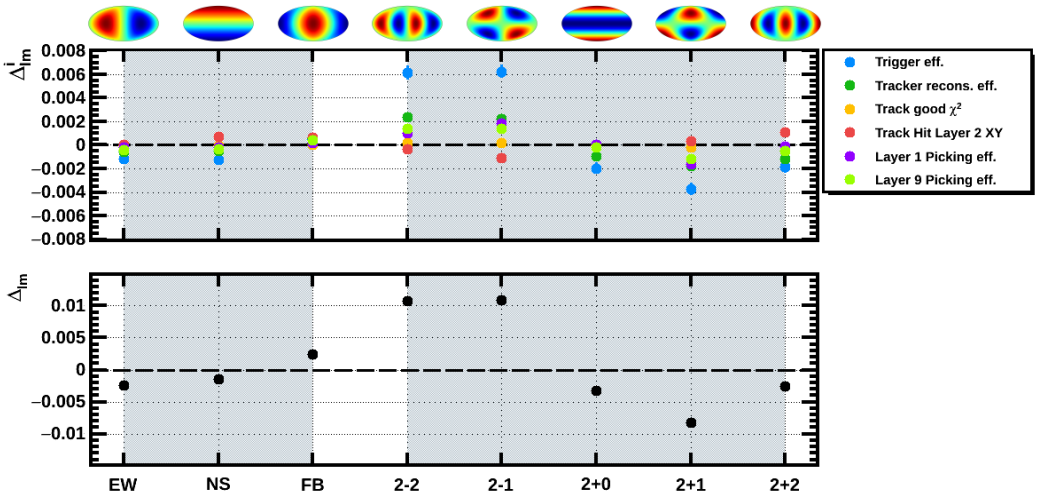

FIGURE 5.21: Individual *(top)* and total *(bottom)* proton efficiency correction for $R > 18$ GV in galactic coordinates. The fact that each direction is affected by efficiency corrections is the consequence of the projection of the geomagnetic North-South axis into galactic coordinates. Again, the most important contribution to the final correction is due to the proton trigger efficiency.

correction is introduced. In figure 5.23, the significance skymap shows no structures or patterns, and the distribution is now consistent with a normal one. The value of the chi-square from the comparison of measured and expected number of events per pixel is now $\chi^2/d.f. = 12431.6/12215$, which further evidences the improvement that the efficiency correction introduces in the description of data.

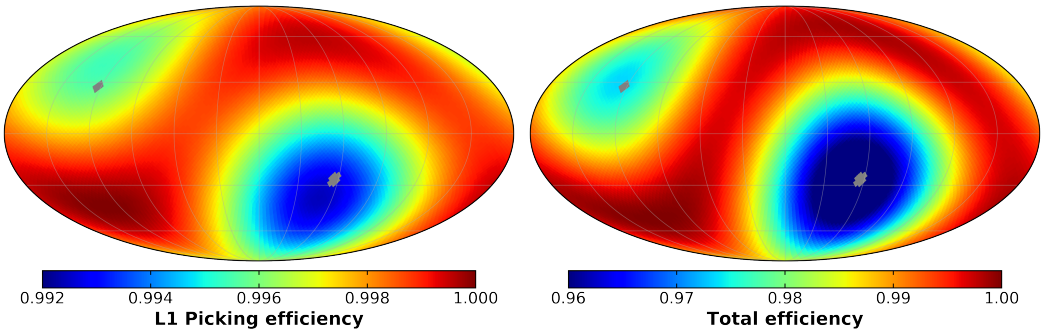

FIGURE 5.22: Galactic skymap of the spherical harmonic parametrization of the proton layer 1 picking efficiency *(left)* and the proton total efficiency *(right)* up to $\ell = 2$, where only the significant components are included.

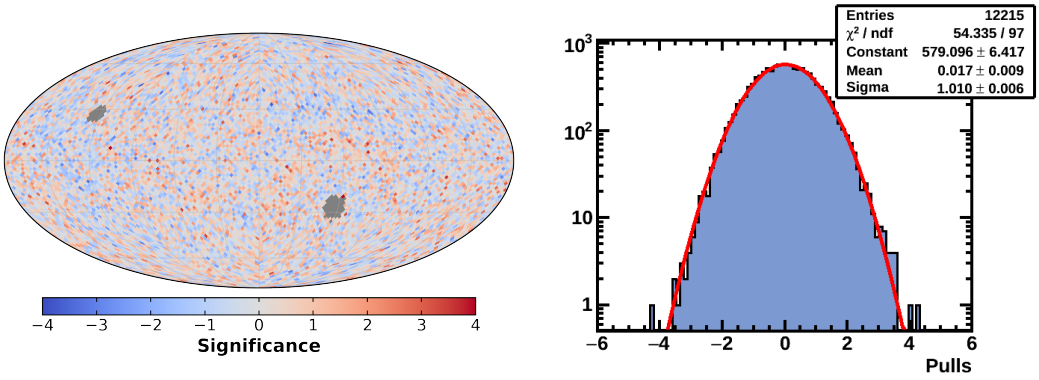

FIGURE 5.23: Significance skymap *(left)* and distribution *(right)* of the proton distribution with respect to the expectation from the corrected exposure for rigidities $R > 18$ GV in galactic coordinates.

5.7 RESULTS ON THE PROTON DIPOLE ANISOTROPY

5.7.1 *Impact of efficiency corrections in the multipole components*

The improvement of the description of the data skymaps due to the introduction of the efficiency corrections in the reference is also reflected in the measured multipole components. The analysis of anisotropies in the cumulative rigidity ranges is performed using corrected and non corrected exposure maps in order to compare the effect of the correction in the multipole components.

In the ISS Geographical Position coordinate system, the quadrupole components are sensitive to high amplitude effects associated to the geomagnetic latitude due to its even symmetry, therefore, their study provides a cross-check of the method and a potential hint of residual corrections not taken into account. For this reason, the two dipole and quadrupole components associated to the North-South direction in this coordinate system, ρ_{NS} and ρ_{2+0}, are shown in figure 5.24. The results of the components in the cumulative energy ranges obtained with a non-corrected reference show strong deviations from isotropy, which are especially noticeable in the quadrupole component, as stated previously. In addition, the value of the efficiency correction in each case, Δ_{NS} and Δ_{2+0} is also presented in the figure as well as its corresponding uncertainty, which is the result of the propagation of the uncertainties of individual efficiency corrections. The efficiency correction reproduces the observed results without correction, so that the corrected multipole components, which satisfy that $\rho_{\ell m} \approx \rho_{\ell m}^{\text{no corr}} + \Delta_{\ell m}$, are consistent with isotropy within the statistical and efficiency correction errors. The deviations with respect to the isotropy hypothesis are quantified in standard deviations in the bottom panels of figure 5.24.

The goodness of the description of data in galactic coordinates also translates into the dipole and quadrupole components. Figure 5.25 shows the components ρ_{EW} and $\rho_{2\text{-}2}$, which inherit part of the effects associated to the North-South direction in ISS Geographical Position coordinates. As in that case, strong deviations appear if the efficiency correction is not included, which are removed when it is introduced

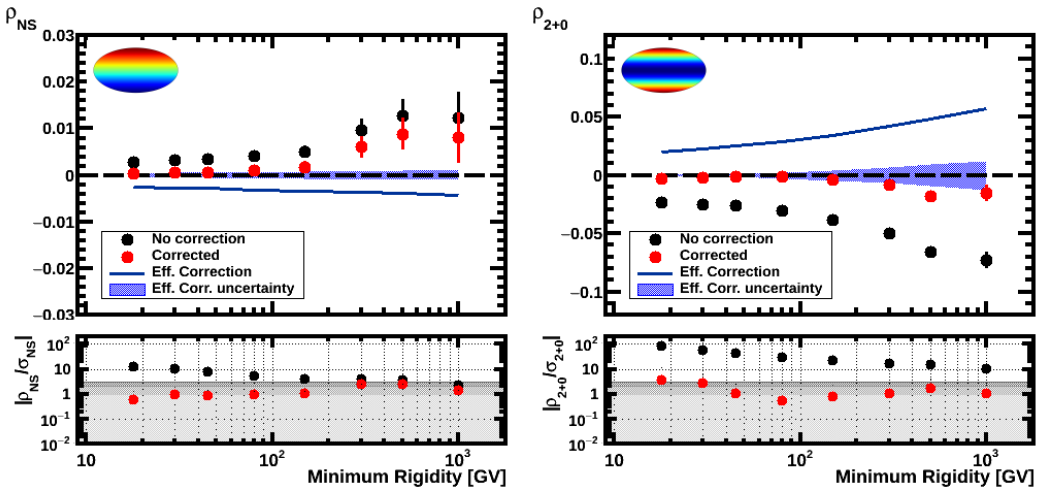

FIGURE 5.24: Components associated to the North-South directions in ISS Geographical Position, ρ_{NS} *(left)* and ρ_{2+0} *(right)* without efficiency correction (black dots) and including the efficiency correction in the reference map (red dots). The error bars on the dots stand for the statistical uncertainty on the component. The value of the efficiency correction is displayed as a solid blue line and the blue band corresponds to its uncertainty, obtained as the propagation of the uncertainties of the individual efficiency corrections. Deviations from isotropy of the measured values are quantified in terms of standard deviations in the bottom panels. The introduction of the efficiency correction is able to cure the strong deviations observed, and the corrected values are, therefore, consistent with isotropy within the statistical and efficiency correction uncertainties.

in the exposure maps. Corrected results are consistent with isotropy within the statistical and the efficiency correction errors.

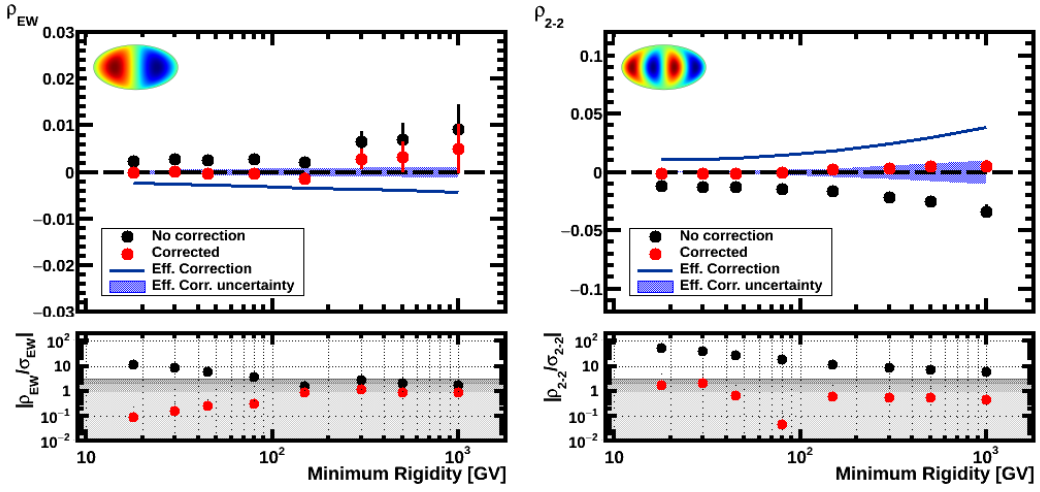

FIGURE 5.25: Proton multipole components ρ_{EW} *(left)* and ρ_{2-2} *(right)* in galactic coordinates without efficiency correction (black dots) and including the efficiency correction in the reference map (red dots). The efficiency correction (solid blue line) explains the deviations observed and the corrected results are, consequently, consistent with isotropy within the statistical (error bars on dots) and efficiency correction uncertainties (solid blue band).

5.7.2 *Uncertainty on dipole components*

5.7.2.1 *Systematic uncertainty due to efficiency corrections*

The efficiency correction applied in the construction of the exposure maps introduces a systematic uncertainty that has to be quantified. In particular, two sources of errors are considered:

- The uncertainty of the total correction, which is the result of the propagation of the uncertainties of the individual efficiency contributions determined to be significant. Since the individual efficiency corrections are ultimately determined by means of a relative analysis of anisotropies of the two N_{ok} and N_{ko} samples, it has a statistical origin. Therefore, the uncertainty of the total efficiency correction is expected to decrease as the sample of analysis increases.
- The uncertainty associated to the choice of significant corrections. The threshold value used to reject non-significant corrections is determined by a scan method in the sigma and mean parameters from a Gaussian fit of the pulls distribution (figures 5.12 and 5.19). This procedure yields an optimum value of the threshold, but alternative values around this one could be used. In particular, in galactic coordinates, where the threshold was found to be 1.2, the impact of an alternative choice in the threshold value is estimated by computing the total efficiency obtained when the threshold is displaced by a symmetric amount ± 0.2 around the used cut value. This value arises from the scan in the mean and sigma parameters as function of the threshold in figure 5.20. Values higher than 1.4 lead to pull distributions non compatible with a normal one, which means that their contribution must be included in the total efficiency correction.

  In this regard, figure 5.26 shows the total efficiency correction in the two opposite cases and the difference between them is taken as a systematic uncertainty. The variation of ± 0.2 around the threshold value does not modify the number of significant efficiency corrections: all efficiency corrections in all three dipole components are significant within that range.

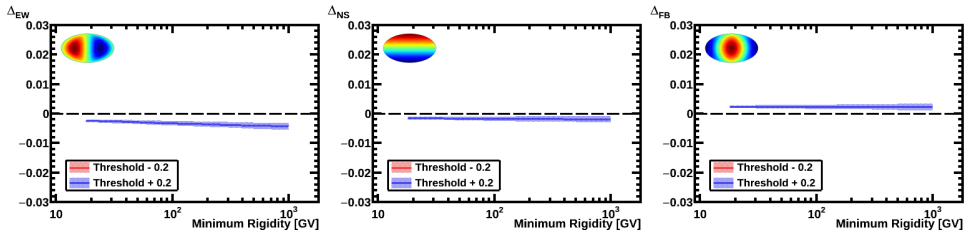

FIGURE 5.26: East-West *(left)*, North-South *(center)* and Forward-Backward *(right)* components of the total efficiency correction obtained after applying a shift of -0.2 (red) or $+0.2$ (blue) to the threshold value in figure 5.20 used to reject non-significant efficiency correction in galactic coordinates. The difference is taken as a systematic due to the variation in the election of the threshold value. In this case, variations of the threshold value in a range of ± 0.2 do not modify the total efficiency correction.

Since the sources of the systematic uncertainty do not affect the three dipole components equally, the *equivalent uncertainty*, σ_{eq}, is defined to quantify both contributions,

$$\sigma_{\text{eq}}^2 = \frac{1}{3}\sum_{k=1}^{3}\sigma_k^2, \tag{5.11}$$

where σ_k is the uncertainty in the dipole component $k = 1, 2, 3$. The total systematic uncertainty is shown in figure 5.27, where the two contributions from efficiency correction and efficiency election are also plotted. The systematic uncertainty is therefore dominated by the efficiency correction uncertainty, with no influence of the election of significant efficiencies.

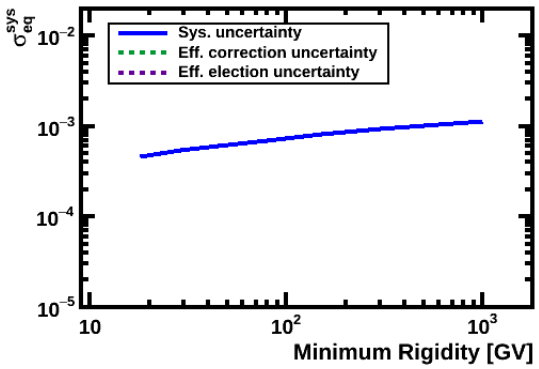

FIGURE 5.27: Contributions to the systematic uncertainty (blue solid line) from the efficiency correction uncertainty (green dotted line) and efficiency election uncertainty (purple dotted line). The systematic uncertainty is dominated by the efficiency correction one, without any contribution from the variation due to the election of significant corrections.

5.7.2.2 *Statistical uncertainty and background contamination*

The uncertainty in the determination of the dipole components is, according to (3.12), inversely proportional to the square root of the sample size, N, which constitutes the statistical uncertainty. However, the presence of background in the proton sample due to rigidity migrations contributes to worsen the statistical power of the sample, therefore, increasing the statistical uncertainty as stated in (3.55).

The computation of the dipole components in cumulative rigidity ranges takes into account the purity of the proton sample at the different reconstructed rigidities from figure 5.4. The effect of the purity due to rigidity migrations can be quantified from the comparison of the statistical uncertainties obtained when the sample is assumed to be pure and when the purity is included in the analysis. Figure 5.28-*left* shows the absolute value of the statistical uncertainty in each case, whereas the ratio of $\sigma_{\text{stat}}^{\text{bkg}}/\sigma_{\text{stat}}$ is displayed in 5.28-*right*. In particular, the degradation in the sensitivity at high rigidities is a consequence of the worsening of the rigidity resolution. As the rigidity approaches the MDR, rigidity migrations are more important, therefore, having a strong impact in the purity of the sample.

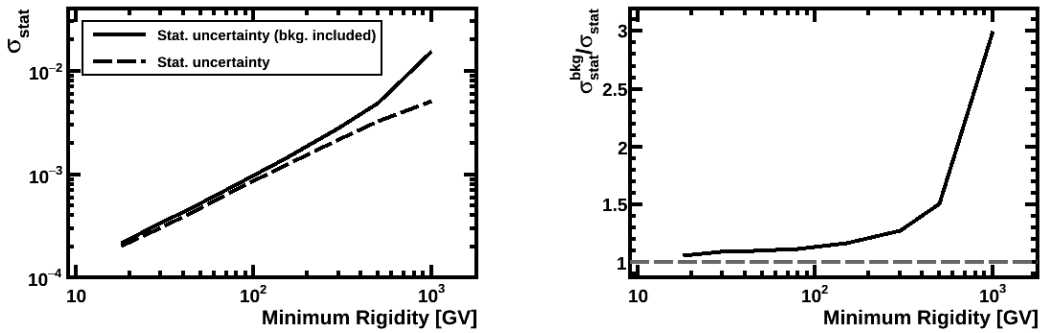

FIGURE 5.28: *(Left)* Absolute values of the statistical uncertainty for the proton sample when the sample is assumed to be pure (dashed line) and in the presence of background due to proton rigidity migrations (solid line). *(Right)* Ratio of the statistical uncertainties in the two cases, which quantifies the worsening in the uncertainty due to the background contamination in the proton sample.

On the other hand, it is possible to calculate the *equivalent sample size* that would give rise to a statistical uncertainty $\sigma_{\text{stat}}^{\text{bkg}}$ (figure 5.29). The effect of the background contamination can be regarded as a reduction of the effective number of events in the analysis. The numerical values of the measured and equivalent samples as well as the ratio of statistical uncertainties are presented in the table 5.4. The comparison between this ratio and the expectation from the purity of the sample given by (3.55) is also shown.

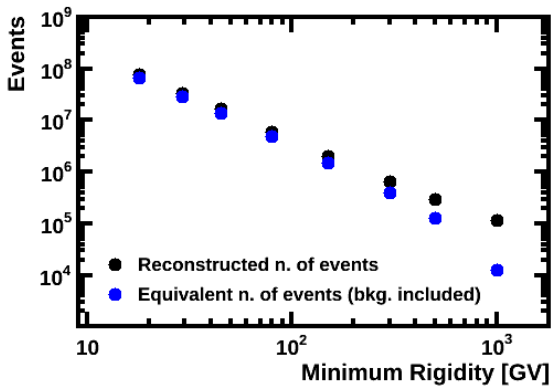

FIGURE 5.29: Comparison between measured number of events and equivalent sample size

5.7.2.3 *Total uncertainty on the dipole components*

Finally, the total uncertainty on the dipole components is the combination of the statistical and systematic uncertainties, $\sigma_{\text{tot}}(\rho_i) = \sigma_{\text{stat}}^{\text{bkg}}(\rho_i) \oplus \sigma_{\text{sys}}(\rho_i)$, which are displayed on figure 5.30-*left*. In addition, the ratio of the systematic and total uncertainties with respect to the statistical error is shown in figure 5.30-*right*. From the two figures, we conclude that the main contribution to the total uncertainty arises from

TABLE 5.4: Effect of the contamination in the proton sample. For each cumulative rigidity range, the measured and equivalent number of protons, the second moment of the purity distribution and the ratio of statistical errors are presented. The expected value of the ratio, calculated from (3.55) is also written.

R_{min} (GV)	Meas. sample $(\times 10^6)$	Eq. sample $(\times 10^6)$	$\langle p^2 \rangle$ (%)	$\sigma^{bkg}_{stat}/\sigma_{stat}$	Expected
18	75.85	67.42	88.89	1.06	1.06
30	34.00	28.42	83.6	1.09	1.09
45	16.58	13.63	82.21	1.10	1.10
80	6.00	4.75	79.21	1.12	1.12
150	1.97	1.44	73.16	1.17	1.17
300	0.57	0.35	61.82	1.27	1.27
500	0.22	0.10	44.90	1.49	1.49
1000	0.05	0.005	11.10	3.00	3.00

the systematic one at low rigidities, whereas for $R_{min} \gtrsim 80$ GV the measurement is no longer dominated by systematics.

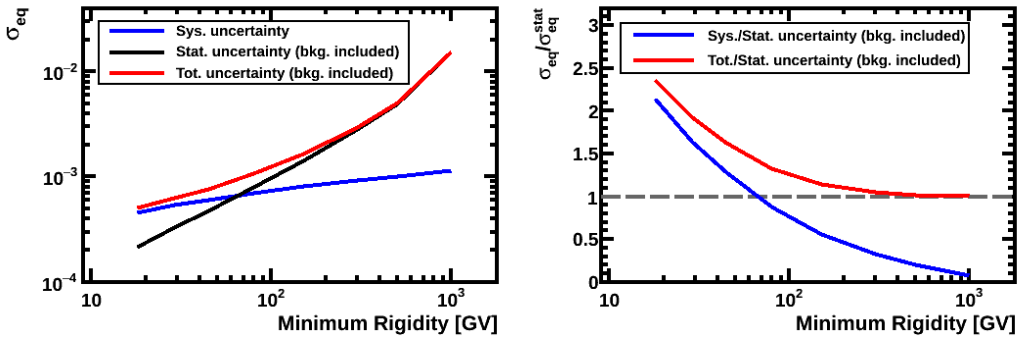

FIGURE 5.30: *(Left)* Statistical, systematic and total equivalent uncertainty of the dipole components. *(Right)* Ratio of the total and systematic equivalent uncertainties with respect to the statistical one. Statistical uncertainty includes the background contamination due to proton rigidity migrations.

5.7.3 *Results*

The results of the three dipole components of the proton absolute anisotropy in galactic coordinates are shown in figure 5.31. The values are obtained with the binned-likelihood fit (3.5.1) using as reference the corrected exposure map and taking into account the purity of the sample due to rigidity migrations. The bands corresponding to the 1 and 2−sigma deviation are also displayed and no signifi-

cant deviation is observed. Therefore, the results are consistent with the isotropy hypothesis for all rigidity ranges and dipole components within the statistics and systematic uncertainties.

The measured values of the dipole components allow to obtain the measured dipole amplitude for the different rigidity ranges (figure 5.32-*left*), which is found to be consistent with the expectation from isotropy within the statistical and systematic uncertainties. In particular, the measured value for the lowest rigidity range is $\delta_{\mathrm{M}}(18\,\mathrm{GV}) = 1.02 \times 10^{-3}$, which means that the technique developed in the construction of the reference maps allows to explore dipole anisotropies with a precision at the 10^{-3} level.

On the other hand, the compatibility with the isotropic case allows to quote a 95% C.I. upper limit for each rigidity range (figure 5.32-*right*). In the lowest rigidity range, the upper limit is found to be $\delta_{\mathrm{U.L.}}^{95\%\mathrm{C.I.}}(18\,\mathrm{GV}) = 1.62 \times 10^{-3}$. At $\mathrm{R_{min}} = 80\,\mathrm{GV}$, where the analysis is no longer dominated by systematics, the upper limit obtained is $\delta_{\mathrm{U.L.}}^{95\%\mathrm{C.I.}}(80\,\mathrm{GV}) = 2.78 \times 10^{-3}$. Additionally, for $R > 300$ GV, the upper limit is $\delta_{\mathrm{U.L.}}^{95\%\mathrm{C.I.}}(300\,\mathrm{GV}) = 1.07 \times 10^{-2}$.

The numerical results corresponding to the dipole components of the proton anisotropy as well as the upper limits computed for each rigidity range are presented in the tables C.1 and C.2 of appendix C.1.

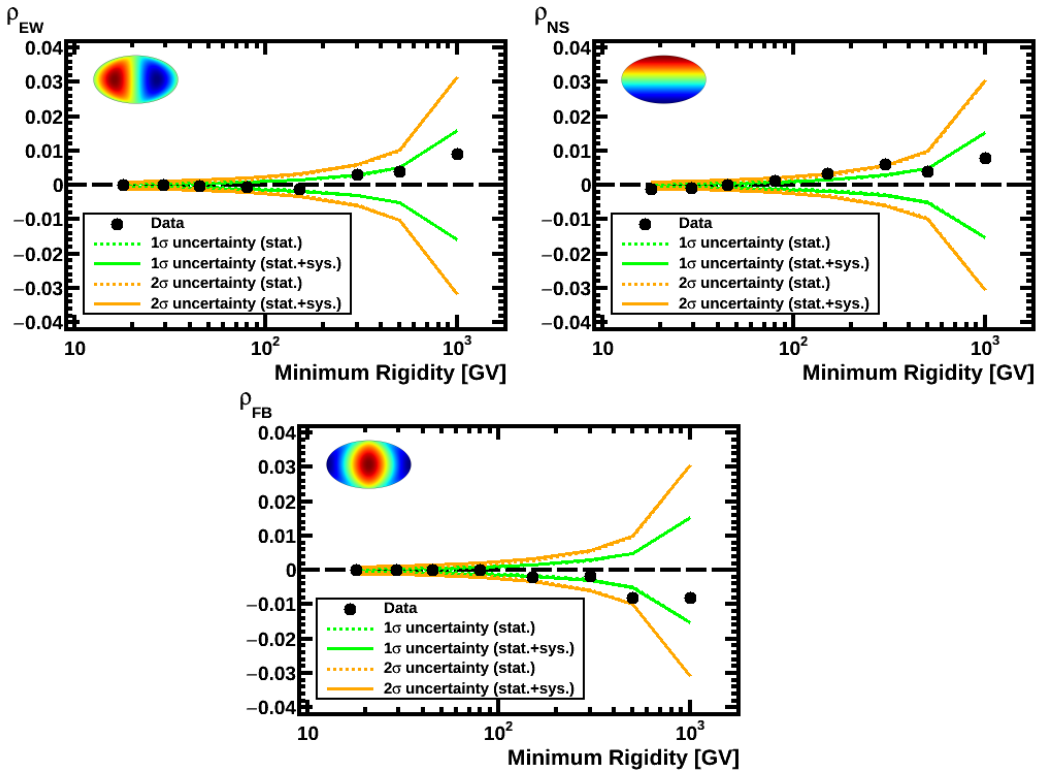

FIGURE 5.31: Values of the absolute East-West *(left)*, North-South *(right)*, and Forward-Backward *(bottom)* dipole components in galactic coordinates. The 1 and 2-sigma deviations from isotropy (green and yellow, respectively) corresponding to the statistical (dotted lines) and total (solid line) uncertainties are shown.

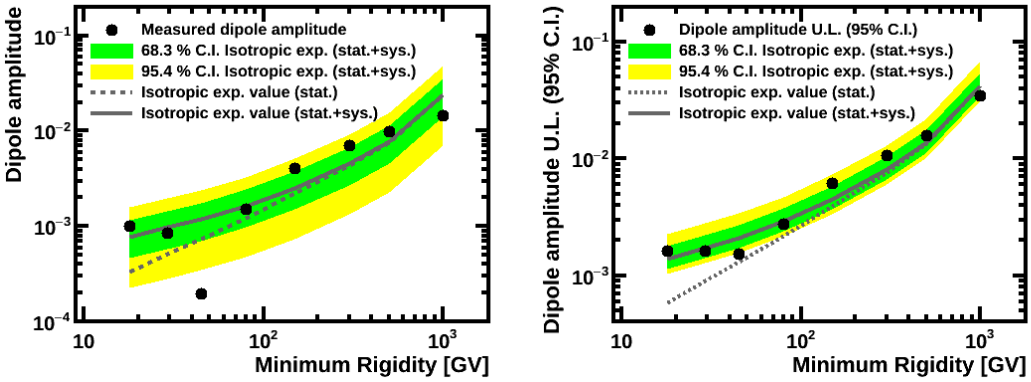

FIGURE 5.32: *(Left)* Measured dipole amplitude as a function of the minimum rigidity. *(Right)* 95% C.I. upper limit on the dipole amplitude as a function of the minimum rigidity. The bands corresponding to the 1 and 2-sigma expectation from isotropy for the total uncertainty are shown in green and yellow, respectively. In each case, the expected value from isotropy given a sample is displayed considering only the statistical uncertainty (dotted line) and the total uncertainty (solid line).

6

MEASUREMENT OF THE DIPOLE ANISOTROPY IN COSMIC RAY e^+ AND e^-

6.1 INTRODUCTION

Due to their relatively low abundance, the level of precision required in the measurement of absolute anisotropies in cosmic ray electrons and positrons is not as challenging as in the case of protons. Nevertheless, the difficulty of the analysis arises from the lepton identification, which aims to provide a high purity sample with a strong suppresion of background protons. Therefore, the combined information from different subdetectors is used to produce not only the samples of study, but also to select the events that participate in the evaluation of the efficiencies and the efficiency corrections applied in the construction of reference maps.

This chapter presents the strategy followed in the determination of the anisotropy in galactic cosmic ray electrons and positrons, starting with the selection and evaluation of the possible contamination of the sample, the assessment of instrumental effects that may spoil the measurement and, finally, the calculation of the dipole components of the relative and absolute anisotropies in galactic coordinates.

6.2 SELECTION OF ELECTRONS AND POSITRONS

The procedure to achieve a highly enriched sample of positrons and electrons consists in an initial preselection, with the goal of providing a sample of particles with charge one; and a selection where a set of quality and lepton identification cuts plays a key role.

As in the proton analysis, the selection of electrons and positrons is based on the data recorded from 2011 May 19 to 2016 May 26, which comprises the first 5 years of AMS data taking.

6.2.1 *Preselection*

An initial preselection, identical to that presented in section 5.2.2 for protons, is carried out. Preselected events include relativistic downward-going particles with measured velocity $\beta > 0.3$ reconstructed with the 4 TOF planes. Consistency with charge $|Z| = 1$ is examined by independent measurements on TOF and Inner Tracker. An Inner Tracker track is also required by demanding at least one hit in all the 4 inner planes and a reconstructed rigidity.

At the end of the preselection, the sample contains unitary charge particles, mainly background protons, from which the $e^{\pm}$ will be separated.

6.2.2 *Selection and lepton identification*

Once the preselection is carried out, a selection of events is performed by requiring particles that satisfy the conditions of the physics trigger and have a track in the TRD and a cluster of hits in the ECAL (Table 6.1). The latter requirements ensure that both TRD and ECAL estimators are available and can be used to discriminate leptons from protons in the analysis. As a consequence, the fiducial volume of the analysis is defined by the extrapolation of the Inner Tracker track being inside of TRD and ECAL geometry.

Additional quality cuts on the Inner Tracker track are applied to select clean and well reconstructed events. This is achieved by requiring a good χ^2 in both X and Y directions, and a good spatial matching between the Inner Tracker track and the ECAL shower. On the other hand, interactions of cosmic rays within AMS material may produce secondary particles that may worsen the measurement. Those events are removed by imposing a single track in the Inner Tracker. The aim of these quality tracking cuts is not only to provide a clean sample, but also to improve the accuracy in the determination of the charge sign, thus reducing the charge confusion.

Identification of electrons and positrons is achieved by means of a cut based selection on TRD and ECAL estimators and requiring a good energy-momentum matching. Finally, the curvature of the Inner Tracker track determines the sign of the charge and allows to separate electrons and positrons. This cut based analysis reduces the proton background to below the percent level, as we will see in section 6.4.

As in the case of protons, to select only primary cosmic rays, the measured energy of the particle is required to be greater than 1.2 the maximum absolute value of the rigidity cutoff within the AMS field of view. Furthermore, the discussion about the definition of good periods and good seconds from the point of view of data taking is also valid in this case.

The measurement of the anisotropy in electrons and positrons is performed in 5 cumulative energy ranges, with a minimum energy of $E_{\text{min}} = 16, 25, 40, 65, 100$ GeV, and a maximum energy of $E_{\text{max}} = 350$ GeV. In addition, each energy range is divided into differential energy bins of width chosen according to the energy resolution. The number of selected electrons and positrons as well as the number of differential energy bins in each cumulative energy range is recorded in table 6.2.

6.3 ELECTRON AND POSITRON EFFICIENCIES

The procedure followed to calculate the electron and positron efficiencies is, conceptually, identical to that used in the case of protons (section 5.3), where the efficiency of a cut is defined in terms of the number of events accepted, N_{ok}, and rejected, N_{ko}.

Likewise, efficiencies are calculated sequentially when possible in order to avoid correlations. Nonetheless, since efficiencies must be calculated on pure lepton samples, some of the identification cuts need to be applied to suppress background

TABLE 6.1: Selection and identification cuts applied to achieve a sample of electrons and positrons for the measurement of anisotropies.

Subdetector	**Selection cuts**
Fiducial volume	• Inner Tracker track extrapolation inside TRD and ECAL
TOF	• Physics trigger • $\beta > 0.7$
ECAL	• ECAL shower
TRD	• TRD track
Inner Tracker	• Inner track $\chi^2(X, Y) < 10$ • $\big($Inner Tracker track - Ecal shower$\big)(x, y)_{L9}$ < 3 cm • No secondary tracks
	Lepton identification cuts
TRD	• TRD Likelihood < 0.6
ECAL	• ECAL BDT > 0
ECAL-Tracker	• $0.65 < \mathrm{E}/\lvert\mathrm{p}\rvert < 5$
	Above cutoff
	• $\mathrm{E_{ECAL}} > 1.2 \max\left\{R^{+}_{\mathrm{cutoff}}, \lvert R^{-}_{\mathrm{cutoff}}\rvert\right\}$

TABLE 6.2: Number of measured electrons and positrons, and differential energy bins in the 5 cumulative energyy ranges of the anisotropy study.

$\mathrm{E_{min}}$ (GeV)	Energy bins	Meas. e^- ($\times 10^3$)	Meas. e^+ ($\times 10^3$)
16	35	1065.63	79.83
25	27	459.72	39.66
40	19	150.96	16.04
65	11	46.41	6.17
100	7	15.94	2.57

protons. For this reason, in some cases the efficiencies cannot be completely computed in a sequential manner. For instance, the efficiencies related to the TRD performance have to be evaluated on a sample of leptons selected by means of the ECAL estimator, and vice versa. However, in that case we take advantage of the negligible correlation between these two subdetectors to assume that both efficiencies are independent.

On the other hand, efficiencies are calculated on a pure sample of electrons and assumed to be identical for positrons. This has two advantages, namely, its higher statistics allows to determine the efficiency with better accuracy; and the opposite charge sign contributes to further reduce the residual proton background.

In addition, although we are interested in the distribution of the efficiencies in the skymap, their behavior has been investigated in terms of several distributions. In particular, control distributions have been examined to ensure the purity of the sample used in each efficiency.

Finally, the lepton efficiencies are classified into three categories according to the kind of cuts applied: trigger efficiency, reconstruction and selection efficiencies, and identification efficiencies. The last two categories are studied following the procedure explained in the scheme of figure 6.1.

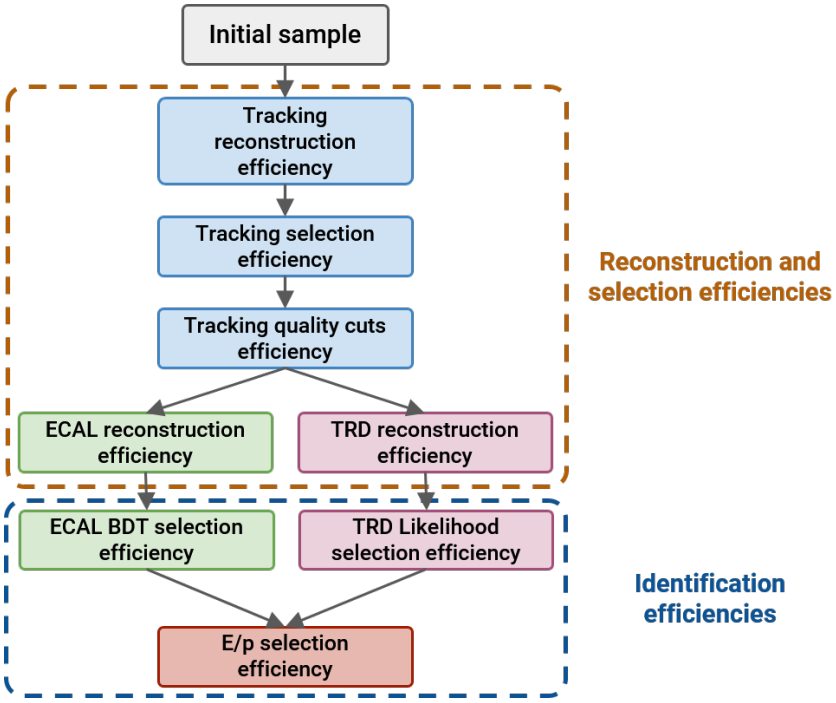

FIGURE 6.1: Scheme of the strategy followed in the evaluation of the electron efficiencies.

6.3.1 *Trigger efficiency*

As in the case of protons, a sample of events passing all selection cuts with looser trigger conditions is used to evaluate the trigger efficiency. In this case, the unbiased sample consists of 1/100 of the events with a coincidence of signals from at least

3 TOF planes of any veto from the ACC. Then, the trigger efficiency is calculated as the fraction of events with physics trigger over the total number of events of the initial sample:

$$\varepsilon_{\text{trig}} = \frac{N_{\text{phys}}}{N_{\text{phys}} + 100 \cdot N_{\text{unbias}}}. \tag{6.1}$$

Contrary to protons, signals in the ECAL associated to an electromagnetic particle disable the ACC veto which makes this efficiency stable as function of the geographical position.

6.3.2 *Reconstruction and selection efficiencies*

6.3.2.1 *Tracking efficiency*

As in the case of protons, the *tracking reconstruction efficiency* accounts for the fraction of events with associated track in the Inner Tracker. Since the tracker track is not available, the TOF track inside the geometry determined by the TRD and ECAL subdetectors define the fiducial volume for the evaluation of the tracking efficiency. The initial sample consists in relativistic downward-going particles with unitary TOF charge. The lepton identification is achieved by means of a tight cut on the ECAL estimator.

Once the Inner Tracker track is available, the sign of the rigidity provides a separation between positive and negative particles. In addition, the extrapolation of the track inside TRD and ECAL determines the fiducial volume for the successive efficiencies.

Finally, the *efficiency of the quality cuts* applied to the track in order to avoid interactions and select a clean sample is studied separately for each cut, as shown in figure 6.2.

6.3.2.2 *TRD and ECAL reconstruction efficiencies*

The *TRD reconstruction efficiency* accounts for the probability that an electron passing the trigger and tracking efficiencies has associated signals in the TRD within the fiducial volume of the analysis. As in the other efficiencies, electrons are selected by means of a tight cut on the ECAL estimator and imposing negative charge sign. Then, the efficiency is evaluated by requiring a TRD track with an associated TRD estimator.

In a similar manner, the *ECAL reconstruction efficiency* describes the fraction of electrons passing the trigger and tracking efficiencies and develop a shower in the ECAL. In this case, since the information in the ECAL is not available, electron identification is performed by means of a tight cut on the TRD estimator and requiring a negative rigidity. In addition, since the energy in the ECAL is not accessible, we use the absolute value of the rigidity as an alternative estimation of the energy. Finally, we evaluate the efficiency by requiring a shower in the ECAL allowing the reconstruction of the ECAL estimator.

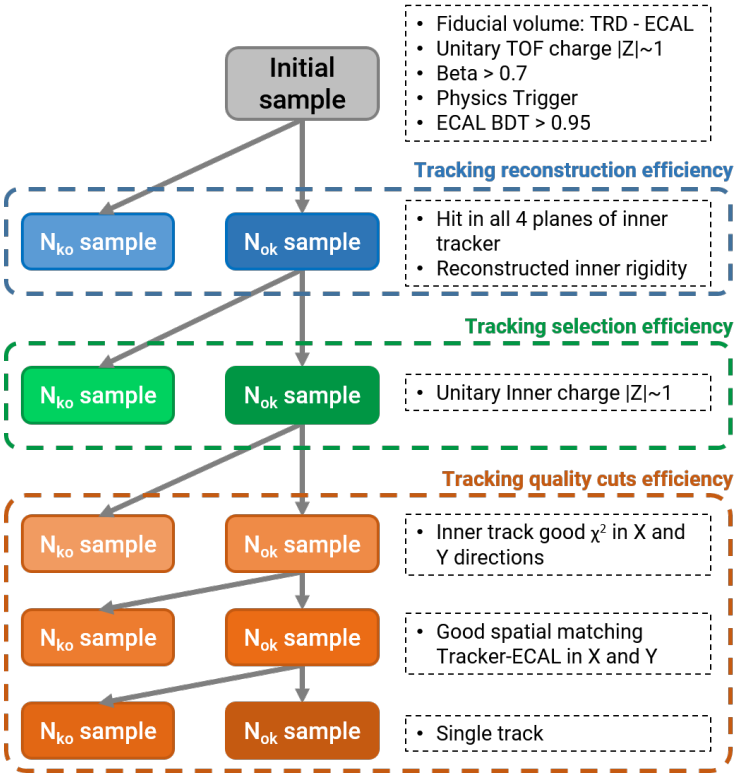

FIGURE 6.2: Scheme of the strategy followed in the calculation of the efficiencies associated to the tracker on the electron sample.

6.3.3 *Lepton identification efficiencies*

Once the trigger and reconstruction/selection efficiencies have been computed, the remaining sample is used to evaluate the efficiency of the cuts applied in the identification of leptons.

Since the proton rejection is mainly achieved through cuts on TRD and ECAL estimators, the calculation of TRD estimator efficiency requires a tight cut on ECAL estimator. Then, the efficiency of the cut applied to the TRD estimator is evaluated on an electron sample.

Alternatively, a tight cut on TRD estimator is needed for the computation of ECAL estimator efficiency. Similarly, the efficiency of the cut on the ECAL estimator is computed on electrons.

Finally, due to the correlation between the measured energy in the ECAL and the ECAL estimator, the efficiency of the cut applied on the E/p ratio is calculated as a last cut, where a sample of electrons is selected by requiring the standard cuts on TRD and ECAL estimators.

6.4 CHARGE CONFUSION AND PROTON CONTAMINATION

The presence of background in the sample used in the analysis of anisotropies contributes to reduce the sensitivity of the measurement according to (3.55). For this

reason, the selection of pure samples is preferred in order to take advantage of the statistical power of the sample. However, this is not always possible and irreducible background may contaminate the selection.

In particular, the positron sample selected by the procedure described in the previous sections is not completely pure and two sources of background may be present, namely, residual protons and charge confused electrons. The electron sample, however, has a negligible contamination of charge confused protons and positrons, and can be considered pure.

6.4.1 *Charge confusion*

Positrons are distinguished from electrons by means of the sign of the reconstructed rigidity in the tracker. A major source of contamination in the positron sample is constituted by electrons whose sign is misreconstructed as positive, therefore, being selected as positrons. This charge confusion effect can be quantified in terms of the fraction of events with a wrong assignment of the rigidity sign:

$$\mathrm{cc} = \frac{N(R^{\mathrm{rec}} \times R^{\mathrm{true}} < 0)}{N_{\mathrm{tot}}}. \tag{6.2}$$

The sources of charge confusion are mainly two: the *spillover* and the existence of *secondary hits*:

- *Spillover* is the dominant source of charge confusion at high energies and it is related to the finite resolution of the tracker rigidity reconstruction. Since the rigidity sign is based on the curvature of the particle inside the tracker, as the energy increases the bending of the trajectory decreases. Consequently, the tracker rigidity resolution steadily worsens and some trajectories might be reconstructed with the opposite sign. This is an intrinsic effect related to the magnet and tracker capabilities and cannot be avoided at high enough energies.
- *Secondary hits*. At low energies, the dominant source of charge confusion is related to spurious signals that may produce multiple tracks or wrong hit associations in the pattern recognition. These spurious hits are connected to noise or interactions in the detector material producing secondary particles.

The standard cuts applied on energy-momentum matching and the quality of the track contribute to reduce the charge confusion in the positron sample. The remaining charge confusion is calculated on a sample of Monte Carlo generated electrons as a function of the generated energy. The fraction of charge confused electrons in the total sample of generated electrons is shown in figure 6.3 as a function of the Monte Carlo generated energy.

Finally, the estimation of the charge confusion together with the measured number of electrons and positrons allow to determine the number of charge confused electrons in each energy bin as $N^{e^-}_{\mathrm{bkg}} = \frac{cc}{1-cc} \cdot N^{e^-}_{\mathrm{meas}}$.

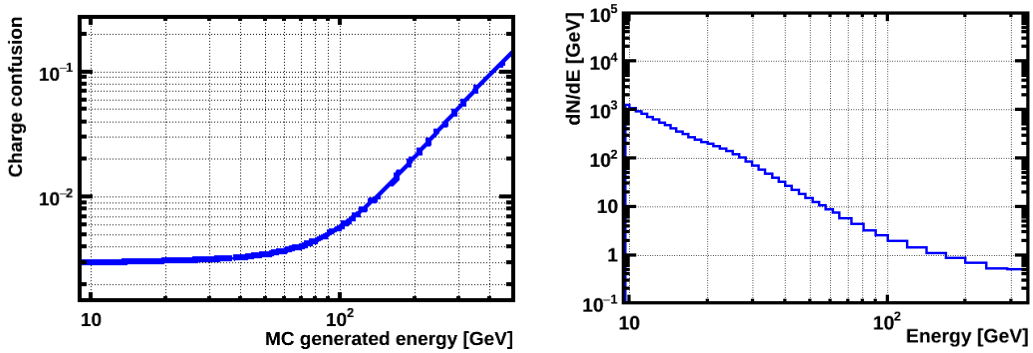

FIGURE 6.3: *(Left)* Charge confusion probability determined from MC simulated electrons as function of the generated energy. *(Right)* Energy distribution of the charge confused electrons.

6.4.2 *Proton contamination*

Apart from the charge confused electrons, a residual number of protons may contaminate the positron sample after the cut based selection. Those background protons satisfy the standard conditions used to select positrons, in particular, the nominal cuts on TRD and ECAL estimators, and the E/p matching.

Two independent procedures, which are based on the negligible correlation between TRD and ECAL estimators, have been applied to evaluate the number of background protons. In both cases, the sample used to determine the residual proton contamination is selected in a similar manner as in the standard e^- and e^+ selection, i.e., clean events with unitary charge inside the fiducial volume determined by TRD and ECAL. Additionally, both methods make use of the high proton rejection power of lepton identification cuts on TRD and ECAL estimators and E/p ratio.

- METHOD I

  1. Select a proton sample with a tight cut on TRD estimator passing the standard cuts on ECAL estimator and E/p.
  2. Divide the previous distribution by the efficiency of the tight cut on TRD estimator to obtain the *initial distribution of protons* that satisfy the standard cuts on ECAL estimator and E/p.
  3. Apply the proton selection efficiency of the standard cut on TRD estimator to obtain the distribution of background protons.

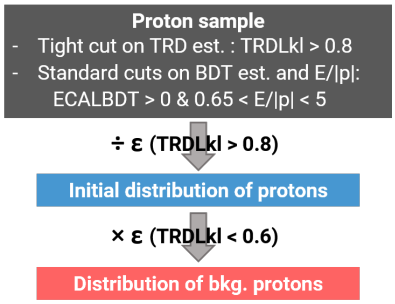

FIGURE 6.4: Scheme of the estimation of proton contamination according to method I.

▶ METHOD II

1. Select a proton sample with a tight cut on ECAL estimator and E/p passing the standard cut on TRD estimator.
2. Divide the previous distribution by the efficiency of the tight cut on ECAL estimator and E/p to obtain the *initial distribution of protons* that satisfy the standard cut on TRD estimator.
3. Apply the proton selection efficiency of the standard cut on ECAL estimator and E/p to obtain the distribution of background protons.

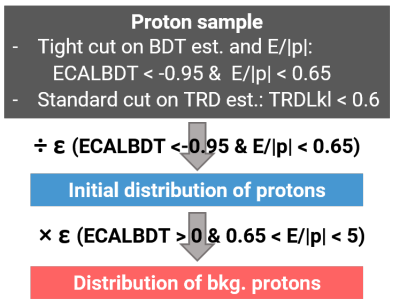

FIGURE 6.5: Scheme of the estimation of proton contamination according to method II.

The proton distributions produced in each step of methods I and II are shown in figure 6.6-*left* and *right*, respectively, as a function of the energy.

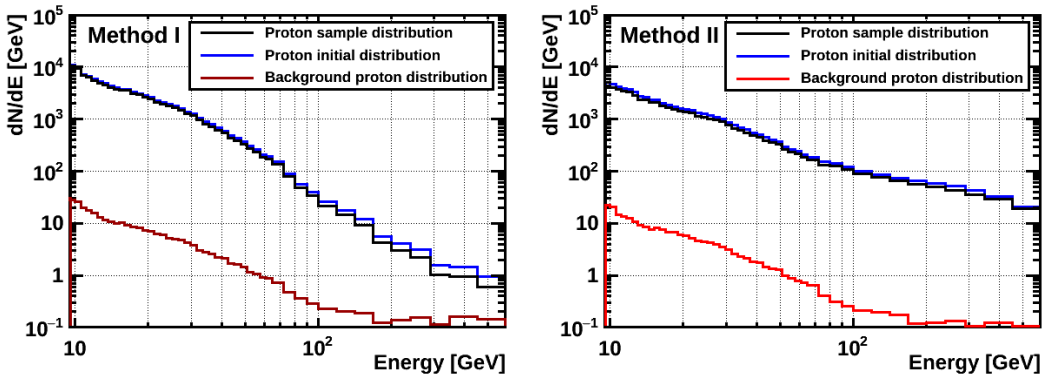

FIGURE 6.6: Energy distribution of the background protons estimated with method I (dark red solid line) and method II (red solid line).

The final background proton distributions are compared on figure 6.7. As can be seen, both methods provide consistent distributions of background protons as a function of the energy, which allow to obtain the average number of residual protons in the positron sample for each cumulative energy range of the analysis (Table 6.3). Therefore, the cut based selection of positrons provides an almost proton free sample, with a proton contamination at the per mil level in the first four energy ranges, and at the percent level in the highest one.

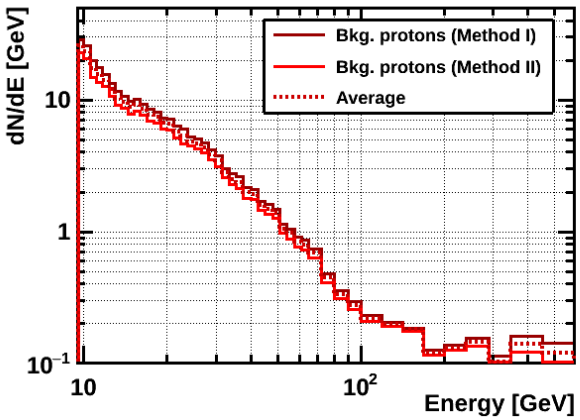

FIGURE 6.7: Estimated background proton distribution according to methods I (dark red) and II (red), and average of both estimations (dotted red line).

TABLE 6.3: Estimated number of background protons in the cumulative energy ranges of the analysis and fraction of proton contamination in the positron sample.

Energy (GeV)	# Bkg. Pr I	# Bkg. Pr II	Average	Fraction Bkg.
16 - 350	200	169	185	2.5×10^{-3}
25 - 350	137	117	127	3.4×10^{-3}
40 - 350	86	75	80	5.2×10^{-3}
65 - 350	53	47	50	8.4×10^{-3}
100 - 350	37	33	35	1.4×10^{-2}

6.4.3 *Purity of the positron sample*

The study of the two sources of background allows to quantify statistically the number of fake positrons in the sample and determine the number of true positrons. The distributions of observed and corrected number of events per energy bin are shown in figure 6.8-*left*, together with the distribution of background protons and charge confused electrons. From these estimations, it is clear that the dominant source of background in the cut based selection is due to charge confusion.

Finally, the purity of the positron sample can be computed as the fraction of the number of true events in the measured selection (figure 6.8-*right*). On the one hand, the fraction of background protons is below the 1% for E < 100 GeV, where the TRD is in its optimal operation regime. On the other hand, the purity of the positron sample shows that the cut based analysis provide a clean sample of positrons with high efficiency.

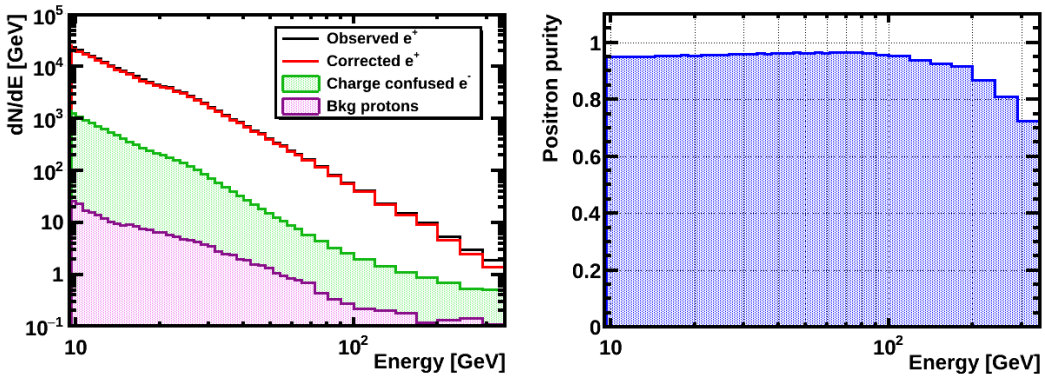

FIGURE 6.8: *(Left)* Energy distribution of the observed and corrected number of positrons (solid black and red lines, respectively), and estimation of the background events due to charge confusion and proton contamination. *(Right)* Purity of the positron sample as a function of the energy.

6.5 VALIDATION OF THE SAMPLE

In the previous sections we have described the procedure to achieve a sample of electrons and positrons, the efficiencies that are involved in the analysis and, finally, the possible irreducible background that may contaminate the sample. In order to assure a good understanding of the sample, the selection of electrons and positrons can be used to calculate the positron fraction as a function of the energy. Figure 6.8 shows the positron fraction obtained in this analysis after accounting for background contamination. The result in the energy interval of this analysis is in good agreement with the latest published measurement by AMS-02 [62], which allows to validate the sample selection and the background estimation.

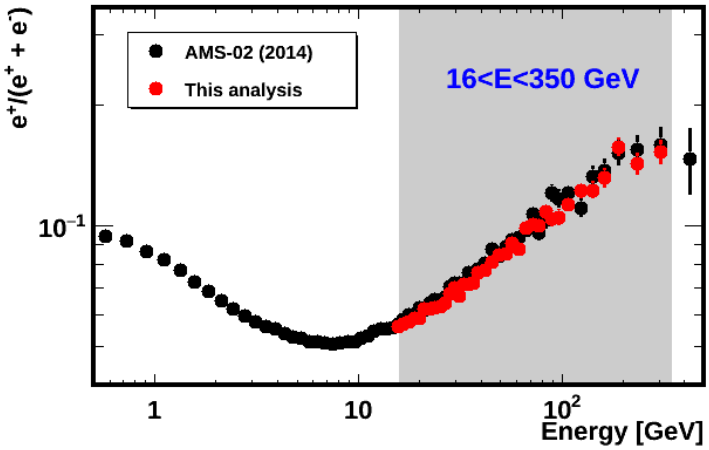

FIGURE 6.9: Positron fraction obtained with the selection used in this analysis (red points) in comparison with the latest result published by the AMS Collaboration.

To further ensure the quality of the selection, the time stability of the rates is investigated on electrons in the energy range from 16 to 350 GeV. As in the case of protons, at low energies the solar modulation may affect the time stability of the rate once the time variation of the efficiencies is considered. Hence, the range 16-350 GeV is divided into two subranges: 16-25 GeV, which is still sensitive to possible solar modulation effects; and 25-350 GeV, which should not be affected.

Figure 6.10-*top* shows the normalized to the average raw rate in monthly intervals for electrons in the range 16-25 GeV. The relative variation of the total efficiency is also shown. Once the time variation of the total efficiencies accounted, the corrected rate in figure 6.10-*bottom* shows a trend which is consistent with the solar activity during the 5 years of the analysis already discussed.

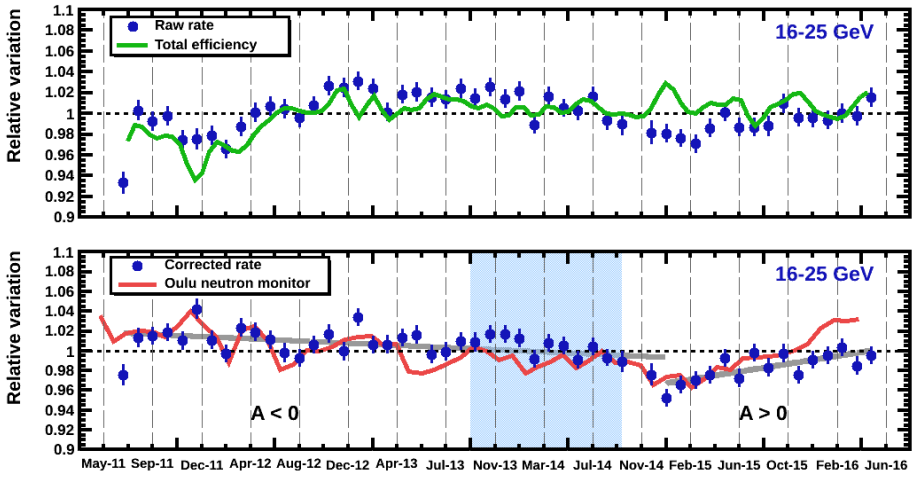

FIGURE 6.10: *(Top)* Time dependence of the normalized electron raw rate (blue dots) and total efficiency (green line) in monthly intervals for 16-25 GeV. *(Bottom)* Time dependence of the normalized corrected electron rate (blue dots) and Oulu neutron monitor count rate (solid red line). The observed trend is consistent with the polarity reversal of the HMF, where the blue shaded area corresponds to the period with no well-defined HMF polarity.

On the other hand, figure 6.11 shows the time variation of both normalized raw rate and normalized total efficiency for the energy range 25-350 GeV. In this case, the time variation of the raw rate is better described by the total efficiency. Consequently, since the energy range is high enough not to be affected by solar modulation, the corrected rate shows no evident pattern and it is constant with time within a systematic uncertainty of 0.5%, much smaller than the 2% uncertainty associated to the determination of the acceptance in the flux measurement [64].

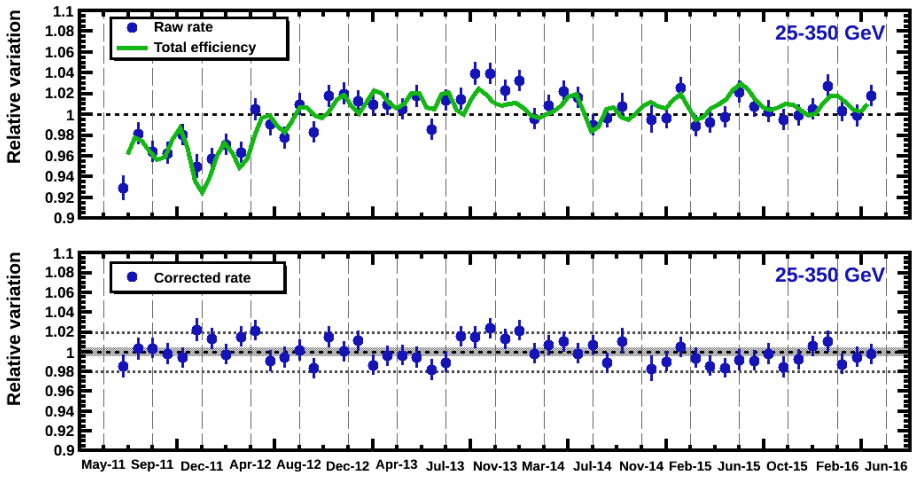

FIGURE 6.11: *(Top)* Time dependence of the normalized electron raw rate (blue dots) and total efficiency (green line) for 25-350 GeV. *(Bottom)* Time dependence of the normalized corrected electron rate (blue dots). No evident time evolution is observed. The time variation is consistent with being constant in time within a systematic of 0.5%.

6.6 PARAMETRIZATION OF THE ELECTRON EFFICIENCIES

In the same manner as protons, the measurement of the anisotropy in electrons and positrons may be affected by instrumental effects, namely, the geographical dependence of efficiencies and the AMS-02 day/night cycles. As in the case of protons, although day/night cycles have no impact in the dipole results in galactic coordinates, the tools developed for the anisotropy analysis provide a reliable characterization of their effect, and a dedicated study is presented in appendix B.

6.6.1 *One-dimensional study in geomagnetic colatitude*

The treatment of the (θ, φ)-dependence of efficiencies in electrons and positrons is similar to that applied in the case of protons (section 5.6). The one-dimensional distribution of the rate and the efficiencies as a function of the geomagnetic colatitude is advantageous to gather preliminary information about its behavior. Due to the higher statistics, the colatitudinal dependence of the electron raw rate, normalized to the average, calculated for the first energy range, $16 < E < 350$ GeV, is shown in figure 6.12-*left*.

As mentioned in 5.6.1-*left*, the fit of the geomagnetic colatitude distributions in terms of the parabolic function (5.5) provides quantitative results about the dipole and quadrupole components in a geographical positional coordinate system. In particular, the raw rate exhibits a drop of $\sim 6\%$ at the high latitude regions, which is evidenced by the North-South asymmetry parameter, p_1, and the symmetric term, p_2. A similar drop in the efficiency is also observed; however, from the parabolic description and the fit parameters, it is clear that the drop in the efficiencies is not sufficient to explain the decrease in the rate. This result is also confirmed by the cor-

rected rate in figure 6.12-*right*, where a residual decrease is still present. A possible reason of this behavior might be due to residual correlations between subdetectors, mainly, because of the lepton identification, which might give rise to an underestimated efficiency determination.

On the other hand, this one-dimensional approach provides a first look on the energy dependence of the colatitudinal shape of electron efficiencies. As an example, figure 6.13-*left* shows the distribution of the TRD reconstruction efficiency normalized to the average for $E_{\text{min}} = 16$ GeV and $E_{\text{min}} = 40$ GeV, both parameterized in terms of 5.5. The ratio of both distributions in figure 6.13-*right* allows us to conclude that the energy dependence of the electron efficiency corrections will be weaker than in the case of protons.

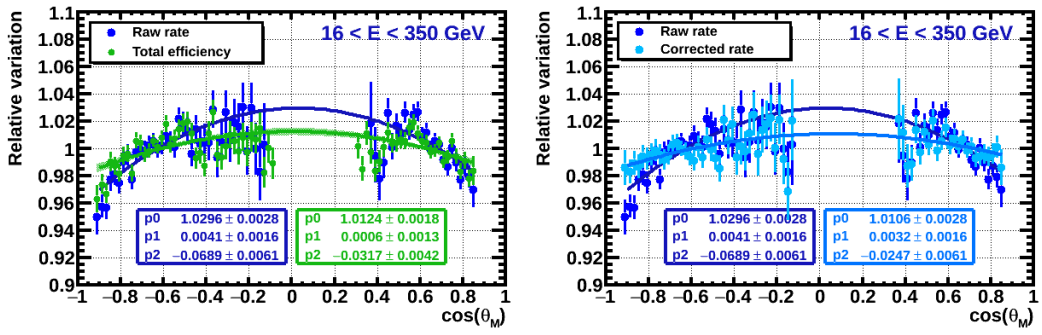

FIGURE 6.12: *(Left)* Geomagnetic colatitude dependence of the electron raw rate (blue) and the total efficiency (green) in the energy range 16-350 GeV. Both quantities are normalized to their average for a direct comparison and exhibit a drop at high latitude regions. *(Right)* Geomagnetic colatitude dependence of the electron raw rate (dark blue) and corrected rate (clear blue). A residual drop at high latitudes in the corrected rate is still present.

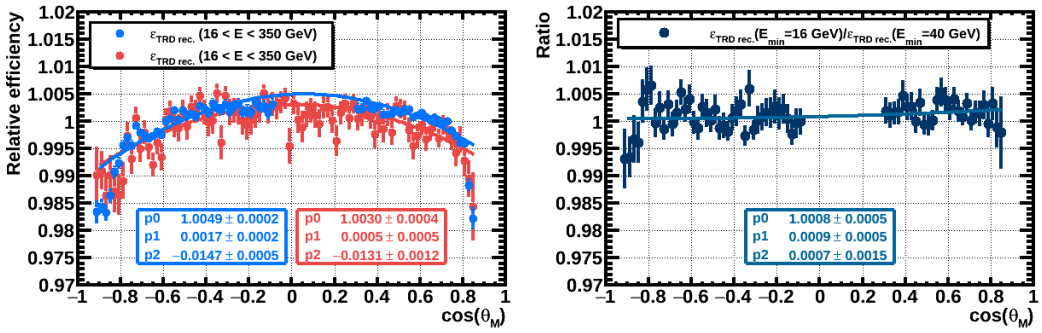

FIGURE 6.13: Geomagnetic latitude dependence of the electron TRD reconstruction efficiency for the energy ranges 16-350 GeV and 80-350 GeV, both normalized to their average *(left)*, and ratio of the two distributions *(right)*.

6.6.2 *Spherical harmonic parametrization in ISS Geographical Position coordinates*

The distributions of events in the sky provide a generalization of the one-dimensional study and a complete description of the issue. Again, due to the higher statistics, the electron sample is used. In this regard, figure 6.14-*left* shows the skymap distribution of the measured number of electrons, $N(\theta, \varphi)$, in the energy range $16 < E < 350$ GeV. The expectation, $\langle N(\theta, \varphi) \rangle$ according to only the exposure time is presented in figure 6.14-*right*.

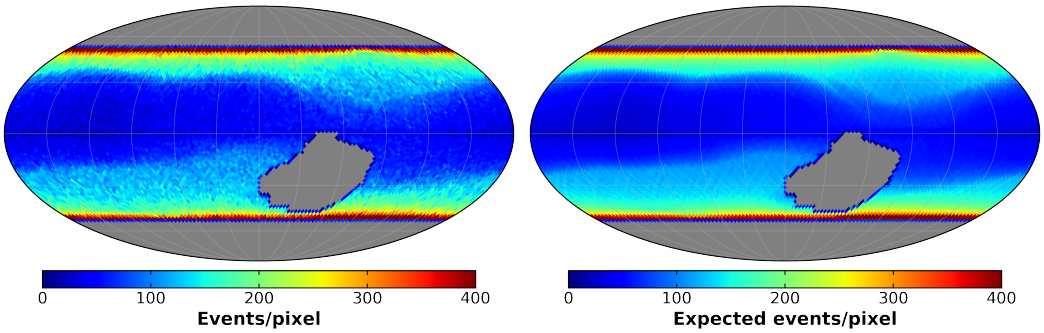

FIGURE 6.14: Skymap distribution of measured electrons *(left)* and expected number of events from the exposure time *(right)* in the energy range $16 < E < 350$ GeV in ISS Geographical Position coordinates.

The comparison between the two skymaps by means of the significance estimator, 5.7, is shown in the skymap[1] and significance distribution in figure 6.15. The significance map shows evident structures in the regions close to the geomagnetic poles, where a negative significance indicates that the measured number of electrons is smaller than the expected from only the exposure time. Due to the smaller statistics, the deviations observed in this case are less significant than those of the proton sample. The comparison of both skymaps yields a chi-square of $\chi^2/d.f. = 818.7/619$, which suggests a poor compatibility between them. This is also confirmed by the histogram in 6.15-*right*. Nevertheless, the fit to a Gaussian provides a sigma parameter of 1.15, which further supports the conclusion that the electron distribution is not consistent with the expectation from only exposure time.

Since ISS Geographical Position is the intrinsic frame to these effects, it is a suitable coordinate system to assess our understanding of electron efficiencies. The spherical harmonic parametrization of electron efficiencies describes its behavior in the complete skymap. The method follows the same procedure applied to the proton analysis, which is summarized in the next three steps

1 Since the electron sample size is smaller than the proton one, in order to be sensitive to possible high deviations and structures in the skymaps, significance maps are built with a smaller HEALPix parameter, $N_{\text{side}} = 8$, which corresponds to 768 pixels, only for display purposes and for this analysis of pulls. The measurement of anisotropies is performed on the usual skymaps of $N_{\text{side}} = 32$ and 12288 pixels.

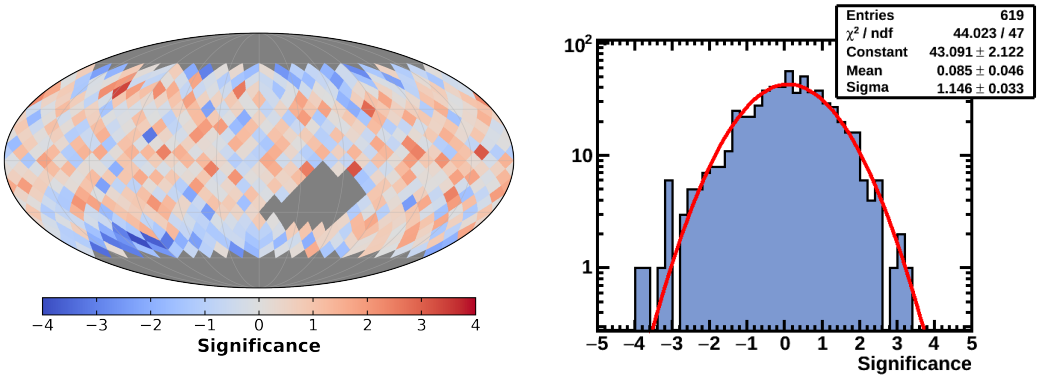

FIGURE 6.15: Significance skymap *(left)* and distribution *(right)* of the electron distribution with respect to the expectation from only the exposure time for the energy range $16 < E < 350$ GeV in ISS Geographical Position coordinates.

1. The relative anisotropy analysis of the sample of accepted and rejected events, N_{ok} and N_{ko}, respectively, provides the multipole components of the corrections $\Delta_{\ell m}$ in the coordinate system of analysis.
2. The energy dependence of the corrections is described in terms of a linear ($\ell = 1$) or quadratic ($\ell = 2$) polynomial function for each efficiency and multipole component in terms of the minimum energy, in a similar manner to (5.10).
3. Finally, the pull distribution allows to establish the cut value used to determine which efficiency contributions are tagged as significant and, therefore, applied to correct the exposure time maps.

The multipole components of each efficiency in the analysis as well as the energy parametrization are obtained according steps 1 and 3. Figure 6.16 shows the results of the corrections Δ_{NS} and Δ_{2+0} for the TRD reconstruction efficiency, obtained from the relative analysis of the samples N_{ok} and N_{ko} in each cumulative energy range. The linear and quadratic polynomials describing the energy dependence are also shown as a function of the minimum energy.

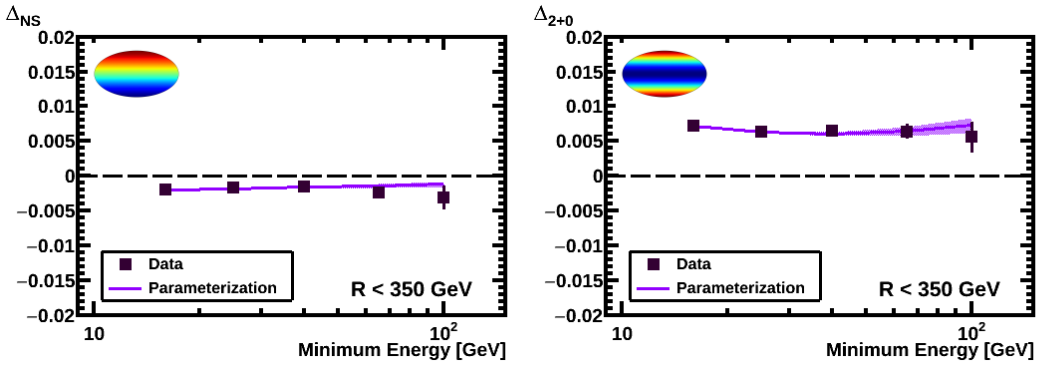

FIGURE 6.16: Results of the corrections Δ_{NS} *(left)* and Δ_{2+0} *(right)* for the electron TRD reconstruction efficiency as a function of the minimum energy. The square dots show the results calculated from the results of the relative analysis of the N_{ko} and N_{ok} samples in cumulative energy ranges, and the shaded line corresponds to the parametrization of the energy dependence of the correction in terms of (5.10) with the associated uncertainty.

On the other hand, the pull distribution built with the efficiency corrections calculated for each energy range and multipole component is shown in figure 6.17. A scan in the threshold value allows to separate the contributions that are significant from the core of those consistent with statistical fluctuations (figure 6.18).

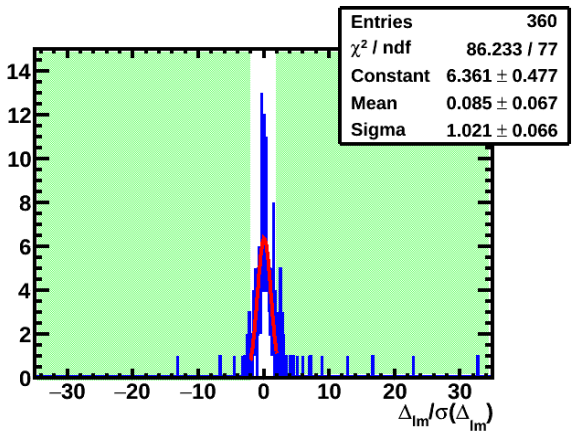

FIGURE 6.17: *(Left)* Distribution of efficiency correction pulls for each energy range (5), dipole and quadrupole components (8) and efficiencies (9) in ISS Geographical Position coordinates. Efficiency corrections whose pull is above a certain threshold in absolute value (in the green colored area) are tagged as significant. Efficiency corrections inside the threshold value are consistent with statistical fluctuations and, therefore, well described by a Gaussian distribution.

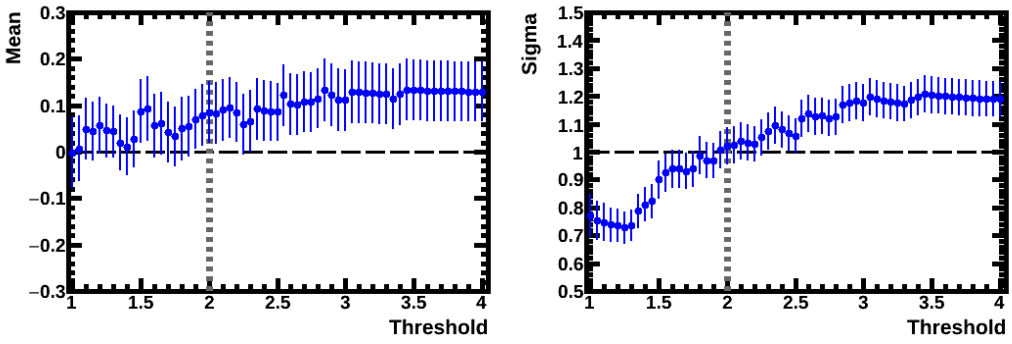

FIGURE 6.18: Scan in the mean *(left)* and sigma *(right)* parameters of the fit to a Gaussian function of the pulls distribution in figure 6.17 as a function of the threshold value. The optimum value of a threshold, which corresponds to mean ~ 0 and sigma ~ 1, ensures that the efficiency corrections with pull below that value are well described by a Gaussian distribution and, therefore, consistent with statistical fluctuations.

As in the proton analysis, in ISS Geographical Position coordinates only few components are significant and, therefore, contribute to correct the exposure time map. The summary plot in figure 6.19 collects the dipole and quadrupole components of each efficiency correction as well as the total efficiency correction for the energy range $16 < E < 350$ GeV. Similarly, the efficiency correction affects mainly the North-South direction, specially, with a high amplitude in the quadrupole component, Δ_{2+0}. Likewise, a Δ_{2-1} correction appears due to the asymmetry of the

geomagnetic poles in ISS Geographical Position. In addition, the electron TRD reconstruction efficiency is the dominant contribution, and it is explained by the high rate of low energetic particles that affect its performance at high geomagnetic latitudes.

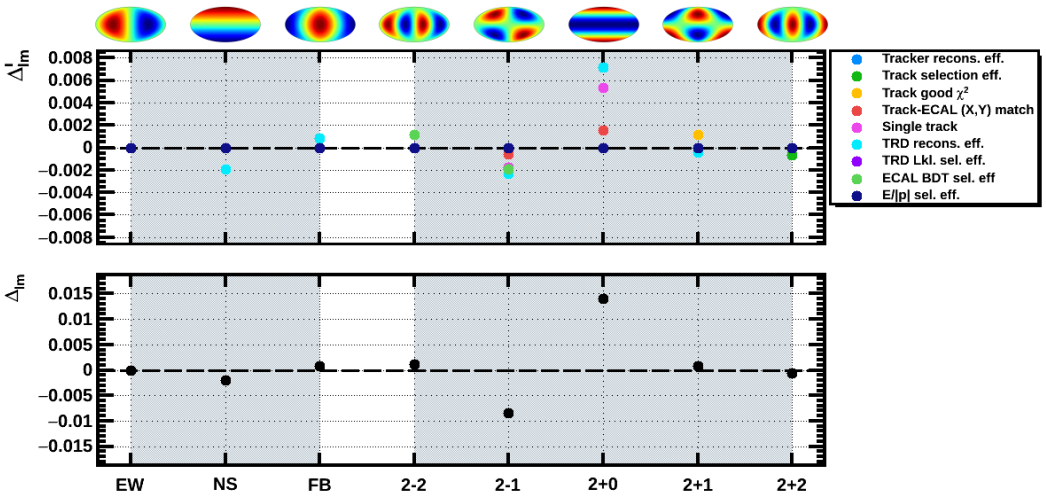

FIGURE 6.19: Individual *(top)* and total *(bottom)* electron efficiency correction for $16 < E < 350$ GeV in ISS Geographical Position coordinates, where the main directions affected are those corresponding to the North-South direction. The correction is dominated by the dependence of the TRD reconstruction efficiency.

As a result of this procedure, the spherical harmonic parametrizations of each efficiency are produced, where only the significant contributions are introduced. For instance, the parametrization of the TRD reconstruction efficiency as well as the total one up to $\ell = 2$ obtained for the energy range $16 < E < 350$ GeV is presented in figure 6.20. The observed structure is consistent with the deviations that appeared in the significance map of figure 6.15.

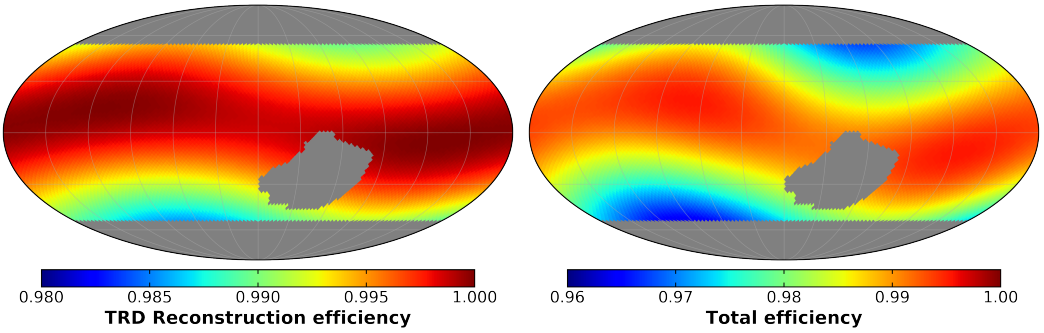

FIGURE 6.20: ISS Geographical Position skymap of the spherical harmonic parametrization of the electron TRD reconstruction efficiency *(left)* and the electron total efficiency *(right)* up to $\ell = 2$, where only the significant components are introduced in the expansion.

The level of agreement between data and reference when the parametrization of the total efficiency is applied to the exposure time map is again evaluated by means of the significance skymap and distribution in figure 6.21. The improvement

is quantified in terms of a reduction in the chi-square, which now is $\chi^2/d.f. = 686.3/619$, and the fit to a Gaussian of the significance distribution provide a sigma parameter of 1.06, closer to 1.

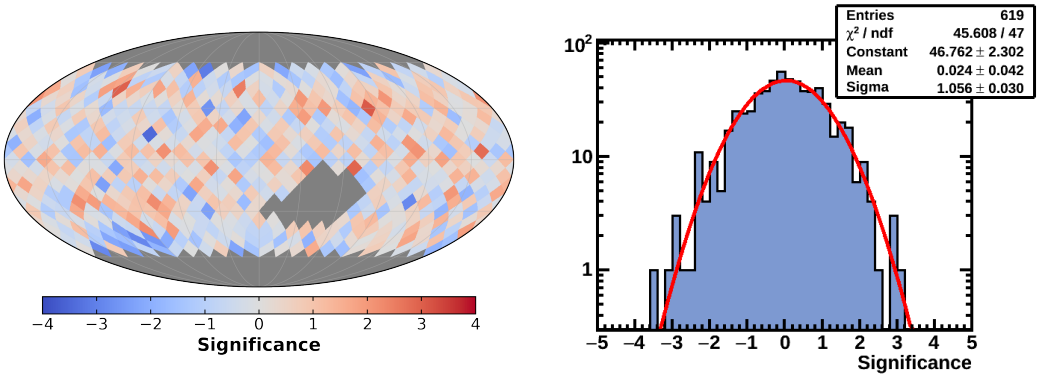

FIGURE 6.21: Significance skymap *(left)* and distribution *(right)* of the electron skymap with respect to the expectation from the corrected exposure for the rigidity range $16 < E < 350$ GeV in ISS Geographical Position coordinates.

6.6.3 *Spherical harmonic parametrization in Galactic coordinates*

The understanding of the effect of efficiencies in the ISS Geographical Position system allows to extend the procedure to galactic coordinates. In this regard, figure 6.22 shows the skymap distributions of measured and expected electrons with energies in the range $16 < E < 350$ GeV in galactic coordinates.

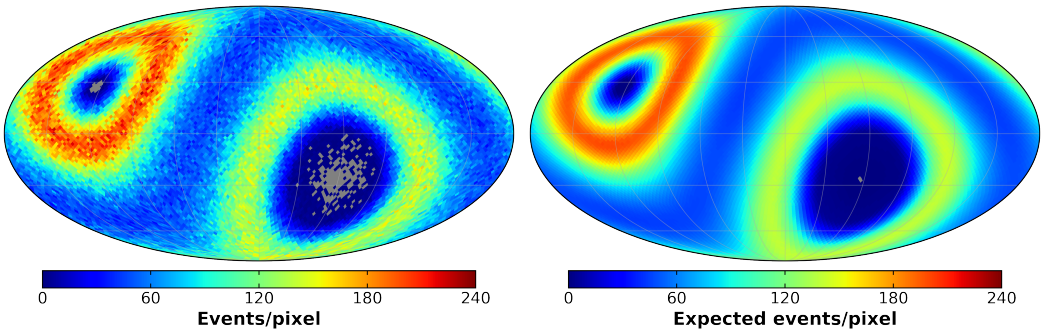

FIGURE 6.22: Skymap distribution of measured electrons *(left)* and expected number of events from the exposure time *(right)* in the energy range $16 < E < 350$ GeV in galactic coordinates.

On the other hand, although the significance skymap in figure 6.23-*left* shows no evident structures and the distribution of figure 6.23-*right* is well reproduced by a Gaussian fit, the need of efficiency corrections in ISS Geographical Position motivates the same study in galactic coordinates.

Similarly, the relative analysis of anisotropies in galactic coordinates applied to the N_{ok} and N_{ko} samples for each efficiency provides the multipole components of the parametrization, from which the efficiency corrections for each cumulative

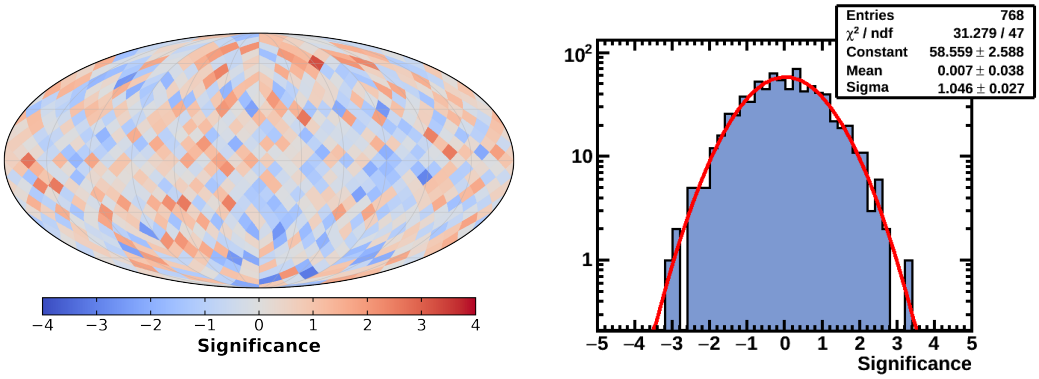

FIGURE 6.23: Significance skymap *(left)* and distribution *(right)* of the electron distribution with respect to the expectation from the exposure time for the energy range $16 < E < 350$ GeV in galactic coordinates.

energy range are derived. The energy dependence of the correction is described in terms of a linear and parabolic function in logarithm of the minimum energy, and the pull distribution allows to separate the significant contributions (figure 6.24). The threshold value, which guarantees that corrections with a pull below that cut are consistent with statistical fluctuations, is estimated by means of a scan in the sigma and mean parameters of a Gaussian fit (figure 6.25).

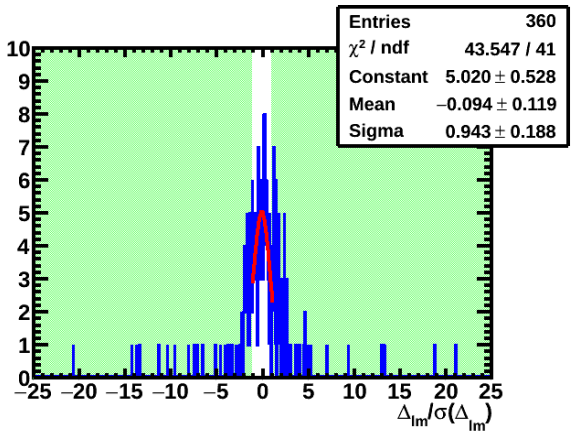

FIGURE 6.24: *(Left)* Distribution of efficiency correction pulls for each rigidity range (8), dipole and quadrupole components (8) and efficiencies (6) in galactic coordinates. Efficiency corrections whose pull is above a certain threshold in absolute value (in the green colored area) are tagged as significant. Efficiency corrections inside the threshold value are consistent with statistical fluctuations and, therefore, well described by a Gaussian distribution.

The multipole components of the correction at $16 < E < 350$ GeV that each efficiency introduces are displayed in the top panel of figure 6.26. The combined contribution is displayed in the bottom panel. As in the case of protons, the efficiency effect, which is focused mainly in the North-South direction in Geographical Position coordinates, is spread in several components in galactic coordinates. It is also

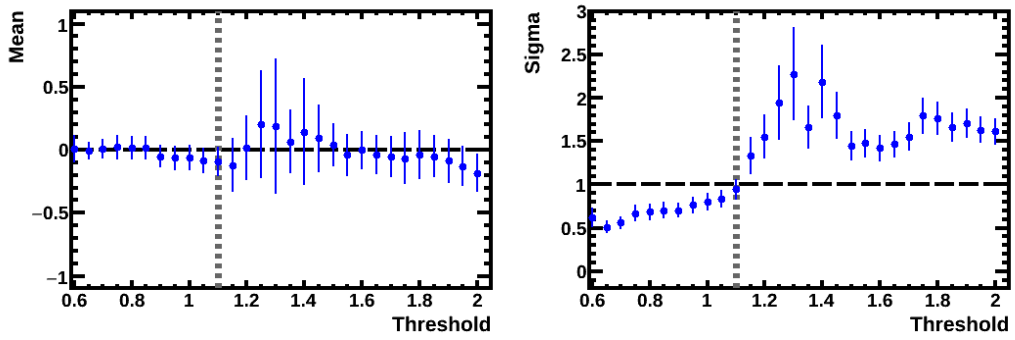

FIGURE 6.25: Scan in the mean *(left)* and sigma *(right)* parameters of the fit to a Gaussian function of the pulls distribution in figure 5.12 as a function of the threshold value. The optimum value of a threshold, which corresponds to mean ~ 0 and sigma ~ 1, ensures that the efficiency corrections with pull below that value are well described by a Gaussian distribution and, therefore, consistent with statistical fluctuations.

noticeable that the multipole component pattern of the total efficiency correction has a similar behavior of that of protons in figure 5.21.

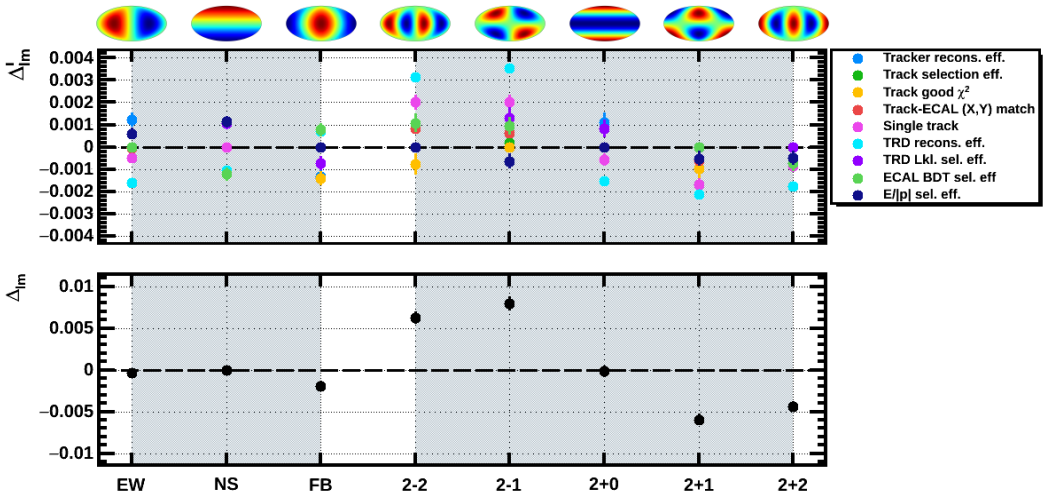

FIGURE 6.26: Individual *(top)* and total *(bottom)* electron efficiency correction for $16 < E < 350$ GeV in galactic coordinates. The fact that each direction is affected by efficiency corrections is the consequence of the projection of the geographic North-South axis into galactic coordinates. Again, the dominant contribution to the final correction is due to the electron TRD reconstruction efficiency.

Finally, the spherical harmonic parametrization of the individual efficiencies is computed with this procedure and the total efficiency allows to correct the exposure time maps. As an example, the skymaps distribution of the parametrization of electron TRD reconstruction efficiency and the total efficiency up to $\ell = 2$ in galactic coordinates for $16 < E < 350$ GeV are presented in figure 6.27.

The observed dependence of electron efficiencies in galactic coordinates is used to correct the exposure time maps. An improvement in the description of the data distribution is evidenced by a reduction in the sigma parameter of the fit to a Gaus-

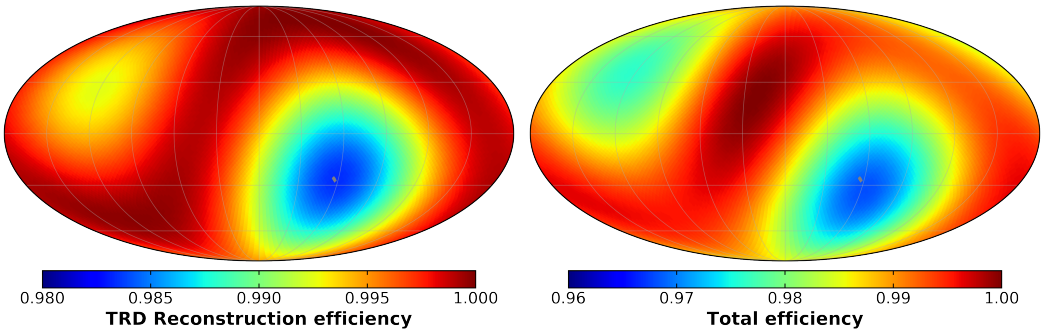

FIGURE 6.27: Galactic skymap of the spherical harmonic parametrization of the electron TRD reconstruction efficiency *(left)* and the electron total efficiency *(right)* up to $\ell = 2$, where only the significant components are included.

sian of the significance distribution in figure 6.28. In addition, the chi-square of the comparison between the skymaps of measured and expected number of events according to the corrected exposure time maps shows an improvement, from an initial value of $\chi^2/d.f. = 839.4/768$ to $\chi^2/d.f. = 790.829/768$. This points out that the quality of the description has improved due to the introduction of the efficiency correction in galactic coordinates.

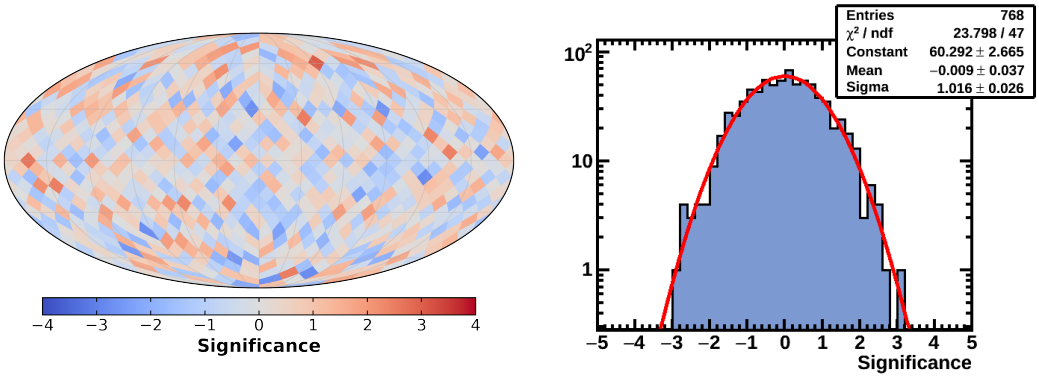

FIGURE 6.28: Significance skymap *(left)* and distribution *(right)* of the electron distribution with respect to the expectation from the corrected exposure for the energy range $16 < E < 350$ GeV in galactic coordinates.

6.7 RESULTS ON THE POSITRON TO ELECTRON RELATIVE ANISOTROPY

The analysis of the positron to electron relative anisotropy provides a complementary characterization of the rise in the positron fraction. In this case, since the corrections determined on the electron sample are identical to those of positrons, the directional fluctuations of the positron to electron flux ratio are examined by the comparison of the skymap distributions of both samples. In this regard, figure 6.29 shows the distribution of positrons and electrons with measured ECAL energy in the range $16 < E < 350$ GeV in galactic coordinates.

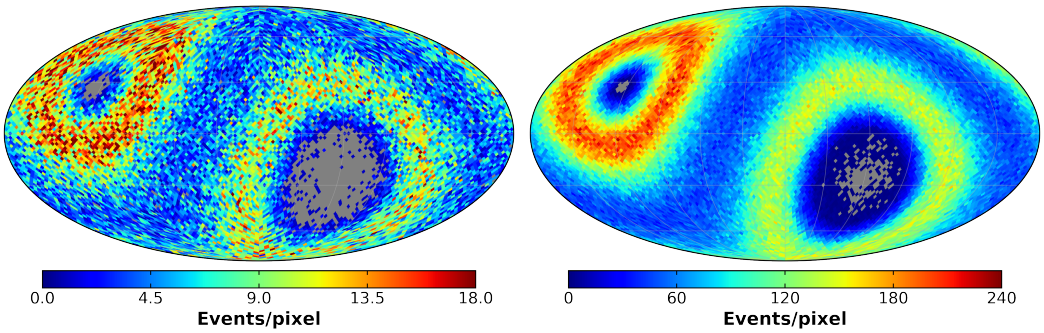

FIGURE 6.29: Skymap distribution of the measured number of positrons *(left)* and electrons *(right)* in the energy range $16 < E < 350$ GeV in galactic coordinates.

The direct comparison of the two event skymaps in terms of the significance estimator is shown in the skymap and distribution of figure 6.30. As can be seen, both distributions are compatible since no evident pattern or structure is observed from the significance skymap, and the distribution is consistent with statistical fluctuactions, therefore well reproduced by a Gaussian.

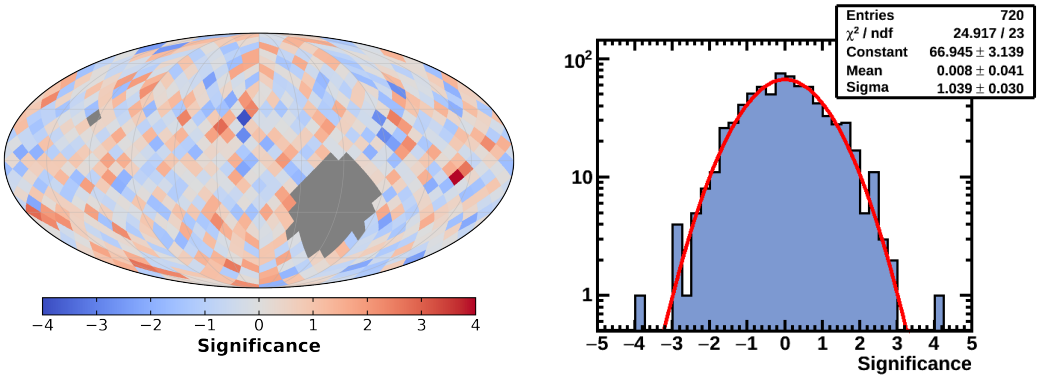

FIGURE 6.30: Significance skymap *(left)* and distribution *(right)* of the positron to electron skymap comparison for the energy range $16 < E < 350$ GV in galactic coordinates.

6.7.1 *Statistical uncertainty and background contamination*

Since the systematic associated to the efficiency correction cancels in the positron to electron ratio, the only uncertainty in the determination of the dipole components of the relative ansotropy arises from the positron sample statistics. Nonetheless, the positron sample is not completely pure and contamination from charged confused electrons and background protons contribute to reduce the sensitivity of the analysis, which turns into an increase of the statistical uncertainty as seen in figure 6.31, where the *equivalent uncertainty* definition of 5.11 has been used for the comparison. In particular, this effect is more evident at high energies, where the contamination due to charge confused electrons becomes more important due to the misidentification of the particle charge sign.

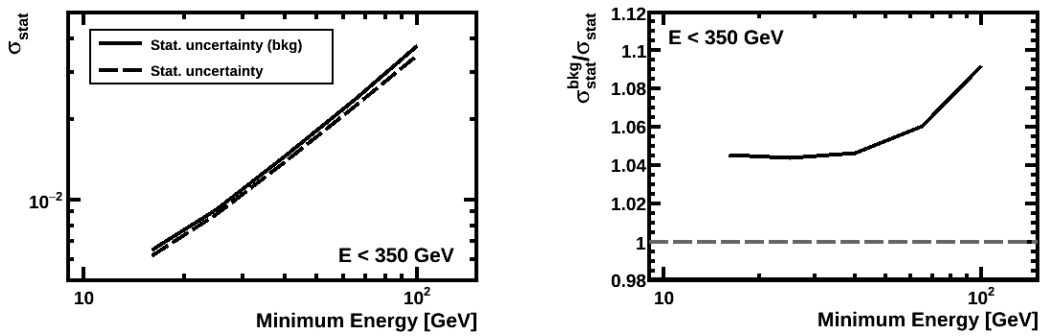

FIGURE 6.31: *(Left)* Absolute values of the statistical uncertainty for the positron relative anisotropy when the sample is assumed to be pure (dashed line) and in the presence of contamination due to charge confusion and background protons (solid line). *(Right)* Ratio of the statistical uncertainties in the two cases, which quantifies the worsening in the uncertainty due to the background contamination in the positron sample.

The increase in the statistical uncertainty can be regarded as a reduction in the sample size. The equivalent sample size that leads to the statistical uncertainty that we have in presence of background is presented in figure 6.32. Finally, table 6.4 collects the measured and equivalent number of events in each cumulative energy range and the ratio between the statistical uncertainty in each case. The second moment of the purity distribution, which according to (3.55) is the relevant variable to quantify the effect of background contamination as well as the expected degradation in the sensitivity are also presented.

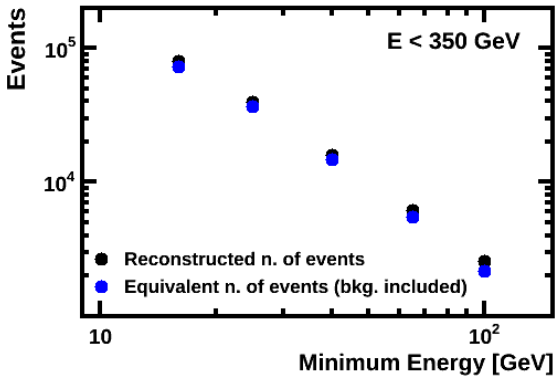

FIGURE 6.32: Comparison between measured number of events and equivalent sample size that lead to the statistical uncertainty in presence of background.

6.7.2 *Results on the positron to electron dipole components*

The determination of the positron to electron relative anisotropy is achieved by means of the binned-likelihood method presented in where the electron sample constitutes the reference. Figure 6.33 shows the results of the three dipole components as a function of the minimum energy of the range, where the purity of the

TABLE 6.4: Effect of the contamination in the positron sample. For each cumulative energy range, the measured and equivalent number of positrons, the integrated charge confusion, the second moment of the purity distribution and the ratio of statistical errors are presented. The expected value of the ratio, calculated from (3.55) is also written.

E_{min} (GeV)	Meas. sample $(\times 10^3)$	Eq. sample $(\times 10^3)$	cc (%)	$\langle p^2 \rangle$ (%)	$\sigma^{bkg}_{stat}/\sigma_{stat}$	Expected
16	79.8	73.0	0.36	91.5	1.05	1.05
25	39.7	36.4	0.41	91.8	1.04	1.04
40	16.0	14.7	0.54	91.4	1.05	1.05
65	6.2	5.5	0.86	89.0	1.06	1.06
100	2.6	2.2	1.46	83.8	1.09	1.09

positron sample at each energy has been accounted. The bands corresponding to the 1 and 2 sigma deviations are presented as well. The absence of significant deviations allows to conclude that positrons are consistent with electrons within the statistical uncertainty at all energy ranges.

From the values of the dipole components, the measured dipole amplitude is computed at the different energy ranges. Figure 6.34-*left* shows the values of the measured dipole amplitude as function of the minimum energy, which are found to be consistent with the expectation from isotropy within the statistical uncertainty. In particular, the measured dipole amplitude at $E_{min} = 16$ GeV is $\delta_M(16\,\text{GeV}) = 1.34\%$.

On the other hand, since the results are consistent with the isotropy hypothesis, a 95% C.I. upper limit on the dipole anisotropy can be quoted at the different energy ranges (figure 6.34-*right*), and at $E_{min} = 16$ GeV it is found to be $\delta^{95\%\text{C.I.}}_{\text{U.L.}}(16\,\text{GeV}) = 2.14\%$.

The numerical results of the positron to electron anisotropy including the fitted dipole components and upper limits for the different cumulative energy ranges are presented in the tables C.3 and C.4 of appendix C.2.

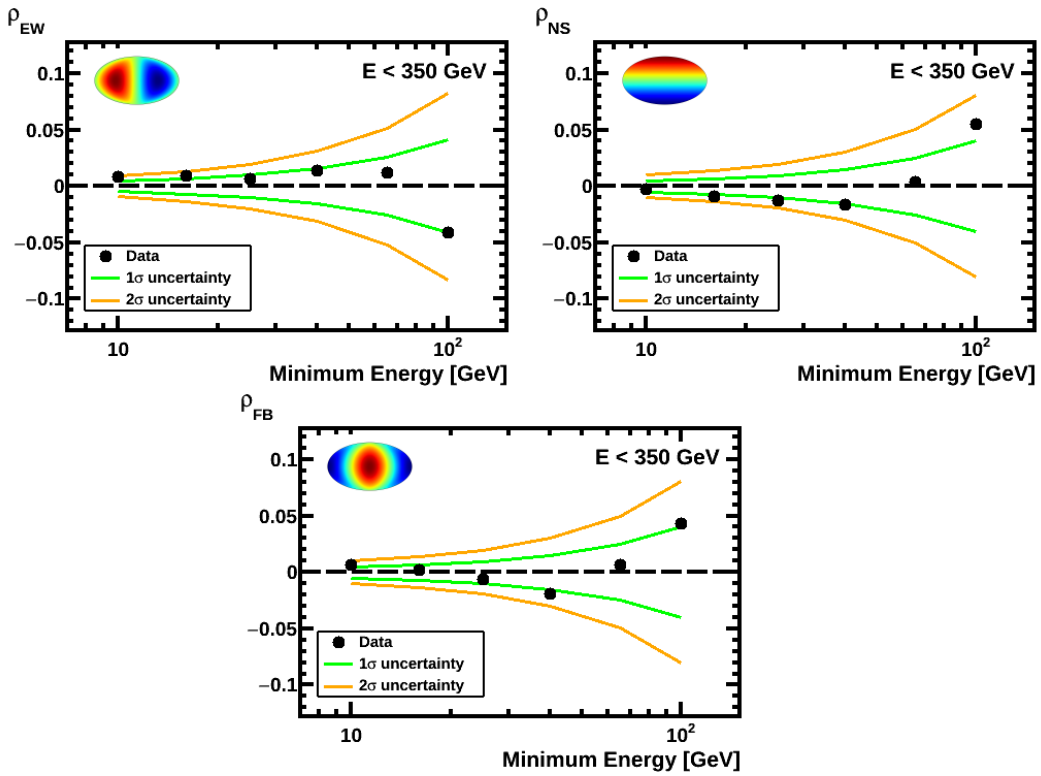

FIGURE 6.33: Values of the East-West *(left)*, North-South *(right)*, and Forward-Backward *(bottom)* dipole components of the positron to electron anisotropy in galactic coordinates as a function of the minimum energy. The 1 and 2-sigma deviations from isotropy (green and yellow solid lines, respectively) corresponding to the statistical uncertainty are shown.

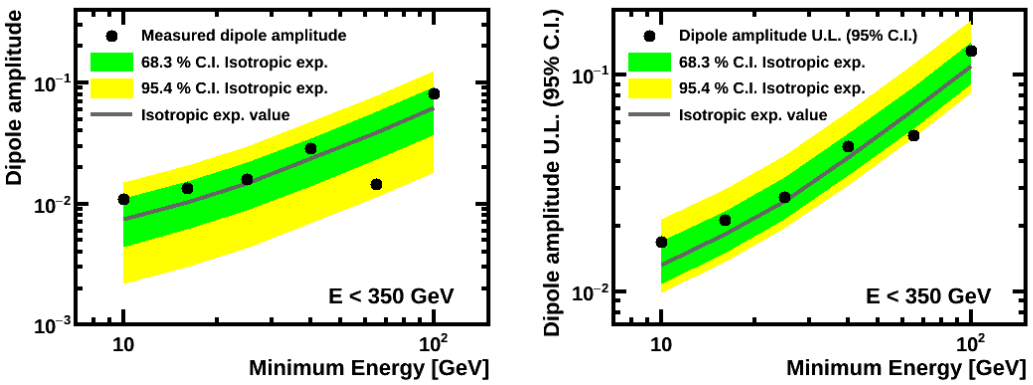

FIGURE 6.34: *(Left)* Measured dipole amplitude of the positron to electron relative anisotropy as a function of the minimum energy in galactic coordinates. *(Right)* 95% C.I. upper limit on the dipole amplitude as a function of the minimum energy. The bands corresponding to the 1 and 2-sigma expectation from isotropy for the total uncertainty are shown in green and yellow, respectively. In each case, the expected value from isotropy given a sample is displayed (solid line).

6.8 RESULTS ON THE ELECTRON ABSOLUTE ANISOTROPY

The measurement of the electron absolute anisotropy constitutes a test of the systematics associated to the efficiency correction that is involved in the measurement of anisotropies of leptons. In this regard, since the analysis in positrons is more sensitive to the existence of primary sources, it is convenient to assess that systematics does not compromise the measurement in the future when more data is collected.

6.8.1 *Impact of efficiency corrections in the multipole components*

The effect of the introduction of the efficiency corrections in the multipole components of the electron absolute anisotropy has been studied by comparing the results obtained before and after the correction is applied.

The North-South associated directions in the dipole and quadrupole components, ρ_{NS} and ρ_{2+0}, in the ISS Geographical Position reference system are shown in figure 6.35. The deviations observed in the dipole and, specially, in the quadrupole components when no corrections are applied are in agreement with the conclusions derived from the significance skymap and distribution in figure 6.15. In addition, the values of the total efficiency correction in each component, Δ_{NS} and Δ_{2+0}, as well as their uncertainty are also displayed. Deviations from zero measured in standard deviations are quantified in the bottom panels.

As can be seen, the efficiency correction contributes to reduce the amplitude of the observed deviations, but it is not sufficient to completely cancel the ρ_{2+0} component, specially at low energies. This result is consistent with the conclusion of the one-dimensional study in figure 6.12-*left* and it might be explained by residual correlations not taken into account in the evaluation of the efficiencies, leading to an underestimation of the correction. For this reason and assuming that ISS Geographical Position constitutes a calibration reference system where a physical signal is not expected, the residual deviation can be regarded as an *effective missing correction* we will need to introduce additionally. This missing correction is taken to be half of the remaining value of the deviation in the North-South direction in ISS Geographical Position, which is the only direction that have impact in galactic coordinates, and its value is also considered as an additional contribution to the systematic uncertainty. In this manner, we ensure that the final value of the multipole component is consistent, within the systematic uncertainty, with both isotropy case and the result obtained with only efficiency correction.

In galactic coordinates, the improvement introduced by the efficiency corrections is particularly evident in the ρ_{2-2} component (figure 6.36). Although no significant deviations from zero are observed within the statistical and efficiency correction uncertainties, the need of additional missing corrections in ISS Geographical Position, where any efficiency effect is enhanced, must be considered in galactic coordinates. In this regard, the missing correction in galactic coordinates and its associated systematic uncertainty are obtained from the matrix transformation of that calculated in ISS Geographical Position coordinates.

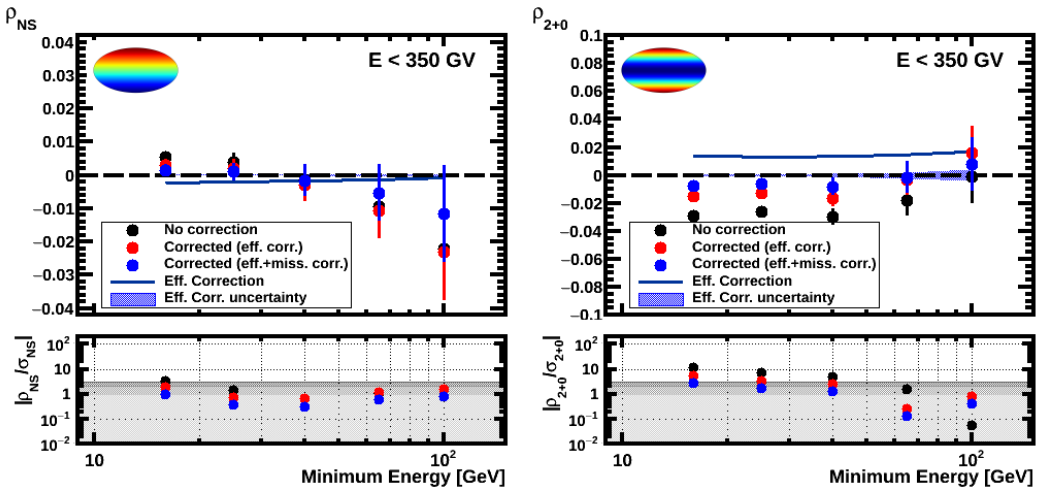

FIGURE 6.35: Electron components associated to the North-South directions in ISS Geographical Position, ρ_{NS} *(left)* and ρ_{2+0} *(right)* without efficiency correction (black dots), including the efficiency correction in the reference map (red dots), and including the additional missing correction (blue dots). The error bars on the dots stand for the statistical uncertainty on the component. The value of the efficiency correction is displayed as a solid blue line and the blue band corresponds to its uncertainty, obtained as the propagation of the uncertainties of the individual efficiency corrections. Distance from isotropy hypothesis is measured in terms of sigmas, which include the statistical, efficiency correction and missing correction uncertainties in each case.

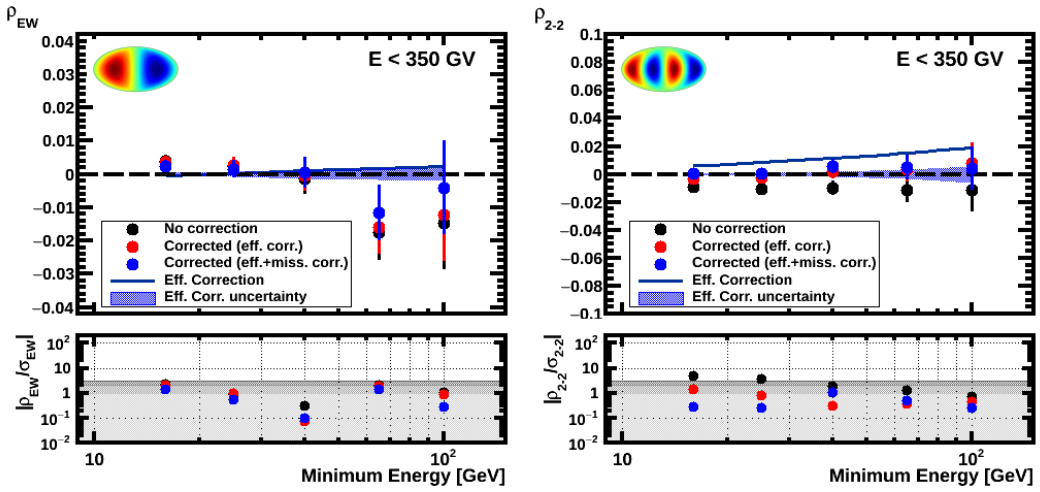

FIGURE 6.36: Electron multipole components ρ_{EW} *(left)* and ρ_{2-2} *(right)* in galactic coordinates without efficiency correction (black dots), including the efficiency correction in the reference map (red dots), and including the additional missing correction (blue dots). The electron total efficiency correction (solid line) and its associated uncertainty (blue band) are also shown. Deviations from zero are quantified in standard deviations.

6.8.2 *Systematic uncertainties on dipole components*

The electron sample can be considered 100% pure and, therefore, the statistical uncertainty on the dipole component is associated directly to the electron sam-

ple size. On the other hand, the systematic uncertainty has several contributions, which arise from the corrections introduced in the construction of the reference maps. Apart from the systematic related to the missing correction, which has been already discussed, two additional contributions from the efficiency corrections are considered, in a similar manner to those of protons:

- The uncertainty of the electron total efficiency correction, obtained as the propagation of the uncertainties associated to the individual efficiency corrections. Ultimately, this uncertainty has a statistical origin since the precision in its determination depends on the size of the samples used to evaluate the efficiency.
- The uncertainty in the determination of significant corrections. As in the case of protons, the effect that a variation of ± 0.2 around the threshold value determined in figure 6.25 has on the total efficiency correction is considered as an additional source of systematics. The dipole components of the total efficiency correction in the two cases are shown in figure 6.37, and the difference is taken as a systematic in the corresponding component. In this regard, minor variations in the total efficiency correction are observed in the East-West and Forward-Backward components, whereas the North-South component is not affected.

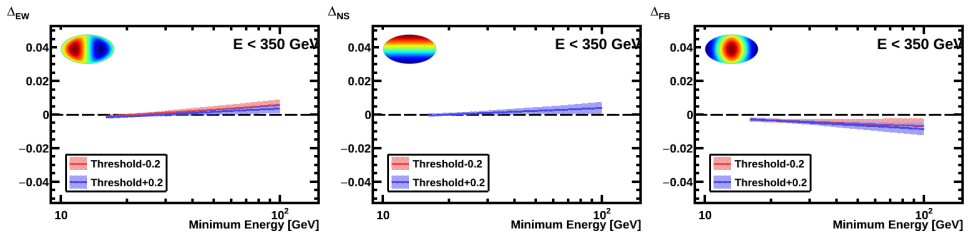

FIGURE 6.37: East-West *(left)*, North-South *(center)* and Forward-Backward *(right)* components of the electron total efficiency correction obtained after applying a shift of -0.2 (red) or $+0.2$ (blue) to the threshold value in figure 6.25 used to reject non-significant efficiency corrections in galactic coordinates. The difference is taken as a systematic.

The contribution of each source to the total systematic uncertainty can be studied in terms of the equivalent uncertainty, σ_{eq}, defined in (5.11), which is shown in figure 6.38. As can be seen, the dominant source of systematic arises from the introduction of the missing correction. This source of systematic may be overestimated, specially at high energies; however, as we will see in the next section, the total uncertainty is dominated by statistics in any case.

On the other hand, the contribution of the election of significant efficiency corrections have a minor impact in the total systematic uncertainty.

6.8.3 *Total uncertainty on dipole components*

The total uncertainty on the dipole components of the electron absolute anisotropy is the combination of the aforementioned statistical and systematic uncertainties, which are shown in figure 6.39-*left*. In addition, the ratio of the systematic and total

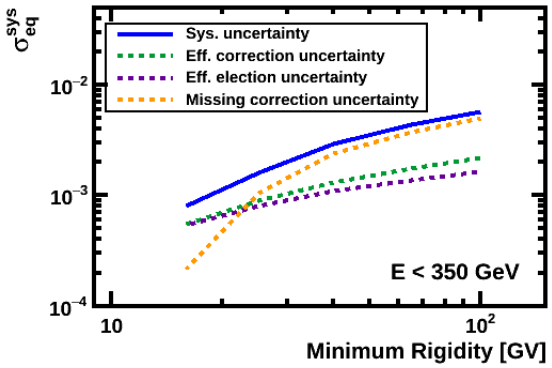

FIGURE 6.38: Contributions to the electron systematic uncertainty (blue solid line) from the efficiency correction uncertainty (green dotted line), efficiency election uncertainty (purple dotted line), and missing correction (yellow dotted line). The dominant contribution is due to the missing correction, with a negligible contribution from the election of significant corrections.

uncertainties with respect to the statistical error is presented in the right panel. As can be seen, statistics is the dominant contribution to the final uncertainty.

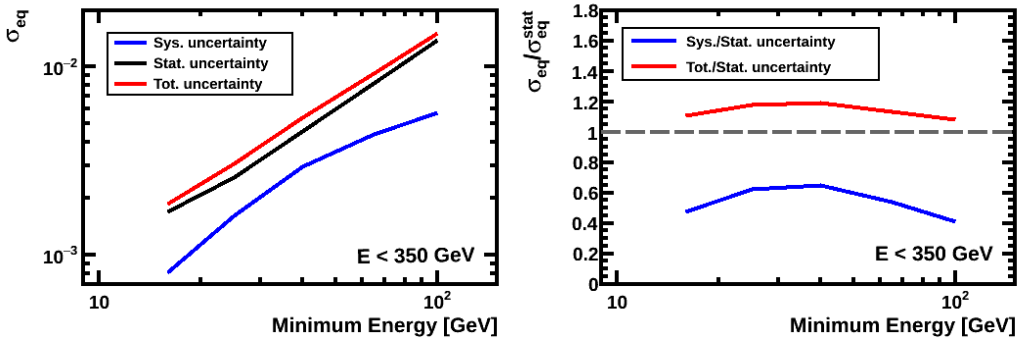

FIGURE 6.39: *(Left)* Statistical, systematic and total equivalent uncertainty of the dipole components of the electron absolute anisotropy in galactic coordinates. *(Right)* Ratio of the total and systematic equivalent uncertainties with respect to the statistical one.

6.8.4 *Results on the electron dipole components*

The measurement of the electron absolute anisotropy is performed in cumulative energy bins using the binned-likelihood fit presented in section 3.5.1 where the reference maps include the efficiency and missing corrections. The value of the three dipole components as function of the minimum energy is presented in figure 6.40, where the bands corresponding to the 1 and 2 sigma deviations from isotropy are shown. The results are compatible with the isotropy hypothesis at all energy ranges within the statistical and systematic uncertainties.

On the other hand, the measured dipole amplitude can be calculated from the dipole components at the different energy ranges (figure 6.41-*left*) The values are

compatible with the expectation from the isotropy within the statistical and systematic uncertainties. In particular, the measured dipole amplitude at $E_{\text{min}} = 16$ GeV is $\delta_{\text{M}}(16\,\text{GeV}) = 0.37\%$.

Since the measurement is consistent with the hypothesis of isotropy, a 95% C.I. upper limit on the dipole amplitude can be established at the different energy ranges (figure 6.41-*right*). In the lowest energy range, the upper limit on the dipole amplitude is found to be $\delta_{\text{U.L.}}^{95\%\text{C.I.}}(16\,\text{GeV}) = 0.6\%$.

The numerical results of the electron anisotropy corresponding to the dipole components of the analysis and the upper limits computed for the different cumulative energy ranges are presented in the table C.7 of appendix C.4.

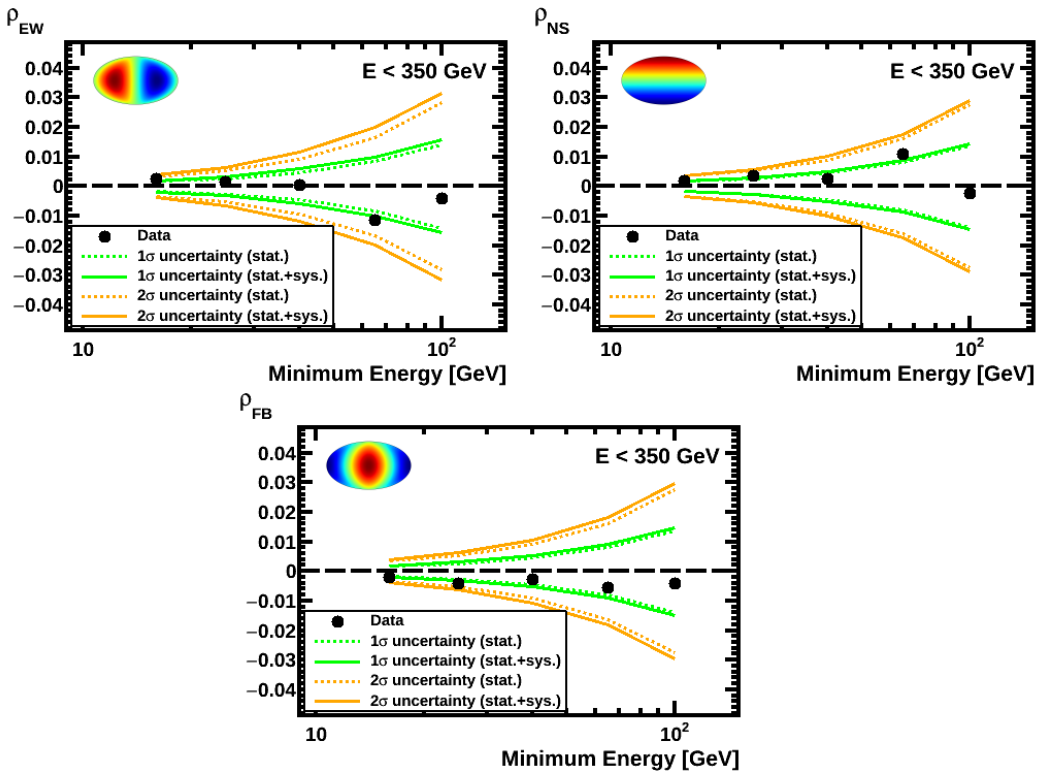

FIGURE 6.40: Values of the East-West *(left)*, North-South *(right)*, and Forward-Backward *(bottom)* dipole components of the electron absolute anisotropy in galactic coordinates. The 1 and 2-sigma deviations from isotropy (green and yellow, respectively) corresponding to the statistical (dotted lines) and total (solid line) uncertainties are shown.

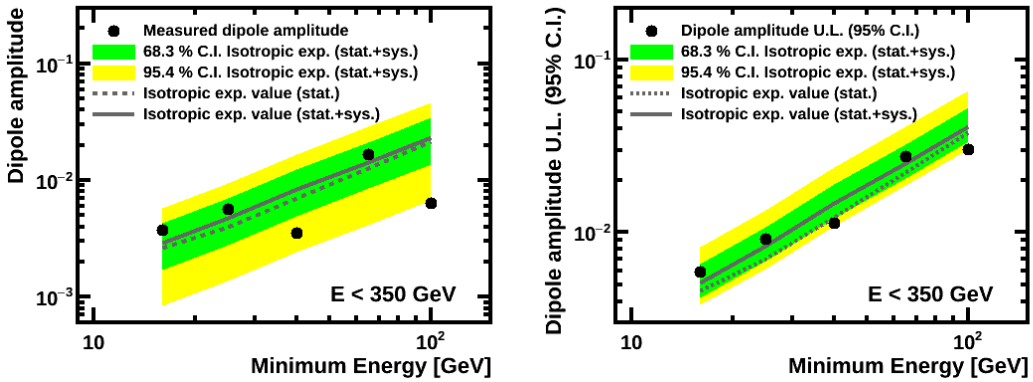

FIGURE 6.41: *(Left)* Measured electron dipole amplitude as a function of the minimum energy in galactic coordinates. *(Right)* 95% C.I. upper limit on the electron dipole anisotropy as a function of the minimum rigidity in galactic coordinates. The bands corresponding to the 1 and 2-sigma expectation from isotropy for the total uncertainty are shown in green and yellow, respectively. In each case, the expected value from isotropy given a sample is displayed considering only the statistical uncertainty (dotted line) and the total uncertainty (solid line).

6.9 RESULTS ON THE POSITRON ABSOLUTE ANISOTROPY

6.9.1 *Impact of efficiency corrections in the multipole components*

Similarly to the electron absolute anisotropy, the effect of the efficiency corrections in the positron dipole components can be studied by comparing the results obtained when the reference includes them or not. The components associated to the North-South direction in ISS Geographical Position, ρ_{NS} and ρ_{2+0}, are presented in figure 6.42, as well as the efficiency correction introduced. Due to the limited sample size, the deviations observed when no correction is introduced are less significant than in the electron case. Nevertheless, an improvement in the dipole and, specially, in the quadrupole component is evident.

On the other hand, due to the higher statistics, the electron analysis pointed out the need for introducing additional missing corrections due to an underestimation of the efficiency correction. Since the positron absolute analysis uses the identical efficiency correction and given that positrons are consistent with electrons, the missing correction determined with the electron sample has to be applied in this case. Likewise, the systematic uncertainty due to the additional missing correction is also considered.

In galactic coordinates the results corresponding to the components ρ_{EW} and ρ_{2-2} are shown in figure 6.43. As can be seen, the dipole component is almost unchanged whereas the quadrupole term suffers a minor variation. In any case, although the results without the introduction of efficiency corrections were consistent with isotropy within the statistical uncertainty, a general improvement is observed when the correction is included in the reference.

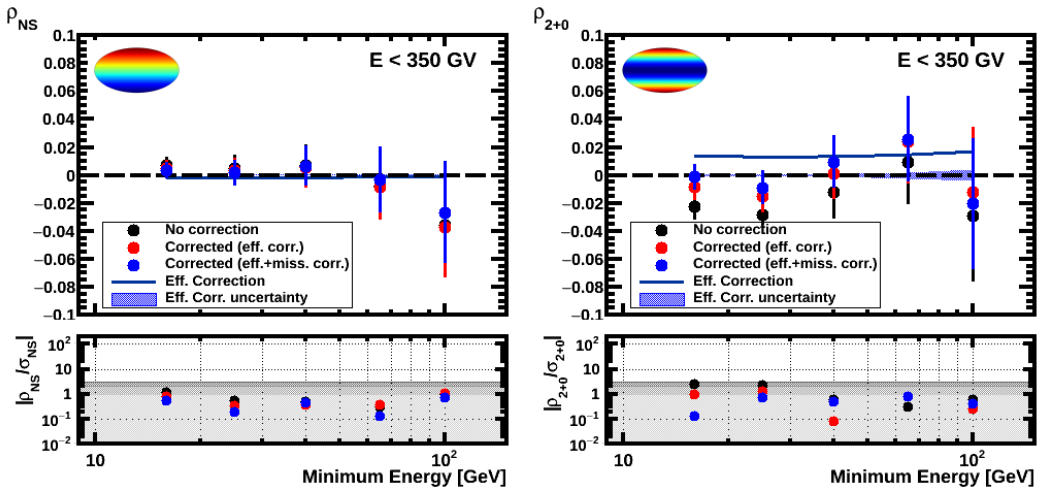

FIGURE 6.42: Positron components associated to the North-South directions in ISS Geographical Position, ρ_{NS} *(left)* and ρ_{2+0} *(right)* without efficiency correction (black dots), including the efficiency correction in the reference map (red dots), and including the additional missing correction (blue dots). The total efficiency correction (solid line) and its associated uncertainty (blue band) are also shown. Deviations from zero are quantified in sigmas.

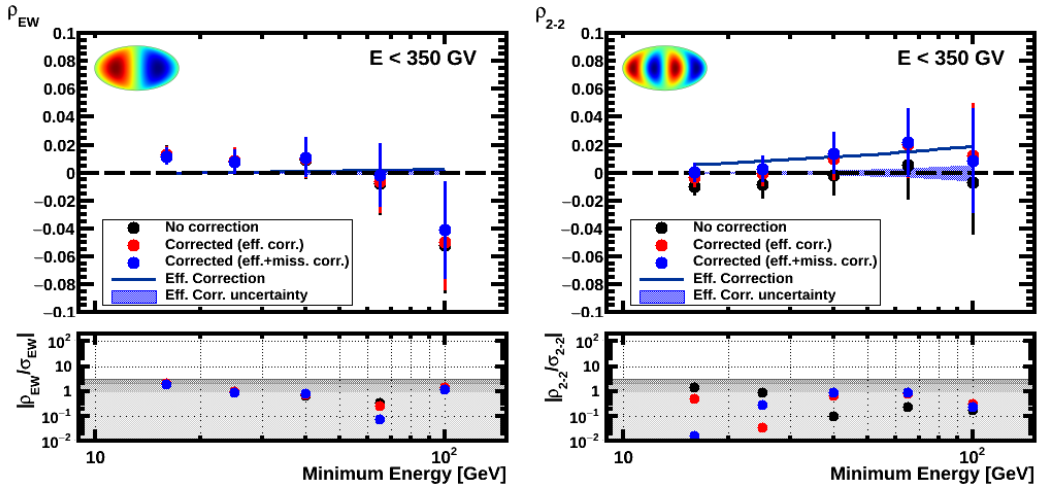

FIGURE 6.43: Positron multipole components ρ_{EW} *(left)* and ρ_{2-2} *(right)* in galactic coordinates without efficiency correction (black dots), including the efficiency correction in the reference map (red dots), and including the additional missing correction (blue dots). The total efficiency correction (solid line) and its associated uncertainty (blue band) are also shown. Deviations from zero are quantified in sigmas.

6.9.2 *Systematic and total uncertainty on positron dipole components*

The uncertainty in the dipole components of the positron absolute anisotropy has two contributions, namely, the statistical uncertainty after the introduction of the positron purity in the analysis, which was already discussed in section 6.7.1; and the systematic uncertainty, which is the identical to that of the electron absolute anisotropy in section 6.8.2. The contribution of the statistical and systematic un-

certainties to the total one are shown in figure 6.44. From the ratio with respect the statistical error, we conclude that the dominant contribution to the total uncertainty of the measurement arises from the size of the sample.

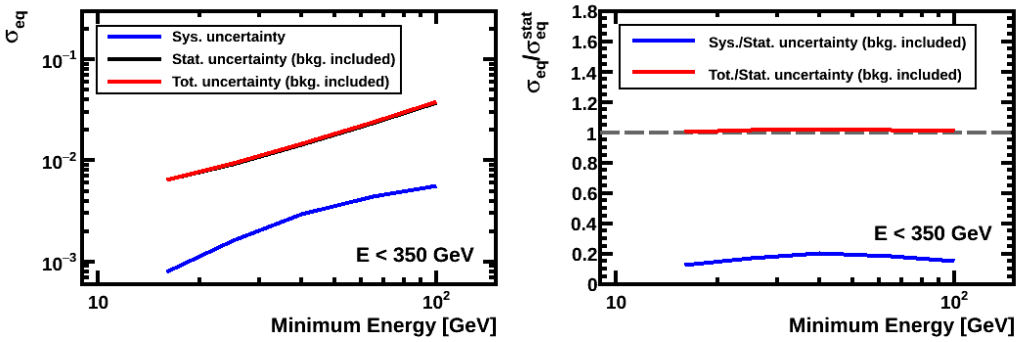

FIGURE 6.44: *(Left)* Statistical, systematic and total equivalent uncertainty of the dipole components of the positron absolute anisotropy in galactic coordinates. *(Right)* Ratio of the total and systematic equivalent uncertainties with respect to the statistical one. Statistical uncertainty includes the purity of the positron sample.

6.9.3 *Results on the positron dipole components*

The determination of the three dipole components of the positron absolute anisotropy in galactic coordinates follows the same procedure as that of the electron analysis. The binned-likelihood fit provides the values of the components at the different energy ranges, using as reference the exposure map with the efficiency and missing corrections and considering the purity of the positron sample at the different energies. The results, which are shown in figure 6.45 as a function of the minimum energy, show no significant deviation from isotropy within the statistical and systematic uncertainties. Furthermore, the results are consistent with those obtained in the positron to electron relative anisotropy.

The values of the dipole components are used to calculate the measured dipole amplitude at the different energy ranges (figure 6.46-*left*), which are found to be compatible with the isotropy expectations within the statistical and systematic uncertainties. At the lowest energy range, $E_{\rm min} = 16$ GeV, the measured dipole amplitude is $\delta_{\rm M}(16\,{\rm GeV}) = 1.4\%$.

Finally, since the results are consistent with isotropy, the 95% C.I. upper limit on the dipole amplitude can be quoted (figure 6.46-*right*). In particular, at $E_{\rm min} = 16$ GeV, the determined upper limit is $\delta^{95\%\,{\rm C.I.}}_{\rm U.L.}(16\,{\rm GeV}) = 2.19\%$, in full agreement with the results obtained in the positron to electron anisotropy.

The numerical results coresponding to the fitted dipole components and upper limits obtained in the measurement of the positron absolute anisotropy are presented in the tables C.6 and C.5 of appendix C.3.

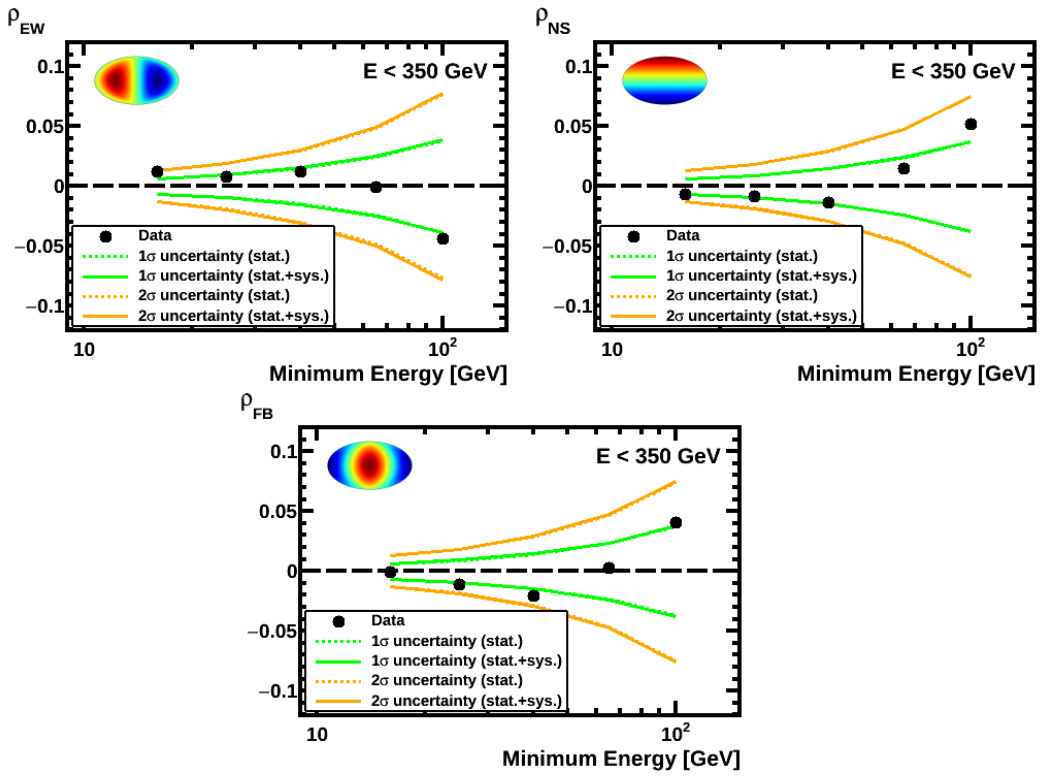

FIGURE 6.45: Values of the East-West *(left)*, North-South *(right)*, and Forward-Backward *(bottom)* dipole components of the positron absolute anisotropy in galactic coordinates. The 1 and 2-sigma deviations from isotropy (green and yellow, respectively) corresponding to the statistical (dotted lines) and total (solid line) uncertainties are shown.

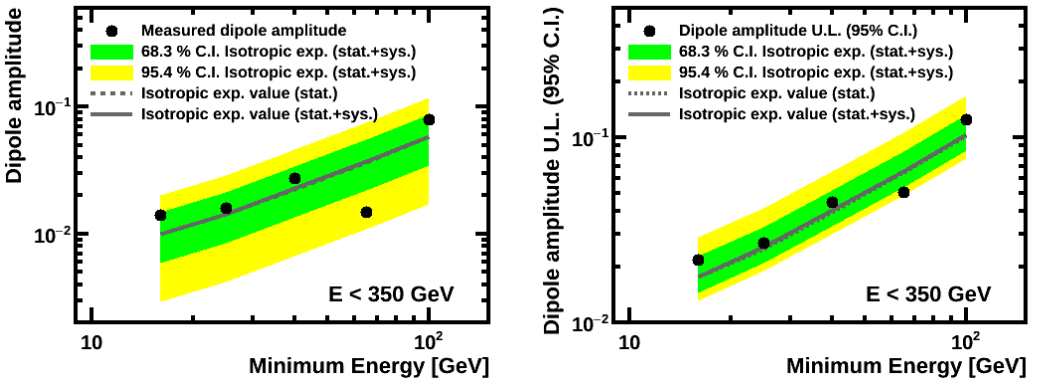

FIGURE 6.46: *(Left)* Measured dipole amplitude as a function of the minimum energy. *(Right)* 95% C.I. upper limit on the dipole amplitude as a function of the minimum rigidity. The bands corresponding to the 1 and 2-sigma expectation from isotropy for the total uncertainty are shown in green and yellow, respectively. In each case, the expected value from isotropy given a sample is displayed considering only the statistical uncertainty (dotted line) and the total uncertainty (solid line).

7

CONCLUSIONS AND OUTLOOK

In the last years, the precision era of Cosmic Ray Physics has started thanks to the high statistics direct measurements conducted by space-based experiments. Particle physics detectors placed on board satellites and the International Space Station profit from a large acceptance to carry out accurate measurements in GeV-TeV galactic cosmic ray particles. The precise results provided by these experiments constitute an open window to new cosmic ray phenomena using the Universe as laboratory.

In particular, high statistics measurements performed by AMS-02 on electrons, positrons and protons defy the current paradigm of cosmic ray propagation and origin. The reported rise in the positron fraction, originated by an steady increase in the positron flux from energies above ~ 10 GeV, challenges the standard picture of cosmic rays, where cosmic ray antimatter is assumed to have a secondary origin. The additional contribution to the tiny secondary component may be produced by nearby primary sources of positrons, whether of astrophysical or exotic origin. Thus, the indirect search for Dark Matter by means of precision measurements on the positron channel provide an open window into fundamental physics.

On the other hand, at rigidities above $R > 100$ GV the proton flux measured by AMS-02 deviates from the traditional single power law assumed by the standard model of cosmic rays. The precise measurement by AMS-02 allowed to characterize the progressively hardening of the spectrum, which may be due to the injection of fresh high rigidity protons by local sources or changes in the diffusive regime in the GMF.

In both cases, the new physics phenomena explaining the features observed in the spectra have implications in other studies, such as the anisotropy of cosmic rays. The directionality of galactic cosmic rays can be regarded as a signature of the new physical mechanisms or additional cosmic ray sources proposed to explain the observed deviations. Therefore, in this multimessenger approach the measurement of the anisotropy in arrival directions of cosmic rays is a complementary tool to characterize the new phenomena observed in their spectra and may help to understand their origin.

The propagation of galactic cosmic rays in the GeV-TeV range is, essentially, diffusive. As a result, the flux observed at Earth is highly isotropic due to the randomization introduced by the galactic magnetic fields. However, the existence of nearby sources or processes in the local environment may induce an small anisotropy whose amplitude varies from 10^{-2} to 10^{-5}.

The measurement of the large scale anisotropy, described at first order by a dipole, is a challenge for any cosmic ray experiment due to the high precision required to achieve such high sensitivity. In particular, an accurate knowledge of the detector behavior is mandatory to ensure that variations of detection efficiencies do not com-

promise the measurement. A precise understanding of detection effects allows to construct reference maps for the absolute determination of the cosmic ray anisotropy. Those reference maps represent the detector exposure to any direction in a given coordinate system and constitute the hypothesis of isotropy in the study.

Traditionally, large scale anisotropies have been measured by ground-based experiments. However, in many cases the skymap coverage is not full and the techniques used to compute the exposure map do not allow a three-dimensional measurement of the dipole. On the other hand, directional studies of cosmic rays by space-based experiments in the new precision era profit from a nearly full coverage of the skymap and an excellent particle identification. Nonetheless, the methods developed and applied by ground-based detectors are not valid for space-based experiments and new reliable techniques to construct reference maps need to be established.

This thesis presents a novel method in the determination of the reference maps and a set of statistical tools developed for anisotropy searches with space-based experiments. A systematic procedure, valid for all cosmic ray species, has been established:

- Acceptance is divided in bins, each of one represents a direction in detector's local coordinates. Exposure time maps and event distribution maps in the coordinate system of analysis are built for each pixel. Analysis in individual bins is performed.
- Geographical dependence of efficiencies may induce spurious signals in cosmic ray arrival directions in the coordinate system of analysis. A parameterization of efficiencies in terms of spherical harmonics has been used to take into account these effects.

A binned-likelihood fit is used to compare the distribution of events under study and the reference map, and takes into account the differences in the exposure for different energies or rigidities due to geomagnetic cutoff, and the purity of the sample.

The analysis motivates the use of two different kind of coordinate systems according to the physics purpose: calibration coordinate systems, such as ISS Geographical Position, are intrinsic to the detector behavior and are suitable to assess the effect of efficiency variations; physics reference frames, such as galactic coordinate systems, are relevant for the analysis and search for physics processes or nearby sources connected to the features observed in the galactic cosmic ray species. Once the effects of the efficiencies are characterized and understood in the ISS Geographical Position coordinate system, a dedicated study in the galactic reference frame is performed.

The results presented in this thesis correspond to the sample of protons, electrons and positrons collected by AMS-02 during its first five years of data taking, from 2011 May 19 to 2016 May 26. Before applying the developed techniques to the AMS-02 data, a Toy Monte Carlo AMS-like detector has been simulated. The simulation allowed to verify that an injected signal is fully recovered without bias, thus allowing to validate the statistical methods established in the determination of the dipole components. In addition, it provided useful information to characterize the trans-

formation of signals from different coordinate systems for an AMS-like detector in the period of analysis.

Due to the high statistics, the measurement of anisotropy in the proton sample requires a high precision in the determination of the reference maps, especially, in the geographical variation of the detection efficiencies. The results in galactic coordinates and true rigidity, after taking into account the effects of the finite rigidity resolution of the AMS-02 Tracker, are consistent with the isotropy expectations at all rigidity ranges. The uncertainties are dominated by statistics at rigidities $R > 80$ GV, and, in particular, for $R > 300$ GV, the upper limit on the proton dipole anisotropy is found to be $\delta^{95\%\text{C.I.}}_{\text{U.L.}}(300\text{ GV}) = 1.07 \times 10^{-2}$.

On the other hand, the measurement of the anisotropy on cosmic ray electrons and positrons has been carried out on pure samples achieved by means of a cut based analysis. Information from different AMS-02 subdetectors, specially TRD, Tracker and ECAL, is used to separate leptons from protons with a proton contamination below the percent level. In addition, a dedicated study of the geographical dependence of electron efficiencies has been presented.

Since the positron flux is dominated by the source term above few tens of GeV, the measurement of the positron anisotropy is a probe of the new phenomena. The identification of positrons and, in general, of antimatter, relies in the sign of the charge, which can be only achieved by magnetic spectrometers. For positrons, consistent results in galactic coordinates on the positron to electron anisotropy and positron absolute anisotropy have been obtained. The results, which take into account the residual proton contamination and charge confusion, are consistent with isotropy at all energy ranges. In particular, for $16 < E < 350$ GeV, the upper limits on the positron dipole anisotropy are set to $\delta^{95\%\text{C.I.}}_{e^+/e^-\text{U.L.}}(16\text{ GeV}) = 2.14\%$ and $\delta^{95\%\text{C.I.}}_{e^+\text{U.L.}}(16\text{ GeV}) = 2.19\%$.

Electrons are used to test the systematics of the measurement on a high statistics sample. In this sense, the analysis is dominated by statistics at all energy ranges and, in particular, systematics will not compromise the measurement on the $200,000$ positrons collected by the end of the AMS-02 data taking in 2024. The upper limit for $16 < E < 350$ GeV on the electron dipole anisotropy in galactic coordinates is found to be $\delta^{95\%\text{C.I.}}_{\text{U.L.}}(16\text{ GeV}) = 0.6\%$.

Future challenges for the proton anisotropy study comprise the increase of statistics by including protons from other track pattern configurations. However, there is a trade off between the gain in statistics as a result of the increased acceptance and the worsening in the rigidity resolution as consequence of a smaller lever arm in the rigidity measurement. In any case, an improvement is expected if a combined measurement of anisotropies is performed on fullspan and L1+Inner protons.

Regarding positrons and electrons, the data collected during the AMS-02 mission will allow to explore positron anisotropies without systematic bias at the 1% level by the end of the data taking at 2024, as shown in figure 7.1.

On the other hand, in order to increase the maximum energy of the lepton analyses a different selection strategy has to be considered. At high energies, where the performance of the TRD rejection decreases, the proton rejection must rely on a template-fit analysis based on a Monte Carlo simulation. In addition, charge con-

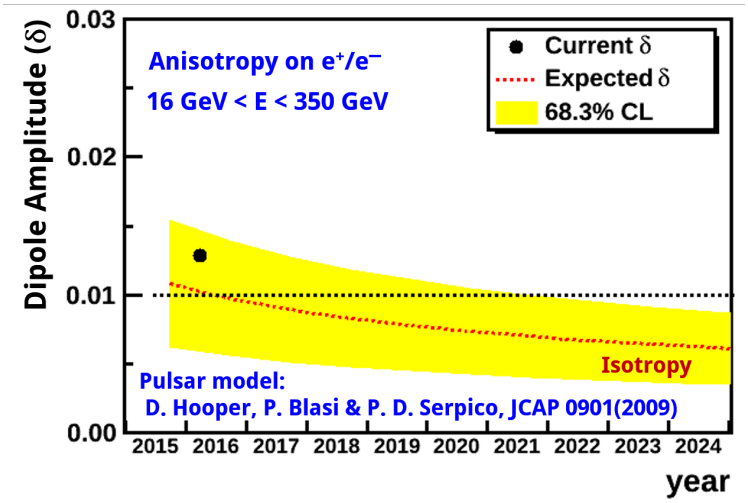

FIGURE 7.1: Projection of the expected dipole amplitude on the e^+/e^- anisotropy for $16 < E < 350$ GeV up to the end of the data taking in 2024. The current dipole amplitude (black dot) and the isotropic expectation (dashed red line and yellow band) projected to 2024 are displayed. In addition, the expectation from a pulsar model based on [146] is shown.

fusion is intrinsically associated to the finite resolution of the tracker and its effect increases at high energies. Thus, to achieve a pure sample of positrons a charge confusion estimator should be considered.

Finally, the method developed in this thesis and applied to electrons, positrons and protons can be extended to other cosmic ray nuclei measured by AMS-02. In this sense, AMS-02 will continue collecting data during the ISS lifetime and the measurement of anisotropies in the different cosmic ray species will provide valuable information about their origin and propagation.

APPENDIX

A

BAYESIAN AND FREQUENTIST UPPER LIMITS ON THE DIPOLE AMPLITUDE

As it was stated in section 3.6, Bayesian and Frequentist approaches can be used to compute upper limits on the dipole amplitude. Bayesian approach, which has been used throughout this thesis, was already presented in that section. This appendix is devoted to describe the Frequentist treatment in the calculation of upper limits and to provide a comparison between the two prescriptions.

In the Frequentist treatment, the classical procedure due to Neyman [220] constructs the one-sided interval such that the upper limit on the true dipole parameter corresponds to the value $\delta_{\rm T}$ which ensures that the probability of measuring a dipole anisotropy less than $\delta_{\rm M}$ is $1-\alpha$, for a certain confidence level, α

$$\int_0^{\delta_{\rm M}} p(\hat{\delta}_{\rm M}|\delta_{\rm T}) d\hat{\delta}_{\rm M} = 1-\alpha \tag{A.1}$$

Therefore, by definition, frequentist intervals include the true value of the parameter with a probability equal to α, called the *coverage probability*, which means that, if there is a large number of realizations, frequentist intervals would exclude the true value in a fraction $1-\alpha$ of the cases. In particular, isotropy hypothesis would be excluded in the $1-\alpha$ fraction of the isotropic samples. On the other hand, Neyman prescription fails to set upper limits for small values of $\delta_{\rm M}$, so that another procedure is used to avoid this problem.

Feldman and Cousins prescription [221] exploits the degree of freedom in the construction of Neyman intervals (the so called *ordering rule* [217, 222]) to establish upper limits in the case of small $\delta_{\rm M}$. However, for large values of $\delta_{\rm M}$, Feldman and Cousins procedure does no longer provide an upper limit, but a two-sided confidence interval.

For these reasons, Frequentist treatment does not provide a unique determination of the upper limits valid for all range of $\delta_{\rm M}$ and satisfying the condition of preserving the coverage probability.

As discussed in section 3.6, projections onto the vertical axis of the distribution in figure A.1-*top left* for a measured value of $\delta_{\rm M}\times\sqrt{N}$ provide the posterior probability needed to compute the upper limit in the Bayesian approach (figure A.1-*bottom left*). In addition, projections onto the horizontal axis provide the distribution $p(\delta_{\rm M}|\delta_{\rm T})$ for a value of $\delta_{\rm T}\times\sqrt{N}$ such that (A.1) is satisfied for a measured $\delta_{\rm M}\times\sqrt{N}$ (figure A.1-*top right*).

In the exampled used, the 95% C.L. obtained in the Neyman prescription for a measured dipole amplitude $\delta_{\rm M}\times\sqrt{N}=4$ corresponds to a value of the measured amplitude $\delta_{\rm T}^{\rm U.L.}\times\sqrt{N}\sim 6.25$, in agreement to the 95% C.I. retrieved in the Bayesian approach, which was found to be $\delta_{\rm T}^{\rm U.L.}\times\sqrt{N}\sim 6.18$.

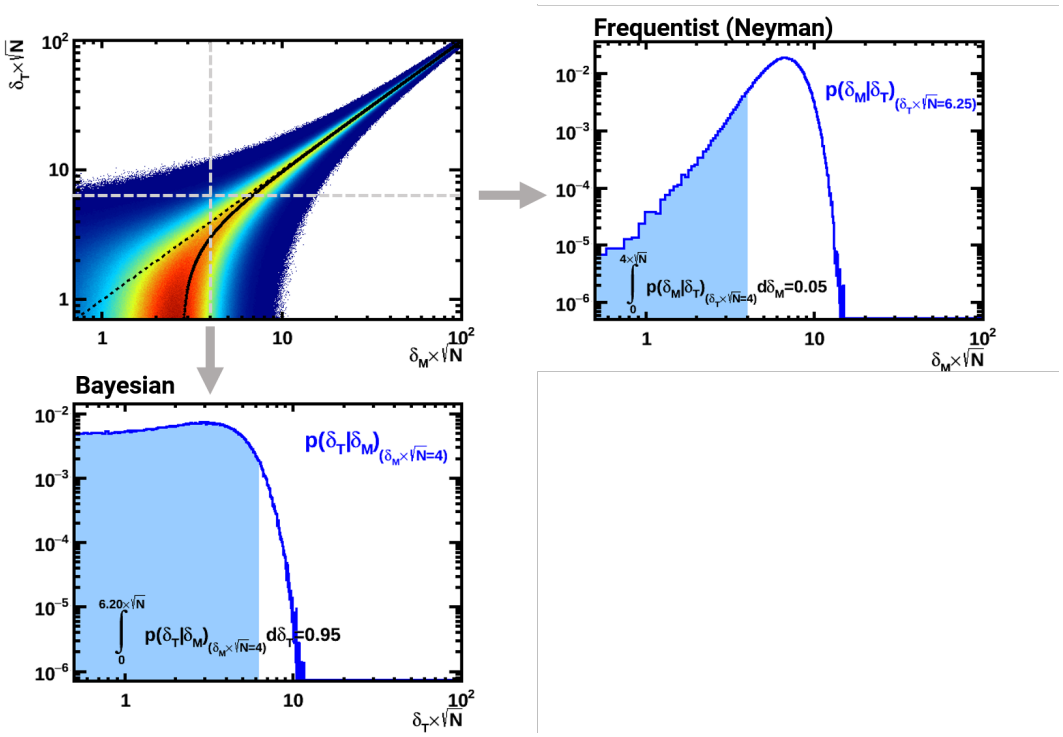

FIGURE A.1: *(Top-left)* Distribution of δ_{M} for different values of δ_{T}, both scaled by the sample size, $\sqrt{N}$. Solid black line shows the expected value of δ_{M} according to the $p(\delta_{\mathrm{M}}|\delta_{\mathrm{T}})$ distribution for each value of δ_{T}. *(Top-right)* Probability distribution function $p(\delta_{\mathrm{M}}|\delta_{\mathrm{N}})$ that ensures a probability content of $1-\alpha=0.05$ for $\delta_{\mathrm{M}}\times\sqrt{N}=4$ according to Neyman prescription. *(Bottom-left)* Posterior probability $p(\delta_{\mathrm{T}}|\delta_{\mathrm{M}})$ for $\delta_{\mathrm{M}}\times\sqrt{N}=4$ and upper limit computation according to Bayesian prescription.

On the other hand, figure A.2-*left* shows the the comparison of the upper limits obtained using the three different approaches. As it was mentioned, Neyman prescription underestimates the upper limit for values $\delta_{\mathrm{M}}\times\sqrt{N}\lesssim 3$. Feldman and Cousins approach does not have this problem for small $\delta_{\mathrm{M}}\times\sqrt{N}$, but it provides a two-sided interval for values $\delta_{\mathrm{M}}\times\sqrt{N}\gtrsim 5$. Bayesian prescription is able to provide a smooth determination of the upper limits for any value of $\delta_{\mathrm{M}}\times\sqrt{N}$.

In addition, as it can be seen in figure A.2-*right*, Bayesian approach agrees numerically within 15% with Frequentist constructions where Frequentist are appliable. This level of agreement lies within the sample variance of the upper limit. For these reasons, Bayesian approach has been chosen to compute upper limits.

A comparison between the Bayesian upper limits obtained in this thesis and the ones computed according to Neyman, and Feldman and Cousins prescriptions is presented in appendix C.5.

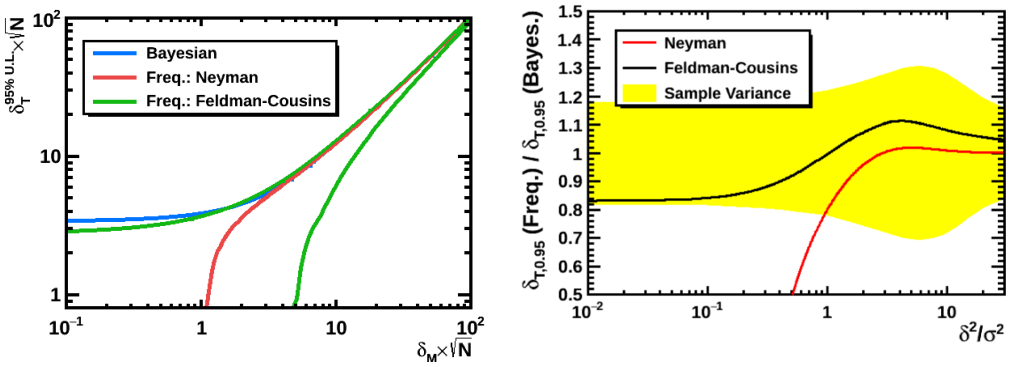

FIGURE A.2: *(Left)* Upper limits on δ_T parameter for any value of measured δ_M, both scaled by the sample size, obtained following Neyman approach (red line), Feldman and Cousins approach (green line) and Bayesian prescription (blue line) *(Right)* Level of agreement of Bayesian prescription and Frequentist approaches, compared to the sample variance.

B

EFFECT OF DAY/NIGHT CYCLES IN AMS-02

B.1 DAY-NIGHT CYCLES ON PROTON ANISOTROPIES

The effects that day-night cycles may induce in the measurement of anisotropies are naturally studied in the GSE coordinate system, where the days and nights are separated and consistently folded, therefore allowing to quantify possible day-night asymmetries.

The measurement of the particle rigidity is critical in any proton analysis with AMS-02. Since the rigidity is determined from the trajectory of the particle measured by the tracker, the correct alignment of the tracker elements is crucial [168, 223]. For this reason, a static alignment was done in three steps: a first one, after the integration using cosmic ray muons; a second one, with test beam protons; and a third, onboard the ISS to correct small displacements during the launch. In addition, short term variations of the temperature along the ISS orbit produce displacements of the outer layers, that are corrected using a dynamic alignment. However, residual shifts in some tracker elements may still occur and give rise to an absolute rigidity scale, which will induce a systematic bias of the rigidity measurement, according to

$$\frac{1}{R'} = \frac{1}{R} + \Delta\left(\frac{1}{R}\right), \tag{B.1}$$

where $\Delta\left(\frac{1}{R}\right)$ is the rigidity scale. This rigidity scale is one the major sources of systematics in the proton and nuclei spectra at high rigidities, and in the case of proton and helium fluxes was found to be smaller than $-1/26$ TV^{-1}.

The effect of the rigidity scale is more important as the rigidity increases and, therefore, can be studied in the ratio of high rigidity over low rigidity protons. The calibration curve in figure B.1-*left* quantifies this effect for three different ranges in the high rigidity sample when a positive or negative bias is applied. A negative bias means that we are selecting protons of lower rigidity. Assuming that the flux is nearly a power law, this implies an increase in the high/low ratio, and vice versa (figure B.1-*right*). On the other hand, from the slopes of the calibration curves it is clear that the effect is more important as the rigidity increases, which is a natural consequence of (B.1)

Since the rigidity scale is sensitive to temperature and tracker configurations, potential day/night variations of the rigidity scale may induce day/night asymmetries in the populations selected with reconstructed rigidity in a given range. This potential asymmetry in the populations translates directly into an artificial day/night anisotropy in the high/low ratio whose amplitude should increase as the rigidity increases. For this reason, a day/night anisotropy is investigated in the

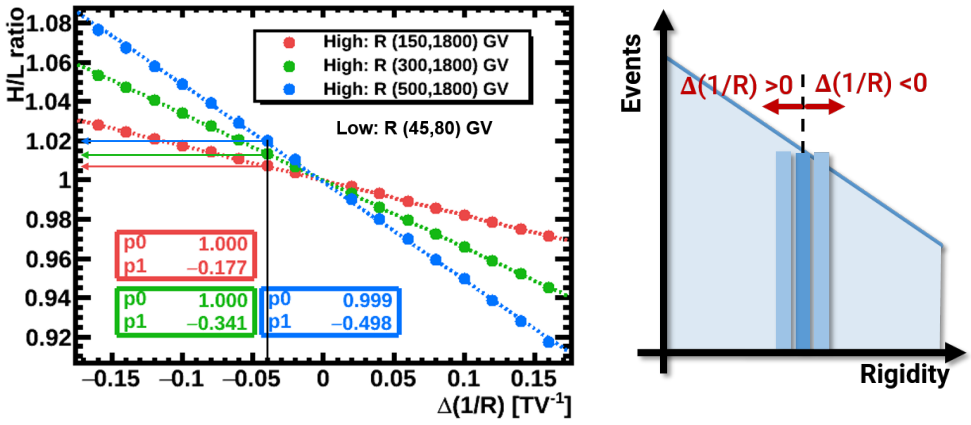

FIGURE B.1: *(Left)* Calibration curves for the effect of a rigidity scale $\Delta(1/R)$ on the high-/low ratio of events in three different rigidity ranges. *(Right)* Illustration of the effect of the rigidity scale in the distribution of events.

ecliptic plane, as a function of the azimuthal angle, φ. Azimuthal variations of the proton high/low ratio are studied in four φ sectors as indicated in figure B.2.

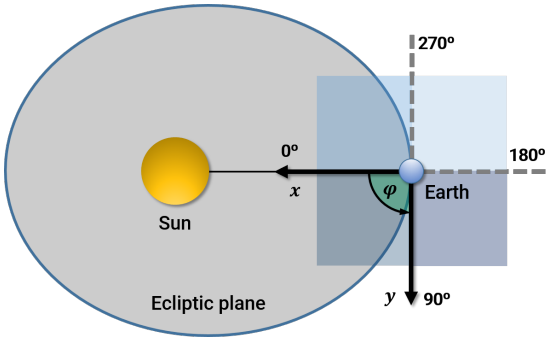

FIGURE B.2: Scheme of the strategy followed in the study of the effect of day/night cycles in AMS-02. The ecliptic plane is divided into 4 azimuthal sectors where variations of the proton high/low ratio and other variables are studied.

Four high rigidity samples are selected: 150-1800 GV, 300-1800 GV, 500-1800 GV and 1000-1800 GV. The low rigidity sample is chosen to be 45-80 GV. The proton high/low ratio is normalized to the average and the results are shown in figure B.3. A harmonic analysis, consisting in a fit to a sinusoidal function with an amplitude, p_0, and a phase, p_1 is performed. The results show that a modulation in the ecliptic plane is observed as a function of the azimuthal angle. This modulation has a maximum at $\varphi \sim 180°$, when looking away from the Sun, and the amplitude increases with the rigidity range.

Since this modulation in the ecliptic plane observed in the proton high/low ratio could be produced by either a day/night variation of the rigidity scale or a true anisotropy, a procedure to discriminate its origin has been established. In this approach, three independent estimators, sensitive to rigidity scale variations, have been investigated.

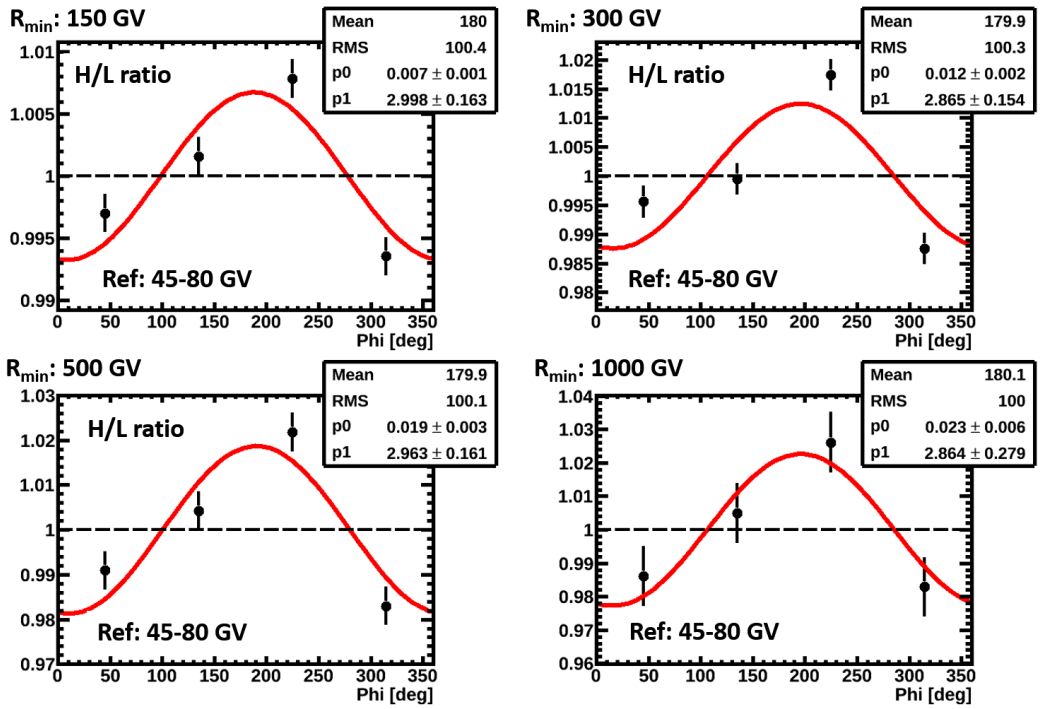

FIGURE B.3: Variation of the proton high/low ratio along the azimuthal angle in the ecliptic plane. Four high rigidity samples are used: 150-1800 GV, 300-1800 GV, 500-1800 GV and 1000-1800 GV. The low rigidity sample corresponds to 45-80 GV. The results of a harmonic analysis are also displayed.

▶ SPILLOVER PROTONS

The fraction of protons that are reconstructed with negative sign ($R < 0$), called *spillover protons*, is very sensitive to the variations of the tracker resolution and rigidity scale. The effect of a rigidity scale on the spillover sample is quantified by means of the calibration curves in figure B.4. A negative bias, $\Delta\left(\frac{1}{R}\right) < 0$, produces an increase of the spillover sample, therefore increasing the fraction of spillover protons, and vice versa.

In order to increase the statistics of the spillover sample and, consequently, improve the sensitivity of this estimation, an extended definition of spillover protons has been used ($1/R < 1/1.8$ TV^{-1}).

It is important to notice that a true signal would increase the spillover fraction in a similar manner. Therefore, the spillover determination may be regarded as an effective upper limit to the rigidity scale variation.

▶ TRD ESTIMATOR

The TRD estimator is another variable that allows to distinguish between a rigidity scale variation or a true signal in the high rigidity sample. This determination exploits the fact that, at low rigidities, the TRD estimator distribution for electrons and protons is separated. As the rigidity increases, the proton distribution gets

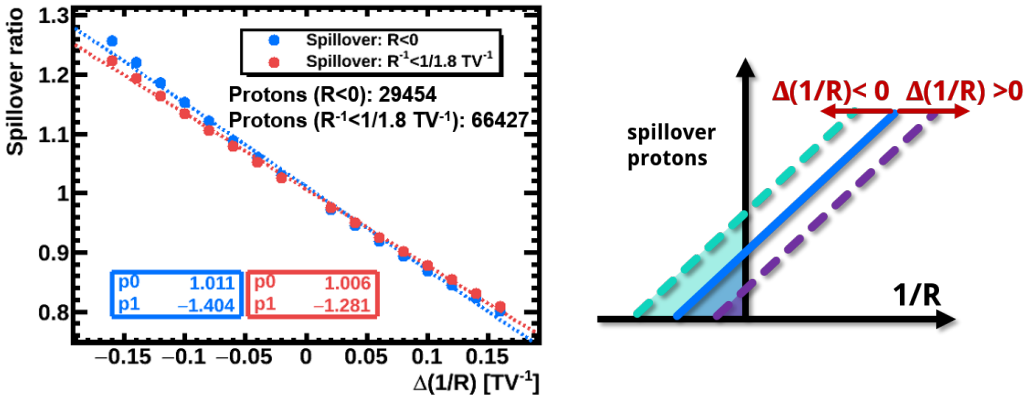

FIGURE B.4: *(Left)* Calibration curves for the effect of a rigidity scale in the fraction of spillover protons. *(Right)* Scheme of the effect of a rigidity scale in the distribution of spillover protons.

closer to that of electrons. For this reason, variations in the mean of the TRD estimator distribution can be associated to variations in the rigidity of the sample.

According to the previous considerations, an excess in the high rigidity sample may be due to a true overabundance of high rigidity protons or may be caused by a negative rigidity scale. However, these two effects have opposite behavior from the point of view of TRD estimator. In fact, a negative bias implies that we are selecting protons of lower rigidity and, consequently, the mean of the TRD estimator moves to higher values, as shown in figure B.5-*right*. In contrast, a true excess of high rigidity protons turns induces a shift in the mean of the TRD estimator distribution to lower values.

The effect of a rigidity scale in the relative variation of the mean of the TRD estimator distribution is quantified in the calibration curves shown in figure B.5-*left*.

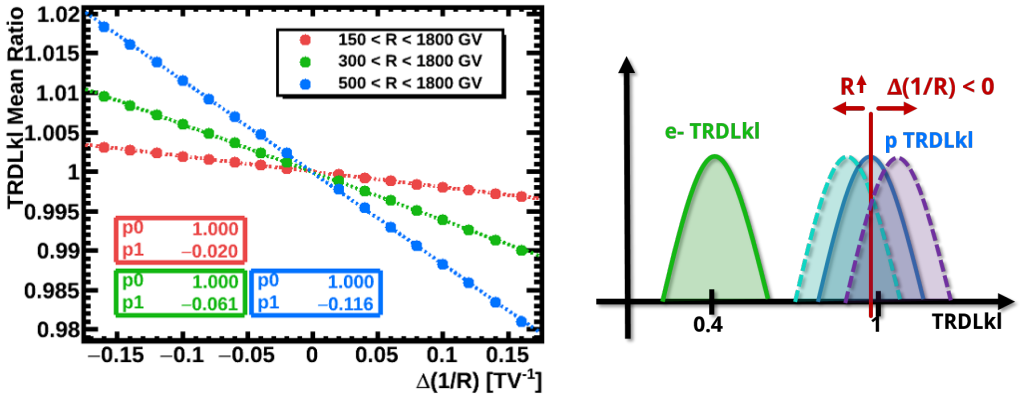

FIGURE B.5: *(Left)* Calibration curves for the effect of a rigidity scale in the mean value of the TRD estimator for three different rigidity ranges. *(Right)* Illustration of the effect of a rigidity scale in the mean value of the TRD estimator distribution.

► ENERGY-MOMENTUM MATCHING

A similar reasoning can be done in the case of the energy-momentum matching. A negative rigidity scale implies that the high rigidity excess is actually caused by biased low rigidity protons. In this situation, the mean of the E/p distribution should move to lower values. However, if the excess of high rigidity protons has a true origin, the impact on the E/p distribution should be negligible (figure B.6-*right*).

Figure B.6-*left* shows the effect of a rigidity scale on the mean of the E/p distribution.

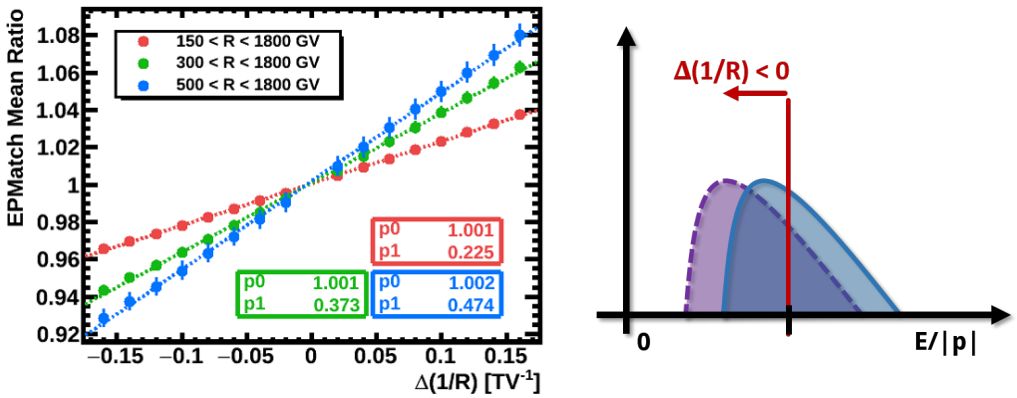

FIGURE B.6: *(Left)* Calibration curves for the effect of a rigidity scale in the mean value of the energy-momentum matching distribution for three different rigidity ranges. *(Right)* Illustration of the effect of a rigidity scale in the mean value of the energy-momentum matching distribution.

The relative variation of these three estimators (fraction of spillover protons, and mean of TRD estimator and energy-momentum matching distributions) has been studied as a function of the azimuthal angle in four φ sectors of the ecliptic plane. A modulation was observed in all three estimators, which can be translated into a modulation of the rigidity scale by means of the calibration curves in figures B.4, B.5 and B.6. Therefore, each estimator provides an independent determination of the rigidity scale, as shown in figure B.7, which are in good agreement among them. Thus, a day/night modulation of the rigidity scale, with an amplitude below $\sim 1/25$ TV^{-1} has been observed.

To further verify the determination of the day/night modulation of the rigidity scale, the predicted modulation in the proton high/low ratio is obtained from figure B.1 for each rigidity range. The results are shown in figure B.8, where the modulation in the proton high/low predicted from the day/night variation of the rigidity scale and on data are in good agreement. Therefore, the observed modulation in the ecliptic plane is consistent with a day/night variation of the rigidity scale, with an amplitude below $1/25$ TV^{-1}.

This result has been cross-checked with a sample of L1+Inner protons and a spherical harmonics analysis using skymaps. Both cases yielded consistent results.

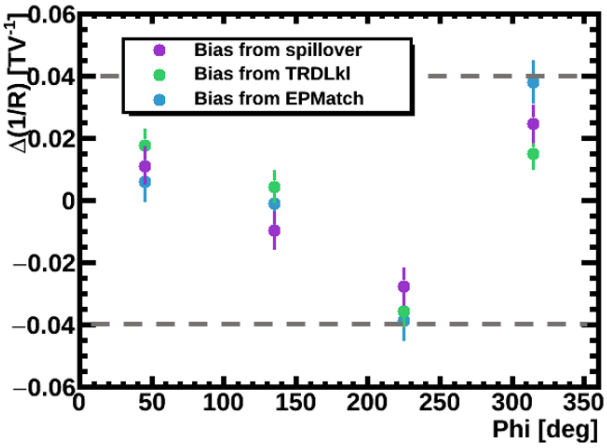

FIGURE B.7: Variation of the rigidity scale along the azimuthal angle in the ecliptic plane estimated independently by means of spillover protons, and mean of TRD estimator and energy-momentum distributions.

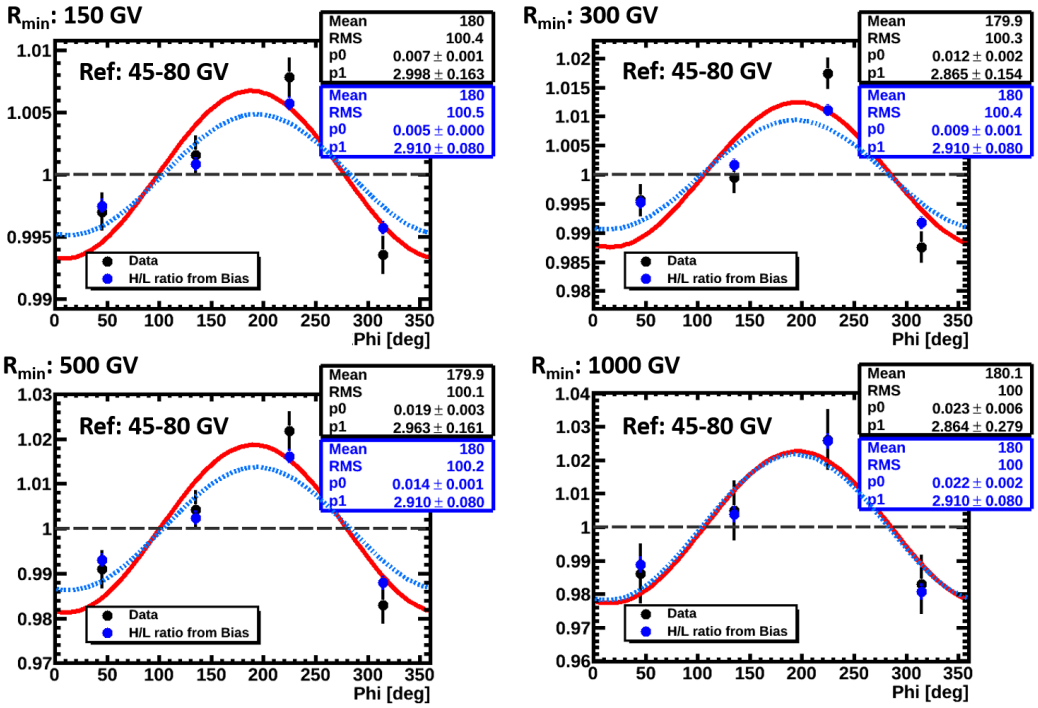

FIGURE B.8: Comparison of the measured variation of the proton high/low ratio (black dots) and the predicted modulation from the observed variation of the rigidity scale (blue dots). The results of the harmonic analysis in both cases are also displayed. The predicted modulation reproduces that observed in data.

Finally, it is important to notice that the day/night variation of the rigidity scale has no impact in the analysis of anisotropies in galactic coordinates. In other coordinate systems, such as ISS Geographical Position or galactic coordinates, days and nights, and, consequently, potential effects are averaged and, therefore, washed out. This can be seen from the corresponding coordinate transformation matrix

(figure 4.11-*right* in section 4.3.3), and has been checked by repeating the analysis in such coordinate systems. On the other hand, this is also true for flux measurements in AMS-02, which are sensitive to an absolute rigidity scale but not to its day/night variation. On the contrary, the analysis of anisotropies is sensitive to such day/night modulations of the rigidity scale and provides tools to characterize and understand this effect.

B.2 DAY-NIGHT CYCLES ON LEPTON ANISOTROPIES

As in the case of the proton rigidity, the measurement of the electron and positron energy may be influenced by the day-night cycles. In particular, the calibration of the ECAL energy is affected by temperature variations due to modifications in the pedestals and the Minimum Ionization Particles (MIPs) values, which are used to equalize the response of the PMTs. Although those variations are accounted in the offline analysis, a residual effect may still be present and induce a day/night modulation of the energy scale.

In general, the consequence of an energy scale is a bias in the energy measurement proportional to the energy

$$E' = E \times (1 + \Delta(E)) \,, \tag{B.2}$$

which implies that the effect, i.e, the change in the population of events, is the same for all energy ranges if the flux is a power law. This can be verified by computing the ratio of events selected in a certain energy range when a bias is applied, N', with respect to those selected in absence of bias, as shown in figure B.9.

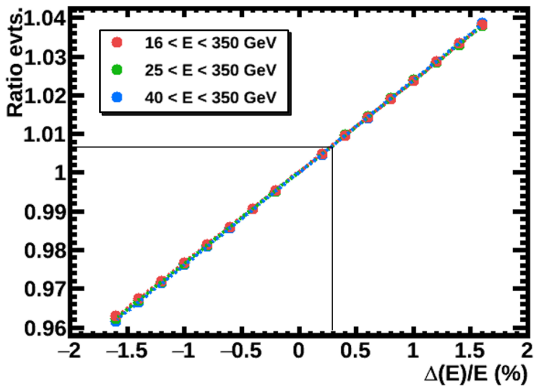

FIGURE B.9: Calibration curves for the effect of an energy scale in the number of events selected in a given energy range.

As in the case of protons, day/night modulations of the energy scale will translate into asymmetries in the populations of events selected in a given energy range, therefore, inducing an anisotropy in the ecliptic plane. However, since the effect of an energy scale is the same for all energies we cannot use a high/low ratio to quantify this variation, and the absolute anisotropy should be considered instead.

Following the same approach as described in the case of protons, an absolute day/night anisotropy is investigated as a function of the azimuthal angle φ in the ecliptic plane. Both event maps and exposure time maps including the efficiency corrections in GSE are projected into the azimuthal angle, and the variations are studied in four φ sectors according to figure B.2. To be sensitive to potential deviations, the electron sample is used in the analysis, and three energy ranges are investigated: 16-350 GeV, 25-350 GeV and 40-350 GeV. A sinusoidal fit, with amplitude p_0 and phase p_1 is performed. The results in figure B.10 exhibit a modulation in the ecliptic plane, with a maximum at $\varphi \sim 100^\circ$, and a nearly constant amplitude 0.7%.

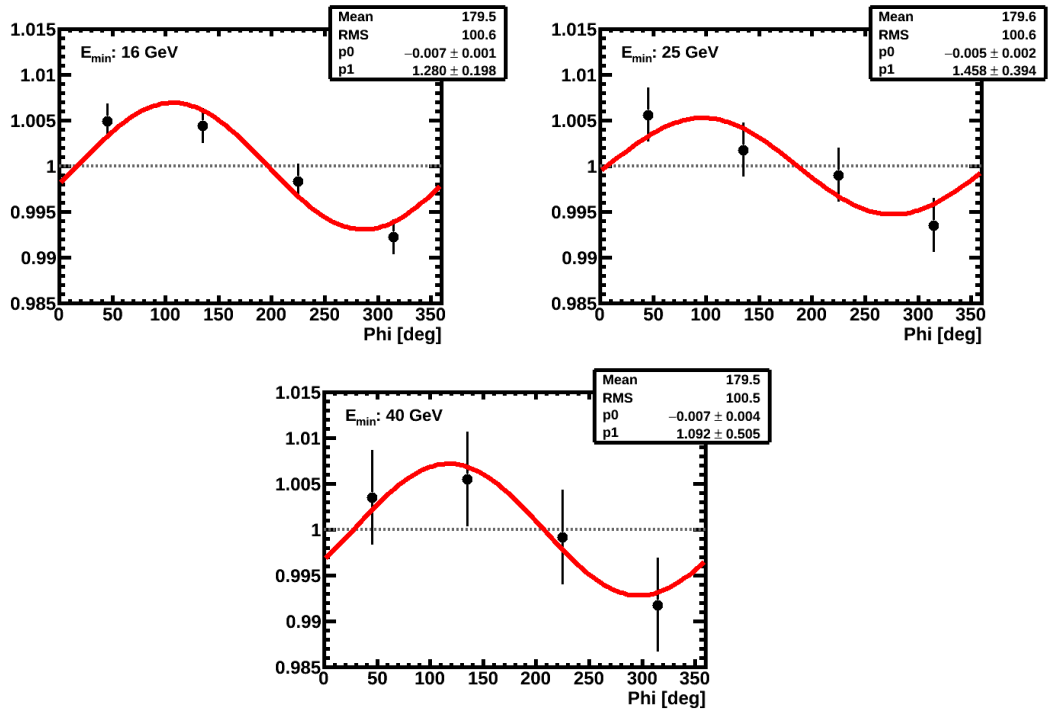

FIGURE B.10: Absolute day/night modulation in the electron sample along the azimuthal angle in the ecliptic plane, observed for $E_{\text{min}} = 16, 25$ and 40 GeV.

Since a modulation of the energy scale along the ecliptic plane could be the origin of this result, the relative variation of the MIP calibration is studied. In particular, a shift in the peak of the MIP distribution would induce a variation in the energy calibration. To determine this effect, the distribution of proton MIPs with rigidity $R > 45$ GV and deposited energy $E < 300$ MeV is obtained for each azimuthal sector (figure B.11), and the variation of its peak with respect to the average is shown. A modulation in the peak position, consistent to that obtained in electrons, is observed.

To further verify the instrumental origin of the day/night modulation in the electrons sample, the bias in the energy due to the MIPs peak position variation can be translated into changes in the population of the electron sample, by means of the curves in figure B.9. Figure B.12 shows the comparison between the modulation observed in electrons and the predicted from the day/night change of the energy

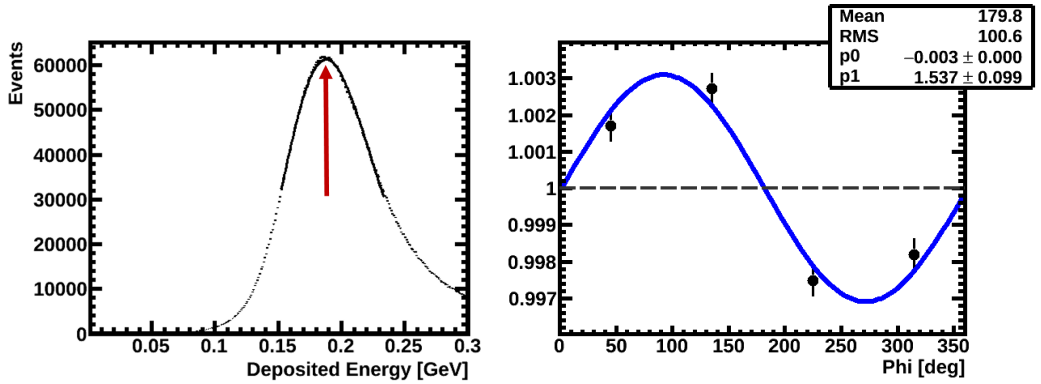

FIGURE B.11: *(Left)* The peak of the MIP distribution is obtained by means of a fit to a log normal distribution. *(Right)* Relative variation of the MIP peak distribution showing a modulation along the azimuthal angle in the ecliptic plane.

scale. Both results are in a good agreement, which confirms the instrumental origin of the excess.

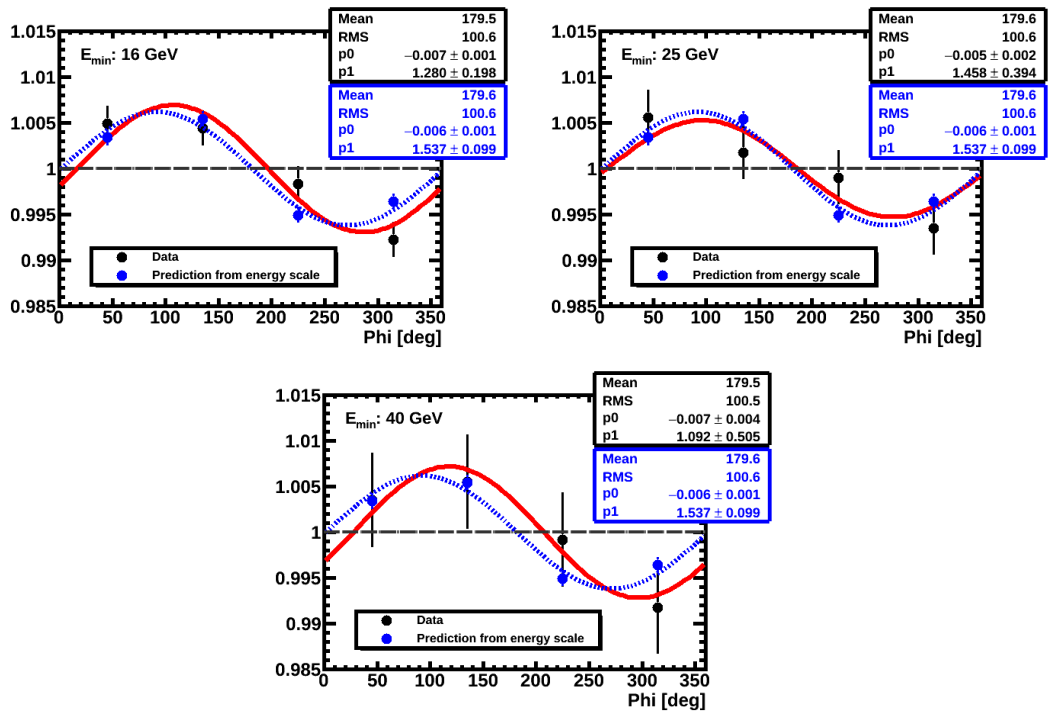

FIGURE B.12: Comparison of the measured absolute day/night modulation in the electron sample (black dots) and the predicted modulation from the observed variation of the energy scale (blue dots). The results of the harmonic analysis in both cases are also displayed. The predicted modulation reproduces that observed in data.

Finally, as mentioned in the case of protons, this day/night variation of the energy scale has no impact in the analysis of anisotropies in galactic coordinates. Similarly, although the flux measurements in AMS-02 may be affected by an absolute energy scale, they are not sensitive to this kind of effects. Only anisotropy measure-

ments, which are sensitivity to directionality of spurious contributions are able to characterize these phenomena.

C

TABLES

This section presents the tables with the numerical results obtained in this thesis corresponding to the measurement of anisotropies in the arrival directions of cosmic ray protons, positrons and electrons in galactic coordinates. In each case, the sample size, and the values of the dipole components with their statistic and systematic uncertainties as well as the standard deviation from zero are quoted. In addition, the amplitude of the measured value and the 95% C.I. upper limit on the dipole anisotropy are also presented.

C.1 PROTON ABSOLUTE ANISOTROPY

TABLE C.1: Numerical results of the proton absolute anisotropy in galactic coordinates including corrections.

R_{min} [GV]	N_p^{meas}	N_p^{eq}	ρ_{EW} (%)	σ_{EW}^{stat} (%)	σ_{EW}^{sys} (%)	$\rho_{EW}/\sigma_{EW}^{tot}$	ρ_{NS} (%)	σ_{NS}^{stat} (%)	σ_{NS}^{sys} (%)	$\rho_{NS}/\sigma_{NS}^{tot}$	ρ_{FB} (%)	σ_{FB}^{stat} (%)	σ_{FB}^{sys} (%)	$\rho_{FB}/\sigma_{FB}^{tot}$	$\delta_M(\%)$	$\delta_{U.L.}^{95\%\,C.I.}(\%)$
18	75914668	75914668	-0.006	0.021	0.046	-0.12	-0.096	0.020	0.046	-1.91	0.015	0.020	0.046	+0.30	0.097	0.157
30	34067502	34067502	0.008	0.031	0.054	+0.13	-0.079	0.030	0.054	-1.28	0.003	0.030	0.054	+0.05	0.079	0.155
45	16648643	16648643	-0.022	0.044	0.061	-0.29	-0.017	0.043	0.061	-0.23	0.002	0.043	0.061	+0.03	0.028	0.150
80	6067385	6067385	-0.033	0.073	0.071	-0.33	0.101	0.071	0.070	+1.01	0.032	0.071	0.070	+0.32	0.111	0.237
150	2033337	2033337	-0.136	0.126	0.081	-0.91	0.253	0.122	0.081	+1.73	-0.141	0.122	0.081	-0.96	0.320	0.498
300	638155	638155	0.271	0.225	0.093	+1.11	0.479	0.217	0.093	+2.03	-0.060	0.219	0.093	-0.25	0.553	0.847
500	289909	289909	0.310	0.334	0.102	+0.89	0.353	0.322	0.102	+1.05	-0.590	0.325	0.101	-1.74	0.754	1.170
1000	116068	116068	0.485	0.528	0.114	+0.90	0.348	0.509	0.114	+0.67	-0.167	0.513	0.113	-0.32	0.620	1.275

TABLE C.2: Numerical results of the proton absolute anisotropy in galactic coordinates including corrections and background contamination.

R_{min} [GV]	N_p^{meas}	N_p^{eq}	ρ_{EW} (%)	σ_{EW}^{stat} (%)	σ_{EW}^{sys} (%)	$\rho_{EW}/\sigma_{EW}^{tot}$	ρ_{NS} (%)	σ_{NS}^{stat} (%)	σ_{NS}^{sys} (%)	$\rho_{NS}/\sigma_{NS}^{tot}$	ρ_{FB} (%)	σ_{FB}^{stat} (%)	σ_{FB}^{sys} (%)	$\rho_{FB}/\sigma_{FB}^{tot}$	$\delta_M(\%)$	$\delta_{U.L.}^{95\%\,C.I.}(\%)$
18	75914668	67481517	-0.004	0.022	0.046	-0.08	-0.100	0.021	0.046	-1.98	0.017	0.021	0.046	+0.33	0.102	0.162
30	34067502	28489602	0.014	0.034	0.054	+0.22	-0.084	0.033	0.054	-1.33	0.004	0.033	0.054	+0.06	0.085	0.161
45	16648643	13698613	-0.018	0.048	0.061	-0.23	0.007	0.047	0.061	+0.09	-0.002	0.047	0.061	-0.02	0.020	0.153
80	6067385	4817755	-0.056	0.082	0.071	-0.52	0.138	0.079	0.070	+1.31	0.015	0.079	0.070	+0.14	0.150	0.278
150	2033337	1494822	-0.117	0.146	0.081	-0.70	0.332	0.142	0.081	+2.03	-0.203	0.143	0.081	-1.24	0.406	0.612
300	638155	392158	0.310	0.287	0.093	+1.03	0.613	0.277	0.093	+2.10	-0.168	0.279	0.093	-0.57	0.707	1.073
500	289909	127601	0.392	0.503	0.102	+0.76	0.407	0.485	0.102	+0.82	-0.796	0.489	0.101	-1.59	0.976	1.574
1000	116068	12882	0.905	1.585	0.114	+0.57	0.803	1.526	0.114	+0.52	-0.814	1.539	0.113	-0.53	1.458	3.497

C.2 POSITRON TO ELECTRON RELATIVE ANISOTROPY

TABLE C.3: Numerical results of the positron to electron relative anisotropy in galactic coordinates.

E_{min} [GeV]	$N_{e^+}^{meas}$	$N_{e^+}^{eq}$	$N_{e^-}^{meas}$	ρ_{EW} (%)	σ_{EW}^{stat} (%)	$\rho_{EW}/\sigma_{EW}^{tot}$	ρ_{NS} (%)	σ_{NS}^{stat} (%)	$\rho_{NS}/\sigma_{NS}^{tot}$	ρ_{FB} (%)	σ_{FB}^{stat} (%)	$\rho_{FB}/\sigma_{FB}^{tot}$	$\delta_M(\%)$	$\delta_{U.L.}^{95\%\ C.I.}(\%)$
16	79828	79828	1065633	0.910	0.641	+1.42	-0.869	0.643	-1.35	0.206	0.644	+0.32	1.275	2.041
25	39661	39661	459723	0.643	0.945	+0.68	-1.211	0.912	-1.33	-0.634	0.910	-0.70	1.511	2.599
40	16041	16041	150958	1.312	1.499	+0.88	-1.545	1.453	-1.06	-1.804	1.444	-1.25	2.713	4.447
65	6167	6167	46408	1.025	2.441	+0.42	0.376	2.385	+0.16	0.649	2.343	+0.28	1.270	4.906
100	2567	2567	15936	-3.809	3.808	-1.00	4.767	3.691	+1.29	3.748	3.690	+1.02	7.161	11.588

TABLE C.4: Numerical results of the positron to electron relative anisotropy in galactic coordinates including background contamination.

E_{min} [GeV]	$N_{e^+}^{meas}$	$N_{e^+}^{eq}$	$N_{e^-}^{meas}$	ρ_{EW} (%)	σ_{EW}^{stat} (%)	$\rho_{EW}/\sigma_{EW}^{tot}$	ρ_{NS} (%)	σ_{NS}^{stat} (%)	$\rho_{NS}/\sigma_{NS}^{tot}$	ρ_{FB} (%)	σ_{FB}^{stat} (%)	$\rho_{FB}/\sigma_{FB}^{tot}$	$\delta_M(\%)$	$\delta_{U.L.}^{95\%\ C.I.}(\%)$
16	79828	73036	1065633	0.958	0.671	+1.43	-0.912	0.673	-1.36	0.213	0.673	+0.32	1.340	2.141
25	39661	36399	459723	0.686	0.986	+0.70	-1.268	0.952	-1.33	-0.665	0.949	-0.70	1.588	2.724
40	16041	14655	150958	1.415	1.567	+0.90	-1.631	1.520	-1.07	-1.903	1.510	-1.26	2.878	4.693
65	6167	5487	46408	1.194	2.584	+0.46	0.409	2.529	+0.16	0.700	2.480	+0.28	1.443	5.232
100	2567	2152	15936	-4.143	4.145	-1.00	5.494	4.031	+1.36	4.306	4.024	+1.07	8.117	12.967

C.3 POSITRON ABSOLUTE ANISOTROPY

TABLE C.5: Numerical results of the positron absolute anisotropy in galactic coordinates including corrections.

E_{min} [GeV]	$N_{e^+}^{meas}$	$N_{e^+}^{eq}$	ρ_{EW} (%)	σ_{EW}^{stat} (%)	σ_{EW}^{sys} (%)	$\rho_{EW}/\sigma_{EW}^{tot}$	ρ_{NS} (%)	σ_{NS}^{stat} (%)	σ_{NS}^{sys} (%)	$\rho_{NS}/\sigma_{NS}^{tot}$	ρ_{FB} (%)	σ_{FB}^{stat} (%)	σ_{FB}^{sys} (%)	$\rho_{FB}/\sigma_{FB}^{tot}$	$\delta_M(\%)$	$\delta_{U.L.}^{95\%\,C.I.}(\%)$
16	79828	79828	1.165	0.618	0.083	+1.87	-0.634	0.620	0.053	-1.02	-0.030	0.620	0.098	-0.05	1.327	2.080
25	39661	39661	0.771	0.905	0.186	+0.83	-0.819	0.874	0.118	-0.93	-1.002	0.872	0.172	-1.13	1.506	2.566
40	16041	16041	1.116	1.422	0.358	+0.76	-1.258	1.378	0.225	-0.90	-1.895	1.371	0.287	-1.35	2.533	4.211
65	6167	6167	-0.166	2.288	0.543	-0.07	1.366	2.232	0.339	+0.61	0.352	2.198	0.414	+0.16	1.420	4.764
100	2567	2567	-4.121	3.519	0.709	-1.15	4.589	3.418	0.442	+1.33	3.677	3.415	0.529	+1.06	7.180	11.369

TABLE C.6: Numerical results of the positron absolute anisotropy in galactic coordinates including corrections and background contamination.

E_{min} [GeV]	$N_{e^+}^{meas}$	$N_{e^+}^{eq}$	ρ_{EW} (%)	σ_{EW}^{stat} (%)	σ_{EW}^{sys} (%)	$\rho_{EW}/\sigma_{EW}^{tot}$	ρ_{NS} (%)	σ_{NS}^{stat} (%)	σ_{NS}^{sys} (%)	$\rho_{NS}/\sigma_{NS}^{tot}$	ρ_{FB} (%)	σ_{FB}^{stat} (%)	σ_{FB}^{sys} (%)	$\rho_{FB}/\sigma_{FB}^{tot}$	$\delta_M(\%)$	$\delta_{U.L.}^{95\%\,C.I.}(\%)$
16	79828	73036	1.229	0.646	0.083	+1.89	-0.668	0.648	0.053	-1.03	-0.040	0.648	0.098	-0.06	1.400	2.187
25	39661	36399	0.830	0.945	0.186	+0.86	-0.862	0.912	0.118	-0.94	-1.062	0.910	0.172	-1.15	1.600	2.705
40	16041	14655	1.235	1.487	0.358	+0.81	-1.337	1.442	0.225	-0.92	-2.030	1.434	0.287	-1.39	2.727	4.482
65	6167	5487	-0.033	2.424	0.543	-0.01	1.455	2.369	0.339	+0.61	0.310	2.330	0.414	+0.13	1.488	5.035
100	2567	2152	-4.411	3.838	0.709	-1.13	5.219	3.739	0.442	+1.39	4.072	3.730	0.529	+1.08	7.955	12.532

C.4 ELECTRON ABSOLUTE ANISOTROPY

TABLE C.7: Numerical results of the electron absolute anisotropy in galactic coordinates including corrections.

E_{min} [GeV]	$N_{e^-}^{meas}$	$N_{e^-}^{eq}$	ρ_{EW} (%)	σ_{EW}^{stat} (%)	σ_{EW}^{sys} (%)	$\rho_{EW}/\sigma_{EW}^{tot}$	ρ_{NS} (%)	σ_{NS}^{stat} (%)	σ_{NS}^{sys} (%)	$\rho_{NS}/\sigma_{NS}^{tot}$	ρ_{FB} (%)	σ_{FB}^{stat} (%)	σ_{FB}^{sys} (%)	$\rho_{FB}/\sigma_{FB}^{tot}$	$\delta_M(\%)$	$\delta_{U.L.}^{95\%\,C.I.}(\%)$
16	1065633	1065633	0.250	0.168	0.083	+1.33	0.181	0.170	0.053	+1.01	-0.206	0.170	0.098	-1.05	0.371	0.595
25	459723	459723	0.152	0.264	0.186	+0.47	0.359	0.257	0.118	+1.27	-0.403	0.257	0.172	-1.30	0.561	0.922
40	150958	150958	0.052	0.462	0.358	+0.09	0.234	0.447	0.225	+0.47	-0.258	0.449	0.287	-0.49	0.353	1.135
65	46408	46408	-1.147	0.831	0.543	-1.15	1.071	0.806	0.339	+1.22	-0.543	0.809	0.414	-0.60	1.660	2.755
100	15936	15936	-0.411	1.412	0.709	-0.26	-0.239	1.379	0.442	-0.17	-0.416	1.382	0.529	-0.28	0.632	3.034

C.5 Comparison of Bayesian and Frequentist upper limits

Proton absolute anisotropy

TABLE C.8: Comparison of the Bayesian and Frequentist upper limits on the proton dipole amplitude in galactic coordinates including corrections.

R_{min} [GV]	ρ_{EW} (%)	σ^{tot}_{EW} (%)	ρ_{NS} (%)	σ^{tot}_{NS} (%)	ρ_{FB} (%)	σ^{tot}_{FB} (%)	$\delta^{Bay.}_{U.L}$ (%)	$\delta^{Ney.}_{U.L.}$ (%)	$[\delta^{F.C.}_{Lower} - \delta^{F.C.}_{Upper}]$ (%)
18	-0.006	0.051	-0.096	0.050	0.015	0.050	0.157	0.159	[0.000 - 0.175]
30	0.008	0.063	-0.079	0.062	0.003	0.062	0.155	0.143	[0.000 - 0.163]
45	-0.022	0.075	-0.017	0.074	0.002	0.074	0.150	0.000	[0.000 - 0.127]
80	-0.033	0.101	0.101	0.100	0.032	0.100	0.237	0.204	[0.000 - 0.242]
150	-0.136	0.150	0.253	0.146	-0.141	0.147	0.498	0.508	[0.000 - 0.554]
300	0.271	0.243	0.479	0.236	-0.060	0.237	0.847	0.863	[0.000 - 0.938]
500	0.310	0.349	0.353	0.338	-0.590	0.340	1.170	1.192	[0.000 - 1.300]
1000	0.485	0.540	0.348	0.521	-0.167	0.525	1.275	1.133	[0.000 - 1.319]

TABLE C.9: Comparison of the Bayesian and Frequentist upper limits on the proton dipole amplitude in galactic coordinates including corrections and background contamination.

R_{min} [GV]	ρ_{EW} (%)	σ^{tot}_{EW} (%)	ρ_{NS} (%)	σ^{tot}_{NS} (%)	ρ_{FB} (%)	σ^{tot}_{FB} (%)	$\delta^{Bay.}_{U.L}$ (%)	$\delta^{Ney.}_{U.L.}$ (%)	$[\delta^{F.C.}_{Lower} - \delta^{F.C.}_{Upper}]$ (%)
18	-0.004	0.051	-0.100	0.051	0.017	0.051	0.162	0.165	[0.000 - 0.181]
30	0.014	0.064	-0.084	0.063	0.004	0.063	0.161	0.152	[0.000 - 0.172]
45	-0.018	0.078	0.007	0.077	-0.002	0.077	0.153	0.000	[0.000 - 0.128]
80	-0.056	0.108	0.138	0.106	0.015	0.106	0.278	0.266	[0.000 - 0.298]
150	-0.117	0.168	0.332	0.164	-0.203	0.164	0.612	0.623	[0.000 - 0.676]
300	0.310	0.301	0.613	0.292	-0.168	0.294	1.073	1.093	[0.000 - 1.187]
500	0.392	0.514	0.407	0.496	-0.796	0.499	1.574	1.597	[0.000 - 1.752]
1000	0.905	1.590	0.803	1.530	-0.814	1.543	3.497	2.654	[0.000 - 3.434]

Positron to electron relative anisotropy

TABLE C.10: Comparison of the Bayesian and Frequentist upper limits on the positron to electron dipole amplitude in galactic coordinates including corrections.

E_{min} [GeV]	ρ_{EW} (%)	σ^{tot}_{EW} (%)	ρ_{NS} (%)	σ^{tot}_{NS} (%)	ρ_{FB} (%)	σ^{tot}_{FB} (%)	$\delta^{Bay.}_{U.L}$ (%)	$\delta^{Ney.}_{U.L.}$ (%)	$[\delta^{F.C.}_{Lower} - \delta^{F.C.}_{Upper}]$ (%)
16	0.910	0.641	-0.869	0.643	0.206	0.644	2.041	2.073	[0.000 - 2.272]
25	0.643	0.945	-1.211	0.912	-0.634	0.910	2.599	2.583	[0.000 - 2.850]
40	1.312	1.499	-1.545	1.453	-1.804	1.444	4.447	4.494	[0.000 - 4.939]
65	1.025	2.441	0.376	2.385	0.649	2.343	4.906	0.000	[0.000 - 4.295]
100	-3.809	3.808	4.767	3.691	3.748	3.690	11.588	11.745	[0.000 - 12.893]

TABLE C.11: Comparison of the Bayesian and Frequentist upper limits on the positron to electron dipole amplitude in galactic coordinates including corrections and background contamination.

E_{min} [GeV]	ρ_{EW} (%)	σ^{tot}_{EW} (%)	ρ_{NS} (%)	σ^{tot}_{NS} (%)	ρ_{FB} (%)	σ^{tot}_{FB} (%)	$\delta^{Bay.}_{U.L}$ (%)	$\delta^{Ney.}_{U.L.}$ (%)	$[\delta^{F.C.}_{Lower} - \delta^{F.C.}_{Upper}]$ (%)
16	0.958	0.671	-0.912	0.673	0.213	0.673	2.141	2.175	[0.000 - 2.383]
25	0.686	0.986	-1.268	0.952	-0.665	0.949	2.724	2.710	[0.000 - 2.990]
40	1.415	1.567	-1.631	1.520	-1.903	1.510	4.693	4.748	[0.000 - 5.216]
65	1.194	2.584	0.409	2.529	0.700	2.480	5.232	0.000	[0.000 - 4.631]
100	-4.143	4.145	5.494	4.031	4.306	4.024	12.967	13.174	[0.000 - 14.435]

Positron absolute anisotropy

TABLE C.12: Comparison of the Bayesian and Frequentist upper limits on the positron dipole amplitude in galactic coordinates including corrections.

R_{min} [GV]	ρ_{EW} (%)	σ^{tot}_{EW} (%)	ρ_{NS} (%)	σ^{tot}_{NS} (%)	ρ_{FB} (%)	σ^{tot}_{FB} (%)	$\delta^{Bay.}_{U.L}$ (%)	$\delta^{Ney.}_{U.L.}$ (%)	$[\delta^{F.C.}_{Lower} - \delta^{F.C.}_{Upper}]$ (%)
16	1.165	0.624	-0.634	0.622	-0.030	0.628	2.080	2.117	[0.000 - 2.313]
25	0.771	0.924	-0.819	0.882	-1.002	0.889	2.566	2.560	[0.000 - 2.823]
40	1.116	1.466	-1.258	1.396	-1.895	1.400	4.211	4.238	[0.000 - 4.664]
65	-0.166	2.351	1.366	2.258	0.352	2.237	4.764	1.223	[0.000 - 4.274]
100	-4.121	3.590	4.589	3.447	3.677	3.456	11.369	11.565	[0.000 - 12.658]

TABLE C.13: Comparison of the Bayesian and Frequentist upper limits on the positron dipole amplitude in galactic coordinates including corrections and background contamination.

R_{min} [GV]	ρ_{EW} (%)	σ^{tot}_{EW} (%)	ρ_{NS} (%)	σ^{tot}_{NS} (%)	ρ_{FB} (%)	σ^{tot}_{FB} (%)	$\delta^{Bay.}_{U.L}$ (%)	$\delta^{Ney.}_{U.L.}$ (%)	$[\delta^{F.C.}_{Lower} - \delta^{F.C.}_{Upper}]$ (%)
16	1.229	0.652	-0.668	0.650	-0.040	0.656	2.187	2.228	[0.000 - 2.433]
25	0.830	0.963	-0.862	0.920	-1.062	0.926	2.705	2.707	[0.000 - 2.982]
40	1.235	1.530	-1.337	1.460	-2.030	1.463	4.482	4.525	[0.000 - 4.975]
65	-0.033	2.484	1.455	2.393	0.310	2.366	5.035	1.155	[0.000 - 4.509]
100	-4.411	3.903	5.219	3.765	4.072	3.767	12.532	12.755	[0.000 - 13.951]

Electron absolute anisotropy

TABLE C.14: Comparison of the Bayesian and Frequentist upper limits on the electron dipole amplitude in galactic coordinates including corrections.

R_{min} [GV]	ρ_{EW} (%)	σ^{tot}_{EW} (%)	ρ_{NS} (%)	σ^{tot}_{NS} (%)	ρ_{FB} (%)	σ^{tot}_{FB} (%)	$\delta^{Bay.}_{U.L}$ (%)	$\delta^{Ney.}_{U.L.}$ (%)	$[\delta^{F.C.}_{Lower} - \delta^{F.C.}_{Upper}]$ (%)
16	0.250	0.188	0.181	0.178	-0.206	0.196	0.595	0.604	[0.000 - 0.662]
25	0.152	0.323	0.359	0.282	-0.403	0.309	0.922	0.931	[0.000 - 1.023]
40	0.052	0.584	0.234	0.501	-0.258	0.533	1.135	0.412	[0.000 - 1.027]
65	-1.147	0.993	1.071	0.875	-0.543	0.909	2.755	2.774	[0.000 - 3.053]
100	-0.411	1.580	-0.239	1.448	-0.416	1.479	3.034	0.000	[0.000 - 2.594]

BIBLIOGRAPHY

[1] C. T. R. Wilson. On the ionisation of atmospheric air. *Proceedings of the Royal Society of London*, 68(444):151–161, 1901.

[2] J. Elster and H. Geitel. Ueber elektricitätszerstreuung in der luft. *Annalen der Physik*, 307(7):425–446, 1900.

[3] T. Wulf. Über die in der atmosphäre vorhandene strahlung von hoher durchdringungsfähigkeit. *Phys.Zeit.*, 10(5):152–157, 1909.

[4] D. Pacini. La radiazione penetrante alla superficie ed in seno alle acque. *Il Nuovo Cimento*, 3:93–100, December 1912. doi: 10.1007/BF02957440.

[5] Victor F. Hess. Über Beobachtungen der durchdringenden Strahlung bei sieben Freiballonfahrten. *Phys. Z.*, 13:1084–1091, 1912.

[6] R. A. Millikan and G. Harvey Cameron. High frequency rays of cosmic origin iii. measurements in snow-fed lakes at high altitudes. *Phys. Rev.*, 28:851–868, Nov 1926. doi: 10.1103/PhysRev.28.851.

[7] M. Nagano. Search for the end of the energy spectrum of primary cosmic rays. *New Journal of Physics*, 11(6):065012, 2009.

[8] S. Mollerach and E. Roulet. Progress in high-energy cosmic ray physics. *Progress in Particle and Nuclear Physics*, 98:85 – 118, 2018. ISSN 0146-6410. doi: https://doi.org/10.1016/j.ppnp.2017.10.002.

[9] A. M. Taylor. Space science: Cosmic rays beyond the knees. *Nature*, 531:43–44, March 2016. doi: 10.1038/531043a.

[10] R. U. Abbasi et al. The Cosmic-Ray Energy Spectrum between 2 PeV and 2 EeV Observed with the TALE detector in monocular mode. 2018.

[11] Thoudam, S., Rachen, J. P., van Vliet, A., Achterberg, A., Buitink, S., Falcke, H., and Hörandel, J. R. Cosmic-ray energy spectrum and composition up to the ankle: the case for a second galactic component. *A&A*, 595:A33, 2016. doi: 10.1051/0004-6361/201628894.

[12] K. Greisen. End to the Cosmic-Ray Spectrum? *Physical Review Letters*, 16: 748–750, April 1966. doi: 10.1103/PhysRevLett.16.748.

[13] G. T. Zatsepin and V. A. Kuz'min. Upper Limit of the Spectrum of Cosmic Rays. *Soviet Journal of Experimental and Theoretical Physics Letters*, 4:78, August 1966.

[14] M. E. Wiedenbeck et al. An Overview of the Origin of Galactic Cosmic Rays as Inferred from Observations of Heavy Ion Composition and Spectra. *Space Science Reviews*, 130:415–429, June 2007. doi: 10.1007/s11214-007-9198-y.

[15] A. M. Hillas. The Origin of Ultra-High-Energy Cosmic Rays. *Astronomy and Astrophysics*, 22:425–444, 1984. doi: 10.1146/annurev.aa.22.090184.002233.

[16] Federico Fraschetti. On the acceleration of ultra-high-energy cosmic rays. 366 (1884):4417–4428, 2008. doi: 10.1098/rsta.2008.0204.

[17] V.L. Ginzburg and S.I. Syrovatskii. The Origin of Cosmic Rays. Vol: 28, 12 1964.

[18] E. Fermi. On the Origin of the Cosmic Radiation. *Phys. Rev.*, 75:1169–1174, Apr 1949. doi: 10.1103/PhysRev.75.1169.

[19] E. G. Berezhko, V. K. Yelshin, and L. T. Ksenofontov. Numerical investigation of cosmic ray acceleration in supernova remnants. *Astroparticle Physics*, 2:215–227, May 1994. doi: 10.1016/0927-6505(94)90043-4.

[20] V. L. Ginzburg and V. S. Ptuskin. On the origin of cosmic rays: Some problems in high-energy astrophysics. *Rev. Mod. Phys.*, 48:161–189, Apr 1976. doi: 10.1103/RevModPhys.48.161.

[21] V. S. Berezinskii, S. V. Bulanov, V. A. Dogiel, and V. S. Ptuskin. *Astrophysics of cosmic rays*. Amsterdam: North-Holland, 1990, edited by Ginzburg, V.L., 1990.

[22] M. Aguilar et al. Precision Measurement of the Boron to Carbon Flux Ratio in Cosmic Rays from 1.9 GV to 2.6 TV with the Alpha Magnetic Spectrometer on the International Space Station. *Phys. Rev. Lett.*, 117:231102, Nov 2016. doi: 10.1103/PhysRevLett.117.231102.

[23] Putze, A., Derome, L., and Maurin, D. A Markov Chain Monte Carlo technique to sample transport and source parameters of Galactic cosmic rays - II. Results for the diffusion model combining B/C and radioactive nuclei. *A&A*, 516:A66, 2010. doi: 10.1051/0004-6361/201014010.

[24] Andrew W. Strong, Igor V. Moskalenko, and Vladimir S. Ptuskin. Cosmic-Ray Propagation and Interactions in the Galaxy. *Annual Review of Nuclear and Particle Science*, 57(1):285–327, 2007. doi: 10.1146/annurev.nucl.57.090506.123011.

[25] Giuseppe Di Bernardo et al. Unified interpretation of cosmic-ray nuclei and antiproton recent measurements. *Astroparticle Physics*, 34(5):274, October 2010. doi: 10.1016/j.astropartphys.2010.08.006.

[26] D. Maurin. *USINE: a new public cosmic ray propagation code Basic phenomenology, sample results, and a bit of USINE*, pages 420–434. WORLD SCIENTIFIC, 2011. doi: 10.1142/9789814329033_0053.

[27] Mathew J. Owens and Robert J. Forsyth. The Heliospheric Magnetic Field. *Living Reviews in Solar Physics*, 10(1):5, Nov 2013. ISSN 1614-4961. doi: 10.12942/lrsp-2013-5.

[28] Marius S. Potgieter. Solar Modulation of Cosmic Rays. *Living Reviews in Solar Physics*, 10(1):3, Jun 2013. ISSN 1614-4961. doi: 10.12942/lrsp-2013-3.

[29] H. Schwabe. Sonnenbeobachtungen im Jahre 1843. Von Herrn Hofrath Schwabe in Dessau. *Astronomische Nachrichten*, 21:233, February 1844. doi: 10.1002/asna.18440211505.

[30] E.N. Parker. The passage of energetic charged particles through interplanetary space. *Planetary and Space Science*, 13(1):9 – 49, 1965. ISSN 0032-0633. doi: https://doi.org/10.1016/0032-0633(65)90131-5.

[31] L. J. Gleeson and W. I. Axford. Solar Modulation of Galactic Cosmic Rays. *Astrophysical Journal*, 154:1011, December 1968. doi: 10.1086/149822.

[32] Rolf Kappl. SOLARPROP: Charge-sign dependent solar modulation for everyone. *Computer Physics Communications*, 207:386 – 399, 2016. ISSN 0010-4655. doi: https://doi.org/10.1016/j.cpc.2016.05.025.

[33] M.S. Potgieter. The charge-sign dependent effect in the solar modulation of cosmic rays. *Advances in Space Research*, 53(10):1415 – 1425, 2014. ISSN 0273-1177. doi: https://doi.org/10.1016/j.asr.2013.04.015. Cosmic Ray Origins: Viktor Hess Centennial Anniversary.

[34] Thule Neutron Monitor from the Bartol Research Insititute of the University of Delaware. URL http://neutronm.bartol.udel.edu/.

[35] C. Størmer. On the Trajectories of Electric Particles in the Field of a Magnetic Dipole with Applications to the theory of Cosmic Radiation. First Communication. *Publications of the Oslo Observatory, vol. 1, pp.Ji-JPIX*, 1, 1933.

[36] J. Clay. Penetrating Radiation I. *Proc.Amsterdam Acad.Sci.*, 30:1115, 1927.

[37] J. Clay. Penetrating Radiation II. *Proc.Amsterdam Acad.Sci.*, 31:1091, 1928.

[38] L. Alvarez and A. H. Compton. A positively charged component of cosmic rays. *Physical Review*, 43(10):835–836, 1933.

[39] Thomas H. Johnson. Progress of the Directional Survey of Cosmic-Ray Intensities and Its Application to the Analysis of the Primary Cosmic Radiation. *Phys. Rev.*, 48:287–299, Aug 1935. doi: 10.1103/PhysRev.48.287.

[40] Bruno Rossi. Directional Measurements on the Cosmic Rays Near the Geomagnetic Equator. *Phys. Rev.*, 45:212–214, Feb 1934. doi: 10.1103/PhysRev.45.212.

[41] J. A. van Allen. Observations of high intensity radiation by satellites 1958 Alpha and 1958 Gamma. In P. A. Hanle, V. D. Chamberlain, and S. G. Brush, editors, *Space Science Comes of Age: Perspectives in the History of the Space Sciences*, pages 58–73, 1981.

[42] G. Lemaitre and M. S. Vallarta. On Compton's Latitude Effect of Cosmic Radiation. *Phys. Rev.*, 43:87–91, Jan 1933. doi: 10.1103/PhysRev.43.87.

[43] G. Lemaitre and M. S. Vallarta. On the Geomagnetic Analysis of Cosmic Radiation. *Phys. Rev.*, 49:719–726, May 1936. doi: 10.1103/PhysRev.49.719.

[44] E. Thébault et al. International Geomagnetic Reference Field: the 12th generation. *Earth, Planets and Space*, 67(1):79, May 2015. ISSN 1880-5981. doi: 10.1186/s40623-015-0228-9.

[45] Nikolai A. Tsyganenko and David P. Stern. Modeling the global magnetic field of the large-scale Birkeland current systems. *Journal of Geophysical Research: Space Physics*, 101(A12):27187–27198. doi: 10.1029/96JA02735.

[46] N. A. Tsyganenko and M. I. Sitnov. Modeling the dynamics of the inner magnetosphere during strong geomagnetic storms. *Journal of Geophysical Research (Space Physics)*, 110:A03208, March 2005. doi: 10.1029/2004JA010798.

[47] A. D. Sakharov. Violation of CP Invariance, C asymmetry, and baryon asymmetry of the universe. *Pisma Zh. Eksp. Teor. Fiz.*, 5:32–35, 1967. doi: 10.1070/PU1991v034n05ABEH002497. [Usp. Fiz. Nauk161,no.5,61(1991)].

[48] Bradley W. Carroll and Dale A. Ostlie. *An Introduction to Modern Astrophysics*. Pearson Education, 2007.

[49] R. Trotta, G. Jóhannesson, I. V. Moskalenko, T. A. Porter, R. Ruiz de Austri, and A. W. Strong. Constraints on Cosmic-ray Propagation Models from A Global Bayesian Analysis. *The Astrophysical Journal*, 729(2):106, 2011.

[50] T. Delahaye, F. Donato, N. Fornengo, J. Lavalle, R. Lineros, et al. Galactic secondary positron flux at the Earth. *Astron.Astrophys.*, 501:821–833, 2009. doi: 10.1051/0004-6361/200811130.

[51] B. Agrinier et al. East-west asymmetry and charge sign ratio of primary cosmic-ray electrons at 8.3 gv rigidity cut-off. *Lettere al Nuovo Cimento (1969-1970)*, 1(1):53–56, Jan 1969. ISSN 1827-613X. doi: 10.1007/BF02753694.

[52] A. Buffington, C. D. Orth, and G. F. Smoot. Measurement of primary cosmic-ray electrons and positrons from 4 to 50 GeV. *Astrophysical Journal*, 199:669–679, August 1975. doi: 10.1086/153736.

[53] D. Mueller and K.-K. Tang. Cosmic-ray positrons from 10 to 20 GeV - A balloon-borne measurement using the geomagnetic east-west asymmetry. *Astrophysical Journal*, 312:183–194, January 1987. doi: 10.1086/164859.

[54] R. L. Golden, B. G. Mauger, S. Horan, S. A. Stephens, R. R. Daniel, G. D. Badhwar, J. L. Lacy, and J. E. Zipse. Observation of cosmic ray positrons in the region from 5 to 50 GeV. *Astronomy and Astrophysics*, 188:145–154, December 1987.

[55] R. L. Golden et al. Observations of cosmic-ray electrons and positrons using an imaging calorimeter. *Astrophysical Journal*, 436:769–775, December 1994. doi: 10.1086/174951.

[56] R. L. Golden et al. Measurement of the positron to electron ratio in the cosmic rays above 5-GeV. *Astrophys. J.*, 457:L103–L106, 1996. doi: 10.1086/309896.

[57] M. Boezio et al. The Cosmic-Ray Electron and Positron Spectra Measured at 1 AU during Solar Minimum Activity. *Astrophys. J.*, 532:653–669, 2000. doi: 10.1086/308545.

[58] J.J. Beatty, A. Bhattacharyya, C. Bower, S. Coutu, M.A. DuVernois, et al. New measurement of the cosmic-ray positron fraction from 5 to 15-GeV. *Phys.Rev.Lett.*, 93:241102, 2004. doi: 10.1103/PhysRevLett.93.241102.

[59] M. Ackermann et al. Measurement of separate cosmic-ray electron and positron spectra with the Fermi Large Area Telescope. *Phys.Rev.Lett.*, 108: 011103, 2012. doi: 10.1103/PhysRevLett.108.011103.

[60] Oscar Adriani et al. An anomalous positron abundance in cosmic rays with energies 1.5-100 GeV. *Nature*, 458:607–609, 2009. doi: 10.1038/nature07942.

[61] M. Aguilar et al. Cosmic-ray positron fraction measurement from 1 to 30-GeV with AMS-01. *Phys.Lett.*, B646:145–154, 2007. doi: 10.1016/j.physletb.2007.01.024.

[62] L. Accardo et al. High Statistics Measurement of the Positron Fraction in Primary Cosmic Rays of 0.5–500 GeV with the Alpha Magnetic Spectrometer on the International Space Station. *Phys. Rev. Lett.*, 113:121101, 2014. doi: 10.1103/PhysRevLett.113.121101.

[63] M. Aguilar et al. First Result from the Alpha Magnetic Spectrometer on the International Space Station: Precision Measurement of the Positron Fraction in Primary Cosmic Rays of 0.5–350 GeV. *Phys.Rev.Lett.*, 110:141102, 2013. doi: 10.1103/PhysRevLett.110.141102.

[64] M. Aguilar et al. Electron and Positron Fluxes in Primary Cosmic Rays Measured with the Alpha Magnetic Spectrometer on the International Space Station. *Phys. Rev. Lett.*, 113:121102, Sep 2014. doi: 10.1103/PhysRevLett.113.121102.

[65] M. A. DuVernois et al. Cosmic ray electrons and positrons from 1-GeV to 100-GeV: Measurements with HEAT and their interpretation. *Astrophys. J.*, 559: 296–303, 2001. doi: 10.1086/322324.

[66] J. Chang, J.H. Adams, H.S. Ahn, G.L. Bashindzhagyan, M. Christl, et al. An excess of cosmic ray electrons at energies of 300-800 GeV. *Nature*, 456:362–365, 2008. doi: 10.1038/nature07477.

[67] S. Torii et al. High-energy electron observations by PPB-BETS flight in Antarctica. 2008.

[68] S. Abdollahi et al. Cosmic-ray electron-positron spectrum from 7 GeV to 2 TeV with the Fermi Large Area Telescope. *Phys.Rev. D*, 95(8):082007, April 2017. doi: 10.1103/PhysRevD.95.082007.

[69] O. Adriani et al. Energy Spectrum of Cosmic-Ray Electron and Positron from 10 GeV to 3 TeV Observed with the Calorimetric Electron Telescope on the International Space Station. *Phys. Rev. Lett.*, 119(18):181101, 2017. doi: 10.1103/PhysRevLett.119.181101.

[70] G. Ambrosi et al. Direct detection of a break in the teraelectronvolt cosmic-ray spectrum of electrons and positrons. *Nature*, 552:63–66, 2017. doi: 10.1038/nature24475.

[71] M. Aguilar et al. Precision Measurement of the $(e^+ + e^-)$ Flux in Primary Cosmic Rays from 0.5 GeV to 1 TeV with the Alpha Magnetic Spectrometer on the International Space Station. *Phys. Rev. Lett.*, 113:221102, 2014. doi: 10.1103/PhysRevLett.113.221102.

[72] F. Aharonian et al. Probing the ATIC peak in the cosmic-ray electron spectrum with H.E.S.S. *Astron. Astrophys.*, 508:561, 2009. doi: 10.1051/0004-6361/200913323.

[73] R. Cowsik, B. Burch, and T. Madziwa-Nussinov. The Origin of the Spectral Intensities of Cosmic-Ray Positrons. *The Astrophysical Journal*, 786(2):124, 2014.

[74] Kfir Blum, Boaz Katz, and Eli Waxman. AMS-02 Results Support the Secondary Origin of Cosmic Ray Positrons. *Phys. Rev. Lett.*, 111:211101, Nov 2013. doi: 10.1103/PhysRevLett.111.211101.

[75] M. A. Malkov, P. H. Diamond, and R. Z. Sagdeev. Positive charge prevalence in cosmic rays: Room for dark matter in the positron spectrum. *Phys. Rev. D*, 94:063006, Sep 2016. doi: 10.1103/PhysRevD.94.063006.

[76] F. Zwicky. Die Rotverschiebung von extragalaktischen Nebeln. *Helvetica Physica Acta*, 6:110–127, 1933.

[77] V. C. Rubin and W. K. Ford, Jr. Rotation of the Andromeda Nebula from a Spectroscopic Survey of Emission Regions. *Astrophysical Journal*, 159:379, February 1970. doi: 10.1086/150317.

[78] V. C. Rubin, W. K. Ford, Jr., and N. Thonnard. Extended rotation curves of high-luminosity spiral galaxies. IV - Systematic dynamical properties, SA through SC. *Astrophysical Journal*, 225:L107–L111, November 1978. doi: 10.1086/182804.

[79] E. Komatsu et al. Seven-Year Wilkinson Microwave Anisotropy Probe (WMAP) Observations: Cosmological Interpretation. *Astrophys. J. Suppl.*, 192:18, 2011. doi: 10.1088/0067-0049/192/2/18.

[80] P. A. R. Ade et al. Planck 2015 results. XIII. Cosmological parameters. *Astron. Astrophys.*, 594:A13, 2016. doi: 10.1051/0004-6361/201525830.

[81] Henk Hoekstra and Bhuvnesh Jain. Weak Gravitational Lensing and Its Cosmological Applications. *Annual Review of Nuclear and Particle Science*, 58(1): 99–123, 2008. doi: 10.1146/annurev.nucl.58.110707.171151.

[82] C. Chang et al. Dark Energy Survey Year 1 Results: Curved-Sky Weak Lensing Mass Map. *Mon. Not. Roy. Astron. Soc.*, 475:3165, 2018. doi: 10.1093/mnras/stx3363.

[83] Jonathan L. Feng. Dark Matter Candidates from Particle Physics and Methods of Detection. *Annual Review of Astronomy and Astrophysics*, 48(1):495–545, 2010. doi: 10.1146/annurev-astro-082708-101659.

[84] Scott Dodelson, Evalyn I. Gates, and Michael S. Turner. Cold Dark Matter. *Science*, 274(5284):69–75, 1996. ISSN 00368075, 10959203.

[85] Troy A. Porter, Robert P. Johnson, and Peter W. Graham. Dark Matter Searches with Astroparticle Data. *Annual Review of Astronomy and Astrophysics*, 49(1):155–194, 2011. doi: 10.1146/annurev-astro-081710-102528.

[86] Joachim Kopp. Constraints on dark matter annihilation from AMS-02 results. *Phys. Rev. D*, 88:076013, Oct 2013. doi: 10.1103/PhysRevD.88.076013.

[87] Lei Feng, Rui-Zhi Yang, Hao-Ning He, Tie-Kuang Dong, Yi-Zhong Fan, and Jin Chang. AMS-02 positron excess: new bounds on dark matter models and hint for primary electron spectrum hardening. *Phys. Lett.*, B728:250–255, 2014. doi: 10.1016/j.physletb.2013.12.012.

[88] Lars Bergstrom, Torsten Bringmann, Ilias Cholis, Dan Hooper, and Christoph Weniger. New limits on dark matter annihilation from AMS cosmic ray positron data. *Phys. Rev. Lett.*, 111:171101, 2013. doi: 10.1103/PhysRevLett.111.171101.

[89] M. Cirelli, M. Kadastik, M. Raidal, and A. Strumia. Addendum including AMS 2013 data to "Model-independent implications of the $e^{\pm}$, $\bar{p}$ cosmic ray spectra on properties of Dark Matter" [Nucl. Phys. B 813 (1-2) (2009) 1-21]. *Nuclear Physics B*, 873:530–533, August 2013. doi: 10.1016/j.nuclphysb.2013.05.002.

[90] Keith R. Dienes, Jason Kumar, and Brooks Thomas. Dynamical Dark Matter and the positron excess in light of AMS results. *Phys. Rev.*, D88(10):103509, 2013. doi: 10.1103/PhysRevD.88.103509.

[91] Qing-Hong Cao, Chuan-Ren Chen, and Ti Gong. Leptophilic Dark Matter and AMS-02 Cosmic-ray Positron Flux. *Chin. J. Phys.*, 55:10, 2016. doi: 10.1016/j.cjph.2016.11.006.

[92] Yuji Kajiyama, Hiroshi Okada, and Takashi Toma. New Interpretation of the Recent Result of AMS-02 and Multi-component Decaying Dark Matters with non-Abelian Discrete Flavor Symmetry. *Eur. Phys. J.*, C74:2722, 2014. doi: 10.1140/epjc/s10052-014-2722-9.

[93] Chuan-Hung Chen, Cheng-Wei Chiang, and Takaaki Nomura. Dark matter for excess of AMS-02 positrons and antiprotons. *Phys. Lett.*, B747:495–499, 2015. doi: 10.1016/j.physletb.2015.06.035.

[94] M. Boudaud, S. Aupetit, S. Caroff, A. Putze, G. Belanger, Y. Genolini, C. Goy, V. Poireau, V. Poulin, S. Rosier, P. Salati, L. Tao, and M. Vecchi. A new look at the cosmic ray positron fraction. *Astronomy and Astrophysics*, 575:A67, March 2015. doi: 10.1051/0004-6361/201425197.

[95] R. Cowsik. Positrons and Antiprotons in Galactic Cosmic Rays. *Annual Review of Nuclear and Particle Science*, 66(1):297–319, 2016. doi: 10.1146/annurev-nucl-102115-044851.

[96] Leila Ali Cavasonza, Henning Gast, Michael Krämer, Mathieu Pellen, and Stefan Schael. Constraints on Leptophilic Dark Matter from the AMS-02 Experiment. *The Astrophysical Journal*, 839(1):36, 2017.

[97] A. Hewish, S. J. Bell, J. D. H. Pilkington, P. F. Scott, and R. A. Collins. Observation of a Rapidly Pulsating Radio Source. *Nature*, 217:709–713, February 1968. doi: 10.1038/217709a0.

[98] Pasquale Blasi and Elena Amato. Positrons from pulsar winds. In *Proceedings, 1st Session of the Sant Cugat Forum on Astrophysics: High-Energy Emission from Pulsars and their Systems: Sant Cugat, Catalonia, Spain, April 12-16, 2010*, pages 623–641, 2011. doi: 10.1007/978-3-642-17251-9_50.

[99] Elena Amato. The theory of pulsar wind nebulae. *International Journal of Modern Physics: Conference Series*, 28:1460160, 2014. doi: 10.1142/S2010194514601604.

[100] Pasquale D. Serpico. Astrophysical models for the origin of the positron 'excess'. *Astropart.Phys.*, 39-40:2–11, 2012. doi: 10.1016/j.astropartphys.2011.08.007.

[101] Tim Linden and Stefano Profumo. Probing the Pulsar Origin of the Anomalous Positron Fraction with AMS-02 and Atmospheric Cherenkov Telescopes. *The Astrophysical Journal*, 772(1):18, 2013.

[102] Ilias Cholis and Dan Hooper. Dark matter and pulsar origins of the rising cosmic ray positron fraction in light of new data from the AMS. *Phys. Rev. D*, 88:023013, Jul 2013. doi: 10.1103/PhysRevD.88.023013.

[103] Anatoly Erlykin and Arnold W. Wolfendale. Cosmic ray positrons from a local, middle-aged supernova remnant. *Astropart. Phys.*, 49:23–27, 2013. doi: 10.1016/j.astropartphys.2013.08.001.

[104] Peng-Fei Yin, Zhao-Huan Yu, Qiang Yuan, and Xiao-Jun Bi. Pulsar interpretation for the AMS-02 result. *Phys. Rev.*, D88(2):023001, 2013. doi: 10.1103/PhysRevD.88.023001.

[105] C. Venter, A. Kopp, A. K. Harding, P. L. Gonthier, and I. Büsching. Cosmic-ray Positrons from Millisecond Pulsars. *The Astrophysical Journal*, 807(2):130, 2015.

[106] Daniele Gaggero, Luca Maccione, Dario Grasso, Giuseppe Di Bernardo, and Carmelo Evoli. PAMELA and AMS-02 e^+ and e^- spectra are reproduced by three-dimensional cosmic-ray modeling. *Phys. Rev. D*, 89:083007, Apr 2014. doi: 10.1103/PhysRevD.89.083007.

[107] N. Fornengo. Astrophysical interpretation of the ASM-02 leptonic data. *Nuclear and Particle Physics Proceedings*, 265:248–250, August 2015. doi: 10.1016/j.nuclphysbps.2015.06.064.

[108] M. Di Mauro, F. Donato, N. Fornengo, R. Lineros, and A. Vittino. Interpretation of AMS-02 electrons and positrons data. *Journal of Cosmology and Astroparticle Physics*, 2014(04):006, 2014.

[109] M. Aguilar et al. Precision Measurement of the Proton Flux in Primary Cosmic Rays from Rigidity 1 GV to 1.8 TV with the Alpha Magnetic Spectrometer on the International Space Station. *Phys. Rev. Lett.*, 114:171103, Apr 2015. doi: 10.1103/PhysRevLett.114.171103.

[110] M. Aguilar et al. Precision Measurement of the Helium Flux in Primary Cosmic Rays of Rigidities 1.9 GV to 3 TV with the Alpha Magnetic Spectrometer on the International Space Station. *Phys. Rev. Lett.*, 115:211101, Nov 2015. doi: 10.1103/PhysRevLett.115.211101.

[111] M. Aguilar et al. Observation of the Identical Rigidity Dependence of He, C, and O Cosmic Rays at High Rigidities by the Alpha Magnetic Spectrometer on the International Space Station. *Phys. Rev. Lett.*, 119:251101, Dec 2017. doi: 10.1103/PhysRevLett.119.251101.

[112] M. Aguilar et al. Observation of New Properties of Secondary Cosmic Rays Lithium, Beryllium, and Boron by the Alpha Magnetic Spectrometer on the International Space Station. *Phys. Rev. Lett.*, 120:021101, Jan 2018. doi: 10.1103/PhysRevLett.120.021101.

[113] Bernard, G., Delahaye, T., Keum, Y.-Y., Liu, W., Salati, P., and Taillet, R. TeV cosmic-ray proton and helium spectra in the myriad model. *A&A*, 555:A48, 2013. doi: 10.1051/0004-6361/201321202.

[114] Vladimir Ptuskin, Vladimir Zirakashvili, and Eun-Suk Seo. Spectra of Cosmic-Ray Protons and Helium Produced in Supernova Remnants. *The Astrophysical Journal*, 763(1):47, 2013.

[115] Pasquale Blasi and Elena Amato. Diffusive propagation of cosmic rays from supernova remnants in the Galaxy. II: anisotropy. *Journal of Cosmology and Astroparticle Physics*, 2012(01):011, 2012.

[116] Aloisio, R., Blasi, P., and Serpico, P. D. Nonlinear cosmic ray Galactic transport in the light of AMS-02 and Voyager data. *A&A*, 583, 2015. doi: 10.1051/0004-6361/201526877.

[117] Pasquale Blasi, Elena Amato, and Pasquale D. Serpico. Spectral Breaks as a Signature of Cosmic Ray Induced Turbulence in the Galaxy. *Phys. Rev. Lett.*, 109:061101, Aug 2012. doi: 10.1103/PhysRevLett.109.061101.

[118] P. Blasi. Non-linear Cosmic Ray Propagation. 2017.

[119] Rainer Beck. Galactic and extragalactic magnetic fields. *Space Sci. Rev.*, 99: 243–260, 2001. doi: 10.1023/A:1013805401252.

[120] G. L. Cassiday, R. Cooper, B. R. Dawson, J. W. Elbert, B. E. Fick, K. D. Green, S. Ko, D. F. Liebing, E. C. Loh, M. H. Salamon, J. D. Smith, P. Sokolsky, P. Sommers, and S. B. Thomas. Evidence for 10^{18}-eV Neutral Particles from the Direction of Cygnus X-3. *Phys. Rev. Lett.*, 62:383–386, Jan 1989. doi: 10.1103/PhysRevLett.62.383.

[121] G. L. Cassiday et al. Mapping the UHE sky in search of point sources. *Nucl. Phys. Proc. Suppl.*, 14A:291–298, 1990. doi: 10.1016/0920-5632(90)90434-V.

[122] Robert W. Atkins et al. Observation of TeV gamma-rays from the Crab nebula with MILAGRO using a new background rejection technique. *Astrophys. J.*, 595:803–811, 2003. doi: 10.1086/377498.

[123] M. Ahlers, S. Y. BenZvi, P. Desiati, J. C. Díaz–Vélez, D. W. Fiorino, and S. Westerhoff. A New Maximum-likelihood Technique for Reconstructing Cosmic-Ray Anisotropy at All Angular Scales. *The Astrophysical Journal*, 823(1):10, 2016.

[124] John Linsley. Fluctuation effects on directional data. *Phys. Rev. Lett.*, 34:1530–1533, 1975. doi: 10.1103/PhysRevLett.34.1530.

[125] W. Gao, S. Chen H.H. He, and S. Cui on behalf of the ARGO-YBJ Collaboration. Study of the dependence of the large scale anisotropy on the nature of the primary cosmic rays with the ARGO-YBJ experiment. In *Proceedings, 35th International Cosmic Ray Conference (ICRC2017): Bexco, Busan, Korea, July 10-20, 2017*.

[126] G. Di Sciascio and R. Iuppa. On the Observation of the Cosmic Ray Anisotropy below 10^{15} eV. 2014.

[127] Antonella Castellina and Fiorenza Donato. *Astrophysics of Galactic Charged Cosmic Rays*, pages 725–788. Springer Netherlands, Dordrecht, 2013. ISBN 978-94-007-5612-0. doi: 10.1007/978-94-007-5612-0_14.

[128] Arthur H. Compton and Ivan A. Getting. An Apparent Effect of Galactic Rotation on the Intensity of Cosmic Rays. *Phys. Rev.*, 47:817–821, Jun 1935. doi: 10.1103/PhysRev.47.817.

[129] M. Aglietta et al. A Measurement of the Solar and Sidereal Cosmic-Ray Anisotropy at E(0) approximately 10^14 eV. *Astrophys.J.*, 470:501, October 1996. doi: 10.1086/177881.

[130] M. Amenomori et al. Observation by an Air-Shower Array in Tibet of the Multi-TeV Cosmic-Ray Anisotropy due to Terrestrial Orbital Motion Around the Sun. *Physical Review Letters*, 93(6):061101, August 2004. doi: 10.1103/PhysRevLett.93.061101.

[131] A. A. Abdo et al. The Large Scale Cosmic-Ray Anisotropy as Observed with Milagro. *Astrophys. J.*, 698:2121–2130, 2009. doi: 10.1088/0004-637X/698/2/2121.

[132] R. Abbasi et al. Measurement of the Anisotropy of Cosmic Ray Arrival Directions with IceCube. *Astrophys. J.*, 718:L194, 2010. doi: 10.1088/2041-8205/718/2/L194.

[133] M. Amenomori et al. Anisotropy and Corotation of Galactic Cosmic Rays. *Science*, 314:439–443, October 2006. doi: 10.1126/science.1131702.

[134] K. Nagashima, K. Fujimoto, and R. M. Jacklyn. Galactic and heliotail-in anisotropies of cosmic rays as the origin of sidereal daily variation in the energy region < 104 GeV. *Journal of Geophysical Research: Space Physics*, 103(A8): 17429–17440. doi: 10.1029/98JA01105.

[135] Kazuo Nagashima, Zenjiro Fujii, and Kazuoki Munakata. Solar modulation of galactic and heliotail-in anisotropies of cosmic rays at Sakashita underground station (320 - 650 GeV). *Earth, Planets and Space*, 56(4):479–483, 2004. doi: 10.1186/BF03352501.

[136] Rahul Kumar and David Eichler. The isotropy problem of Sub-ankle Ultra-high energy cosmic rays. *Astrophys. J.*, 781(1):47, 2014. doi: 10.1088/0004-637X/781/1/47.

[137] M. G. Aartsen et al. Anisotropy in Cosmic-Ray Arrival Directions in the Southern Hemisphere Based on Six Years of Data from the IceCube Detector. *The Astrophysical Journal*, 826(2):220, 2016.

[138] A. Chiavassa et al. KASCADE-Grande experiment measurements of the cosmic ray spectrum and large scale anisotropy. *Nucl. Part. Phys. Proc.*, 279-281: 56–62, 2016. doi: 10.1016/j.nuclphysbps.2016.10.009.

[139] P. Abreu et al. Search for First Harmonic Modulation in the Right Ascension Distribution of Cosmic Rays Detected at the Pierre Auger Observatory. *Astropart. Phys.*, 34:627–639, 2011. doi: 10.1016/j.astropartphys.2010.12.007.

[140] P. Abreu et al. Constraints on the origin of cosmic rays above 10^{18} eV from large scale anisotropy searches in data of the Pierre Auger Observatory. *Astrophys. J.*, 762:L13, 2012. doi: 10.1088/2041-8205/762/1/L13.

[141] A. Aab et al. Observation of a large-scale anisotropy in the arrival directions of cosmic rays above 8×10^18 eV. *Science*, 357(6357):1266–1270, 2017. ISSN 0036-8075. doi: 10.1126/science.aan4338.

[142] Stefano Profumo. An observable electron-positron anisotropy cannot be generated by dark matter. *JCAP*, 1502(02):043, 2015. doi: 10.1088/1475-7516/2015/02/043.

[143] Miguel Pato, Massimiliano Lattanzi, and Gianfranco Bertone. Discriminating the source of high-energy positrons with AMS-02. *Journal of Cosmology and Astroparticle Physics*, 2010(12):020, 2010.

[144] Ignacio Cernuda. Cosmic ray electron Anisotropies as a tool to discriminate between Exotic and Astrophysical sources. *Astropart.Phys.*, 34:59–69, 2010. doi: 10.1016/j.astropartphys.2010.05.003.

[145] Enrico Borriello, Luca Maccione, and Alessandro Cuoco. Electron anisotropy: A tool to discriminate dark matter in cosmic rays. *J. Phys. Conf. Ser.*, 375: 012031, 2012. doi: 10.1088/1742-6596/375/1/012031.

[146] Dan Hooper, Pasquale Blasi, and Pasquale Dario Serpico. Pulsars as the sources of high energy cosmic ray positrons. *Journal of Cosmology and Astroparticle Physics*, 2009(01):025, 2009.

[147] Tim Linden and Stefano Profumo. Probing the Pulsar Origin of the Anomalous Positron Fraction with AMS-02 and Atmospheric Cherenkov Telescopes. *The Astrophysical Journal*, 772(1):18, 2013.

[148] S. Della Torre, M. Gervasi, P.G. Rancoita, D. Rozza, and A. Treves. Pulsar Wind Nebulae as a source of the observed electron and positron excess at high energy: The case of Vela-X. *Journal of High Energy Astrophysics*, 8:27 – 34, 2015. ISSN 2214-4048. doi: https://doi.org/10.1016/j.jheap.2015.08.001.

[149] S. Manconi, M. Di Mauro, and F. Donato. Dipole anisotropy in cosmic electrons and positrons: inspection on local sources. *Journal of Cosmology and Astroparticle Physics*, 2017(01):006, 2017.

[150] Jorge Casaus. Determination of anisotropy with AMS. In *Proceedings, 33rd International Cosmic Ray Conference (ICRC2013): Rio de Janeiro, Brazil, July 2-9, 2013*, page 1261.

[151] O. Adriani et al. Search for Anisotropies in Cosmic-ray Positrons Detected By the PAMELA Experiment. *The Astrophysical Journal*, 811(1):21, 2015.

[152] S. Abdollahi et al. Search for Cosmic-Ray Electron and Positron Anisotropies with Seven Years of Fermi Large Area Telescope Data. *Phys. Rev. Lett.*, 118: 091103, Mar 2017. doi: 10.1103/PhysRevLett.118.091103.

[153] G. Ambrosi. AMS, a particle detector in space: results from the precursor flight and status of AMS-02. *Nuclear Physics B - Proceedings Supplements*, 125:236 – 244, 2003. ISSN 0920-5632. doi: https://doi.org/10.1016/S0920-5632(03)90997-2. Innovative Particle and Radiation Detectors.

[154] J. Alcaraz et al. Protons in near earth orbit. *Physics Letters B*, 472(1):215 – 226, 2000. ISSN 0370-2693. doi: https://doi.org/10.1016/S0370-2693(99)01427-6.

[155] J. Alcaraz et al. Leptons in near earth orbit. *Physics Letters B*, 484(1):10 – 22, 2000. ISSN 0370-2693. doi: https://doi.org/10.1016/S0370-2693(00)00588-8.

[156] M. Aguilar et al. The Alpha Magnetic Spectrometer (AMS) on the International Space Station: Part I – results from the test flight on the space shuttle. *Physics Reports*, 366(6):331 – 405, 2002. ISSN 0370-1573. doi: https://doi.org/10.1016/S0370-1573(02)00013-3.

[157] J. Alcaraz et al. Search for antihelium in cosmic rays. *Physics Letters B*, 461(4):387 – 396, 1999. ISSN 0370-2693. doi: https://doi.org/10.1016/S0370-2693(99)00874-6.

[158] J. Alcaraz et al. Helium in near Earth orbit. *Physics Letters B*, 494(3):193 – 202, 2000. ISSN 0370-2693. doi: https://doi.org/10.1016/S0370-2693(00)01193-X.

[159] J. Alcaraz et al. Cosmic protons. *Physics Letters B*, 490(1):27 – 35, 2000. ISSN 0370-2693. doi: https://doi.org/10.1016/S0370-2693(00)00970-9.

[160] M. Aguilar et al. A study of cosmic ray secondaries induced by the Mir space station using AMS-01. *Nuclear Instruments and Methods in Physics Research Section B: Beam Interactions with Materials and Atoms*, 234(3):321 – 332, 2005. ISSN 0168-583X. doi: https://doi.org/10.1016/j.nimb.2005.01.015.

[161] Samuel Ting. The Alpha Magnetic Spectrometer on the International Space Station. *Nuclear Physics B - Proceedings Supplements*, 243-244:12 – 24, 2013. ISSN 0920-5632. doi: https://doi.org/10.1016/j.nuclphysbps.2013.09.028. Proceedings of the IV International Conference on Particle and Fundamental Physics in Space.

[162] Andrei Kounine. The Alpha Magnetic Spectrometer on the International Space Station. *International Journal of Modern Physics E*, 21(08):1230005, 2012. doi: 10.1142/S0218301312300056.

[163] S. Ahlen et al. An antimatter spectrometer in space. *Nuclear Instruments and Methods in Physics Research Section A: Accelerators, Spectrometers, Detectors and Associated Equipment*, 350(1):351 – 367, 1994. ISSN 0168-9002. doi: https://doi.org/10.1016/0168-9002(94)91184-3.

[164] Hesheng Chen. Permanent magnet system of alpha magnetic spectrometer. *Science in China Series A: Mathematics*, 43(9):996–1008, Sep 2000. ISSN 1862-2763. doi: 10.1007/BF02879806.

[165] K. Lübelsmeyer et al. Upgrade of the Alpha Magnetic Spectrometer (AMS-02) for long term operation on the International Space Station (ISS). *Nuclear Instruments and Methods in Physics Research Section A: Accelerators, Spectrometers, Detectors and Associated Equipment*, 654(1):639 – 648, 2011. ISSN 0168-9002. doi: https://doi.org/10.1016/j.nima.2011.06.051.

[166] Sadakazu Haino. Performance of the AMS-02 silicon tracker in the ISS mission. *Nuclear Instruments and Methods in Physics Research Section A: Accelerators, Spectrometers, Detectors and Associated Equipment*, 699:221 – 224, 2013. ISSN 0168-9002. doi: https://doi.org/10.1016/j.nima.2012.05.060. Proceedings of the 8th International "Hiroshima" Symposium on the Development and Application of Semiconductor Tracking Detectors.

[167] Paolo Zuccon. AMS-02 Track reconstruction and rigidity measurement. In *Proceedings, 33rd International Cosmic Ray Conference (ICRC2013): Rio de Janeiro, Brazil, July 2-9, 2013*, page 1064.

[168] G. Ambrosi et al. Alignment of the AMS-02 silicon Tracker. In *Proceedings, 33rd International Cosmic Ray Conference (ICRC2013): Rio de Janeiro, Brazil, July 2-9, 2013*, page 1260, 2013.

[169] G. Ambrosi, V. Choutko, C. Delgado, A. Oliva, Q. Yan, and Y. Li. The spatial resolution of the silicon tracker of the Alpha Magnetic Spectrometer. *Nuclear Instruments and Methods in Physics Research Section A: Accelerators, Spectrometers, Detectors and Associated Equipment*, 869:29 – 37, 2017. ISSN 0168-9002. doi: https://doi.org/10.1016/j.nima.2017.07.014.

[170] Zhaoyi Qu, Sadakazu Haino, Paolo Zuccon, and Minggang Zhao. New track finding based on cellar automaton for AMS-02 detector. *Nuclear Instruments and Methods in Physics Research Section A: Accelerators, Spectrometers, Detectors and Associated Equipment*, 869:135 – 140, 2017. ISSN 0168-9002. doi: https://doi.org/10.1016/j.nima.2017.07.007.

[171] Pierre Saouter. Nuclear charge measurement with the AMS-02 Silicon Tracker. In *Proceedings, 33rd International Cosmic Ray Conference (ICRC2013): Rio de Janeiro, Brazil, July 2-9, 2013*, page 0789.

[172] S. Vitillo et al. Nuclei Charge measurement with the AMS-02 Silicon Tracker. *PoS*, ICRC2015:429, 2016.

[173] P. Saouter. Nuclei identification with the AMS-02 Silicon Tracker. In *2014 IEEE Nuclear Science Symposium and Medical Imaging Conference (NSS/MIC)*, pages 1–6, Nov 2014. doi: 10.1109/NSSMIC.2014.7431209.

[174] X. Artru, G. B. Yodh, and G. Mennessier. Practical theory of the multilayered transition radiation detector. *Phys. Rev. D*, 12:1289–1306, Sep 1975. doi: 10.1103/PhysRevD.12.1289.

[175] V.L Ginzburg and V.N Tsytovich. Several problems of the theory of transition radiation and transition scattering. *Physics Reports*, 49(1):1 – 89, 1979. ISSN 0370-1573. doi: https://doi.org/10.1016/0370-1573(79)90052-8.

[176] Boris Dolgoshein. Transition radiation detectors. *Nuclear Instruments and Methods in Physics Research Section A: Accelerators, Spectrometers, Detectors and Associated Equipment*, 326(3):434 – 469, 1993. ISSN 0168-9002. doi: https://doi.org/10.1016/0168-9002(93)90846-A.

[177] Th. Kirn. The AMS-02 transition radiation detector. *Nuclear Instruments and Methods in Physics Research Section A: Accelerators, Spectrometers, Detectors and Associated Equipment*, 581(1):156 – 159, 2007. ISSN 0168-9002. doi: https://doi.org/10.1016/j.nima.2007.07.052. VCI 2007.

[178] Henning Gast et al. Identification of cosmic-ray positrons with the transition radiation detector of the AMS experiment on the International Space Station. In *Proceedings, 33rd International Cosmic Ray Conference (ICRC2013): Rio de Janeiro, Brazil, July 2-9, 2013*, page 0359, 2013.

[179] M. Heil et al. Operations and Alignment of the AMS-02 Transition Radiation Detector. In *Proceedings, 33rd International Cosmic Ray Conference (ICRC2013): Rio de Janeiro, Brazil, July 2-9, 2013*, page 1232, 2013.

[180] V. Bindi, G.M. Chen, H.S. Chen, E. Choumilov, V. Choutko, A. Contin, A. Lebedev, Y.S. Lu, N. Masi, A. Oliva, F. Palmonari, L. Quadrani, and Q. Yan. Calibration and performance of the AMS-02 time of flight detector in space. *Nuclear Instruments and Methods in Physics Research Section A: Accelerators, Spectrometers, Detectors and Associated Equipment*, 743:22 – 29, 2014. ISSN 0168-9002. doi: https://doi.org/10.1016/j.nima.2014.01.002.

[181] Lucio Quadrani. The AMS-02 time of flight (TOF) system: construction and overall performances in space. In *Proceedings, 33rd International Cosmic Ray Conference (ICRC2013): Rio de Janeiro, Brazil, July 2-9, 2013*, page 1046.

[182] F. Giovacchini. Performance in space of the AMS-02 RICH detector. *Nuclear Instruments and Methods in Physics Research Section A: Accelerators, Spectrometers, Detectors and Associated Equipment*, 766:57 – 60, 2014. ISSN 0168-9002. doi: https://doi.org/10.1016/j.nima.2014.04.036. RICH2013 Proceedings of the Eighth International Workshop on Ring Imaging Cherenkov Detectors Shonan, Kanagawa, Japan, December 2-6, 2013.

[183] Hu Liu, J. Casaus, F. Giovacchini, A. Oliva, and X. Xia. The RICH detector of AMS-02: 5 years of operation in space. *Nuclear Instruments and Methods in Physics Research Section A: Accelerators, Spectrometers, Detectors and Associated Equipment*, 876:5 – 8, 2017. ISSN 0168-9002. doi: https://doi.org/10.1016/j.nima.2016.12.011. The 9th international workshop on Ring Imaging Cherenkov Detectors (RICH2016).

[184] P. A. Čerenkov. Visible Radiation Produced by Electrons Moving in a Medium with Velocities Exceeding that of Light. *Phys. Rev.*, 52:378–379, Aug 1937. doi: 10.1103/PhysRev.52.378.

[185] I. M. Frank and I. E. Tamm. Coherent visible radiation of fast electrons passing through matter. *Compt. Rend. Acad. Sci. URSS*, 14(3):109–114, 1937. doi: 10.1007/978-3-642-74626-0_2,10.3367/UFNr.0093.196710o.0388. [Usp. Fiz. Nauk93,no.2,388(1967)].

[186] Francesca Giovacchini. In-flight determination of the AMS-RICH photon yield. In *Proceedings, 33rd International Cosmic Ray Conference (ICRC2013): Rio de Janeiro, Brazil, July 2-9, 2013*, page 1028.

[187] Stefano Di Falco. Performance of the AMS-02 Electromagnetic Calorimeter in Space. In *Proceedings, 33rd International Cosmic Ray Conference (ICRC2013): Rio de Janeiro, Brazil, July 2-9, 2013*, page 0855, 2013.

[188] C. Adloff et al. The AMS-02 lead-scintillating fibres Electromagnetic Calorimeter. *Nuclear Instruments and Methods in Physics Research Section A: Accelerators, Spectrometers, Detectors and Associated Equipment*, 714:147 – 154, 2013. ISSN 0168-9002. doi: https://doi.org/10.1016/j.nima.2013.02.020.

[189] G Gallucci and the AMS-02 ECAL group. Performance of the AMS-02 Electromagnetic Calorimeter in Space. *Journal of Physics: Conference Series*, 587(1): 012028, 2015.

[190] Sylvie Rosier-Lees and on behalf of the AMS02 collaboration). Performance of the AMS02 Electromagnetic Calorimeter in space. *Journal of Physics: Conference Series*, 404(1):012034, 2012.

[191] M. Vecchi et al. The electromagnetic calorimeter of the AMS-02 experiment. In *Week of French Astrophysics: Semaine de l'Astrophysique Francaise (SF2A 2012) Nice, France, June 5-8, 2012*, 2012.

[192] Ph. von Doetinchem, W. Karpinski, Th. Kirn, K. Lübelsmeyer, St. Schael, and M. Wlochal. The AMS-02 Anticoincidence Counter. *Nuclear Physics B - Proceedings Supplements*, 197(1):15 – 18, 2009. ISSN 0920-5632. doi: https://doi.org/10.1016/j.nuclphysbps.2009.10.025. 11th Topical Seminar on Innovative Particle and Radiation Detectors (IPRD08).

[193] URL http://www.ams02.org.

[194] A. Basili et al. The TOF-ACC flight electronics for the fast trigger and time of flight of the AMS-02 cosmic ray spectrometer. *Nuclear Instruments and Methods in Physics Research Section A: Accelerators, Spectrometers, Detectors and Associated Equipment*, 707:99 – 113, 2013. ISSN 0168-9002. doi: https://doi.org/10.1016/j.nima.2012.12.089.

[195] Maura Graziani, Bruna Bertucci, and Matteo Duranti. Time dependence of electron and positron fluxes measured with the AMS-02 spectrometer, Dec 2015.

[196] X. Cai. On board computing system for AMS-02 mission. *International Cosmic Ray Conference*, 3:373, 2005.

[197] M. Capell, E. Cortina, and AMS-02 Collaboration. AMS-02 Electronics. *International Cosmic Ray Conference*, 4:2173, July 2003.

[198] A Lebedev. The AMS-02 Electronics System. 2005.

[199] Wenhao Sun. Introduction to AMS Operations, 03 2016. Internal note.

[200] URL https://earth.esa.int/web/eoportal/satellite-missions/i/iss-ams.

[201] Peter Duffett-Smith and Jonathan Zwart. *Practical Astronomy with your Calculator or Spreadsheet*. Cambridge University Press, 2017. doi: 10.1017/CBO9780511861161.

[202] Jean H. Meeus. *Astronomical Algorithms*. Willmann-Bell, Inc., 1991. ISBN 0943396352.

[203] Kenneth R. Lang. *Astrophysical Formulae: Volume I & Volume II: Radiation, Gas Processes and High Energy Astrophysics / Space, Time, Matter and Cosmology (Astronomy and Astrophysics Library)*. Springer-Verlag New York, Inc., Secaucus, NJ, USA, 2006. ISBN 3540296921.

[204] M. Fränz and D. Harper. Heliospheric coordinate systems. *Planetary and Space Science*, 50:217–233, February 2002. doi: 10.1016/S0032-0633(01)00119-2.

[205] M.A. Hapgood. Space physics coordinate transformations: A user guide. *Planetary and Space Science*, 40(5):711 – 717, 1992. ISSN 0032-0633. doi: https://doi.org/10.1016/0032-0633(92)90012-D.

[206] S. Della Torre, C. Consolandi, and D. Grandi. Coordinates and Sun Position for AMS-02, 02 2012. Internal note.

[207] G.B. Arfken and H.J. Weber. *Mathematical Methods for Physicists*. Mathematical Methods for Physicists. Elsevier Science, 2013. ISBN 9781483288062.

[208] Prey. The theory of spherical and ellipsoidal harmonics. *Monatshefte für Mathematik und Physik*, 41(1):A22–A22, Dec 1934. ISSN 1436-5081. doi: 10.1007/BF01697927.

[209] E. T. Whittaker and G. N. Watson. *A Course of Modern Analysis*. Cambridge Mathematical Library. Cambridge University Press, 4 edition, 1996. doi: 10.1017/CBO9780511608759.

[210] J. Berdugo, J. Casaus, C. Mana, and M. A. Velasco. On the upper limits for dipole anisotropies in cosmic-ray positrons. 2015.

[211] G. La Vacca. Search for Cosmic Ray Anisotropy with the Alpha Magnetic Spectrometer on the International Space Station. In *25th European Cosmic Ray Symposium (ECRS 2016) Turin, Italy, September 04-09, 2016*, 2016.

[212] D. E. Alexandreas et al. Point source search techniques in ultrahigh-energy gamma-ray astronomy. *Nucl. Instrum. Meth.*, A328:570–577, 1993. doi: 10.1016/0168-9002(93)90677-A.

[213] J.D. Sullivan. Geometrical factor and directional response of single and multi-element particle telescopes. *Nucl.Instrum.Meth.*, 95:5–11, 1971. doi: 10.1016/0029-554X(71)90033-4.

[214] K.M. Gorski, Eric Hivon, A.J. Banday, B.D. Wandelt, F.K. Hansen, et al. HEALPix - A Framework for high resolution discretization, and fast analysis of data distributed on the sphere. *Astrophys.J.*, 622:759–771, 2005. doi: 10.1086/427976.

[215] T.-P. Li and Y.-Q. Ma. Analysis methods for results in gamma-ray astronomy. *Astrophysical Journal*, 272:317–324, September 1983. doi: 10.1086/161295.

[216] James O. Berger, Jose M. Bernardo, and Dongchu Sun. Objective Priors for Discrete Parameter Spaces. *Journal of the American Statistical Association*, 107 (498):636–648, 2012. doi: 10.1080/01621459.2012.682538.

[217] C. Maña. *Probability and Statistics for Particle Physics*. UNITEXT for Physics. Springer International Publishing, 2017. ISBN 9783319557380.

[218] O. Adriani et al. Time Dependence of the Electron and Positron Components of the Cosmic Radiation Measured by the PAMELA Experiment between July 2006 and December 2015. *Phys. Rev. Lett.*, 116:241105, Jun 2016. doi: 10.1103/PhysRevLett.116.241105.

[219] Cosmic Ray Station of the University of Oulu. URL http://cosmicrays.oulu.fi/.

[220] J. Neyman. Outline of a Theory of Statistical Estimation Based on the Classical Theory of Probability. *Phil. Trans. Roy. Soc. Lond.*, A236(767):333–380, 1937. doi: 10.1098/rsta.1937.0005.

[221] Gary J. Feldman and Robert D. Cousins. Unified approach to the classical statistical analysis of small signals. *Phys. Rev. D*, 57:3873–3889, Apr 1998. doi: 10.1103/PhysRevD.57.3873.

[222] Luca Lista. Statistical Methods for Data Analysis in Particle Physics. *Lect. Notes Phys.*, 909:pp.1–172, 2016. doi: 10.1007/978-3-319-20176-4.

[223] J. Berdugo, V. Choutko, C. Delgado, and Q. Yan. Determination of the rigidity scale of the Alpha Magnetic Spectrometer. *Nuclear Instruments and Methods in Physics Research Section A: Accelerators, Spectrometers, Detectors and Associated Equipment*, 869:10 – 14, 2017. ISSN 0168-9002. doi: https://doi.org/10.1016/j.nima.2017.07.012.